Design and Optimisation of Solar Sail Orbits in Proximity of Asteroids

Iain Moore

Submitted in fulfilment of the requirements for the
Degree of Doctor of Philosophy

James Watt School of Engineering
College of Science and Engineering
University of Glasgow

Supervised by
Dr. Matteo Ceriotti
Prof. Colin R. McInnes

October 2022

In loving memory of
Julio, Sandra and Sarai

Abstract

A solar sail is a large reflective membrane which is capable of producing thrust for a spacecraft by the reflection of sunlight. Such a propellant-less propulsion system can offer solutions to high-energy missions which would be impossible for conventional propulsion systems. As a result, this technology has been proposed by many authors as the ideal candidate for a multiple asteroid rendezvous mission.

At the time of writing, there are more than 30,000 known near-Earth asteroids (NEAs) alone. Adding to this those contained in the main belt and elsewhere in the solar system, the abundance of these small rocky worlds becomes apparent. Focusing only on the NEAs, there are many reasons for interest in missions to these bodies. In the first instance, they represent the earliest building blocks of the rocky worlds of the solar system, and are often still in pristine condition, similar to how they would have been since these earliest moments. As such, there is massive scientific interest in visiting and extracting samples of their constituent materials. There is another community which is also interested in the extraction of these materials: the future asteroid miners. This mining could provide propellant for deep space missions, materials for in-space infrastructure and potentially also in the return of minerals which are rare on Earth, and so of great value. However, although these bodies provide many opportunities, they are not without threat. Although the frequency of impacts of large bodies capable of causing considerable damage to Earth-based infrastructure is relatively low, there are still recent examples of just such events. With the potential for large scale loss of life due to an asteroid impacting populated areas, the science of planetary defence requires greater knowledge of the make-up of these bodies. Yet another reason for mission designers to examine further options in achieving efficient missions to these bodies.

It would be beneficial, in terms of cost, for a single spacecraft to be able to carry out a mission to multiple asteroids. Such a high-energy mission is ideally suited to the solar sail. Although the literature has provided many works on orbital transfers to multiple bodies, the operation of the sail when in proximity of the asteroid has not received quite as much attention. It is in this phase of the mission, where the science objectives would be carried out, that this thesis focuses. There are numerous challenges which the sail faces in the near-asteroid environment. These include the irregular gravity field, the strength of the acceleration provided by the sail in a relatively weak gravitational field, the often fast rotational velocities of the asteroid and higher demands

on slew rates for the sail due to the shorter period of low-altitude orbits.

The work will consider three main proximity phases. The first operation is in the control of an orbit using the solar sail in an irregular gravity field. In this operation, the sail must counter the perturbative effects of a non-spherical body. This manifests in the rotation of the orbit node line, referred to as nodal regression. A new tool, referred to as the Control Transition Matrix (CTM), which aids in forcing a periodic orbit solution over multiple orbits is then presented. The second operation deals with the control of a sail at the point of and subsequent to the deployment of a lander and during the deployment of a series of small ChipSat probes. The landing conditions for deployments from various locations around the asteroid are analysed before the deployment is presented from a low-asteroid orbit. The control of the sail along a nominal orbit while the lander is still on-board is presented before the sail control subsequent to the lander deployment is considered. Given the high velocity impacts for a ballistic lander deployed at large distances from the surface, an alternative mission scenario of the deployment of small ChipSat probes is presented. These probes are envisaged to carry out their science goals during the descent and so the landing conditions are less important. The final operation is in the gravitational capture of the sail around the asteroid. This work provides a preliminary analysis of the capability of the sail in achieving this by using a simple on/off control law. Following this, a more detailed two-phase approach is presented. In the first "initial capture" phase, the sail uses the value of Jacobi constant in the 3-body system as a guide to reduce the orbit radius to within a defined region. After this, the "orbit shaping" phase aims to circularise the orbit at this radius. Subsequently, preliminary investigations into an optimal approach are presented.

In controlling the effects due to the non-spherical asteroid shape, an optimally controlled solution, where a minimum effort control law is sought, is presented. Following this, a novel method of updating a control law was successfully applied to force a periodic orbit. In the work carried out on lander deployment, it was found that the sail was capable of maintaining a periodic orbit after the point of lander separation by application of time-delay feedback control. For the deployment of a series of small probes, it was found that maintaining a fixed attitude for the sail during the deployment was not considerably different in station-keeping performance compared with LQR control, and performed this with no effort required of the sail. Finally, in the work on capture, the two-phase approach provided successful capture trajectories down to the desired orbit radius. The work showed that, for reducing size of asteroid, there was a reduction in the time to capture. This is due to the fact that the same size of sail is used in the weakening gravity field of each asteroid. This makes the sail relatively more powerful and so able to affect quicker capture. It was also seen that long period capture trajectories are compounded by the need for the sail to spend periods of time waiting for the position of the Sun relative to the orbit to be in such a way as to permit the capture operations to proceed. There was also the successful demonstration of an optimally controlled capture which minimised the orbit semi-parameter over one orbit revolution.

The work contained in this thesis provides preliminary analysis for the consideration of future solar sail mission designers in the proximity operations of a sail near an asteroid. The findings presented here have shown that the sail can be of considerable utility in these proximity operations. They also present challenges to the mission designer given the continuous thrust that they may provide. Where a powerful sail may benefit the interplanetary phase of a mission in reaching many more asteroids further from the Earth, this can also present a challenge in the relatively weak asteroid gravitational field. However, these challenges are not insurmountable and so the sail remains a promising option for these high-energy missions.

Contents

List of Tables

List of Figures

Acknowledgements

The last four years have brought a mix of experiences and emotions as I carried out this PhD. From the great privilege and joy of being able to spend my time working in areas that I find so utterly spellbinding and to work with so many incredible people, to the uncertainties and anxieties of a two-year pandemic and to the pain of the loss of several family and friends. These years have certainly contained defining moments in my life and I would like to take some space here to thank those who have helped me along the way.

First, I would like to thank my supervisors Matteo Ceriotti and Colin McInnes. Matteo and I first met in my 2nd year of undergraduate studies at the University of Glasgow and since that time he has been a constant source of knowledge and guidance and I am incredibly grateful for all of his support in reaching this point. Colin and I met more recently at the beginning of my PhD studies and since that time his inexhaustible knowledge and ideas have served to strengthen the work we have done and have helped me to grow as a researcher. It has been a great privilege to have worked with two very kind and genuine people who have so much passion for what they do.

I would also like to thank Jan Thimo Grundmann. Since the early days of my PhD, Thimo was a source of great inspiration for everything solar sailing and planetary defence. I have loved every second of the work I have been involved with in Thimo's group and look forward to many more collaborations in the years to come.

In this final version of my thesis, and having passed the oral examination, I would like to thank the Viva committee of Joan Pau Sanchez Cuartielles, Kevin Worrall and Angela Busse for what turned out to be an enjoyable experience, far from the scary prospect I had imagined it would be. I would also like to thank them very much for their excellent comments which I feel have done much to strengthen this final version of the thesis.

Thanks are also due to my very good friend, and first astrodynamics teacher, Leonel Palacios. Although fate has conspired to always place us on different continents, your advice and friendship have always been greatly appreciated.

The journey is often only as good as the company and I have been blessed with great company in the SET group at the University of Glasgow. I would like to thank every member of the group as much for the laughs at lunch as for their insights on my work. I would especially like to thank Merel and Giulia for their friendship over these last few years and for all of their

encouragement and willingness to be available for the "stupid" questions you don't want to take to supervisors!

As it should be, my biggest thanks of all are reserved for my family who have supported me in everything I have ever done. Given there is more to thank them for than I could possibly fit into this thesis, I will restrict this to some specific thanks from the period of this PhD. Without the countless hours of childcare my mum has provided, there is no way I would have been able to complete this work. For this, and everything else, I am beyond grateful. To Susana, thank you for being such a loving and supportive companion in life. Your understanding and passion for helping people grow is a greater strength than I think you know, and I am eternally grateful for it. Finally, to my daughter Maya; you are, and always will be, the most important thing in my life. If you are reading this when you are grown up, I hope you have found a vocation that you are passionate about. But if not, then don't worry, it took me a while too. The most important thing is to never stop looking!

Declaration

I hereby declare that this submission is my own work and that, to the best of my knowledge and belief, it contains no material previously published or written by another person nor material which to a substantial extent has been accepted for the award of any other degree or diploma of the university or other institute of higher learning, except where due acknowledgment has been made in the text.

Glasgow, Scotland
October 27th, 2022

Iain Moore

Nomenclature

Acronyms

ACI	Asteroid-centred inertial reference frame
AEP	Artificial equilibrium point
AOP	Argument of periapsis
AU	Astronomical Unit
BF	Body-fixed reference frame
CTM	Control transition matrix
DU	Distance Unit
ECC	Orbit eccentricity
EM	Energy margin
GA	Genetic algorithm
HR3BP	Hill's restricted 3-body problem
INC	Orbit inclination
LQR	Linear quadratic regulator
MA	Mean anomaly
MEE	Mean equinoctial element
MSE	Mean square error
NEA	Near-Earth asteroid
RAAN	Right ascension of ascending node
RF2BP	Restricted full 2-body problem
SMA	Semi-major axis
SSHR3BP	Solar sail Hill's restricted 3-body problem
SRP	Solar radiation pressure
STM	State transition matrix
SYN	Synodic reference frame
TA	True anomaly
TDFC	Time-delayed feedback control
TOF	Time of flight
TU	Time unit

VU	Velocity unit
ZVC	Zero-velocity curve

Latin Characters

$\mathbf{a}$	Acceleration vector
a	Orbit semi-major axis
a_c	Characteristic acceleration
a_e	Ellipsoid dimension
a_v	Vertical stability coefficient
$\mathbf{A}$	Jacobi matrix
A	Area
$\mathbf{b}$	Event constraint
b_e	Ellipsoid dimension
$\mathbf{B}$	Linear dynamics matrix
$\mathbf{c}$	Path constraint
c	Speed of light
c_e	Ellipsoid dimension
C	Jacobi Constant
$C_{l,m}$	Harmonic coefficient
C_t	Targeted Jacobi constant
e	Orbit eccentricity
$\mathbf{E}_e$	Dyad related to polyhedron edge
E	Energy
E_{ef}	Electric field vector
E_n	Equilibrium point
f	Mean equinoctial element
$\mathbf{F}_f$	Dyad related to polyhedron face
F	Force
g	Mean equinoctial element
G	Newton's gravitational constant
h	Mean equinoctial element
i	Orbit inclination
$\mathbf{I}$	Identity matrix
I	Moment of inertia
j	Indexing variable
J	Cost function
J_2	Zonal harmonic coefficient

k	Mean equinoctial element
$\mathbf{K}$	Controller gain matrix
K_R	Mesh intervals
L	Mean equinoctial element
L_c	Lagrange cost function
L_e	Logarithm related to potential of a 1-D straight wire
m	mass
m_0	Rest mass
M	Mayer cost function
$\hat{\mathbf{n}}$	Sail surface unit normal
n	Orbit mean motion
p	Orbit semi-parameter
p_m	Photon momentum
$\mathbf{P}$	Riccati matrix
P	Solar pressure
$P_{l,m}$	Legendre polynomial
q	Integral constraint
$\mathbf{Q}$	Matrix related to state in LQR control
r	radius
r_0	Mean radius
r_p	Radius of sphere containing points in Monte Carlo simulation
$\mathbf{R}$	Matrix related to control effort in LQR control
R	Disturbing potential function
R_p	Planetary radius
$\mathbf{s}$	State vector
s	Mean equinoctial element parameter
$\hat{\mathbf{S}}$	Sun-line unit vector
$S_{l,m}$	Harmonic coefficient
t	Time
t_0	Initial time
t_f	Final time
T	Orbit period
T_k	Mesh points
$\mathbf{u}$	Control vector
U	Potential function
v_{esc}	Escape velocity
v_L	Landing velocity
V	Effective potential function

w	Mean equinoctial element parameter
w_f	final spacecraft weight
W	Invariant manifold
Y	Eigenvector

Greek Characters

α	Cone angle
α_r	Root
β	LQR weighting parameter
β_r	Root
γ	Sail slew angle
δ	Clock angle
ε	Error/displacement
ζ	torque
ζ_p	Position coordinate
η_p	Position coordinate
η_r	reflectivity coefficient
θ	True Anomaly
θ_{umb}	Umbra angle
κ	Continuation parameter
λ	Eigenvalue
Λ	Legendre polynomial angle
μ	Gravitational parameter
ν	Frequency of photon
ξ_p	Position coordinate
ρ	Density
ρ_A	Areal density
σ	Mass-to-area ratio
σ_r	Root
τ	Orbital period
τ_r	Root
ϕ	Latitude
Φ_C	Control transition matrix
Φ_M	Monodromy matrix
Φ_S	State transition matrix
χ	Predictor/Corrector angle
ψ	Longitude

ω	Rotational velocity
ω_f	Signed solid angle
ω_k	Argument of periapsis
$\mathbf{\Omega}$	Rotational Velocity Matrix
Ω	Rotational velocity
Ω_k	Right ascension of ascending node

Subscripts

ACI	Defined in the ACI frame
avg	Average
BF	Defined in the BF frame
bus	Parameter related to the spacecraft bus
crit	Critical value
f	Final point
h	Normal component
j	Indexing variable
l	Harmonic expansion order
m	Harmonic expansion degree
r	Radial component
s	Parameter related to the sail
SYN	Defined in SYN frame
0	Initial point
θ	Radial component

Superscripts

nom	Parameter related to the use of the nominal control law
new	Parameter related to the use of the new, or updated, control law

Chapter 1

Introduction

Throughout history, the heavens have leant meaning and solace to humanity. From the earliest days where mythology reigned, to more modern times, the cosmos has offered us the chance to find significance even in our apparent insignificance.

The motion of those celestial bodies which are visible in the night sky have served agriculture in predicting the seasons, held religious meaning for many and have been fundamental to seafarers as they navigated the high-seas. The earliest recorded astronomers in Mesopotamia were able to record details of the periodic motion of these bodies. Later, Greek astronomers made the first attempts at measuring the cosmos. As the cosmic catalogue began to develop, our place in the solar system became clearer; not as the focus but as a participant in the great cosmic dance.

As technologies and scientific methods improved, so too has our understanding of the Universe. Not only was our star orbited by other planets, but many of the debris leftover from the formation of those planets was still wandering through this great expanse, effectively unchanged since those earliest moments of the formation of our solar system.

With the rapid advances made through the 20th century, ideas which had long been contained in the realm of science fiction soon became possible. The development of vehicles capable of reaching beyond the thin atmosphere of home made possible the first artificial satellites, soon followed by more curious passengers. Then, on April 12th 1961, a monumental day in human history took place: Yuri Gargarin lifted off from the Baikonur Cosmodrome in Kazakhstan aboard Vostok 1, the first human to travel into space. This mission formed part of the "space race" which eventually led to the successful delivery and return of the Apollo astronauts to the Moon, inspiring generations of scientists and engineers to take up the mantle and drive forward human exploration of the solar system.

Alongside these achievements in human space flight, perhaps even greater advances were being made in the arena of robotic space flight. All through the 1960s and 1970s, a plethora of robotic missions reached out to every major body in the solar system. Probes delivered data during their many flybys and landers dropped down through the most inhospitable of atmospheres

to reveal the secrets contained below. An era of exploration had begun which dwarfed even the grandest of terrestrial ventures over the preceding centuries. Now, the sky was no longer the limit: it was simply the doorway.

1.1 Motivation for this work

Many of the current trends in space mission design are focused on the advancement of robotic small body missions. Given that many of these bodies remain as the earliest remnants from the formation of our solar system, they contain vital information on the conditions at that time and so are of great scientific interest. Their abundance of natural resources have also attracted the attentions of government agencies as potential refuelling stations and the source of materials for infrastructure as humans expand out into the solar system, as well as to the new space-entrepreneurs looking to exploit materials such as platinum-group metals which, on Earth, may fetch a handsome price. With many thousands of asteroids contained in the near-Earth space, there is also the need to mitigate against potential asteroid impacts, which still remain a real threat to the continuation of civilisation here on Earth.

The abundance of these bodies bring an interesting headache for the scientific community in the selection of which to visit and where to focus attentions. This is where the concept of a single mission to visit multiple bodies becomes very attractive. The difficulty in such a mission from an orbital mechanics perspective is the high energy requirement to make numerous orbital transfers. Often, these bodies will not be in similar orbital planes. Orbital plane change manoeuvres are notoriously expensive in terms of energy [10], and for a single spacecraft to rendezvous, conduct the required proximity operations for the mission goals, and then transfer to another body would be extremely constrained by the available propellant. Missions, such as the Voyager missions, which have visited multiple bodies tend to have done so by conducting flybys, often utilising gravity assist manoeuvres to enable the transfer to the subsequent body. However, with the abundance of potential targets, a method to visit several asteroids and spend enough time in proximity to conduct meaningful science, a new propulsion system which can meet these challenges is necessary.

A number of studies have shown the utility of the solar sail in achieving rendezvous with multiple targets. The solar sail is capable of such high-energy missions due to its propellant-less nature. However, there remains a gap in the available literature on proximity operations for a solar sail around small-bodies. As such, this thesis attempts to address some of the areas where this knowledge is lacking. Specifically around those operations which would be necessary to orbit the asteroid and interact with the surface.

1.2 Aim of this work

The aim of this work will be to show the efficacy of a solar sail as the primary propulsion system for a spacecraft while conducting proximity operations around an asteroid. There are numerous operations required of a spacecraft while conducting the science phase of any mission, normally requiring the spacecraft to be in the vicinity of the body. The literature contains a considerable body of work on the interplanetary transfers from Earth to asteroids using solar sails, but relatively little on the operations of a solar sail while conducting such proximity operations. Given the current interest in asteroid missions, and the technological advancements which have seen real-world sails launch and deploy, this thesis aims provide a timely treatment of the problem.

1.3 Solar Sails

1.3.1 A Short History

Solar sails have existed in human consciousness since the late 19th century, when science fiction first appears to have considered spacecraft propelled by light. It was not until the early 20th century that solar sailing as a practical propulsion method received attention. The legendary Russian rocket scientist, Konstantin Tsiolkovsky, and his colleague Fridrickh Tsander, wrote of the use of reflective surfaces to produce thrust from light pressure in the 1920's. Tsander appears to have been the first to write about practical solar sailing in 1924 [11].

However, it was not until the 1970's that the idea of solar sailing took on a more serious tone. NASA began investing in studies of the practicability of this propulsion system and a proposal was made for a sail powered mission to visit comet Halley in the mid-1980's. However, the proposal was finally rejected in favour of solar electric propulsion (SEP), which was subsequently rejected due to cost. Figure 1.1 shows an artists impression of a solar sail mission (NASA's NanoSail-D2[1]).

More recently, and owing to the advocacy of a dedicated body of engineers and scientists across the globe, solar sailing has found firmer footing (and funding) allowing for the first missions to be successfully flown.

1.3.2 Solar Sail Missions

The first solar sail took the form of the Japanese solar power sail IKAROS [12] mission to Venus. So not only the first solar sail mission to fly, but also the first interplanetary solar sail mission. The IKAROS sail was a $(20\text{ m})^2$ membrane made of ultra-thin polymide resin, with a thickness of 7.5μm. Thin solar cells are distributed over 5% of the sail surface to generate up to 300 W of electrical power for the onboard systems. A thrust value of 1 mN was measured on the sail and

[1] `https://www.nasa.gov/mission_pages/smallsats/11-010.html`, accessed on 29/03/2023

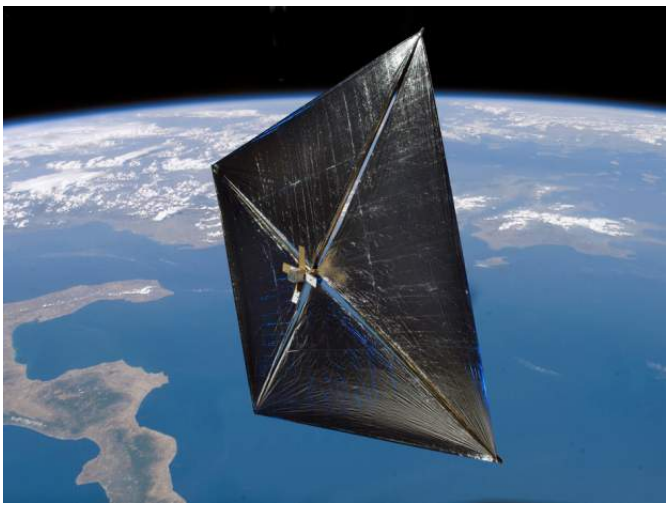

Figure 1.1: NASA NanoSail-D2 solar sail. Image credit: NASA

over a period of 6 months, a total Δv of 100 m/s was measured [13]. The first mission success was in the deployment of the sail, completed on June 9th, 2010. The mission also demonstrated the successful use of SRP for attitude control. The sail made its flyby of Venus on December 8th, 2010 [14]

Following this, NASA launched the Nanosail-D2 mission as a technology demonstrator, after the loss of Nanosail-D during launch [15]. This mission had two main objectives: eject a nano-satellite from a micro-satellite and to deploy its sail from a highly compacted volume and low-mass system. Both of these objectives were achieved, after which the NanoSail-D2 became the first sail to orbit around the Earth and only the second to deploy its sail in space [16].

It was then the turn of citizen science, as the crowd funded LightSail and LightSail 2 missions from the Planetary Society launched into low-Earth orbit. These missions were funded entirely by crowd funding [17]. The sail of the LightSail 2 mission was successfully deployed on July 23rd, 2019 [18]. The first recorded raising of a solar sail orbit under SRP alone was announced at the 5th International Symposium on Solar Sailing in Aachen, Germany in August 2019.

The next step in the solar sail journey was due to be the NEA-Scout mission from NASA which was intended flyby a Near-Earth Asteroid (NEA) [19]. However, after a successful launch by NASA's new Space Launch System (SLS), there was no contact with NEA Scout, and so the mission was lost.

Table 1.1 gives the approximate characteristic acceleration values for a selection of sail missions which have been flown.

1.4 Asteroids

Since the discovery of the first asteroid in the 19th century, scientists have sought to discover the truths of their origins [22]. In recent decades, advances in scientific methods and space-faring

Table 1.1: Some examples of solar sail performance values

Mission	Years Active	Characteristic Acceleration (mm/s^2)
IKAROS	2010 - 2015	0.01 [13]
LightSail	2015	0.05 [20]
LightSail 2	2019 - 2022	0.06 [18]
NEA Scout	2023 (Mission Failed)	0.07 [21]

capabilities have led to huge advances in this field. Given the small size of these bodies, it is incredibly difficult to make conclusive statements about their physical properties from Earth based observations alone. However, given the threats and opportunities posed, there has been much focus on improving our understanding.

1.4.1 Physical Properties

Asteroids are not a homogeneous group of rocks. There is a considerable range of type of asteroid, divided into taxonomic classes based on their physical parameters. The main 3 types of asteroid are the carbonaceous (C-type), metallic (M-type) and siliceous (S-type) [23]. The classification of these bodies is normally as a result of spectral measurements [24], of which there are several methods [25] including space-based infra-red telescopes [26].

In addition to spectral methods of determining the physical composition of an asteroid, radar observations can also be used. Radar has the ability to spatially resolve objects which cannot be resolved by other ground-based methods [27]. The utilisation of multiple data sources can lead to improved accuracy in determining the physical and surface properties of asteroids [28].

The apparent abundance of one type of asteroid over another can be attributed to their constituent materials. The S-type asteroids have a higher reflectivity, making them easier to spot from Earth observation [24], and so appear to be the most abundant [29].

The population of NEAs is dynamic, given resupply by main-belt objects and comets, which is a theory justified by the observation of the distribution of taxonomic classes of NEAs being similar to that of main-belt objects [29]. This re-population of NEAs from the main belt is made possible by the YORP and Yarkovsky [30] effects [31, 32].

These populations of NEAs are not limited to single objects. They also exist in binaries which are a pair of asteroids which orbit a common barycentre, as well as pairs, or even clusters, of asteroids which share similar orbits and have very low relative velocities. The YORP effect has been found to power the spin-up process of these multi-body systems, with rotation fission and post-fission dynamics explaining their formation [33].

Further technological advances have also allowed for the study of asteroid interiors. Understanding of an asteroids interior can provide crucial information on their evolution. These studies are a combination of measurement and theory which allow the development of constraints on the interior environment [34].

1.4.2 Orbital Parameters

In addition to taxonomic classification based on their physical properties, there are also orbital classes of asteroids. As this work focuses on NEAs, only those types are discussed here. The Amor class of asteroid are those which cross the orbit of Mars and can get as close as 1.3 AU to the Sun. This means that there is the potential for an Amor asteroid to impact Mars, though Earth remains safe from these bodies. The Apollo class of asteroid can extend its orbit to 2.29 AU from the Sun and as close as 0.65 AU [23]. As such, these asteroid can cross the orbits of Venus, Earth and Mars, and so can pose a threat to any of these planets. A third group of asteroid which orbit between 0.79 AU and 1.14 AU from the Sun are referred to as Aten asteroids. These asteroids cross the orbit of only one planet: the Earth. Finally, the Atira class of asteroid has their orbit completely contained within the Earth's orbit around the Sun.

There are currently over 28,000 discovered NEAs, with thousands more being discovered each year. As a result, the possibility of an object of significant size impacting the Earth is very real [35]. There have been recordings of objects of considerable size entering the Earth's atmosphere, such as in Chelyabinsk in 2013 [36] and the Tunguska event of 1908 [37]. This reality has driven the development of several missions to better understand these bodies.

1.4.3 Small Body Missions

The first successful mission to an asteroid was carried out by the NEAR-Shoemaker mission to asteroid 433 Eros, which arrived there in February 2000. This mission was the first to orbit an asteroid and the first to make comprehensive scientific measurements of an asteroid's surface composition, geology, physical properties, and internal structure [38].

The Dawn mission was tasked with visiting two of the largest asteroids in the solar system, Vesta and Ceres. This mission successfully rendezvoused with Vesta and Ceres, carrying out studies of surface topography, composition and gravitational fields [39].

The Hayabusa mission from JAXA would provide a first ever sample return from an asteroid to the Earth. Arriving at 25143 Itokawa in September 2005, and despite some operational issues, a small sample of asteroid material was returned to Earth in June 2010 [40, 41].

Following on from the success of Hayabusa, JAXA conducted the even more ambitious Hayabusa2 mission to asteroid 162173 Ryugu, arriving in June 2018. After several excursions to the asteroid surface and successful in-orbit observations, the Hayabusa2 spacecraft descended to extract a sample from the surface of the asteroid [42]. This sample was then successfully returned to the Earth in December of 2020.

NASA has also conducted a sample return mission, the OSIRIS-Rex mission to asteroid 101955 Bennu [43]. After making a successful sample collection in October 2020, the spacecraft is now on its way back to Earth and is due to arrive in September 2023.

The European Space Agency (ESA) has also conducted a small body mission, with the

Rosetta spacecraft to comet 67P/Churyumov–Gerasimenko [44]. The mission successfully rendezvoused and conducted a wealth of scientific measurements with the comet. In addition, a small lander was deployed to the surface of the body.

As well as dedicated missions to small bodies, there have also been encounters of opportunity. During the long voyage to comet 67P/Churyumov–Gerasimenko, the Rosetta spacecraft made a flyby of asteroids 2867 Steins and 21 Lutetia. Similarly, the NEAR-Shoemaker spacecraft made a flyby of 253 Mathilde in June 1997. Observations of asteroid 4179 Toutatis were also made by the Chinese Chang'e-2 spacecraft [45].

Phobos and Deimos are unique in the solar system. Although they are two of the only three terrestrial satellites, they have many commonalities with small bodies of the outer solar system [46]. As such, these too can provide many insights into the earliest stages of the formation of terrestrial planets. As such, several of the Martian missions have spent time analysing these small moons.

1.4.4 Review of Asteroid Shape Modelling

Given their size, asteroids tend not to conform with the spherical shape of larger bodies such as planets and their larger satellites. As the asteroids are comparatively small, they do not exert a sufficient gravitational force on their constituent materials to compress them into this spherical form and so they tend to be of irregular shape [47]. One of the great challenges in the near-asteroid environment is the effect that this irregular shape (as well as a sometimes irregular spin state) has on the gravitational field surrounding the asteroid. Figure 1.2 shows actual images for asteroids Eros and Dimorphos taken by the NEAR-Shoemaker and DART missions respectively.

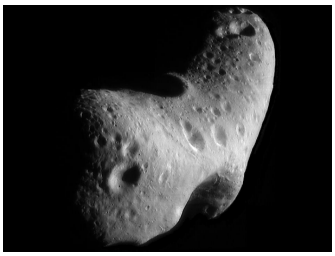

(a) Eros (Image credit: NASA)

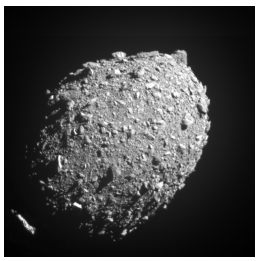

(b) Dimorphos (Image credit: NASA/Johns Hopkins APL)

Figure 1.2: Examples of irregular asteroid shapes

As it is not possible to obtain a detailed shape model from Earth-based observations alone, very few exist. Most observations have been made by measuring the light curve of the asteroid or by taking radar images for those which pass closer to the Earth [23]. The only high resolution models available are for those which have been studied in-situ by a spacecraft. As such, some approximations to the real shape have been made throughout the literature, some of these methods are detailed here and the mathematical formulations for some can be found in Appendix

A.

Harmonics Expansions

Harmonic expansions have been used to great success in modelling irregular gravity fields. The extensive measurements made of the Earth over the years has allowed for very high resolution spherical harmonic expansion (SHE) models to exist. Though it is also possible to apply spherical harmonics to model simpler shapes, such as ellipsoids, there are also ellipsoidal harmonic expansions (EHE). Where the SHE is the solution to Laplace's equation based on spherical coordinates, the EHE is the solution to Laplace's equation in ellipsoidal coordinates.

Bucha and Sansó use SHEs to model the irregular gravity field around asteroid Bennu [48]. In their work, they examine the accuracy of three distinct approaches. They find that the spectral forward modelling via external spherical harmonics diverges considerably. However, application of least-squares estimation from surface gravitational data using external spherical harmonics and also a combination of internal and external series expansions,ensured relative accuracy from $\sim 10^{-6}$ to 10^{-8}.

Peñarroya and Paoli developed a tool for the development of a spherical harmonic model onboard a spacecraft. Using polyhedron model for ground testing, the work simulates the study of an asteroid shape from which the harmonic coefficients can be calculated [49].

Feng *et al* use spherical harmonics to model and analyse periodic orbits around a contact binary asteroid [50]. In this work, the SHE model is used to combine the ellipsoidal and spherical shapes of each member of the pair. At degree and order 8, the SHE is found to have relative errors at less than 2% at the circumscribing sphere. It was also found that the tesseral harmonics introduced large variations in the frozen orbits, and that the perturbing effects of the irregular shape are reduced around the polar region.

Takahashi and Scheeres [51] discuss the interior Brillouin sphere where the gravity field converges interior to the Brillouin surface. This is incredibly important in modelling the dynamics of a spacecraft very close to the asteroid surface, though only possible when some knowledge of the asteroids shape is available.

Hu and Jekeli [52] argue that, especially for highly irregular bodies but even for moderately non-spherical bodies, an ellipsoidal model will provide the most accurate results, given the reduced area of divergence. However, ellipsoidal models are computationally very expensive and so Sebera *et al* [53] and Reimond and Baur [54] argue that a spheroidal model gives the best compromise between the simplicity of the spherical model and the accuracy of the ellipsoidal model. In fact, it has also been shown that ellipsoids up to a certain eccentricity can also be modelled using SHE [55].

Homogeneous Ellipsoid

Another method of modelling an ellipsoid, presented in the literature [4, 56–58], is that of the tri-axial ellipsoid modelled using elliptical integrals.

In their work on the shape and surface environment of 2016 HO_3, Li and Scheeres establish a tri-axial ellipsoid shape model using light curve data. Using this model, the behaviour of surface regolith is studied, with the influence of shape, density, cohesion and angle of friction on the distribution of regolith discussed.

Ferrari *et al* use the tri-axial ellipsoid to model the gravitational contribution of Dimorphos to the Didymos binary asteroid system [59, 60]. In this work, the authors provide trajectory options for the Milani CubeSat which will form part of the Hera mission.

In their work on transfers and orbital maintenance of spatial retrograde orbits, Pushparaj *et al* model the Martian moon, Phobos, using a tri-axial ellipsoid. In this work, the ellipsoidal model is added to the 3-body dynamics of the Mars-Phobos system, and presents periodic orbits along with invariant manifold transfers for the JAXA MMX mission [61].

Polyhedron Model

The most accurate modelling tool for irregular bodies is using their, often very high resolution, polyhedron models. The lower resolution models tend to be those established by light curve data. An improvement can be made on the resolution by use of radar measurements. However, by far the most detailed models exist for those bodies which have been measured in-situ by an orbiting [62], or passing [63], spacecraft.

The method has been applied in the analysis of surface motion of particles on the asteroid Bennu [64]. In this work, the authors found that particles with zero initial velocity have a tendency to stop in the low latitude regions of the asteroid, regardless of their initial latitude. This could be attributed to the higher effective potential at higher latitudes. The availability of a high resolution shape model for Bennu is crucial to the accuracy of such a study. Further studies have shown the utility in this model for rover trajectories [65, 66], where the authors show the capabilities of hopping rovers, capable to manoeuvring over the rough asteroid terrain. In fact, the polyhedron model is crucial to accurate studies of any trajectory which comes close to, or in contact with the asteroid surface. Zeng *et al* used the polyhedron method for their work on ballistic lander trajectories over potential rubble-pile asteroids [67]. In this work, the authors used the flexibility of the polyhedron model to alter geometries of individual facets to allow small modifications to the surface topology to gain an understanding of the effect of uncertainties in the asteroid shape to the trajectories of a spacecraft/lander

One of the main drawbacks to using the polyhedron method is the length of computation time. Each facet of the model requires several calculations, and there are often many thousands of facets. As such, each time step in a numerical integration can require tens of thousands of calculations. Wu [68] proposes a new modified Parker's method for efficient gravitational forward

modelling and inversion using general polyhedral models which shows promise for increased efficiency in these calculations, as well as the facility for 3-dimensional, density distribution.

Mass Concentration Models

Mass concentration (Mascon) models use discrete point masses to represent the irregular distribution of mass on an irregular body. The circumscribed volume is filled with point masses which have a total mass equivalent to the body being modelled, and the force exerted is the sum of the vectors of force of each mass on the spacecraft [69].

The mascon model has been used as a replacement for the relative computational intensity of the SHE model for on-board flight software for a lunar mission [70]. In this work, it was found that the highest-fidelity model demonstrated equivalent accuracy and memory footprint to a 60 degree and order spherical harmonics expansion.

Rathinum and Dempster used the novel octree method to populate a mascon model of asteroids Itokawa and Toutatis [71]. This method was found to be more efficient than the polyhedron method in computation. However, where a high number of mascons were used, the polyhedron method became more efficient. As such, the mascon model is preferable to the polyhedron method only where the number of mascons used is not excessive in comparison to the numbers of faces contained in the polyhedron model.

Dumbbell Models

Goździewski *et al* [72] propose to model irregular bodies, which could consist of two lobes, in a "dumbbell" configuration. In this configuration, the problem is tackled as a Circular Restricted 3-Body Problem (CR3BP), a full treatment of which can be found in [73] and [5].

The dipole segment model was applied by Zhang *et al* in their study on periodic motion around dumbell shaped asteroid [74]. This work showed the method as a simple model for modelling the dynamics near these bodies, as well as in the investigation of nonlinear dynamics. The study also found some new types of periodic orbits.

Cube Model

Presenting a shape which has a closed form solution brings great benefit in the reduced computational requirements. Such a model is presented by Venditti and Prado [75] where they propose modelling the asteroid as a cube.

The work begins by analysing the effects of inclination change for a spacecraft which is in a circular orbit around a non-rotating cube. With the orbit starting above the centre point of one of the faces, it is shown that equatorial and polar orbits ($i = 0^\circ, i = 90^\circ$) experience less perturbation than an orbit of $i = 45^\circ$. This is explained as the orbit of $i = 45^\circ$ must pass over the

vertex of the cube. Passing over the vertex as opposed to the edges, brings the spacecraft closer to the body, resulting in it experiencing a higher perturbation.

Following this, the work examined the effect of a rotating cube. The rotations seem to decrease the perturbations in general with some differences shown between polar and equatorial orbits. With the rotation about the z-axis, polar orbits experience higher perturbations compared with equatorial orbits. This could be explained by the fact that the rotations will now bring the vertex underneath the passing spacecraft. Equatorial orbits experienced the lowest perturbation. The rotational period also has a considerable effect on the perturbations experienced. For rotations around the x-axis, the perturbation effects over all orbital inclinations are almost constant.

The cube certainly provides a simpler method by which to approximate an irregular body. However, the form seems so far detached from what a true shape may look like that, in the opinion of this author at least, the shape cannot be considered for good approximations. It certainly is possible to take something from this work, even if a complete mission cannot be well analysed. The passes of the spacecraft over the vertex of the cube provide interesting insights into the perturbations a spacecraft may experience over a peak altitude surface mass concentration on a body. The study of different rotation periods and axes also provide some good insights into the effects of irregular spin states. So, although the model may not be useful for simulating complete orbits, there are certainly points on the orbit which provide interesting analysis.

Hybrid Models

Another form of unevenly distributing mass is to combine some of the aforementioned models into a "hybrid" gravitational model. Feng *et al* [50] present a hybrid of a spherical harmonic expansion and a homogeneous ellipsoid in order to model a contact binary asteroid. Herrera-Sucarrat *et al* [76] use a combination of spherical harmonics and spherical Bessel functions to allow integration of trajectories both close to the surface and far from it.

The combination of a SHE model outside of the Brillouin surface with the polyhedron model inside the Brillouin surface has also been proposed [77]. It is also possible to use the polyhedron model to establish the harmonic coefficients to arbitrary degree and order [78].

Wittick and Russell applied mascon modelling with small radius spherical harmonics to provide magnitude faster computational speeds, with equivalent accuracy, to polyhedron modelling, with example use at 433 Eros [79].

1.5 The Potential of Solar Sail Technology in Irregular Gravity Fields

The sheer number of small bodies which exist, even in the near-Earth region, have prompted many mission studies in the literature. Due to the propellantless nature of the solar sail, the potential for a high energy mission to visit multiple bodies has been proposed [80]. In this, and subsequent works [81, 82], options are provided for the selection of sequences of NEAs to be visited by a single solar sail. Further work [83] has shown how advances in computer science can allow for intelligent selection of sequences with a modest computation time. These mission studies have focused on the interplanetary phase of the mission, and so a study of the literature which deals with the topics related to proximity operations, which is the focus of this thesis, are presented here.

1.5.1 Controlling the Effects on an Orbit from the Irregular Gravity Field

A key phase of a mission to an asteroid will be the operation of the spacecraft in the near-asteroid space. In this region, the effects of the non-spherical nature of the body become very important. For highly irregular bodies, these perturbations can lead to orbital escape [84]. Therefore, it is beneficial to have a method of alleviating these effects on the spacecraft.

Macdonald and McInnes [85] have proposed the blending of optimal control laws for station-keeping manoeuvres. In this work, the Earth-centred "GeoSail" mission is used as an example, where the orbit lies in the ecliptic plane. To maintain a Sun-pointing periapsis, which maintains the orbit apoapsis in the Earth's magnetotail, the sail orientation is chosen such that the accelerations experienced are able to countenance the secular variation of the argument of periapsis. The work found that, even from a range of initial conditions, the algorithms are able to maintain optimality. Additionally, it is noted that the value of sail characteristic acceleration to escape from a polar orbit would increase exponentially as the initial altitude decreases.

Biggs and McInnes [86] present the application of Time-Delayed Feedback Control (TDFC) to maintain bound motion around a highly eccentric ellipsoid; in this case applied to asteroid 433 Eros. The TDFC uses the same algorithm as the Linear Quadratic Regulator (LQR), but rather than depending on some reference trajectory, this method utilises the state known one period previous to the current state as the reference. Such a method allows for an adaptive approach to the problem; which is useful where the gravity field is not known *a priori*, which is often the case for an asteroid mission. This method finds application in this work and so will be discussed in more detail in subsequent chapters.

Oliveira and Prado [87] presented work in station-keeping using a solar sail to offset various perturbations. This work utilises PID control of the solar sail to counteract the accelerations experienced by the spacecraft due to perturbations. The method finds success in addressing the accelerations experienced, and shows the versatility of the solar sail in mission applications.

However, the work does not consider the feasibility of resulting control laws for a real-world sail. Given their large size, a rapidly changing control law would require a powerful ADCS in order to achieve the necessary rotational rates. As such, it is beneficial if the control law can be optimised for the overall control effort required of the sail.

In a series of works, Farrés *et al.* propose using the sail in order to offset undesirable effects from the non-linear dynamics of multi-body systems. In Refs. [88, 89], the authors propose to use the sail to stabilise a spacecraft's orbit around an unstable equilibrium point in the Circular Restricted 3 Body Problem (CR3BP). The objective is to allow the sail to escape along the unstable manifold before changing the sail orientation such that the stable manifold is brought into the path of the sail, thus allowing the spacecraft to remain bound in orbit around the equilibrium point. Later, this strategy was applied to a halo orbit in the CR3BP [90]. The authors then apply the same method to the Elliptical Restricted 3 Body Problem (ER3BP) [91] before proposing strategies of stabilising vertical Lyapunov orbits in the CR3BP using both LQR control and Floquet Modes [92].

1.5.2 Interaction With the Surface of a Body

There have already been several examples of the successful deployment of a lander from a spacecraft, as well as the landing of a spacecraft itself, to the surface of an asteroid. The first landing on an asteroid was performed in February 2001 by the NEAR-Shoemaker mission at asteroid Eros [93]. This landing was not a part of the set objectives but was improvised at the end of the mission. A mission which seeks to interact with the surface of an asteroid must also deal adequately with the irregular gravity field generated by the uneven mass distribution of the small body. This uneven mass distribution has a considerable effect on the system dynamics within a few body radii of the surface [55, 94]. Outside of a few radii, it is sufficient to model the body as a point mass. There has been much work in the literature regarding the multi-body dynamics of the Sun-asteroid-spacecraft system. This model is referred to as Hill's problem [73], where the mass ratio of the smaller primary body to the larger primary body tends to zero. This body of work has shown the existence of families of periodic orbits [90, 95–98], provided analysis of the motion of a solar sail [99, 100], the limitations of a solar sail in the weak gravitational field of the asteroid [101] and shown the feasibility of controlling a solar sail around artificial equilibrium points [102], themselves displaced by the addition of the solar sail to the system dynamics.

Jiang *et al* have conducted research on the dynamics of the asteroid effective potential [6, 103–107]. This work has shown the complex nature of the potential field of a rotating, highly irregular-shaped body, with a focus not only on the system equilibrium points, but also on periodic orbits around such points. There is also research on the effects of rotational velocity on the potential field. The body of work offers an extensive contribution to the study of such potential fields, with useful classification tools related to the stability of the equilibria. The work, however, only considers the natural system dynamics. The addition of a continuous thrust

system (eg. solar sail, solar electric propulsion (SEP)) into the potential field brings a change. Yang *et al* present a study of the SEP case [108] and the effects on the dynamics of the system. However, the solar sail case is more complex still, given that the acceleration provided by the sail is referenced to the position of the Sun.

In their work on mission design to the Trojan asteroids of Jupiter [100], Farrés, Soldini and Tsuda present the two distinct phases of a solar power sail mission deploying a lander to the surface of an asteroid. In this work, the two phases consist of the far-field dynamics for the sail monitoring of the lander after deployment, and the descent of the lander to the asteroid surface with focus on bouncing trajectories and ensuring the lander remains on the surface. This work demonstrates the unique ability of the sail to offer out-of-plane observation locations. Although the work by Farrés *et al* addressed the problem of ensuring the lander remained on the asteroid surface, it did not study the problem at the point of lander separation and the control of the sail thereafter.

Lander Deployment in Hayabusa2 Mission

The Hayabusa2 mission by the Japanese Aerospace Exploration Agency (JAXA) marked an important milestone in the exploration of asteroids [42, 109]. The first successful deployment of mobile rovers (MINERVA II1 and MINERVA II2) to the surface of a small body, deployment of the "hopping" MASCOT landers developed by DLR and CNES, deployment of target markers (TMs) and subsequent descent of the main spacecraft to collect a sample which was returned to the Earth.

The Hayabusa2 spacecraft was never in orbit around the asteroid itself. Instead, it remained in one of three pre-defined boxes for different mission stages. The spacecraft remained on the Earth side of the asteroid for the full mission. Between November 23rd and December 29th, 2018, the spacecraft-asteroid entered into a conjunction with the Earth when they passed behind the Sun, as seen from the Earth. During this period, the spacecraft was set on an auto-return trajectory with a maximum distance of 108 km. The natural elliptical three-body restricted dynamics, together with the solar radiation pressure, brought the spacecraft back to its "Home Position" (HP), 20 km above the asteroid surface. Descent of the spacecraft towards the surface was made almost linearly along the Earth-Asteroid line, by applying feedback control. The trajectory of the spacecraft was not synchronised with the rotation of the asteroid, but was approximately linear with respect to the asteroid-centred inertial frame.

Deployment of MINERVA II Rovers The two MINERVA II rovers would become the first mobile rovers to be successfully deployed to the surface of a small body. The deployment was made at 4:06 UT on September 21st, 2018. The deployment was made with a horizontal $\Delta v = 0.2$ m/s to compensate for the fast ejection velocity of the rovers. This assured that the rovers would not exceed the escape velocity of Ryugu.

Deployment of MASCOT lander The MASCOT lander was deployed on October 3rd, 2018, at 1:57 UT. The deployment was made from an altitude of 51 m, though no horizontal Δv was required owing to the slow release velocity of 0.05 m/s. The lander was capable of "hopping" on the asteroid surface, allowing more than one location to be surveyed.

Pre-landing modelling indicated a landing velocity of 0.19 m/s [110]. Post-landing analysis has shown that, even in the worst case, the lander impact velocity did not exceed the escape velocity of Ryugu (0.36 m/s).

Deployment of Artificial Landmarks To assist the guided descent of the Hayabusa2 spacecraft to the surface, two Target Markers (TM) were deployed to the surface [111]. These were 10-cm balls covered with a retro-reflective sheet. The combination of the TM and the flash lamp on board Hayabusa2 enabled relative control by bright-spot tracking [42].

The TMs were deployed from an altitude below 40 m and were designed to dissipate kinetic energy. The TMs were originally planned for use in velocity compensation. However, upon arrival at Ryugu, it was discovered that the surface was covered in in a high abundance of boulders. As such, a post-arrival strategy was developed using the TMs as artificial landmarks (AL) to assist in precise control of the spacecraft position. Hayabusa2 contained five TMs, two of which were used as ALs.

Given the high abundance of boulders, the target area for the sample extraction was just 3 m wide [112].

Lander Deployment in OSIRIS-REx Mission

The OSIRIS-REx mission will also return samples to the Earth from an asteroid. This mission rendezvoused with asteroid Bennu in 2018 and is scheduled to return the successfully obtained sample to the Earth in 2023 [43].

There were five primary objectives for the mission [22]:

- Return and analyse a sample
- Map Bennu's global properties
- Document the sample site
- Study the Yarkovsky effect
- Improve asteroid astronomy

1.5.3 Gravitational Capture

Several works have considered the problem of capture around planetary bodies using the sail as the primary propulsion method. In Ref. [113], the authors have shown that the sail is capable

of correcting for approach dispersion at Mercury and inserting a spacecraft into a 100 x 7500 km sun-synchronous orbit. The sail then manoeuvres the spacecraft into a 100 km parking orbit over a period of 28 days. Although the work did not patch the interplanetary arrival to the planetocentric approach, it has still shown that the sail is capable of such manoeuvring.

In earlier work [114], Macdonald and McInnes discuss the uniqueness of the arrival conditions for a solar sail. The optimal interplanetary trajectories for solar sails often arrive at the planet with zero hyperbolic excess velocity. Normally a reverse escape trajectory is calculated which uses a semi-major axis control law to spiral out to the boundary of the sphere of influence. However, this demands that the interplanetary arrival conditions match those at the end of the reverse escape trajectory. Use of the semi-major axis control law is also prohibitive as it only allows changes to the size of the orbit, and not its shape and orientation. This work also discusses the limits on the B-plane aiming points due to the varying intensity of the Solar Radiation Pressure (SRP) during the orbit of Mercury around the Sun. Similarly, these limits as a function of capture inclination are also discussed. The work also describes the dependence of the maximum permissible hyperbolic excess velocity on the sail characteristic acceleration, rather than onboard propellant as is the case for conventional spacecraft. This found that there is no minimum B-plane aim point. Instead, there is a minimum hyperbolic excess velocity for safe capture in the Mercurian system. For a given aim point, the required hyperbolic excess velocity increases for an increasing sail characteristic acceleration.

So far as these authors have found, there exists no work in the literature for the capture of a solar sail around an asteroid where the sail is the primary propulsion system. The challenges of such a concept include the weak gravitational field and the relatively powerful effect of SRP in this regime.

1.6 Objectives of this work

The main objectives of this work will be:

1. To show the ability of a solar sail to counter nodal regression induced by an ellipsoidal asteroid shape model

2. Achieve a periodic orbit using the sail as the primary propulsion system by application of a novel control method

3. To analyse and implement control of a sailcraft during the deployment of small probes and a single large lander

4. To achieve capture of a sailcraft around an asteroid during a ballistic transit trajectory

In the first case, the countering of nodal regression is addressed as a demonstration that the solar sail can be employed to counter effects on the orbit due to a particular perturbative effect; in

this case, due to the non-spherical shape of the body. Although the work here aims to minimise the rate of nodal regression, it could equally be applied to obtain a specific nodal regression rate within a given tolerance, e.g. to achieve Sun-synchronicity for an orbit which may not otherwise be synchronous. This work, where possible, attempts to maintain a level of generality such that a specific science goal is not the objective but the demonstration of a method to achieve certain goals is established.

Upon establishing control laws to maintain periodic orbits using optimisation methods, the very sensitive dynamics close to the asteroid mean that on each orbit the control law must be updated to maintain that orbit. If it was required to re-run the optimisation on each orbit, this would prove computationally very intensive. As such, in the second objective, a quick method of updating the control law is sought. Here, we will employ the Control Transition Matrix, which is an extension of the State Transition Matrix. This will be shown to allow rapid calculation of a new control law given the final state error in the previous orbit.

The third objective addresses the problem of controlling the orbit of a solar sail after the deployment of mass from the sail which results in an instantaneous change to the sail performance metric, the characteristic acceleration. Here, it will be shown that the deployment of a single large lander results in a considerable change to the system dynamics and that it is possible to control the sail using a feedback control method which forces a periodic orbit. For the deployment of a series of small probes which have very low mass, the problem presents a gradual increase in sail performance and a comparison is presented between using a fixed attitude to hold a hover location and feedback control for the same.

Finally, the fourth objective will show the utility of the sail in achieving a captured orbit around an asteroid. Where the literature has treated the capture of a sail around various planets in the solar system, the same has not been shown for a solar sail, to the knowledge of the author.

1.7 Research Outputs

This PhD work has produced a number of papers, both published in journals and presented at conferences. The work presented at the 5th International Symposium on solar Sailing 2019, and subsequently published work in Advances in Space Research in 2020, make up some of the content contained in Chapter 4. The work presented at the 31st AAS/AIAA Space Flight Mechanics Meeting in 2021 and the later work published in Acta Astronautica in 2022 make up some of the content contained in Chapter 5.

Conference Papers

1. Iain Moore and Matteo Ceriotti, “Solar Sails for Perturbation Relief: Application to Asteroid Proximity Operation” in *5th International Symposium on Solar Sailing*, Aachen, Germany, 2019

2. Iain Moore and Matteo Ceriotti and Colin R. McInnes, “Asteroid Landing With a Solar Sail: Lander Deployment” in *31st AAS/AIAA Space Flight Mechanics Meeting*, Virtual, 2021

Journal Papers

1. Iain Moore and Matteo Ceriotti, “Solar sails for perturbation relief: Application to asteroids”, *Advances in Space Research*, August 2020, DOI: 10.1016/j.asr.2020.08.014

2. Iain Moore and Matteo Ceriotti and Colin R. McInnes, “Station-keeping for a solar sail during lander/probe deployment using feedback control”, *Acta Astronautica*, September 2022, DOI: 10.1016/j.actaastro.2022.09.005

Chapter 2

Tools and Methods

This chapter will introduce the tools and methods which have been utilised during the course of this PhD. First, the different frames of reference used will be introduced. Then, mathematical models such as those used to model the shape of an asteroid and the solar sail acceleration will be given along with the definition of dynamical regimes, which will be important to the work throughout this thesis. Through the course of this research, several methods of controlling the sail have been proposed and each will be described. Finally, the numerical methods used will be detailed.

2.1 Frames of Reference

This section will detail each of the frames of reference used in this work. These include the Asteroid-Centred Inertial (ACI) frame, the Body-Fixed (BF) frame and the Synodic (SYN) frame.

2.1.1 Asteroid-Centred Inertial Frame

The asteroid-centred inertial (ACI) frame is an inertial frame of reference which is centred on the asteroid with the x_{ACI}-axis in the direction of the first point of Aries, the z_{ACI}-axis along the asteroid rotational axis and the y_{ACI}-axis completing the right-handed set.

Asteroids do not tend to always have their rotational axis perpendicular to their orbit plane. However, for the purposes of generalising the work carried out here, the rotational axis will be set perpendicular to the orbital plane in all cases. This case is sufficiently relevant for the understanding on the capability of a solar sail to control the motion of a spacecraft in proximity of an asteroid.

In this frame, as the position of the Sun rotates around the asteroid at a slow rate of 0.9856 degrees per day it is possible for short-term simulations to ignore the apparent rotation of the solar position. However, for longer term simulations this rotation must be accounted for. The

ACI frame is predominantly used in this work for the calculation of orbital elements and analysis of trajectories which were originally calculated in another frame.

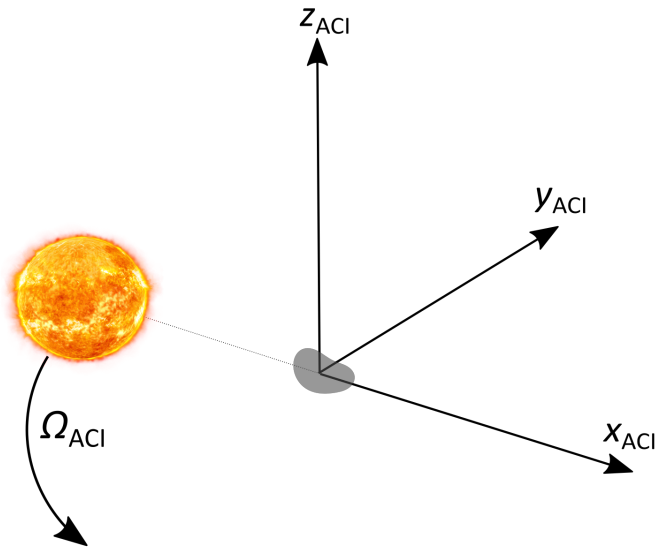

Figure 2.1: Asteroid-Centred Inertial (ACI) reference frame.

2.1.2 Body-Fixed Frame

The body-fixed (BF) frame is used where the gravitational effect from the Sun is ignored, but where the shape and the rotation of the asteroid play an important part in the gravitational field. The frame of reference is fixed on the asteroid and rotates with it. Where the shape model used is that of an ellipsoid, the x_{BF}-axis is set along the largest dimension of the ellipsoid, the z_{BF}-axis along the axis of rotation and the y_{BF}-axis completes the right-handed set. Where the high resolution polyhedron models are used, the axis directions are defined by the models which are obtained from observation data, with the z_{BF}-axis always along the axis of rotation. This reference frame is illustrated in Fig. 2.2. At the initial time point on any simulation, the BF frame is aligned with the ACI frame. As suvch, the x_{BF}-axis is in the direction on the first point of Aries. At this instant, the Sun is in the opposite direction.

2.1.3 Synodic Frame

The synodic (SYN) frame is centred on the asteroid and rotates with the Sun-asteroid line, with the Sun's position fixed along the x_{SYN}-axis. The z_{SYN}-axis is aligned with the system rotation and the y_{SYN}-axis completes the right-handed set. This reference frame is illustrated in Fig. 2.3 and is used where the sail is sufficiently distant from the asteroid that the effect of the shape and

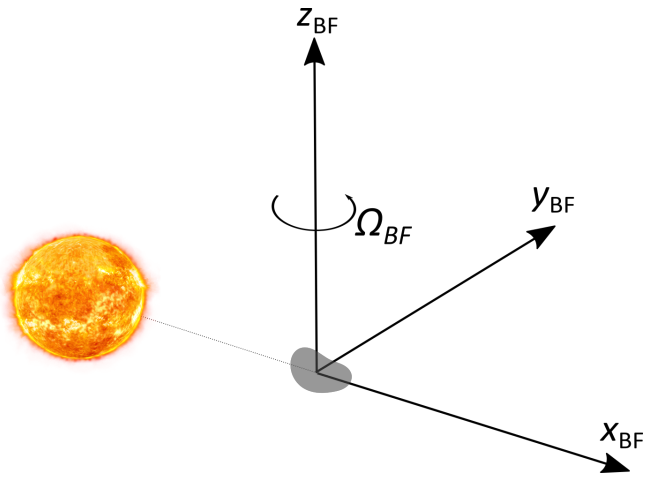

Figure 2.2: Body-fixed reference frame

rotation of the body is negligible and so can be ignored. The SYN frame is employed for 3-body problems where the gravitational effect from the Sun cannot be ignored.

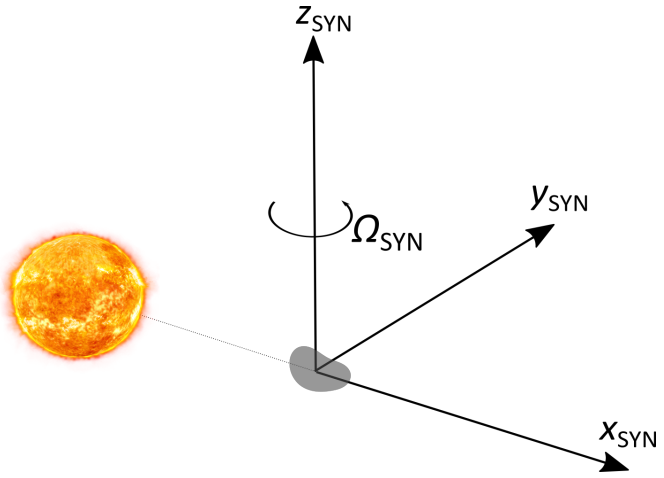

Figure 2.3: Synodic reference frame centred on the asteroid

2.2 Mathematical Models

During the course of this work, several different mathematical models were used to facilitate computer simulations. This section will present the solar sail force model, provides a review of the various asteroid shape models used throughout the literature and the dynamical models which have been implemented in this work.

2.2.1 Solar Sail Model

The correct theoretical basis for the existence of radiation pressure was first formulated by James Clerk Maxwell in 1873. The first experiment to successfully isolate radiation pressure was

performed by Peter Lebedew at the University of Moscow in 1900. There exist two descriptions of radiation pressure; the quantum and electromagnetic descriptions [11].

Solar Radiation Pressure: Quantum Description

In quantum mechanics, radiation pressure considers the momentum transfer of photons. The energy transported by a photon can be obtained by Planck's law:

$$E = h\nu \tag{2.1}$$

where h is Planck's constant and ν is the frequency of the photon. Additionally, the mass-energy equivalence of special relativity gives the total energy as:

$$E^2 = m_0^2 c^4 + p_m^2 c^2 \tag{2.2}$$

where m_0 is the rest mass and p_m is the momentum of the body. Considered to effectively have a rest mass of zero, though a finite rest mass is considered to be a reality [115] with many experiments being made to try to define, if not the rest mass itself, an upper limit to the rest mass [116], the photon energy can be written as:

$$E = p_m c \tag{2.3}$$

As such, the momentum transported by a photon is given by:

$$p_m = \frac{h\nu}{c} \tag{2.4}$$

To calculate the pressure exerted on a body, the energy flux at a distance r_s from the Sun is given by:

$$W = W_e \left(\frac{AU}{r_s} \right)^2 \tag{2.5}$$

where AU is the mean Earth-Sun distance, L_s is the solar luminosity and:

$$W_e = \frac{L_s}{4\pi AU^2} \tag{2.6}$$

The energy transported across a surface area, A, normal to the incident radiation is given by:

$$\Delta E = WA\Delta t \tag{2.7}$$

which transports a momentum $\Delta p_m = \frac{\Delta E}{c}$. The pressure exerted is then defined as the momentum transported per unit time, per unit area [11]:

$$P = \frac{1}{A}\frac{\Delta p_m}{\Delta t} = \frac{W}{c} \tag{2.8}$$

Solar Radiation Pressure: Electromagnetic Description

The electromagnetic description of light describes the momentum transfer to the solar sail by electromagnetic waves. An electromagnetic wave is defined by its velocity and directional energy flux [117]. The energy density of an electromagnetic wave is given by:

$$E_d = \frac{\Delta E}{Ac\Delta t} \tag{2.9}$$

where ΔE is the energy contained in the volume element. The energy flux across the surface is given by:

$$W = \frac{1}{A}\frac{\Delta E}{\Delta t} \tag{2.10}$$

which means that the energy density can be re-written as:

$$E_d = \frac{W}{c} \tag{2.11}$$

The pressure exerted by an electromagnetic wave is given by [117]:

$$P = \frac{I}{v} \tag{2.12}$$

where $I = \frac{E_{ef} \times B}{\tilde{\mu}}$ with E_{ef} being the electric field vector, B the magnetic field vector and $\tilde{\mu}$ the permeability of the medium of the wave.

Sail Acceleration Model

A solar sail is a large thin membrane which provides thrust by reflecting photons radiated by the Sun. This reflection results in a momentum transfer from the photon to the sail. The performance metric of the sail used in this work is the characteristic acceleration, defined as the acceleration experienced by the sail at 1 AU when facing the Sun, and given by [11]:

$$a_c = \frac{2\eta_r P}{\sigma} \tag{2.13}$$

where η_r is the reflectivity coefficient ($\eta_r = 1$ for the perfect reflector used in this work), $P = 4.56 \times 10^{-6}$ Nm^{-2} and $\sigma = m/A$, where m is the overall mass of the sailcraft and A is the area of the sail.

Figure 2.4 shows the the angles which define the sail attitude: the cone angle, α, and the clock angle, δ.

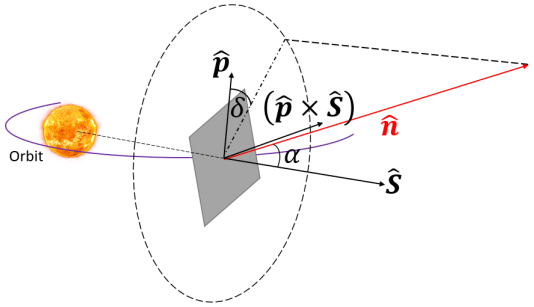

Figure 2.4: Definition of sail clock and cone angles in the frame of reference centred on the spacecraft

The unit vector $\hat{\mathbf{S}}$ gives the radial direction from the Sun to sail, $\hat{\mathbf{p}}$ is in the orbit transversal direction and $\hat{\mathbf{p}} \times \hat{\mathbf{S}}$ is the unit vector normal to the orbit plane. The sail itself is centred on the $[\hat{\mathbf{S}}, \hat{\mathbf{p}} \times \hat{\mathbf{S}}, \hat{\mathbf{p}}]$ frame. The angle of rotation, δ, around the $\hat{\mathbf{S}}$ axis is referred to as the clock angle and the angle, α, which defines the slope of the cone is referred to as the cone angle. With $\delta \in [0, 2\pi]$ and $\alpha \in [0, \pi/2]$, the sail attitude can be fully defined by these two angles, with the unit normal given by [118]:

$$\hat{\mathbf{n}} = [\cos(\alpha), \sin(\alpha)\sin(\delta), \sin(\alpha)\cos(\delta)]^T \tag{2.14}$$

As the sail used throughout this thesis is considered to be perfectly reflecting and flat, the sail normal unit vector $\hat{\mathbf{n}}$ is coincident with the sail thrust vector. Therefore, the sail control can be defined either in terms of the cone and clock angles, or in terms of $\hat{\mathbf{n}}$, where the sail acceleration for a flat, perfectly reflecting solar sail at 1 AU, is given by [99]:

$$\mathbf{a}_s = a_c \left(\hat{\mathbf{S}} \cdot \hat{\mathbf{n}}\right)^2 \hat{\mathbf{n}} \tag{2.15}$$

Solar sails which have actually flown have had very modest values of a_c. For near to mid-term missions, values of a_c ranging from 0.10 mm/s^2 to 1.00 mm/s^2 can be expected [119]. In this thesis, a value of $a_c = 0.20$ mm/s^2 will be the preferred value so as to link previous work on multi-asteroid rendezvous missions which used this value.

Throughout this work, a perfectly reflecting sail was considered. In reality, not all of the photons which intersect with the surface of the sail will be reflected. As such, a real-world sail would experience a reduced magnitude of acceleration. This can be accounted for by multiplying the acceleration by a reflectivity coefficient. Often in the literature, the non-perfect reflection coefficient is set to 0.85. However, given this is simply a reduction in the sail acceleration magnitude, the perfectly reflecting model is considered sufficient for early mission design.

Another factor which can affect the performance of the sail is the billowing of the sail material. This billowing has the effect that the thrust vector provided by the sail is no longer coincident with the unit normal to the sail surface. Again, this level of detail is not necessary in early mission design and so in this work a flat sail is considered where the thrust vector and sail

surface unit normal are coincident.

Solar Sail Performance in the Weak Asteroid Gravity Field

The value of characteristic acceleration used throughout this thesis is $a_c = 0.2$ mm/s^2, unless otherwise stated in analysis which varies that value. This value was chosen so as to link with other works related to the interplanetary phase of a multi-asteroid rendezvous mission [81, 82]. By maintaining the same value as shown by those authors, the current work can be proposed as a direct connection to that phase of the mission. The same value was also proposed in Ref. [80] for a multi-asteroid rendezvous. Indeed, many authors have proposed solar sail missions with higher performance sails [120–123].

However, given the weak gravity field around an asteroid, there are cases where the magnitude of the sail acceleration exceeds the magnitude of the asteroid gravitational acceleration. Morrow and Scheeres [124] define upper limits for a size of sail which can maintain bound motion around an asteroid of a given size with the maximum characteristic acceleration, given as:

$$a_c^M = \frac{r_{au}^2}{16}\frac{\bar{\mu}}{r_0} \tag{2.16}$$

where r_{au} is the distance of the sun to the asteroid in AU and $\bar{\mu}$ is the asteroid gravitational parameter in dimensional units. When the sail and asteroid are far from the Sun, given the inverse square scaling for the magnitude of the sail acceleration, operations around smaller asteroids are possible. The sail performance also needs to be such that it is capable of making the interplanetary transfer to the asteroid, or to multiple asteroids, and this has been shown possible even for lower performance sails [125].

2.2.2 Asteroid Shape Models

Spherical Harmonics Expansion (SHE)

Spherical harmonic expansions (SHE) are obtained by solving Laplace's equation in spherical coordinates corresponding to a position vector $\vec{r} = x\hat{x} + y\hat{y} + z\hat{z}$, denoted by:

$$\begin{aligned} r &= \sqrt{x^2 + y^2 + z^2} \\ \sin\phi &= \frac{z}{r} \\ \tan\psi &= \frac{y}{x} \end{aligned}$$

Here, ϕ represents the latitude, ψ is the longitude, and r is the orbital radius of the spacecraft. And so, the general form of the spherical harmonic potential for a gravity field is given by:

$$U(r,\phi,\psi) = \frac{\mu}{r}\sum_{l=0}^{\infty}\sum_{m=0}^{l}\left(\frac{r_0}{r}\right)^l P_{l,m}(\sin\phi)\left[C_{l,m}\cos m\psi + S_{l,m}\sin m\psi\right]$$

with $\mu = GM$ where M is the mass of the body and G is Newton's gravitational constant. $C_{l,m}$ and $S_{l,m}$ and the harmonic coefficients and $P_{l,m}$ are the Legendre functions given by a recursive calculation [5]:

$$\begin{aligned}
P_{l,0}[\cos\Lambda] &= \frac{(2l-1)\cos\Lambda P_{l-1,0}[\cos\Lambda] - (l-1)P_{l-2,0}[\cos\Lambda]}{l} && (l \geq 2)\\
P_{l,m}[\cos\Lambda] &= P_{l-2,m}[\cos\Lambda] + (2l-1)\cos(\phi)P_{l-1,m-1}[\cos\Lambda] && (m \neq 0, m < l)\\
P_{l,l}[\cos\Lambda] &= (2l-1)\cos(\phi)P_{l-1,l-1}[\cos\Lambda] && (l \neq 0)
\end{aligned} \tag{2.17}$$

where Λ is the angle between the spacecraft position vector and the position vector of an infinitesimal point on the large attracting body. The starting values are given by:

$$\begin{aligned}
P_{0,0}[\cos\Lambda] &= 1\\
P_{1,0}[\cos\Lambda] &= \cos\Lambda = \sin(\phi)\\
P_{1,1}[\cos\Lambda] &= \cos(\phi)
\end{aligned} \tag{2.18}$$

The acceleration produced by the spherical harmonics representation are given by [5]:

$$\mathbf{a} = \frac{\partial U}{\partial r}\left(\frac{\partial r}{\partial \mathbf{r}}\right) + \frac{\partial U}{\partial \phi}\left(\frac{\partial \phi}{\partial \mathbf{r}}\right) + \frac{\partial U}{\partial \psi}\left(\frac{\partial \psi}{\partial \mathbf{r}}\right)$$

where

$$
\begin{aligned}
\frac{\partial U}{\partial r} &= -\frac{\mu}{r^2}\sum_{l=2}^{\infty}\sum_{m=0}^{l}\left(\frac{R}{r}\right)^l (l+1)\,P_{l,m}\left[\sin(\phi)\right]\left\{C_{l,m}\cos(m\psi)+S_{l,m}\sin(m\psi)\right\}\\
\frac{\partial U}{\partial \phi} &= \frac{\mu}{r}\sum_{l=2}^{\infty}\sum_{m=0}^{l}\left(\frac{R}{r}\right)^l \left\{P_{l,m+1}\left[\sin(\phi)\right]-m\tan(\phi)P_{l,m}\left[\sin(\phi)\right]\right\}\\
&\quad\times\left\{C_{l,m}\cos(m\psi)+S_{l,m}\sin(m\psi)\right\}\\
\frac{\partial U}{\partial \psi} &= \frac{\mu}{r}\sum_{l=2}^{\infty}\sum_{m=0}^{l}\left(\frac{R}{r}\right)^l mP_{l,m}\left[\sin(\phi)\right]\left\{S_{l,m}\cos(m\psi)-C_{l,m}\sin(m\psi)\right\}\\
\frac{\partial r}{\partial \mathbf{r}} &= \frac{\mathbf{r}}{r}\\
\frac{\partial \phi}{\partial \mathbf{r}} &= \frac{1}{\sqrt{x^2+y^2}}\left(z\frac{\mathbf{r}}{r^2}+\frac{\partial z}{\partial \mathbf{r}}\right)\\
\frac{\partial \psi}{\partial \mathbf{r}} &= \frac{1}{x^2+y^2}\left(x\frac{\partial y}{\partial \mathbf{r}}-y\frac{\partial x}{\partial \mathbf{r}}\right)
\end{aligned}
$$

and so, the final accelerations are given by [5]:

$$
\begin{aligned}
a_x &= \left(\frac{1}{r}\frac{\partial U}{\partial r}-\frac{z}{r^2\sqrt{x^2+y^2}}\frac{\partial U}{\partial \phi}\right)x-\left(\frac{1}{x^2+y^2}\frac{\partial U}{\partial \psi}\right)y-\frac{\mu}{r^3}x\\
a_y &= \left(\frac{1}{r}\frac{\partial U}{\partial r}-\frac{z}{r^2\sqrt{x^2+y^2}}\frac{\partial U}{\partial \phi}\right)y+\left(\frac{1}{x^2+y^2}\frac{\partial U}{\partial \psi}\right)x-\frac{\mu}{r^3}y\\
a_z &= \frac{1}{r}\frac{\partial U}{\partial r}z+\frac{\sqrt{x^2+y^2}}{r^2}\frac{\partial U}{\partial \phi}-\frac{\mu}{r^3}z
\end{aligned}
\tag{2.19}
$$

With this, we now only require the harmonic coefficients in order to proceed.

The harmonic coefficients are what define the gravitational potential around the chosen shape model. Simple forms such as spheres, spheroids and ellipsoids can be used to represent a body of unknown shape. The "surface" of the body is what is referred to as the Brillouin sphere, spheroid or ellipsoid. Figure 2.5 shows the Brillouin sphere around the body which it represents via spherical harmonics. The gravitational field on the outside of this sphere will converge [52], whereas attempts to model within the sphere are prone to divergence.

Hu and Jekeli [52] argue that, especially for highly irregular bodies but even for moderately non-spherical bodies, an ellipsoidal model will provide the most accurate results, given the reduced area of divergence. This is shown in Fig. 2.6 where the area of divergence is greatly reduced compared to that of the sphere. However, ellipsoidal models are computationally very expensive and so Sebera *et al* [53] and Reimond and Baur [54] argue that a spheroidal model gives the best compromise between the simplicity of the spherical model and the accuracy of the

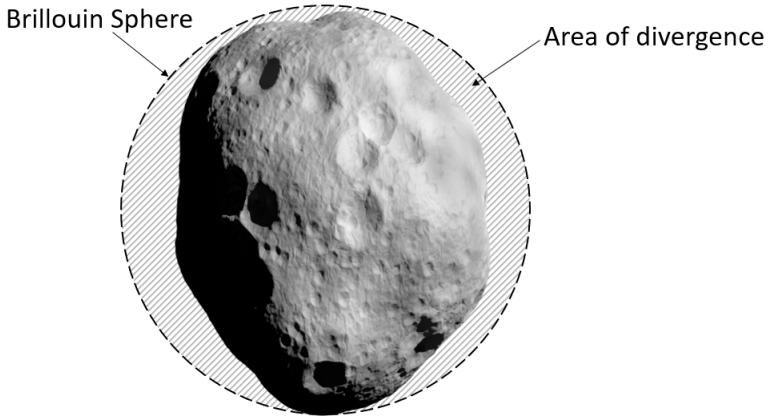

Figure 2.5: Brillouin Sphere representation around asteroid with area of divergence shown in shaded area

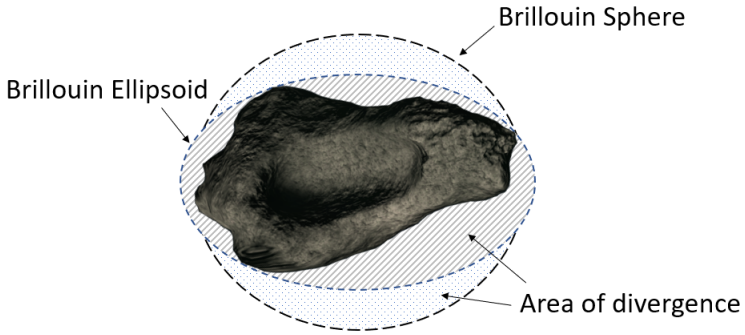

Figure 2.6: Brillouin Sphere-Ellipsoid comparison for highly irregular body. Area of divergence seen to be smaller for ellipsoid model.

ellipsoidal model.

As shape models are only available for a select number of asteroids, an initial approximation can be made using the Brillouin surface as the reference surface for the asteroid. Figure 2.7 shows the dimensions of the ellipsoid with the semi-axes represented by a_e along the major dimension and b_e and c_e along the minor dimensions. Note that the body fixed coordinate system is also fixed along these dimensions with the x-axis along the semi-major axis. For all cases, $c_e \leq b_e \leq a_e$.

With the computationally intensive task encountered on trying to model ellipsoidal harmonics, it is interesting to note that, for a ellipsoid of eccentricity less than $1/\sqrt{2}$, the gravity field converges using the spherical model with the following lower order coefficients [4]:

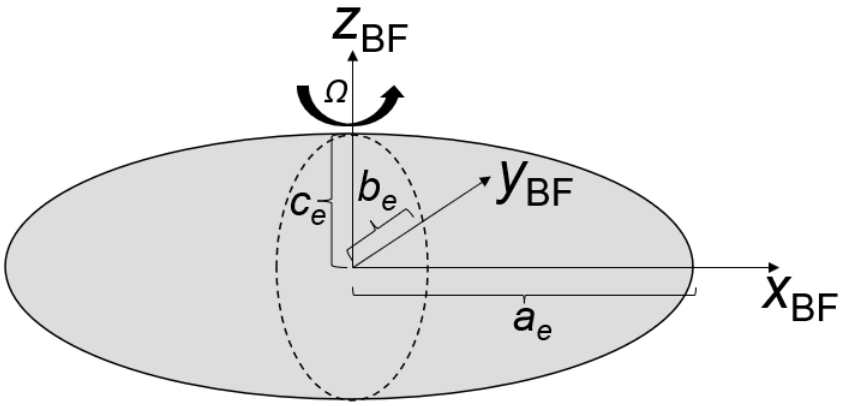

Figure 2.7: Dimensions of ellipsoid, as presented in [4]

$$C_{20} = \frac{1}{5r_0}^2 \left(c_e^2 - \frac{a_e^2 + b_e^2}{2} \right)$$
$$C_{22} = \frac{1}{20r_0^2} \left(a_e^2 - b_e^2 \right)$$
$$C_{40} = \frac{15}{7} \left(C_{20}^2 + 2C_{22}^2 \right)$$
$$C_{42} = \frac{5}{7} C_{20} C_{22}$$
$$C_{44} = \frac{5}{28} C_{22}^2$$

where r_0 is some normalising radius (in this case it will be the length of the longest dimension, a_e).

Polyhedron Model

One of the more accurate ways of modelling a body, particularly where there is knowledge regarding the true shape, is that of polyhedral modelling. Polyhedral modelling uses a number of triangular faces to approximate the surface geometry of a body. Higher numbers of faces allow for higher resolution models, though these higher resolution models come with the inherent increase in computational intensity.

The geometry of the problem is shown in Fig. 2.8, where point P is a distance r from a differential mass element dm on the body being modelled [126].

Gauss's divergence theorem dictates that the potential of a body can be written as:

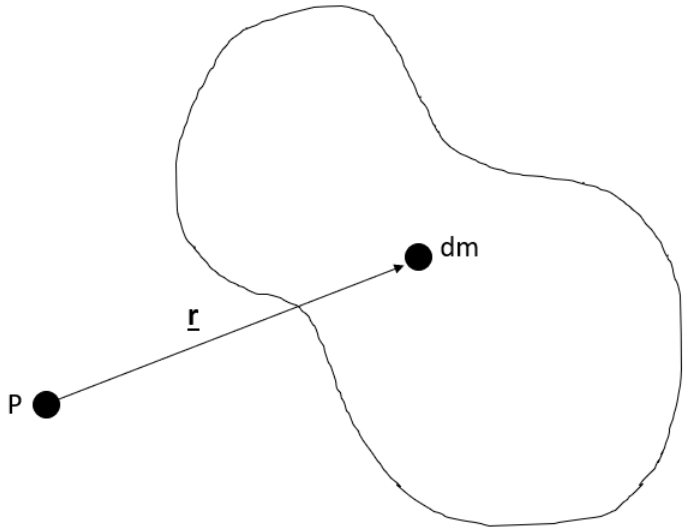

Figure 2.8: Model of polyhedron setup where field point P is at distance r from differential element of body

$$\begin{aligned} U(\mathbf{r}) &= G \int\int\int_M \frac{1}{r} \mathrm{d}m \\ &= \frac{1}{2} G\rho \int\int_S \hat{\mathbf{n}} \cdot \hat{\mathbf{r}} \mathrm{d}S \end{aligned} \tag{2.20}$$

where ρ is the density of the body, G is the universal gravitational constant, $\underline{\hat{n}}$ is the unit normal to the element surface, S is the surface of the body and $\underline{\hat{r}}$ is the direction of point P relative to the differential mass element [69].

For a polyhedron, the potential can be written as the sum of Eq. 2.20 over all faces of the body:

$$U(\mathbf{r}) = \frac{1}{2} G\rho \sum_{f \in faces} \hat{\mathbf{n}}_f \cdot \hat{\mathbf{r}}_f \int\int_f \frac{1}{r} \mathrm{d}S \tag{2.21}$$

By now including both the edges and the faces, the total potential is given by:

$$U(\mathbf{r}) = \frac{1}{2} G\rho \sum_{e \in edges} \mathbf{r}_e \cdot \mathbf{E}_e \cdot \mathbf{r}_e \cdot L_e - \frac{1}{2} G\rho \sum_{f \in faces} \mathbf{r}_f \cdot \mathbf{F}_f \cdot \mathbf{r}_f \cdot \omega_f \tag{2.22}$$

where $\mathbf{E}_e$ is a dyad defined in terms of the face and edge normal vectors associated with each edge, L_e is a logarithmic term expressing the potential of a 1-D straight wire, $\mathbf{F}_f$ is a dyad defined for each face as the outer product of the face unit normal with itself and ω_f is the signed solid angle subtended by a face when viewed from the field point [69]. A complete derivation of the above can be obtained from Ref. [78]. By including the rotation of the asteroid, the polyhedron effective potential is given by:

$$V(\mathbf{r}) = \frac{1}{2}(\boldsymbol{\omega} \times \mathbf{r}) \cdot (\boldsymbol{\omega} \times \mathbf{r}) + U(\mathbf{r}) \tag{2.23}$$

2.2.3 Dynamical Models

This section will describe the various dynamical models used for simulations in this work. The dynamical regime is discussed first and is defined by the distance of the spacecraft from the attracting body. At large distances, the shape and spin-state of the attracting body have a negligible effect, though the gravitational effects from the Sun may not be negligible. In such cases, a 3-body point-mass model can be applied. Where the spacecraft close to the attracting body, and where the asteroid gravity dominates the gravitational effect from the Sun, a point-mass two body problem can be applied. Operations closer to the surface of the attracting body demand consideration of the effects from any irregular shape as well as the rotation and so one of the aforementioned shape models must be applied, though the gravitational effects of the Sun can be discounted.

Dynamical Regimes

This research focuses on the orbits of a spacecraft in proximity of an asteroid. The proximity in this work is defined by two distinct dynamic regimes: the "inner" regime and the "outer" regime.

The inner regime is defined by a sphere which is centred on the asteroid and whose radius is the distance from the asteroid centre to the point at which the effects on the gravitational field from the shape of the asteroid become negligible. This is equivalent to searching for the distance from the asteroid centre at which point the gradient of the potential field of the true shape model and a point-mass model are equal. The outer regime is all of the space which lies beyond the inner regime.

The gradient of the potential field, $\nabla U = [a_x, a_y, a_z]$, is obtained for both a point-mass and polyhedron model for a range of eleven NEAs. The difference between the point-mass and polyhedron values along the x, y and z directions $(\Delta a_x, \Delta a_y, \Delta a_z)$ are measured separately. That is:

$$\begin{aligned}
\Delta a_x &= \nabla U^{Polyhedron}(x,0,0) - \nabla U^{PointMass}(x,0,0) \\
\Delta a_y &= \nabla U^{Polyhedron}(0,y,0) - \nabla U^{PointMass}(0,y,0) \\
\Delta a_z &= \nabla U^{Polyhedron}(0,0,z) - \nabla U^{PointMass}(0,0,z)
\end{aligned} \tag{2.24}$$

The acceleration values are scaled by the acceleration at the distance of a synchronous orbit with 1:1 resonance. The acceleration values are rounded to two decimal places and convergence is achieved where $\Delta a_x \approx \Delta a_y \approx \Delta a_z \approx 0$.

Figure 2.9 shows the difference in gravitational acceleration between the point-mass and

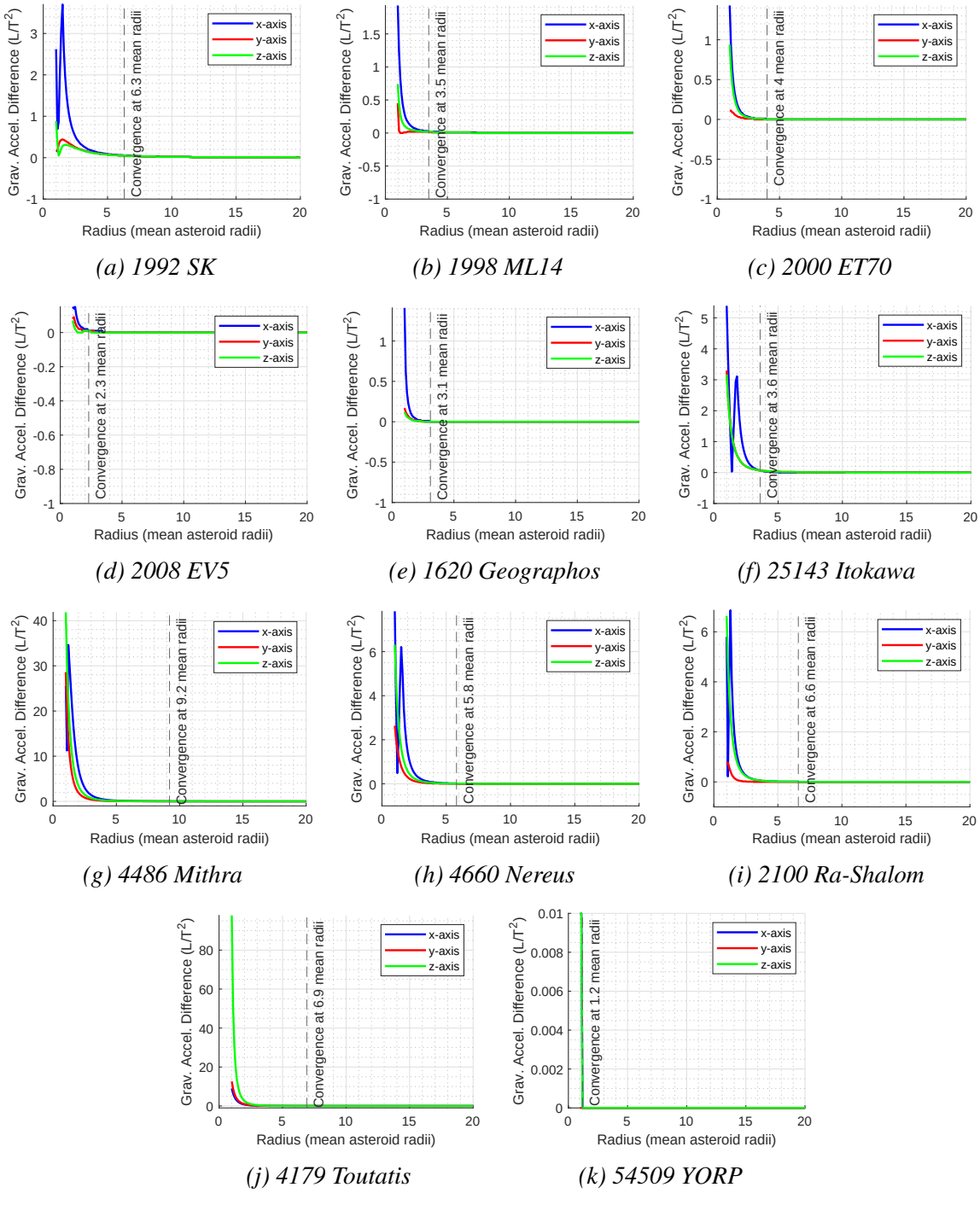

(a) 1992 SK *(b) 1998 ML14* *(c) 2000 ET70*

(d) 2008 EV5 *(e) 1620 Geographos* *(f) 25143 Itokawa*

(g) 4486 Mithra *(h) 4660 Nereus* *(i) 2100 Ra-Shalom*

(j) 4179 Toutatis *(k) 54509 YORP*

Figure 2.9: Difference between potential from point-mass model and polyhedron model. Values of potential taken along x, y and z axes as indicated on the plots.

polyhedron models. Table 2.1 lists the value of mean asteroid radius at which the values converge for each asteroid. It is found that the mean value of these radii is 4.8. As such, in all work for the thesis, a value of 5 mean asteroid radii will be used as the boundary between the outer and inner regimes.

Table 2.1: Point-mass and polyhedron convergence radii for 11 Near-Earth Asteroids

Asteroid	Convergence Sphere Radius
1992 SK	$6.3r_0$
1998 ML14	$3.5r_0$
2000 ET70	$4.0r_0$
2008 EV5	$2.3r_0$
1620 Geographos	$3.1r_0$
25143 Itokawa	$3.6r_0$
4486 Mithra	$9.2r_0$
4660 Nereus	$5.8r_0$
2100 Ra-Shalom	$6.6r_0$
4179 Toutatis	$6.9r_0$
54509 YORP	$1.2r_0$
Mean Value	$4.8r_0$

With this analysis, the radius at which the inner and outer regimes, the relevant dynamical and shape models and reference frames are presented in Table 2.2.

Table 2.2: Dynamical regimes with the radius at which the regime applies in terms of asteroid mean radius (r_0) and associated dynamical models, shape models and reference frames

	Outer regime	Inner regime
Regime operational radius	$> 5r_0$	$\leq 5r_0$
Dynamical model	SSHR3BP	Two-body
Shape model	Point-mass	Ellipsoid/Polyhedron
Reference frame	Sun-Asteroid Synodic	Body-fixed

Two-body Equation

The simplest dynamical model used in this work is that of the two-body model where the attracting body is considered a point mass. The model starts from Newtons second law and universal law of gravitation [5]:

$$\mathbf{F}_g = -\frac{Gm_b m_s}{r^2}\frac{\mathbf{r}}{r} \tag{2.25}$$

where G is the gravitational constant, m_b is the mass of the large attracting body and m_s is the mass of the spacecraft. Considering an inertial frame of reference, the equation of motion can be determined. First the inertial force of the large attractor is given by:

$$\mathbf{F}_{g_b} = m_b \ddot{\mathbf{r}}_b = \frac{G m_b m_s}{r^2} \frac{\mathbf{r}}{r} \tag{2.26}$$

and the inertial force of the spacecraft by:

$$\mathbf{F}_{g_s} = m_s \ddot{\mathbf{r}}_s = -\frac{G m_b m_s}{r^2} \frac{\mathbf{r}}{r} \tag{2.27}$$

where $\mathbf{r}_b$ is the position of the large attractor in the inertial frame and $\mathbf{r}_s$ is the position of the spacecraft in the inertial frame, where:

$$\mathbf{r} = \mathbf{r}_s - \mathbf{r}_b \tag{2.28}$$

Therefore:

$$\begin{aligned} \ddot{\mathbf{r}} &= -\frac{G m_b}{r^2} \frac{\mathbf{r}}{r} - \frac{G m_s}{r^2} \frac{\mathbf{r}}{r} \\ &= -\frac{G(m_b + m_s)}{r^2} \frac{\mathbf{r}}{r} \end{aligned} \tag{2.29}$$

Given that the mass of the spacecraft is negligible compared with that of the large attractor, and substituting $\mu = G m_b$, this becomes:

$$\ddot{\mathbf{r}} = -\frac{\mu}{r^2} \frac{\mathbf{r}}{r} \tag{2.30}$$

This is the basic two-body equation of motion [5] in its form relative to the large attracting body.

Restricted Full 2-Body Problem (RF2BP)

For operations in the inner regime, where the sailcraft is not approaching the asteroid surface, an ellipsoidal model will be implemented in the Restricted Full 2-Body Problem (RF2BP) [127]. In this problem, the mass ratio of the smaller body to the larger body tends to zero, the case for a massless particle orbiting the large primary. This dynamical model uses the BF frame for all calculations, though some transformations are made later to the ACI frame for analysis. The potential function for the RF2BP is given by:

$$V(x,y,z) = -\frac{1}{\sqrt{x_{\mathrm{BF}}^2 + y_{\mathrm{BF}}^2 + z_{\mathrm{BF}}^2}} - \frac{1}{2}\left(x_{\mathrm{BF}}^2 + y_{\mathrm{BF}}^2 + z_{\mathrm{BF}}^2\right) + U \tag{2.31}$$

where U is the potential due to the non-spherical shape of the asteroid. The non-dimensional equations of motion for the RF2BP are given by:

$$\begin{aligned} \ddot{x}_{\mathrm{BF}} - 2\dot{y}_{\mathrm{BF}} &= -\frac{\partial V}{\partial x_{\mathrm{BF}}} \\ \ddot{y}_{\mathrm{BF}} - 2\dot{x}_{\mathrm{BF}} &= -\frac{\partial V}{\partial y_{\mathrm{BF}}} \\ \ddot{z}_{\mathrm{BF}} &= -\frac{\partial V}{\partial z_{\mathrm{BF}}} \end{aligned} \tag{2.32}$$

To consider a simple ellipsoidal potential, the sectoral harmonic [5] C_{22} gravity coefficient, which gives the body ellipticity, can be used [86, 127]. It is possible to define the C_{22} gravity coefficient from the dimensions of the ellipsoidal body. The ellipsoid dimensions are shown in Fig. 2.7. Using these dimensions, the gravity coefficient is given by [128]:

$$\bar{C}_{22} = \frac{1}{20\bar{r}_0^2}\left(\bar{a}_e^2 - \bar{b}_e^2\right) \tag{2.33}$$

where r_0 is the ellipsoid mean radius and the bar notation again denotes dimensional units. The normalised gravity coefficient is then given by:

$$C_{22} = \left(\frac{\bar{\mu}}{\bar{\Omega}^2}\right)^{-\frac{2}{3}} \bar{r}_0^2 \bar{C}_{22} \tag{2.34}$$

The non-dimensional ellipsoidal potential is then given by [86, 127]:

$$U_{22} = -\frac{3\,C_{22}\left(x_{\mathrm{BF}}^2 - y_{\mathrm{BF}}^2\right)}{\left(x_{\mathrm{BF}}^2 + y_{\mathrm{BF}}^2\right)^{5/2}} \tag{2.35}$$

which can be included in the potential function:

$$V(x,y,z) = -\frac{1}{\sqrt{x_{\mathrm{BF}}^2 + y_{\mathrm{BF}}^2 + z_{\mathrm{BF}}^2}} - \frac{1}{2}\left(x_{\mathrm{BF}}^2 + y_{\mathrm{BF}}^2 + z_{\mathrm{BF}}^2\right) + U_{22} \tag{2.36}$$

A system of normalisation [84] then sets the reference length as the orbital radius of a 1:1 synchronous orbit around a spherical body:

$$DU = \left(\frac{\bar{\mu}}{\bar{\Omega}^2}\right)^{\frac{1}{3}} \tag{2.37}$$

Time is then normalised by $TU = \bar{\Omega}^{-1}$.

Where the spacecraft is approaching the surface of the asteroid, it becomes necessary to account for the true surface topology. In these instances, the higher resolution polyhedron models available can be implemented by replacing the U_{22} term in Eq. 2.36 with the potential function for the polyhedron model in Eq. 2.22.

Solar Sail Hill's Restricted 3-Body Problem (SSHR3BP)

In the case of the Sun-asteroid-spacecraft system, the vanishingly small mass ratio of the small primary to the large primary allows some modification to the standard Circular Restricted 3-Body Problem (CR3BP). For such a scenario, Hill's Restricted 3-Body Problem (HR3BP) can be used [73]. In the HR3BP dynamical model, the synodic reference frame described in Section 2.1.3 is used. The HR3BP is normalised using the Hill radius, which gives length unit:

$$DU = \left(\frac{\bar{\mu}}{3\bar{\Omega}^2} \right)^{\frac{1}{3}} \tag{2.38}$$

where $\bar{\mu}$ is the asteroid gravitational parameter and $\bar{\Omega}$ is the orbital angular velocity of the asteroid, with the bar notation denoting dimensional units. In the non-dimensional system, $\mu = 3$ and $\Omega = 1$. As such, the non-dimensional equations of motion for the SSHR3BP are given by [124]:

$$\begin{aligned} \ddot{x}_{\text{SYN}} &= 2\dot{y}_{\text{SYN}} - \frac{\mu}{r_{\text{SYN}}^3} x_{\text{SYN}} + 3x_{\text{SYN}} + a_{x_{\text{SYN}}} \\ \ddot{y}_{\text{SYN}} &= -2\dot{x}_{\text{SYN}} - \frac{\mu}{r_{\text{SYN}}^3} y_{\text{SYN}} + a_{y_{\text{SYN}}} \\ \ddot{z}_{\text{SYN}} &= -\frac{\mu}{r_{\text{SYN}}^3} z_{\text{SYN}} - z_{\text{SYN}} + a_{z_{\text{SYN}}} \end{aligned} \tag{2.39}$$

where $r_{\text{SYN}} = \sqrt{x_{\text{SYN}}^2 + y_{\text{SYN}}^2 + z_{\text{SYN}}^2}$ and the sail acceleration ($\mathbf{a}_s = [a_{x_{\text{SYN}}}, a_{y_{\text{SYN}}}, a_{z_{\text{SYN}}}]$) is given by Eq. 2.15.

The continuous acceleration provided by the momentum transfer from photon to sail has a considerable effect on the dynamics of the 3-body system, not least of which is a positional change in the system equilibrium points. This work will leverage such artificially displaced equilibrium points (AEPs) of the restricted 3-body problem. These AEPs provide convenient deployment locations for probes sent towards the surface of the asteroid. The equilibrium points of the system are obtained from:

$$\begin{aligned} 0 &= -\frac{\mu}{r_{\text{SYN}}^3} x_{\text{SYN}} + 3x_{\text{SYN}} + a_{x_{\text{SYN}}} \\ 0 &= -\frac{\mu}{r_{\text{SYN}}^3} y_{\text{SYN}} + a_{y_{\text{SYN}}} \\ 0 &= -\frac{\mu}{r_{\text{SYN}}^3} z_{\text{SYN}} - z_{\text{SYN}} + a_{z_{\text{SYN}}} \end{aligned} \tag{2.40}$$

This can also be written in vector form as:

$$\nabla U = -\mathbf{a}_s \tag{2.41}$$

where U is the effective gravitational potential in the HR3BP. The sail orientation can then be

obtained from [99, 129]:

$$\hat{\mathbf{n}} = -\frac{\nabla U}{|\nabla U|} \tag{2.42}$$

With this, it is possible to calculate the required sail characteristic acceleration to maintain an AEP for a particular sail attitude from:

$$a_c = -\frac{\nabla U \cdot \hat{\mathbf{n}}}{(\hat{\mathbf{S}} \cdot \hat{\mathbf{n}})^2} \tag{2.43}$$

As an example, the contours of a_c for asteroid Vesta can be established, similar to those results shown in Figs. [99, 124]. These contours contain the AEPs for each value of a_c at different sail orientations, and are shown in Fig. 2.10 with the labels showing the value of a_c at those contours.

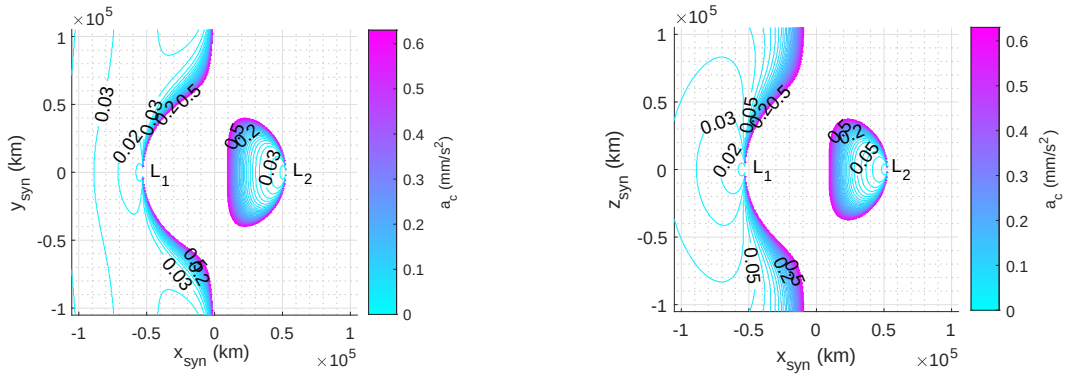

(a) x-y plane *(b) x-z plane*

Figure 2.10: Contours of AEPs for varying characteristic acceleration

The natural equilibrium points, L_1 and L_2, are indicated in Fig. 2.10. It can be seen that the inability of the sail to produce thrust in the negative radial direction limits the range of AEPs to lie on the Sun-side of the natural equilibrium points. The L_2 AEPs are all contained in the enclosed region shown between the natural L_2 point and the asteroid, and the L_1 AEPs are all contained on the solar side of the asteroid.

2.2.4 Modelling Eclipses

When the sail passes on the side of the asteroid in the anti-Sun direction, there are periods where no sunlight reaches the sail. When this happens, it is not possible for the sail to thrust. At large distances from the asteroid, these eclipse periods are of very short duration and so can be ignored. However, in orbits which are close to the asteroid, they can form considerable portions of the orbital period. As such, it becomes necessary to account for these in trajectory calculations for the sail. Eclipses are simulated as discussed in Ref. [5], and outlined in Fig.

2.11. Although the asteroids considered are of irregular shape, the eclipse model is based on a simplified spherical body.

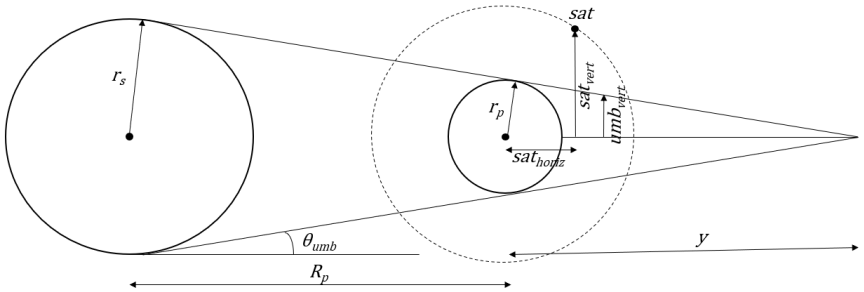

Figure 2.11: Eclipse model, as given in Ref. [5]

The angle of umbra is given by:

$$\sin(\theta_{umb}) = \frac{r_s - r_p}{R_p} \tag{2.44}$$

where r_s is the radius of the Sun, r_p is the radius of the planet or body and R_p is the distance between the Sun and the planet/body. The vertical length of the umbra region is then calculated by:

$$umb_{vert} = \tan(\theta_{umb})(y - sat_{horiz}) \tag{2.45}$$

where $y = \frac{r_p}{\sin(\theta_{umb})}$ and sat_{horiz} is the component of the satellite position in the ecliptic plane. When the spacecraft is on the side of the asteroid in which the umbra region exists, and when $sat_{vert} \leq umb_{vert}$, the spacecraft is considered to be in umbra. Where this is the case, the sail acceleration is set to zero and the trajectory becomes purely ballistic.

The eclipse model was applied to the work contained in Chapter 5 for the pre- and post-deployment orbits for the single large landers.

2.2.5 Selected Asteroids for This Work

In order to model the gravity field of an asteroid, some parameters must be known. The required parameters depends on the shape and dynamical model being used. For a point mass model, only the mass of the asteroid is required to be known. For an ellipsoid, the ellipsoidal dimensions are required in addition to the mass. For the complex polyhedron models, the face and vertex coordinates are required. In order to fulfil these requirements, we select a number of asteroids for study in this work. The selection of the asteroids contained here is not with a mission proposal to that asteroid in mind, but instead was made principally based on their variety of shape.

Table 2.3 gives some of the data for the selected asteroids. In this work there are two variants of asteroid Florence, due to an error made in Chapter 4 where the mean diameter was mistaken

for the mean radius. As such, Florence$_a$ has twice the mean radius of Florence$_b$. All of the polyhedron models were obtained from an online catalogue[1].

Table 2.3: Selected asteroids and their parameters. Assumed values denoted by *.

Asteroid	Mass (kg)	Mean Radius (km)	Density (g/cm^3)	μ (km^3/s^2)	a_e (km)	b_e (km)	c_e (km)	Polyhedron Model
Castalia	1.40×10^{12}	0.70	9.36×10^{-8}	2.10	-	-	-	Y
Eros	6.69×10^{15}	8.42	2.68	4.00×10^{-4}	-	-	-	Y
Florence$_a$	1.39×10^{15}	4.90	3.50*	9.28×10^{-5}	4.90	4.50	4.30	N
Florence$_b$	1.74×10^{14}	2.45	3.50*	1.00×10^{-5}	2.45*	2.25*	2.15*	N
Geographos	3.21×10^{13}	2.70	3.50*	2.14×10^{-6}	-	-	-	Y
Itokawa	3.15×10^{10}	0.17	1.67	2.10×10^{-9}	-	-	-	Y
Mithra	8.86×10^{12}	0.92	3.50*	5.92×10^{-7}	-	-	-	Y
Vesta	2.59×10^{20}	262.70	3.46	21.92	286.30	278.60	223.20	Y

Those asteroids which were never represented by an ellipsoid have no ellipsoidal dimensions listed for them. Additionally, any values which were unknown have been assumed. This is often the case for the density of the asteroid material. Where this is the case, a value of 3.50 g/cm^3 is used [128].

2.3 Control

2.3.1 Control Transition Matrix

The errors in state at time t, due to variations at t_0, are given by (to a linear approximation):

$$\delta\mathbf{s}(t) = \Phi_S(t,t_0)\delta\mathbf{s}(t_0) \tag{2.46}$$

where Φ_S is the State Transition Matrix (STM) [5,130]. In this work, the interest lies in the effect that variations of control, rather than initial state, will have on the final state of the spacecraft. As such, this work now extends the linear theory of the STM to include these control variations. An equivalent matrix to the STM will be referred to as the Control Transition Matrix (CTM). Each entry of the CTM represents the variation in the final states for a unitary variation in each of the controls. The matrix size is therefore $6\times2N$, where N is the number of control nodes. The controls are the sail cone and clock angles, α and δ. The CTM is built numerically, thus alleviating any complicated mathematical formulations, by the following method:

1. The nominal orbit and control law are obtained from some optimisation method, such as a Genetic Algorithm. The control law for the nominal orbit will contain two controls, the sail cone angle, α, and the sail clock angle, δ, as part of the solution vector. This solution will contain a $1\times N$ array for α and a $1\times N$ array for δ.

2. Let us now define an indexing variable over the control nodes, i.

[1] `https://3d-asteroids.space/asteroids/`

3. Variations will first be made to control, α
4. A small variation in $\alpha(i)$ is made
5. The orbit is propagated with this altered control law
6. The final state error is recorded at the end of this orbit and is inserted to the first column of the CTM. The value of $\alpha(i)$ is reset to the nominal value
7. i is incremented so that $i = i+1$
8. Steps 4-7 are repeated for $i = 1,2,...,N$ for the first control, α.
9. Now, we move to the other control, δ
10. A small variation in $\delta(i)$ is made
11. The orbit is propagated with this altered control law
12. The final state error is recorded at the end of this orbit, divided by the magnitude of the variation, and is inserted to the first column of the CTM. The value of $\delta(i)$ is reset to the nominal value
13. i is incremented
14. Steps 4-7 are repeated for $i = 1,2,...,N$ for the first control, δ.

Completion of these steps results in the $6 \times 2N$ CTM. By replacing Φ_S, of Eq. 2.46, with the CTM, Φ_C:

$$\delta\mathbf{s}(t_f) = \Phi_C \delta\mathbf{u}(t) \tag{2.47}$$

where $\delta\mathbf{u}(t)$ are the deviations in control vector $\mathbf{u}_{nom}(t)$. The objective is to correct the nominal control law to account for errors in the initial state. The variation of the controls that produces a variation in $\delta\mathbf{s}(t_f)$, is (at least in a first order approximation):

$$\delta\mathbf{u}(t) = \Phi_C^{-1} \delta\mathbf{s}(t_f) \tag{2.48}$$

Therefore, in order to remove an error in $\delta\mathbf{s}_0$ after one period, the aim is to achieve a final error of:

$$\delta\mathbf{s}(t_f) = -\delta\mathbf{s}_0 \tag{2.49}$$

This assumes that the linearisation of the CTM is still valid for the perturbed orbit, allowing the perturbed orbit to be corrected towards the nominal orbit. As the CTM is not a square matrix,

its inverse is not uniquely defined. The Moore-Penrose pseudo-inverse [131] is used to obtain Φ_C^{-1}, which results in a $2N \times 6$ matrix. To update the control law, the nominal control is added to the control variation:

$$\mathbf{u}(t) = \mathbf{u}_{nom}(t) + \delta\mathbf{u}(t) \tag{2.50}$$

2.3.2 Linear Quadratic Regulator

The linear quadratic regulator (LQR) provides a robust, and optimal, control algorithm for many applications. LQR control requires that the equations of motion are re-written as a first-order differential system, $\dot{\mathbf{s}} = \mathbf{f}(t, \mathbf{s})$. The linear dynamics are given in the BF frame by [132]:

$$\delta\dot{\mathbf{s}}(t) = \mathbf{A}(t)\delta\mathbf{s}(t) + \mathbf{B}\mathbf{u}(t) \tag{2.51}$$

where:

$$\mathbf{A}(t) = \begin{bmatrix} \mathbf{0} & \mathbf{I} \\ \mathbf{V}'' & -\mathbf{\Omega} \end{bmatrix} \tag{2.52}$$

and $\mathbf{0}$ is a 3×3 matrix of zeros, $\mathbf{I}$ is a 3×3 identity matrix, and:

$$\mathbf{\Omega} = \begin{bmatrix} 0 & -2 & 0 \\ 2 & 0 & 0 \\ 0 & 0 & 0 \end{bmatrix} \quad \mathbf{V}'' = \begin{bmatrix} \frac{\partial^2 V}{\partial x^2} & \frac{\partial^2 V}{\partial xy} & \frac{\partial^2 V}{\partial xz} \\ \frac{\partial^2 V}{\partial yx} & \frac{\partial^2 V}{\partial y^2} & \frac{\partial^2 V}{\partial yz} \\ \frac{\partial^2 V}{\partial zx} & \frac{\partial^2 V}{\partial zy} & \frac{\partial^2 V}{\partial z^2} \end{bmatrix} \tag{2.53}$$

$$\mathbf{B} = \begin{bmatrix} 0 & 0 & 0 & 1 & 0 & 0 \\ 0 & 0 & 0 & 0 & 1 & 0 \\ 0 & 0 & 0 & 0 & 0 & 1 \end{bmatrix}^T \tag{2.54}$$

This system approximates the real system at a given time and close to the reference trajectory. In order to establish an optimal feedback control law, the following objective function is used:

$$J(\mathbf{u}, t) = \int_0^\infty \left(\delta\mathbf{s}(t)^T \mathbf{Q} \delta\mathbf{s}(t) + \mathbf{u}(t)^T \mathbf{R}\mathbf{u}(t) \right) dt \tag{2.55}$$

where $\mathbf{Q}$ and $\mathbf{R}$ are weighting matrices which give the cost of each state and control. Minimisation of Eq. 2.55 leads to the algebraic Riccati equation [133]:

$$\dot{\mathbf{P}}(t) = \mathbf{P}(t)\mathbf{B}\mathbf{R}^{-1}\mathbf{B}^T\mathbf{P}(t) - \mathbf{A}(t)^T\mathbf{P}(t) - \mathbf{P}(t)\mathbf{A}(t) - \mathbf{Q} \tag{2.56}$$

$\mathbf{Q}$ is a real symmetric positive definite matrix. Equation 2.56 must then be integrated simultaneously with the equations of motion with $\dot{\mathbf{P}}(0) = 0$, $\mathbf{Q} = \mathbf{I}_{n\times n}$ and $\mathbf{R} = \beta\mathbf{I}_{m\times n}$. The free parameter, β, is the weighting parameter which allows the optimal preference to be shifted between min-

imising the effort required to force the periodic orbit, and the best periodic solution. Solution of Eq. 2.56 then allows calculation of the gain matrix:

$$\mathbf{K} = \mathbf{R}^{-1}\mathbf{B}^{T}\mathbf{P}(t) \tag{2.57}$$

where $\mathbf{R}$ is a real symmetric positive definite matrix and $\mathbf{B}$ is a constant $n \times m$ matrix where m is the number of controls and n is the dimension of $\mathbf{s}(t)$. The required control is then obtained from [132]:

$$\mathbf{u}(t) = -\mathbf{K}\delta\mathbf{s} \tag{2.58}$$

Throughout this work, the control parameters contained in $\mathbf{u}(t)$ are the control angles, α and δ.

2.3.3 Time-Delay Feedback control

Time-delayed Feedback Control (TDFC) is a method for stabilising unstable periodic orbits [86, 134] which does not require a reference trajectory but rather depends on the state of the spacecraft one period in the past. This method of control lends itself well to a mission scenario where a reference solution is not known *a priori*. The method uses the LQR algorithm outlined in Section 2.3.2. However, rather than depend on the error between the current state at time t and the reference state, the method uses the state one period in the past:

$$\mathbf{u}(t) = -\mathbf{K}\left(\mathbf{s}(t) - \mathbf{s}(t-\tau)\right) \tag{2.59}$$

where τ is the period of the orbit and $\mathbf{K}$ is the gain matrix. As such, the only orbital parameter which is required to be defined *a priori* is the orbital period.

2.4 Numerical Methods

2.4.1 Genetic Algorithm

The purpose of using the GA in this work is to provide a means of finding an optimal control law where an initial guess close enough to the optimal solution for a direct method to converge is difficult to obtain. The GA provides a method for both constrained and unconstrained optimisation based on the principles of evolution. Having defined "individuals" that encode the solution vector, the algorithm combines pairs of "parents" to produce the next generation of "children". Over successive generations, the "population" will converge to the optimal solution [94]. The algorithm for the GA is as follows:

1. A random initial population is created
2. GA creates a new population using the following process:

(a) Fitness value of each population is computed

(b) These raw fitness scores are scaled

(c) Best fitness values are chosen as the parents for the next generation

(d) The very best fitness scores at each generation are chosen as the "elite"

(e) "Children" are produced either by making random changes in a single parent (mutation), or by combining the vector entries of a pair of parents (crossover)

(f) The current population is replaced with the children to form the next generation

3. Once the pre-defined stopping criteria are met, the algorithm stops

4. Linear and integer constraints require the algorithm to take modified steps

5. There is further modification for the use of nonlinear constraints

The benefit of this algorithm, for the purposes of this work, is that it requires no initial guess from the user. However, it is important to note that the algorithm is stochastic, and the convergence to the global optimum is not guaranteed; in fact, a solution provided from one initial population can be different from the optimal solution for another initial population. As such, it is often necessary to run multiple instances, or "seeds", in order to obtain a true optimal solution. In this work, the GA function contained in the MATLAB software is used.

2.4.2 Radau Collocation Method

In order to solve several of the optimal control problems posed in this thesis, a direct collocation method is employed. In particular, the software used for this employs the Radau collocation method. A general optimal control problem aims to solve the Mayer cost functional [133]:

$$J = M\left(\mathbf{s}(t_0), t_0, \mathbf{s}(t_f), t_f\right) \tag{2.60}$$

subject to the dynamic constraints:

$$\dot{\mathbf{s}} = \mathbf{f}\left(\mathbf{s}(t), \mathbf{u}(t), t\right) \tag{2.61}$$

with the inequality path constraints:

$$\mathbf{c}_{\min} \leq \mathbf{c}\left(\mathbf{s}(t), \mathbf{u}(t), t\right) \leq \mathbf{c}_{\max} \tag{2.62}$$

the integral constraints:

$$q_i = \int_{t_0}^{t_f} g_i\left(\mathbf{s}(t), \mathbf{u}(t), t\right) dt, \quad \left(i = 1, ..., n_q\right) \tag{2.63}$$

and the event constraints:

$$\mathbf{b}_{\min} \leq \mathbf{b}\left(\mathbf{s}(t_0), t_0, \mathbf{s}(t_f), t_f, \mathbf{q}\right) \leq \mathbf{b}_{\max} \tag{2.64}$$

This work uses the *hp* Radau collocation method, which combines the *h* and *p* methods. In the *h* method, the time interval is divided into a mesh and a fixed-degree polynomial can be used in each mesh to approximate the state [9, 135, 136]. In the *p* method, a Lagrange polynomial is typically used to approximate the state and the support points of the polynomial are chosen as points associated with Gaussian quadrature [136, 137]. In the hybrid *hp* method, the number of mesh intervals, as well as the degree of approximating polynomial in each mesh interval, are variable and can be adjusted to achieve a specific accuracy in the approximation of the continuous-time problem [136, 138].

To apply the *hp* Radau collocation method, the optimal control problem is amended as follows. First, time is defined in terms of a new parameter, $\tau \in [-1, 1]$:

$$t = \frac{t_f - t_0}{2}\tau + \frac{t_f + t_0}{2} \tag{2.65}$$

With the optimal control problem now defined in terms of τ, the cost functional becomes:

$$J = M\left(\mathbf{s}(-1), t_0, \mathbf{s}(1), t_f, \mathbf{q}\right) \tag{2.66}$$

subject to the dynamics constraints:

$$\dot{\mathbf{s}} = \frac{t_f - t_0}{2}\mathbf{f}\left(\mathbf{s}(\tau), \mathbf{u}(\tau); t_0, t_f\right) \tag{2.67}$$

the inequality path constraints:

$$\mathbf{c}_{\min} \leq \mathbf{c}\left(\mathbf{s}(\tau), \mathbf{u}(\tau), \tau; t_0, t_f\right) \leq \mathbf{c}_{\max} \tag{2.68}$$

with the integral constraints:

$$q_i = \frac{t_f - t_0}{2}\int_{-1}^{1} g_i\left(\mathbf{s}(\tau), \mathbf{u}(\tau), \tau; t_0, t_f\right) d\tau, \quad \left(i = 1, ..., n_q\right) \tag{2.69}$$

and the event constraints:

$$\mathbf{b}_{\min} \leq \mathbf{b}\left(\mathbf{s}(-1), t_0, \mathbf{s}(1), t_f, \mathbf{q}\right) \leq \mathbf{b}_{\min} \tag{2.70}$$

If the interval $\tau \in [-1, 1]$ is divided into K_R mesh intervals $[T_{k-1}, T_k]$, $k = 1, ..., K_R$, where $(T_0, ..., T_{K_R})$ are the mesh points, and these have the property $-1 = T_0 < T_1 < T_2 < \cdots < T_{K_R} = T_f = 1$. The state and control in the mesh interval k are given by $\mathbf{s}^{(k)}(\tau)$ and $\mathbf{u}^{(k)}(\tau)$, and the optimal control problem can be be written as follows, with the cost functional given by:

$$J = M\left(\mathbf{s}^{(1)}(-1), t_0, \mathbf{s}^{K_R}(1), t_f, \mathbf{q}\right) \tag{2.71}$$

with the dynamics constraints:

$$\dot{\mathbf{s}}^{(k)}(\tau^{(k)}) = \frac{t_f - t_0}{2}\mathbf{f}\left(\mathbf{s}(\tau^{(k)}), \mathbf{u}^{(k)}(\tau^{(k)}), \tau^{(k)}; t_0, t_f\right), \quad (k = 1, ..., K_R) \tag{2.72}$$

the path constraints:

$$\mathbf{c}_{\min} \leq \mathbf{c}\left(\mathbf{s}^{(k)}(\tau^{(k)}), \mathbf{u}^{(k)}(\tau^{(k)}), \tau^{(k)}; t_0, t_f\right) \leq \mathbf{c}_{\max}, \quad (k = 1, ..., K_R) \tag{2.73}$$

the integral constraints:

$$q_i = \frac{t_f - t_0}{2}\sum_{k=1}^{K_R}\int_{T_{k-1}}^{T_k} g_i\left(\mathbf{s}^{(k)}(\tau^{(k)}), \mathbf{u}^{(k)}(\tau^{(k)}), \tau^{(k)}; t_0, t_f\right), \quad \left(i = 1, ..., n_q, k = 1, ..., K_R\right) \tag{2.74}$$

and the event constraints:

$$\mathbf{b}_{\min} \leq \mathbf{b}\left(\mathbf{s}^{(1)}(-1), t_0, \mathbf{s}^{(K_R)}(1), t_f, \mathbf{q}\right) \leq \mathbf{b}_{\min} \tag{2.75}$$

As the state needs to be continuous at each internal mesh point, it is necessary that $\mathbf{s}^{(k)}(T_k) = \mathbf{s}^{(k+1)}(T_k)$ at the interior mesh points $(T_1, ..., T_{K_R-1})$ [136].

As with other direct optimisation methods, the Radau collocation method requires an initial guess of the solution. How close to the optimal solution that this guess needs to be depends on the problem itself and the definition of the optimal control problem. In this work, the Radau collocation method is applied using the GPOPS II software, which is described in Refs. [136] and [139].

2.5 Simulation Parameters

In this section, the parameters applied to all simulations, including the GA and Radau collocation optimisations, are listed. In most cases, the simulations were run with standard parameters. However, some variations were made and maintained throughout.

2.5.1 General Simulation Parameters

Throughout this work the main focus is on proximity operations around NEAs. However, it was also the intention to maintain, as far as possible, the generality of the work. To this end, and given that the focus of this work is on NEAs, all asteroid orbits here were given a fixed radius of 1 AU. In addition to this, to maintain the sail performance constant throughout each simulation,

the asteroid orbit was considered circular. This maintains the generality without consideration of the true ellipticity of the asteroid orbit. As was mentioned in Section 2.2.1, the solar sail characteristic acceleration was set as $a_c = 0.2$ mm/s^2.

2.5.2 Genetic Algorithm Parameters

For the GA, the only parameter which was changed from the default was the maximum iterations. Table. 2.4 lists a selection of the parameters used where all but the maximum iterations were the default values.

Table 2.4: Selected parameters used in Genetic Algorithm optimisations

Parameter	Value
Crossover Fraction	0.8
Function Tolerance	10^{-4}
Max Generations	200
Max Stall Generations	100
Mutation Function	Mutation Adapt Feasible
Nonlinear Constraint Algorithm	Penalty
Pareto Fraction	0.35
Population Size	200
Population Type	Double Vector
Selection Function	Selection Tournament

2.5.3 Radau Collocation Parameters

For the Radau collocation method, the GPOPS-II software was used. In this, some variations were made to the standard parameters. The parameters used in the work in Chapter 4 are listed in Table 2.5.

Table 2.5: Selected parameters used in Radau collocation optimisations

Parameter	Value
Mesh method	hp-LiuRao-Legendre
Mesh tolerance	0.002
Mesh max iterations	15
Mesh max collocation points	6
Mesh min collocation points	4
NLP solver	SNOPT
NLP tolerance	10^{-4}
NLP linear solver	ma57
Derivatives method	sparseCD
Derivatives level	second
Derivatives dependencies	spase
Scales method	automatic bounds
Method	RPM-Differentiation

Chapter 3

Analysis of the Inner and Outer Regime

In this chapter the inner and outer regimes, discussed in Chapter 2, are analysed in detail. The objective of this chapter is to define the concepts related to the dynamics around an asteroid, and the effect the solar sail has on them, before they are applied in later chapters. For the inner regime, the potential field of a number of asteroids are studied. The system equilibrium points are established along with their stability characteristics. The effect of applying the continuous acceleration from a solar sail is then analysed. Following this, the dynamics in the outer regime are presented with the system equilibria, their related orbits and the stability characteristics.

3.1 Inner Regime

As discussed in Chapter 2, the inner regime is the space contained within a sphere of radius equal to five times the asteroid mean radius. In this region, the shape and spin-state of the asteroid are important factors in the gravitational field and must be considered. This section will detail the complexities of this regime, using several asteroid shape models to show the uniqueness of each field. Unless otherwise stated, the work contained in this section is defined in the BF frame.

3.1.1 Zero Velocity Curves

The Zero Velocity Curves (ZVCs) represent boundaries which delimit accessible space based on the spacecraft's energy. The ZVCs are defined where the effective potential is equal in value to the Jacobi constant. The Jacobi constant is given by [6]:

$$C = \frac{1}{2}\dot{\mathbf{r}} \cdot \dot{\mathbf{r}} + V(\mathbf{r}) \tag{3.1}$$

and the ZVCs are found where [140]:

$$C = V(\mathbf{r}) \tag{3.2}$$

Therefore, in 2-dimensions, the ZVCs are the contour lines of the effective potential. The effective potential function, $V(\mathbf{r})$, is given in Eq. 2.23 for the polyhedron shape model in Section 2.2.2.

3.1.2 Equilibrium Points

The equilibrium points of a system are the critical points of the effective potential [6]. Therefore, the equilibrium points are obtained where:

$$\nabla V(\mathbf{r}) = 0 \tag{3.3}$$

A numerical grid search, using a quasi-Newton method of unconstrained minimisation at each point of the grid, is performed in the near-asteroid space to find these minima around the high-resolution polyhedron shape models. After the full process is complete, the localised minimisations at each grid point are combined and duplicates removed to obtain the global minima. For asteroids Geographos, Castalia and Eros, Fig. 3.1 shows the equilibrium points in red along with the ZVCs.

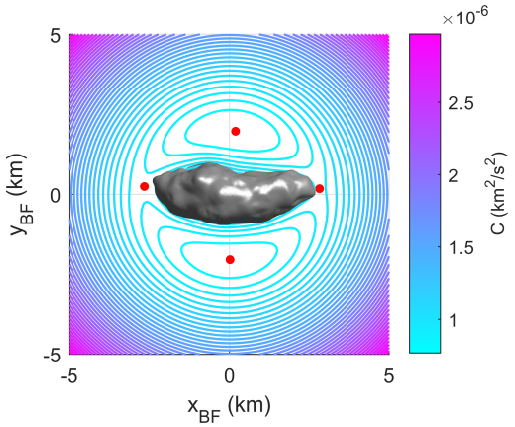

(a) Geographos

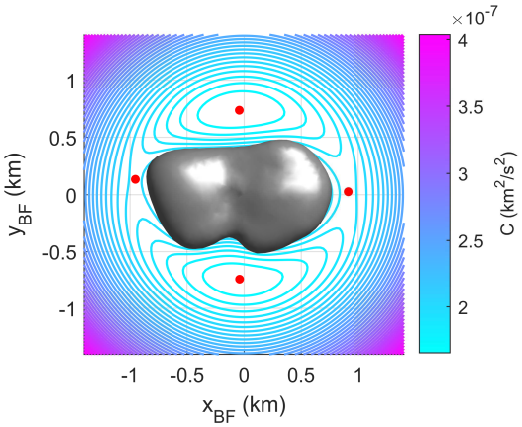

(b) Castalia

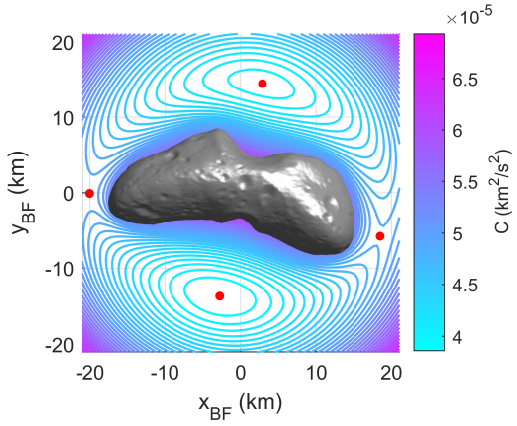

(c) Eros

Figure 3.1: Zero velocity curves with equilibrium points represented by red dots

3.1.3 The Potential Ridge Line

The potential ridge line is presented by Tardivel in his PhD thesis as well as subsequent publications [141, 142]. This ridge line represents the locus of points around the asteroid where the gradient of the potential is close to zero, necessarily including the equilibrium points. An algorithm for the calculation of the ridge line is provided in Section 2.1.4.4 of Ref. [143] in which the method of bisection allows for rapid calculation of the point of zero acceleration along the primary calculation axis, and the reader is directed there for a complete description of how this ridge line is calculated.

The locus of points represented by the continuous black line in Figure 3.2 is the potential ridge line, with the natural equilibrium points represented by red circles for asteroid 4769 Castalia. As stated in Ref. [143], it is not always necessary that the ridge line is planar, but it is necessary for there to be a minimum of two equilibrium points for the ridge line to exist.

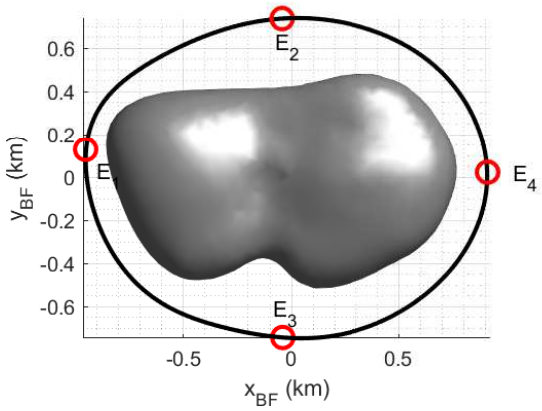

Figure 3.2: Potential ridge line for asteroid 4769 Castalia. Equilibrium points shown in red circles.

3.1.4 Stability Analysis

A study of the stability of the system equilibria requires linearisation of the equations of motion around the equilibrium point. As such, the following transformations are made:

$$\begin{aligned} \xi_p &= x_{\mathrm{BF}} - x_E \\ \eta_p &= y_{\mathrm{BF}} - y_E \\ \zeta_p &= z_{\mathrm{BF}} - z_E \end{aligned} \tag{3.4}$$

where $(x_E, y_E, z_E)^T$ is the Cartesian position of the equilibrium point in the BF frame. The second derivative terms of the effective potential will be denoted as follows:

$$\begin{aligned} V_{xx} &= \left(\frac{\partial^2 V}{\partial x^2}\right)_E \quad V_{yy} = \left(\frac{\partial^2 V}{\partial y^2}\right)_E \quad V_{zz} = \left(\frac{\partial^2 V}{\partial z^2}\right)_E \\ V_{xy} &= \left(\frac{\partial^2 V}{\partial x \partial y}\right)_E \quad V_{yz} = \left(\frac{\partial^2 V}{\partial y \partial z}\right)_E \quad V_{xz} = \left(\frac{\partial^2 V}{\partial x \partial z}\right)_E \end{aligned} \tag{3.5}$$

The full equation of motion is given by:

$$\ddot{\mathbf{r}} + 2\boldsymbol{\omega} \times \dot{\mathbf{r}} + \nabla V(\mathbf{r}) = 0 \tag{3.6}$$

Combining Eqs. 3.4 and 3.5 with Eq. 3.6, the linearised equations of motion relative to the equilibrium point can be written as [6]:

$$\begin{aligned} \ddot{\xi}_p - 2\omega\dot{\eta}_p + V_{xx}\xi_p + V_{xy}\eta_p + V_{xz}\zeta_p &= 0 \\ \ddot{\eta}_p + 2\omega\dot{\xi}_p + V_{xy}\xi_p + V_{yy}\eta_p + V_{yz}\zeta_p &= 0 \\ \ddot{\zeta}_p + V_{xz}\xi_p + V_{yz}\eta_p + V_{zz}\zeta_p &= 0 \end{aligned} \tag{3.7}$$

These equations can also be expressed in the form:

$$\mathbf{M}\ddot{\mathbf{X}} + \mathbf{G}\dot{\mathbf{X}} + \mathbf{K}\mathbf{X} = 0 \tag{3.8}$$

where:

$$\begin{aligned} \mathbf{X} &= [\xi_p, \eta_p, \zeta_p]^T \qquad \mathbf{M} = \begin{bmatrix} 1 & 0 & 0 \\ 0 & 1 & 0 \\ 0 & 0 & 1 \end{bmatrix} \\ \mathbf{G} &= \begin{bmatrix} 0 & -2\omega & 0 \\ 2\omega & 0 & 0 \\ 0 & 0 & 0 \end{bmatrix} \quad \mathbf{K} = \begin{bmatrix} V_{xx} & V_{xy} & V_{xz} \\ V_{yx} & V_{yy} & V_{yz} \\ V_{zx} & V_{zy} & V_{zz} \end{bmatrix} \end{aligned} \tag{3.9}$$

It should also be noted that $V_{xz} = V_{zx}$, $V_{yz} = V_{zy}$ and $V_{xy} = V_{yx}$ and $\mathbf{K}$ is the gravity gradient matrix, $\nabla(\nabla V)$. The eigenvalues, λ, are then obtained from the Jacobian matrix:

$$\mathbf{A} = \begin{bmatrix} \mathbf{0} & \mathbf{M} \\ \mathbf{K} & -\mathbf{G} \end{bmatrix} \tag{3.10}$$

The stability of the equilibrium point is defined by the nature of the eigenvalues, and these are divided into 5 classes in Refs. [6] and [1] and are shown here in Table 3.1. There are six eigenvalues which must be a combination of the following: a pair of opposite real roots ($\pm\alpha_r$), a pair of conjugate imaginary roots ($\pm j\beta_r$) or two pairs of complex conjugate roots ($\pm\sigma_r \pm i\tau_r$) [1].

The following section presents the analysis for two asteroids considered in further chapters of this work; 4769 Castalia and 433 Eros. Analysis for other asteroids can also be found in Appendix B.

Table 3.1: Classification of non-degenerate and non-resonant equilibrium points. Taken from Ref. [1]. LS = linearly stable and U = unstable.

Case	Eigenvalues	Stability	No. of periodic orbits
1	$\pm j\beta_r^{(k)}\left(\beta_r^{(k)} \in \mathbf{R}^+; k = 1,2,3\right)$	LS	3
2	$\pm\alpha_r^{(k)}\left(\alpha_r^{(k)} \in \mathbf{R}^+; k = 1\right), \pm i\beta_r^{(k)}\left(\beta_r^{(k)} \in \mathbf{R}^+; k = 1,2\right)$	U	2
3	$\pm\alpha_r^{(k)}\left(\alpha_r^{(k)} \in \mathbf{R}^+; k = 1,2\right), \pm j\beta_r^{(k)}\left(\beta_r^{(k)} \in \mathbf{R}^+; k = 1\right)$	U	1
4a	$\pm\alpha_r^{(k)}\left(\alpha_r^{(k)} \in \mathbf{R}^+; k = 1\right), \pm\sigma_r \pm j\tau_r\,(\sigma_r, \tau_r \in \mathbf{R}^+)$	U	0
4b	$\pm\alpha_r^{(k)}\left(\alpha_r^{(k)} \in \mathbf{R}^+; k = 1,2,3\right)$	U	0
5	$\pm\sigma_r \pm j\tau_r\,(\sigma_r, \tau_r \in \mathbf{R}^+), \pm j\beta_r^{(k)}\left(\beta_r^{(k)} \in \mathbf{R}^+; k = 1\right)$	U	1

3.1.5 4769 Castalia

Asteroid 4769 Castalia is an Apollo class asteroid with bulk density of 2.1 g/cm^3 and rotational period of 4.095 hours [6]. Figure 3.3 shows the equilibrium points and ZVCs for Castalia, with the shape model obtained from Ref. [144].

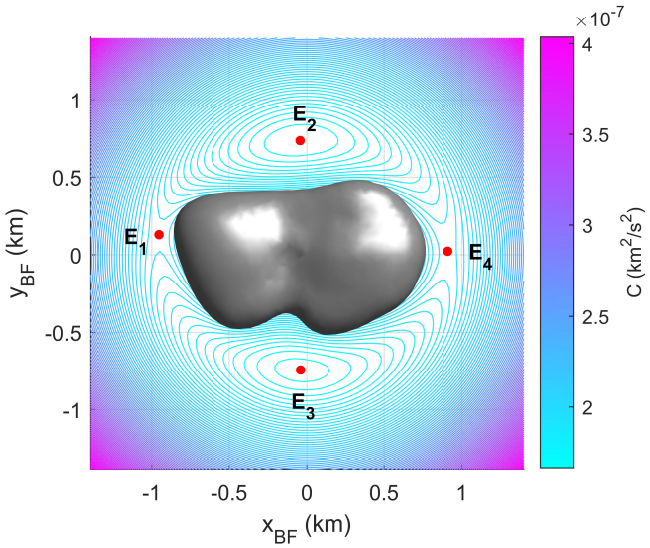

Figure 3.3: Zero velocity curves with equilibrium points represented by red dots for asteroid Castalia

Table 3.2 shows the Cartesian position of each equilibrium point and Table 3.3 shows the respective eigenvalues.

Comparison of the eigenvalues obtained here and those of Ref. [6] are presented in Fig. 3.4. The black asterisks represent the eigenvalues from Ref. [6] and the red circles represent the eigenvalues of Table 3.3. Again, although the stability criteria match, and the distribution of the eigenvalues is very similar, there are discrepancies in the eigenvalues between those of this work and those of Ref. [6]. A possible source for the discrepancy may be in the tolerances applied to the numerical calculation of the asteroid gravitational field and the equilibria.

Table 3.2: Position of equilibrium points in the effective potential field of asteroid Castalia

	x_{BF} (km)	y_{BF} (km)	z_{BF} (km)
E_1	-0.9530	0.1290	0.0300
E_2	-0.0430	0.7360	0.0030
E_3	-0.0400	-0.7440	0.0090
E_4	0.9100	0.0230	0.0340

Table 3.3: Eigenvalues for equilibrium points in effective potential field of asteroid Castalia

$\times 10^{-4}$ s^{-1}	λ_1	λ_2	λ_3	λ_4	λ_5	λ_6	Case	Stability
E_1	-5.3837	5.3837	5.5427i	-5.5427i	5.8816i	-5.8816i	2	U
E_2	2.3636 + 3.7774i	2.3636 - 3.7774i	-2.3636 + 3.7774i	-2.3636 - 3.7774i	4.3551i	-4.3551i	5	U
E_3	-2.4361 + 3.7712i	-2.4361 - 3.7712i	2.4361 + 3.7712i	2.4361 - 3.7712i	4.4448i	-4.4448i	5	U
E_4	4.1751	-4.1751	5.5827i	-5.5827i	4.7536i	-4.7536i	2	U

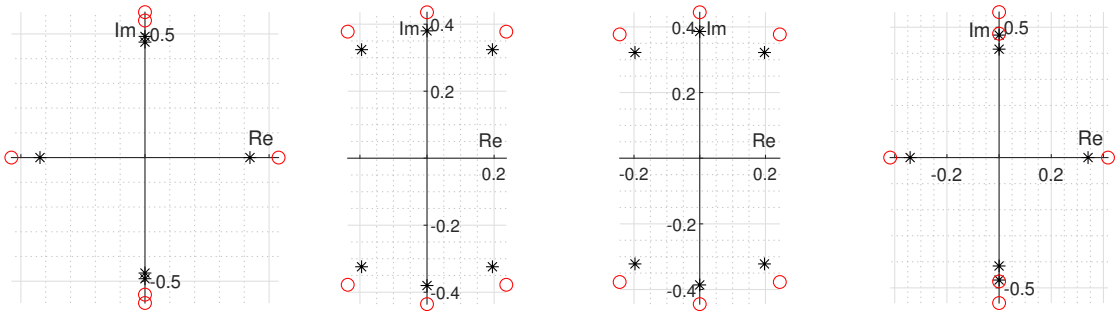

(a) E_1 *(b) E_2* *(c) E_3* *(d) E_4*

Figure 3.4: Comparison of eigenvalues from [6] for asteroid Castalia (shown by black asterisks) and the eigenvalues of this work (shown by red circles)

3.1.6 433 Eros

Asteroid 433 Eros is an Amor class asteroid with bulk density of 2.67 g/cm^3 and rotational period of 5.270 hours [93]. Figure 3.5 shows the equilibrium points and ZVCs for asteroid Eros, where the shape model was obtained from Ref. [145].

Table 3.4 shows the Cartesian position of each equilibrium point and Table 3.5 shows the respective eigenvalues.

Table 3.4: Position of equilibrium points in the effective potential field of asteroid Eros

	x_{BF} (km)	y_{BF} (km)	z_{BF} (km)
E_1	-20.0260	-0.1030	0.1300
E_2	-2.7470	-13.7190	-0.0730
E_3	2.8910	14.4620	-0.0620
E_4	18.4740	-5.7550	0.1470

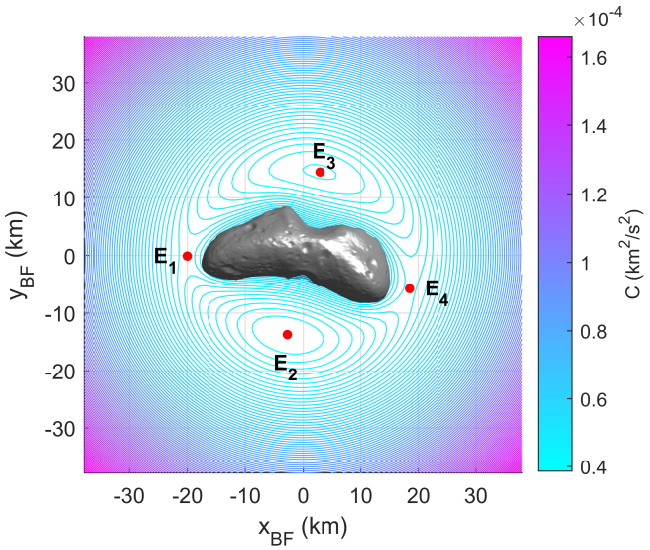

Figure 3.5: Zero velocity curves with equilibrium points represented by red dots for asteroid Eros

Table 3.5: Eigenvalues for equilibrium points in effective potential field of asteroid Eros

$\times 10^{-4}$ s^{-1}	λ_1	λ_2	λ_3	λ_4	λ_5	λ_6	Case	Stability
E_1	-5.0745	5.0745	5.0006i	-5.0006i	4.7623i	-4.7623i	2	U
E_2	-1.9452 + 3.0621i	-1.9452 - 3.0621i	1.9452 + 3.0621i	1.9452 - 3.0621i	3.2785i	-3.2785i	5	U
E_3	-1.7103 + 2.8739i	-1.7103 - 2.8739i	1.7103 - 2.8739i	1.7103 - 2.8739i	3.3565i	-3.3565i	5	U
E_4	-4.2496	4.2496	4.5335i	-4.5335i	4.4092i	-4.4092i	2	U

3.1.7 Summary of the Asteroid Phase Space and Equilibria

In the case of asteroid 433 Eros, there was no readily available comparison in the literature for validation of the eigenvalues of the equilibria. However, once again it is shown that, for an elongated body, the equilibria are all unstable. We have seen in the analysis presented here that, as a body becomes more elongated, the number of equilibria reduces and the minimum number of points found in this work has been four, where we are only concerned with the equilibria external to the asteroid surface. For bodies which are more spherical in shape, the number of equilibria can be high. For a perfect sphere, the equilibria would be expected to form a continuous line at the 1:1 synchronous orbit radius.

3.1.8 Analysis of the Phase Space of the Inner Regime at 4769 Castalia with the Solar Sail

This section will present analysis on the effect that adding a solar sail to the dynamics of the asteroid gravitational field will have. The complexities of the variations in dynamics are compounded in the BF frame as the Sun is seen to rotate around the asteroid with the often short rotational period of the asteroid.

Artificial Equilibrium Points (AEPs)

By varying the attitude and performance of the sail, the position of the equilibrium points can be artificially displaced. These new equilibrium points are referred to as Artificial Equilibrium Points (AEPs) [108]. For clarity, the notation of the AEPs will be AEP_n and the natural equilibrium points will maintain the form E_n, the subscript n is the index of the equilibrium point. The range of variation in the position of the AEP for varying sail attitude is limited by the sail performance [146].

Effects of Sail Performance on AEPs Figure 3.6 shows how the changing performance of the sail displaces the equilibria when time is frozen at t_0. In this example, the sail attitude is set with $\alpha = \delta = 0^\circ$ and the sail performance is varied in the range $a_c \in [0, 0.4]$ mm/s^2. AEP_1 and AEP_2 vanish at the critical performance value of approximately $a_c = 0.06$ mm/s^2. AEP_3 moves in the negative x-direction while AEP_4 descends towards the surface of the asteroid where it will eventually collide, and vanish, with the internal equilibrium point of Castalia at $a_c = 0.20$ mm/s^2.

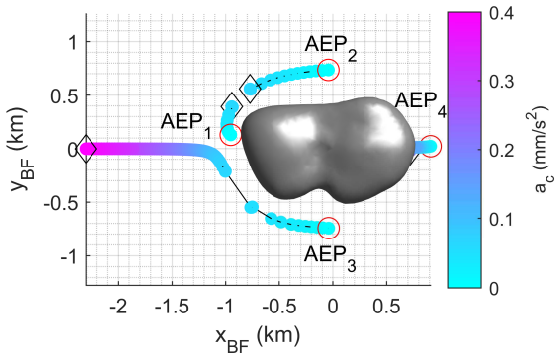

Figure 3.6: Motion of the equilibria for $\alpha = \delta = 0^\circ$ and $a_c \in [0, 0.4]$ mm/s^2. Red circle represents initial point and black diamond represents end points, with the black line tracing the path of motion.

The fact that Castalia is a small body, with a relatively weak gravitational field, the movement of the AEPs takes place at relatively modest values of a_c. Indeed, at the targeted value of a_c that is maintained throughout this work ($a_c = 0.2$ mm/s^2), there remains only a single AEP: AEP_3. This gives some indication to how sensitive the system may prove to be for operations of a sail of this size in proximity of such a small body.

Effects of a revolving Sun on AEPs As the sail attitude is referenced to the direction of the Sun, the acceleration provided by the sail is necessarily dependent on the position of the Sun as the asteroid rotates around its own principal axis, giving an apparent revolution of the position

of the Sun around the asteroid, in the BF frame. As such, it is reasonable to assume that there is an additional effect on the position of the AEPs. At the performance level of $a_c = 0.20$ mm/s^2, only one AEP remains, AEP$_3$. Figure 3.7 shows the variation in position of AEP$_3$, for several different sail attitudes, during one complete rotation of the asteroid. The red diamond represents the initial and final positions. The initial and final positions are equal as the Sun returns to its initial position relative to the asteroid. It should be noted that the locus of points do not represent a feasible trajectory for a spacecraft to follow, but distinct, instantaneous equilibria which are defined only with zero-velocity at that point.

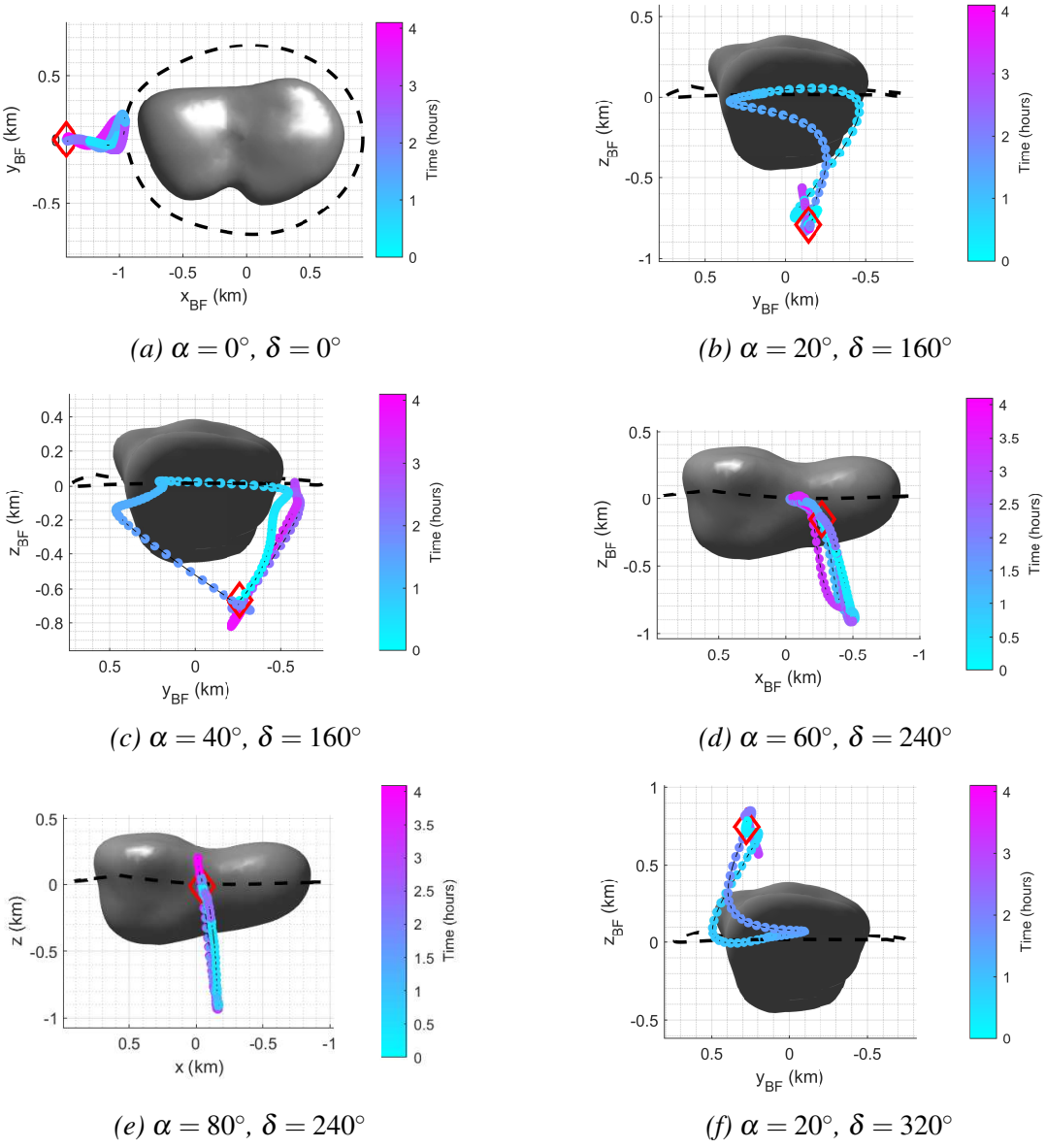

(a) $\alpha = 0°$, $\delta = 0°$ *(b)* $\alpha = 20°$, $\delta = 160°$

(c) $\alpha = 40°$, $\delta = 160°$ *(d)* $\alpha = 60°$, $\delta = 240°$

(e) $\alpha = 80°$, $\delta = 240°$ *(f)* $\alpha = 20°$, $\delta = 320°$

Figure 3.7: Selection of trajectories for AEP$_3$ with $a_c = 0.20$ mm/s^2 during one complete rotation of the asteroid for varying values of α and δ. The red diamond marks the AEP at t_0 and t_f. Potential ridge line is shown as black dashed line.

Figure 3.8 shows the changing eigenvalues of AEP$_3$ for each set of sail attitudes in Fig. 3.7.

These show the transition in stability characteristics, referenced to those listed in Table 3.1 by case number. The black circles represent the initial eigenvalues and the black crosses represent the final eigenvalues. Most of the AEPs remain unstable throughout the asteroid rotation. However, there are examples, as shown in Figs 3.8c to 3.8f, of the AEPs transitioning briefly to linearly stable points of case 1. Although these plots do not themselves represent feasible trajectories for the sail, these linearly stable regions may provide arcs of a trajectory for the sail.

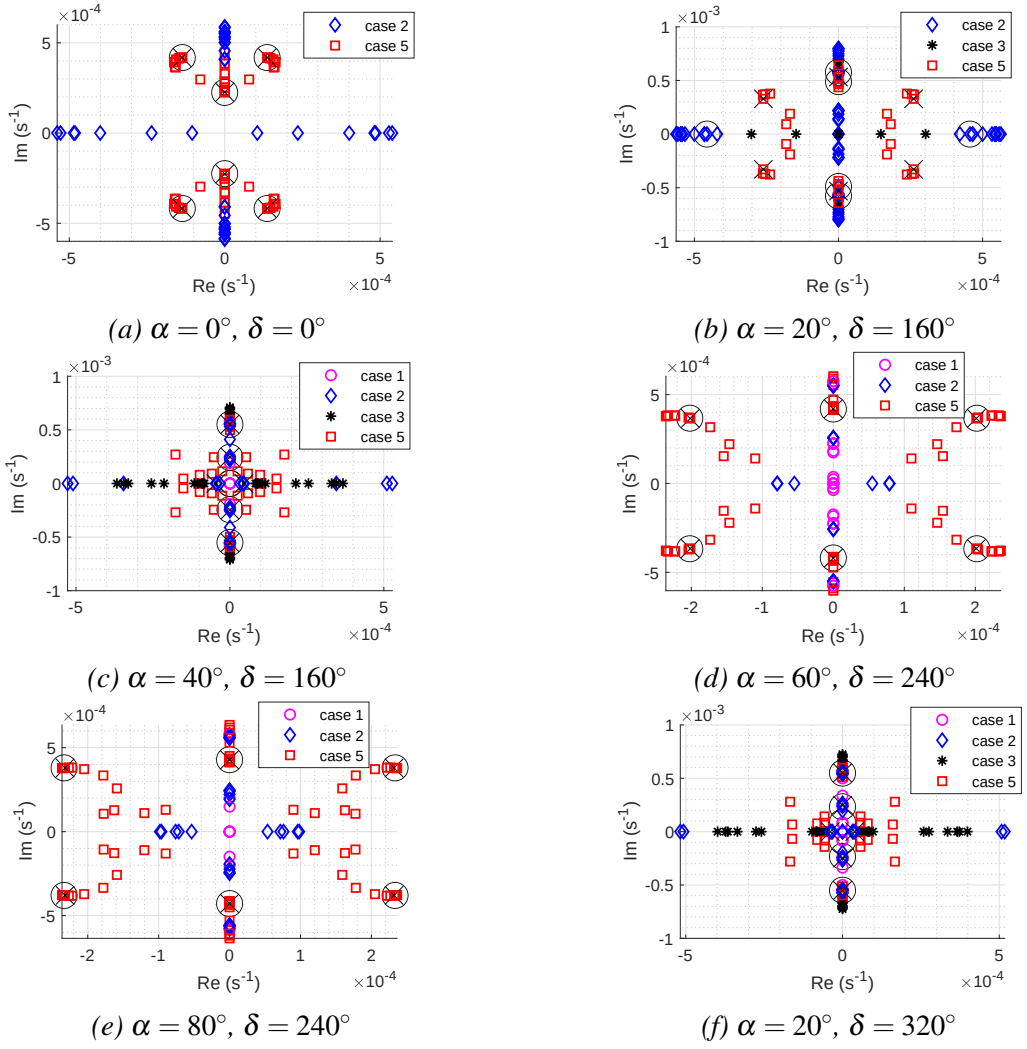

(a) $\alpha = 0°$, $\delta = 0°$ *(b)* $\alpha = 20°$, $\delta = 160°$

(c) $\alpha = 40°$, $\delta = 160°$ *(d)* $\alpha = 60°$, $\delta = 240°$

(e) $\alpha = 80°$, $\delta = 240°$ *(f)* $\alpha = 20°$, $\delta = 320°$

Figure 3.8: Eigenvalues during rotation of the asteroid for trajectories shown in Fig 3.7

Effects of sail performance on the potential ridge line

Application of the solar sail also has an effect on the size, and eventual existence, of the potential ridge line. The ridge line is only defined while the asteroid has a minimum of two equilibrium points. Here, we examine the effects on the ridge line until the first equilibrium point vanishes. As such, when the performance of the sail reaches such a point that the equilibria begin to disappear, the ridge line is considered lost. Figure 3.9 shows the contraction of the ridge line

as a_c increases up to the critical point, the point at which AEP_1 and AEP_2 disappear, which is approximately at $a_c = 0.06$ mm/s^2 and at the initial time point, t_0.

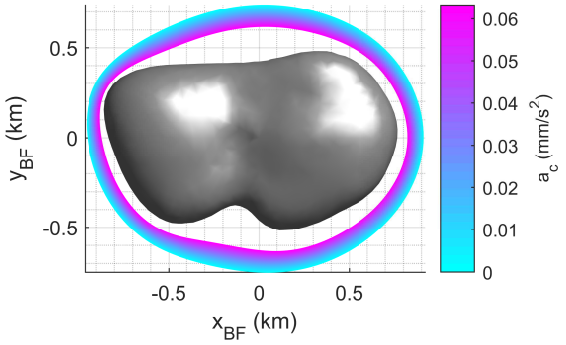

Figure 3.9: Variation in the potential ridge line for changing sail characteristic acceleration, $a_c \in [0, 0.06]$ mm/s^2

3.2 Outer Regime

As discussed in Chapter 2, when the spacecraft is in the space outside of a sphere centred on the asteroid and of radius equal to five times the mean asteroid radius, the asteroid shape and rotation no longer play an important role in the gravitational field. As such, at these distances, the asteroid can be modelled as a point-mass. However, at these distances, the Sun begins to play an increasingly important role in the gravitational field. As such, it is fundamental to include the gravitational effect of the Sun in a 3-body dynamical system.

In the case of the Sun-asteroid-spacecraft system, the vanishingly small mass ratio enables use of the Hill's Restricted 3-Body Problem (HR3BP) [73]. In this system, the SYN frame of reference is centred on the asteroid with the particle experiencing the Sun as a distant perturbation. The system rotates with the Sun-Asteroid frame, with the Sun position fixed along the x-axis. As the asteroid is at a considerable distance from the Sun, the Sun-sail line can be assumed equal to the Sun-Asteroid line. Addition of the solar sail to this dynamical system gives rise to the Solar Sail Hill's Restricted 3-Body Problem (SSHR3BP) and this was described in Section 2.2.3. The notation for the system equilibria which was used in the description of the inner regime in Section 3.1 is maintained here, where E_n denotes a natural equilibrium point and AEP_n denotes an artificially displaced equilibrium point.

3.2.1 Equilibrium Points

As for the inner regime, the equilibrium points of the system are obtained by finding the locations where the gradient of the potential function, which includes the sail, is zero. For the outer

regime, using the SSHR3BP model, the equilibrium points were defined in Section 2.2.3.

3.2.2 Zero Velocity Curves

The Zero Velocity Curves (ZVCs) provide some insight into the possible trajectories for a spacecraft with a given energy. As such, a study of the ZVCs requires definition of the spacecraft energy. This is defined by the Jacobi constant.

To find an expression for the Jacobi constant, which is the constant of integration of the Jacobi integral, we first multiply Eq. 2.39 by $\dot{x}_{\text{SYN}}$, $\dot{y}_{\text{SYN}}$ and $\dot{z}_{\text{SYN}}$ respectively:

$$\begin{aligned}
\dot{x}_{\text{SYN}}\ddot{x}_{\text{SYN}} &= 2\dot{x}_{\text{SYN}}\dot{y}_{\text{SYN}} - \frac{3}{r_{\text{SYN}}^3}\dot{x}_{\text{SYN}}x_{\text{SYN}} + 3\dot{x}_{\text{SYN}}x_{\text{SYN}} + a_{x_{\text{SYN}}}\dot{x}_{\text{SYN}} \\
\dot{y}_{\text{SYN}}\ddot{y}_{\text{SYN}} &= -2\dot{x}_{\text{SYN}}\dot{y}_{\text{SYN}} - \frac{3}{r_{\text{SYN}}^3}\dot{y}_{\text{SYN}}y_{\text{SYN}} + a_{y_{\text{SYN}}}\dot{y}_{\text{SYN}} \\
\dot{z}_{\text{SYN}}\ddot{z}_{\text{SYN}} &= -\frac{3}{r_{\text{SYN}}^3}\dot{z}_{\text{SYN}}z_{\text{SYN}} - 3\dot{z}_{\text{SYN}}z_{\text{SYN}} + a_{z_{\text{SYN}}}\dot{z}_{\text{SYN}}
\end{aligned} \tag{3.11}$$

Now, summing Eqs. 3.11:

$$\begin{aligned}
\dot{x}_{\text{SYN}}\ddot{x}_{\text{SYN}} + \dot{y}_{\text{SYN}}\ddot{y}_{\text{SYN}} + \dot{z}_{\text{SYN}}\ddot{z}_{\text{SYN}} = &-\frac{3}{r_{\text{SYN}}^3}(\dot{x}_{\text{SYN}}x_{\text{SYN}} + \dot{y}_{\text{SYN}}y_{\text{SYN}} + \dot{z}_{\text{SYN}}z_{\text{SYN}}) + \\
&(3\dot{x}_{\text{SYN}}x_{\text{SYN}} - \dot{z}_{\text{SYN}}z_{\text{SYN}}) + a_{x_{\text{SYN}}}\dot{x}_{\text{SYN}} \\
&+ a_{y_{\text{SYN}}}\dot{y}_{\text{SYN}} + a_{z_{\text{SYN}}}\dot{z}_{\text{SYN}}
\end{aligned} \tag{3.12}$$

Substitutions can be made where:

$$\begin{aligned}
\dot{x}_{\text{SYN}}\ddot{x}_{\text{SYN}} + \dot{y}_{\text{SYN}}\ddot{y}_{\text{SYN}} + \dot{z}_{\text{SYN}}\ddot{z}_{\text{SYN}} &= \frac{d}{dt}\frac{1}{2}v_{\text{SYN}}^2 \\
-\frac{1}{r_{\text{SYN}}^3}(\dot{x}_{\text{SYN}}x_{\text{SYN}} + \dot{y}_{\text{SYN}}y_{\text{SYN}} + \dot{z}_{\text{SYN}}z_{\text{SYN}}) &= \frac{d}{dt}\frac{1}{r_{\text{SYN}}} \\
3\dot{x}_{\text{SYN}}x_{\text{SYN}} - \dot{z}_{\text{SYN}}z_{\text{SYN}} &= \frac{d}{dt}\frac{1}{2}(3x_{\text{SYN}}^2 - z_{\text{SYN}}^2) \\
a_{x_{\text{SYN}}}\dot{x}_{\text{SYN}} &= \frac{d}{dt}a_{x_{\text{SYN}}}x_{\text{SYN}} \\
a_{y_{\text{SYN}}}\dot{y}_{\text{SYN}} &= \frac{d}{dt}a_{y_{\text{SYN}}}y_{\text{SYN}} \\
a_{z_{\text{SYN}}}\dot{z}_{\text{SYN}} &= \frac{d}{dt}a_{z_{\text{SYN}}}z_{\text{SYN}}
\end{aligned} \tag{3.13}$$

Therefore, substitution of Eqs. 3.13 into 3.12, and simplifying gives:

$$\frac{d}{dt}\left[\frac{1}{2}v_{\text{SYN}}^2 - \frac{3}{r_{\text{SYN}}} - \frac{1}{2}\left(3x_{\text{SYN}}^2 - z_{\text{SYN}}^2\right) + \mathbf{a}_S \cdot \mathbf{r}_{\text{SYN}}\right] = 0 \tag{3.14}$$

where the bracketed term must be a constant. This being the constant of integration, the Jacobi Constant:

$$C = \frac{1}{2}v_{\mathrm{SYN}}^2 - \frac{3}{r_{\mathrm{SYN}}} - \frac{1}{2}\left(3x_{\mathrm{SYN}}^2 - z_{\mathrm{SYN}}^2\right) + \mathbf{a}_S \cdot \mathbf{r}_{\mathrm{SYN}} \tag{3.15}$$

The ZVCs are defined where the value of the Jacobi constant is equal to the value of the effective potential. As such, the ZVCs can be plotted as the contours of the Jacobi constant at zero-velocity, as shown in Fig. 3.10 for the ballistic case ($a_c = 0$ mm/s^2) for asteroid Vesta, where the small black circles represent the equilibrium points.

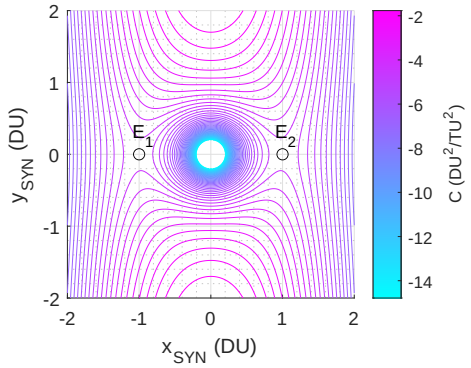

Figure 3.10: Zero Velocity Curves around the Hill's region for asteroid Vesta

Villac and Scheeres [147] present an expression for the critical value of Jacobi constant, in dimensional units, at which point the necks at E_1 and E_2 open up:

$$C_{crit} = -\frac{1}{2}\left(9\mu\Omega\right)^{\frac{2}{3}} \tag{3.16}$$

which, in non-dimensional units with $\mu = 3$ and $\Omega = 1$, gives a value of $C_{crit} = -4.5$ DU^2/TU^2. A trajectory with $C < C_{crit}$ will not be able to transit between the interior region, the asteroid region and the exterior region of the phase space, as there will be an energetic barrier, in the form of the ZVC. In his 2006 PhD thesis [148], Bookless presents some example trajectories which are bound to the asteroid region. These are replicated here as validation of the methods employed.

Taking trajectories either side of C_{crit}, Fig. 3.11 shows that indeed the neck regions are closed for $C = -4.52$ DU^2/TU^2 and open for $C = -4.48$ DU^2/TU^2. Both plots take initial conditions of $x_{\mathrm{SYN},0} = -0.9$ DU, $y_{\mathrm{SYN},0} = 0$ DU and $\dot{x}_{\mathrm{SYN},0} = 0$ DU/TU. The value of $\dot{y}_{\mathrm{SYN},0}$ is obtained by re-arranging Eq. 3.15.

The theories applied here will find application in the capture process of Chapter 6, where the value of C is used as a guide to ensure the captured spacecraft operates within a certain radius from the asteroid by setting the value of C such that the ZVC encloses that region.

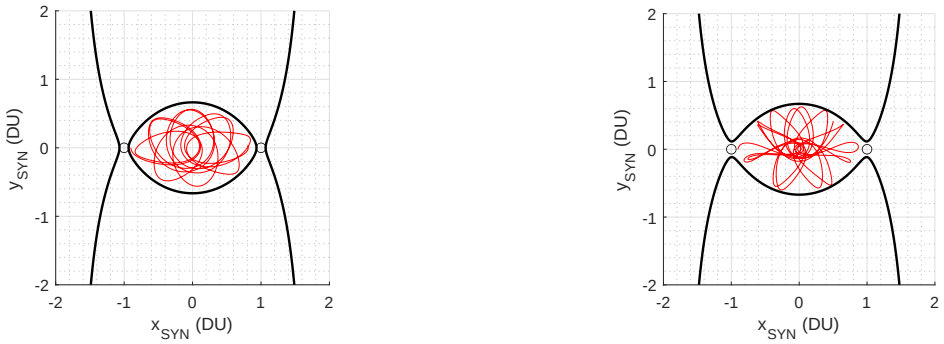

(a) $C = -4.52\ DU^2/TU^2$ *(b)* $C = -4.48\ DU^2/TU^2$

Figure 3.11: ZVCs for trajectories either side of the critical value of Jacobi constant

3.2.3 Periodic Orbits: Planar Case

The collinear equilibrium points, denoted E_1 and E_2, provide the gateway between the exterior region of the phase space, the interior region and the asteroid region (these regions are defined in Fig. 3.12). In order to calculate a transfer between these regions, we begin with calculating a planar family of orbits, described in Ref. [97], around the collinear equilibrium points. Similarly, the higher dimensional orbits, which are not utilised directly in this work but may be of interest to the reader, are described in Appendix C.

State Transition Matrix

The State Transition Matrix (STM) is a tool which gives information on how small changes to the initial conditions of a trajectory will effect the final state of the trajectory. With the system equation of motion given in the SYN frame by:

$$\dot{\mathbf{s}} = \mathbf{f}(\mathbf{s}, t) \tag{3.17}$$

Supposing some initial condition, $\mathbf{s}_0(t_0)$, leads to the trajectory $\mathbf{s}_0(t)$ and a nearby trajectory can be written as:

$$\mathbf{s}(t) = \mathbf{s}_0(t) + \delta\mathbf{s}(t) \tag{3.18}$$

then substitution into Eq. 3.17 and expansion in a Taylor series about $\delta\mathbf{s} = 0$ leads to:

$$\begin{aligned} \dot{\mathbf{s}} &= \dot{\mathbf{s}}_0 + \delta\dot{\mathbf{s}} \\ &\approx \mathbf{f}(\mathbf{s}_0, t) + \frac{\partial \mathbf{f}}{\partial \mathbf{s}}\delta\mathbf{s} \end{aligned} \tag{3.19}$$

The partial derivative term can be abbreviated to $\mathbf{A}(t) = \frac{\partial \mathbf{f}}{\partial \mathbf{s}}$:

$$\mathbf{A}(t) = \begin{bmatrix} \mathbf{0} & \mathbf{I} \\ \mathbf{U}'' & -\mathbf{\Omega} \end{bmatrix} \tag{3.20}$$

where $\mathbf{0}$ is a 3×3 matrix of zeros, $\mathbf{I}$ is a 3×3 identity matrix, and:

$$\mathbf{\Omega} = \begin{bmatrix} 0 & -2\Omega & 0 \\ 2\Omega & 0 & 0 \\ 0 & 0 & 0 \end{bmatrix} \quad \mathbf{V}'' = \begin{bmatrix} \frac{\partial^2 V}{\partial x^2} & \frac{\partial^2 V}{\partial xy} & \frac{\partial^2 V}{\partial xz} \\ \frac{\partial^2 V}{\partial yx} & \frac{\partial^2 V}{\partial y^2} & \frac{\partial^2 V}{\partial yz} \\ \frac{\partial^2 V}{\partial zx} & \frac{\partial^2 V}{\partial zy} & \frac{\partial^2 V}{\partial z^2} \end{bmatrix} \tag{3.21}$$

where V is the effective potential function for the system in question. The State Transition Matrix (STM), $\mathbf{\Phi}_S$, can then be obtained by numerical integration of:

$$\dot{\mathbf{\Phi}}_S(t,t_0) = \mathbf{A}(t)\mathbf{\Phi}_S(t,t_0) \tag{3.22}$$

with the initial condition $\mathbf{\Phi}_S(t_0,t_0) = \mathbf{I}$.

Numerical Search for Families of Periodic Orbits

In order to efficiently search for a periodic orbit, we take advantage of the symmetry of the orbit. The planar Lyapunov orbits, and their related vertical orbits, are symmetrical about the x_{SYN}-z_{SYN} plane. As such, on each crossing of that plane, the search for initial conditions can be reduced to just three parameters, $x_{\text{SYN},0}$, $z_{\text{SYN},0}$ and $\dot{y}_{\text{SYN},0}$. For the ith orbit, the initial state is given by:

$$\mathbf{s}^{(i)}_{\text{SYN},0} = \left[x_{\text{SYN},0}, 0, z_{\text{SYN},0}, 0, \dot{y}_{\text{SYN},0}, 0\right]^T \tag{3.23}$$

where superscript i denotes a generic step.

In order to find the full family of orbits, we apply a predictor/corrector method, as outlined in Ref. [149]. Here we outline the same 3-dimensional problem which will later be reduced to a 2-dimensional analysis. The first guess of the $(i+1)$ orbit is provided by:

$$\mathbf{s}^{(i+1)}_{\text{SYN},0} = \left[x^{(i)}_{\text{SYN},0} + \delta x_{\text{SYN},0}, 0, z^{(i)}_{\text{SYN},0} + \delta z_{\text{SYN},0}, 0, \dot{y}^{(i)}_{\text{SYN},0} + \delta \dot{y}_{\text{SYN},0}, 0\right]^T \tag{3.24}$$

where the values of $\delta x_{\text{SYN},0}$, $\delta z_{\text{SYN},0}$ and $\delta \dot{y}_{\text{SYN},0}$ are unknown though where sufficient constraints are applied which forces the displacement of the initial point onto the x_{SYN}-z_{SYN} plane. This requires introduction of the angle χ which is given by:

$$\chi = \tan^{-1}\left[z^{(i)}_{\text{SYN},0} - z^{(i-1)}_{\text{SYN},0} / x^{(i)}_{\text{SYN},0} - x^{(i-1)}_{\text{SYN},0}\right] \tag{3.25}$$

In the first iteration, the value of χ must be defined by the user. Where an out-of-plane orbit is sought from an in-plane initial condition, a value of $\chi = \pi/2$ must be set [149]. The

displacements can then by obtained from:

$$\begin{aligned} \delta x_{\mathrm{SYN},0} &= r_1 \cos(\chi) + r_2^{(i+1)} \sin(\chi) \\ \delta z_{\mathrm{SYN},0} &= z_{\mathrm{SYN},0}^{(i)} + r_1 \sin(\chi) - r_2^{(i+1)} \cos(\chi) \end{aligned} \tag{3.26}$$

The parameter r_1 is in the direction of χ and r_2 is perpendicular to it. The only unknown values here are $r_2^{(i+1)}$ and $\delta \dot{y}_{\mathrm{SYN},0}$. Initial values for these parameters can be selected as $r_2^{(i+1)} = 0$ and $\delta \dot{y}_{\mathrm{SYN},0} = 0$. This means that the initial guess does not change the direction of motion of the initial point and maintains the same initial velocity as the previous solution [149].

In order to find the correct values of $r_2^{(i+1)}$ and $\dot{y}_{\mathrm{SYN},0}^{(i+1)}$, the corrector step is applied. In this step, a numerical optimisation method is employed (in this case the *trust-region dogleg* algorithm is employed via the *fsolve* function in MATLAB). This optimisation integrates the equations of motion from the initial point to the subsequent crossing of the x_{SYN}-z_{SYN} plane. At this point, it seeks initial conditions which will result in a perpendicular crossing of this plane.

The process of finding the family of orbits begins with a small amplitude orbit, close to the equilibrium point around which the family exists, to aid convergence. Once this initial orbit is found, it is possible to continue along some parameter which allows the full family of orbits to be obtained. In the planar case, the x-amplitude of the orbit, A_x, is used to establish the initial position along the x-axis [150]. The initial y-velocity of the previous orbit is used as an initial guess for that of the current orbit. Figure 3.12 shows a single Lyapunov orbit at each of the Lagrange points, E_1 and E_2 with the regions of the phase space defined.

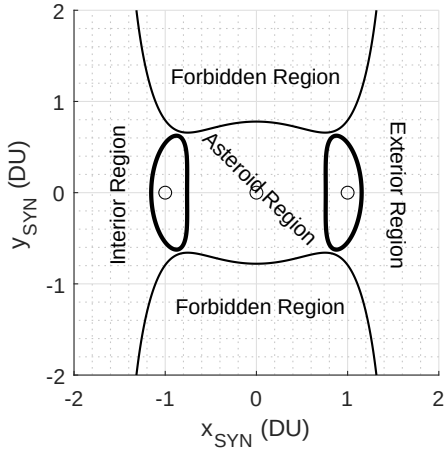

Figure 3.12: Planar Lyapunov orbits at E_1 and E_2 which details the various regions of the phase space

3.2.4 Invariant Manifold Transfers

Due to the limitations on computational capacity, the exploitation of the natural dynamics of the solar system in aiding low energy transfers was not studied in detail until the latter half of the

20th century [151–154]. The work in this section will follow the process outlined in Ref. [150] for the calculation of these manifolds and their connections.

With the periodic orbits calculated in Sections 3.2.3, by integration of the STM along the orbit, the monodromy matrix, $\mathbf{\Phi}_M$, is obtained at the end of one orbital period. To clarify:

$$\mathbf{\Phi}_M = \mathbf{\Phi}_S(T) \tag{3.27}$$

where T is the orbital period. The eigenvalues of $\mathbf{\Phi}_M$ are referred to as the Floquet or characteristic multipliers. For the planar Lyapunov orbit, the four eigenvalues of $\mathbf{\Phi}_M$ are $\lambda_1 > 1$, $\lambda_2 = \frac{1}{\lambda_1}$ and $\lambda_3 = \lambda_4 = 1$ [150]. The eigenvector related to λ_1 is in the unstable direction and the eigenvector related to λ_2 is in the stable direction.

First, we denote the initial state as $\mathbf{s}_0$ and the state at some arbitrary time, t, as $\mathbf{s}(t)$. If $Y^s(\mathbf{s}_0)$ denotes the stable unit eigenvector and $Y^u(\mathbf{s}_0)$ denotes the unstable unit eigenvector, then the approximate stable manifolds can be calculated by:

$$\mathbf{s}^s(\mathbf{s}_0) = \mathbf{s}_0 + \varepsilon Y^s(\mathbf{s}_0) \tag{3.28}$$

where ε is a small displacement from $\mathbf{s}_0$. The value of this displacement as given in the non-dimensional system should be $\varepsilon = 1 \times 10^{-6}$ [153]. The approximate unstable manifold can be obtained from:

$$\mathbf{s}^u(\mathbf{s}_0) = \mathbf{s}_0 + \varepsilon Y^u(\mathbf{s}_0) \tag{3.29}$$

Numerically integrating the unstable vector forwards in time, for both ε and $-\varepsilon$, trajectories which shadow the two branches of the unstable manifold, W^{u+} and W^{u-}, can be established. This can then be repeated, though integrating backwards in time, for the stable vector, providing W^{s+} and W^{s-}. For the manifold at $\mathbf{s}(t)$, the STM can transport the eigenvectors from $\mathbf{s}_0$ to $\mathbf{s}(t)$:

$$Y^s(\mathbf{s}(t)) = \mathbf{\Phi}_S(t,0)Y^s(\mathbf{s}_0) \tag{3.30}$$

It should be noted that the STM does not preserve the norm, and so the resulting vector requires normalisation after transportation.

Once the manifolds are established, and in order to facilitate ballistic connections between stable and unstable manifolds, Poincaré sections can be applied. The Poincaré section is a section in the n-dimensional state space which is useful for the analysis of swirling flows [130]. A periodic trajectory will repeatedly pierce this section in the same location on each pass. By choosing where in the state space to place the section, the periodicity can be analysed. For the connection of invariant manifolds, two sections are placed in the asteroid region. In this case, the sections are placed along the y_{SYN}-axis at $x_{\text{SYN}} = 0$ DU. The sections are reduced to 2-dimensions in y_{SYN} and $v_{y_{\text{SYN}}}$.

Figure 3.13 shows the stable (green) and unstable (red) manifolds which connect the interior

and exterior regions via the asteroid region for $C = -3.8499$ DU^2/TU^2. The Poincaré sections are also shown with the shaded area representing the location where all of the ballistic connections are contained. To obtain a ballistic trajectory which transits through each of these regions, one must simply choose the y_{SYN} and $\dot{y}_{\text{SYN}}$ co-ordinates which lie in the shaded region. From here, all that is required is $\dot{x}_{\text{SYN}}$, which can be obtained from Eq. 3.15. Figure 3.14 shows a ballistic transfer (blue line) from the interior region to the exterior region, via the asteroid region at $C = -3.8499$ DU^2/TU^2.

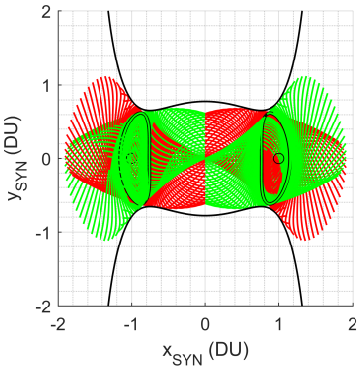

(a) Stable (green) and unstable (red) manifolds connecting the exterior, capture and interior realms.

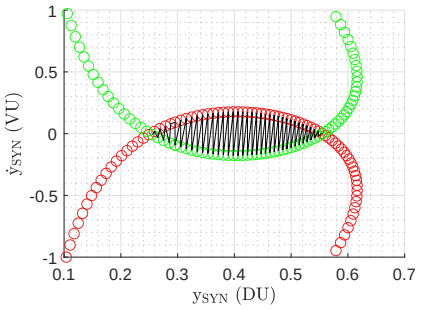

(b) Poincaré section along the +y_{SYN}-axis

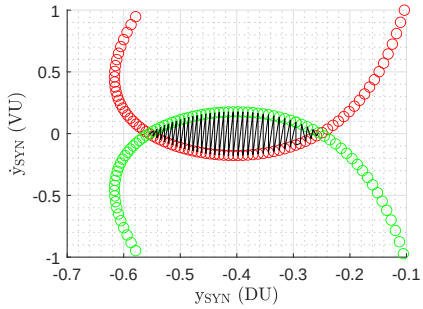

(c) Poincaré section along the -y_{SYN}-axis

Figure 3.13: Invariant manifolds and Poincaré sections for $C = -3.8499$ DU^2/TU^2

3.2.5 Effect of the Solar Sail on the Outer Regime

When $a_c \neq 0$, there is an additional acceleration term which has a considerable effect on the geometry of the ZVCs and positions of equilibrium points. The new set of equilibria are referred to, as in the inner regime, as AEPs. Both the direction and the magnitude of the acceleration provided by the sail play a critical part in the geometry of the phase space.

Figure 3.15 shows the effect of increasing sail performance on the geometry of the ZVCs for $\alpha = 0°$.

From the ZVCs in Fig. 3.15, it is clear that the sail performance not only has an effect on the geometry of the ZVCs, but also on the existence of equilibrium points. In fact, at $a_c = 0.1$ mm/s^2, there appears to be just one potential saddle point in the Hill's region.

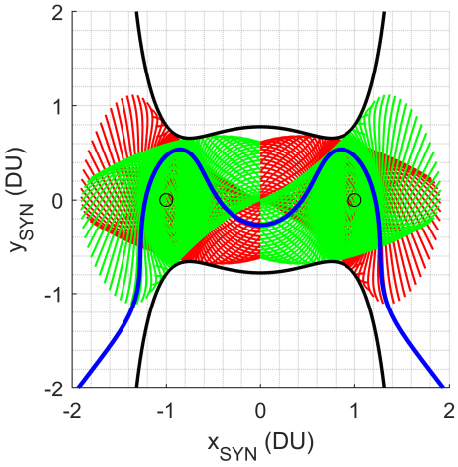

Figure 3.14: Transfer from interior to exterior region via the capture region. Transfer trajectory is shown in blue.

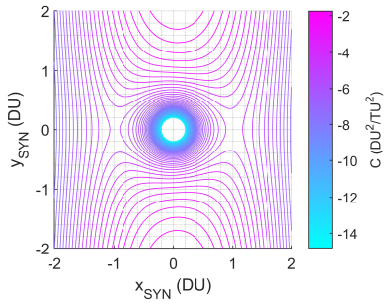

(a) $a_c = 0.001$ *mm/s*^{2}

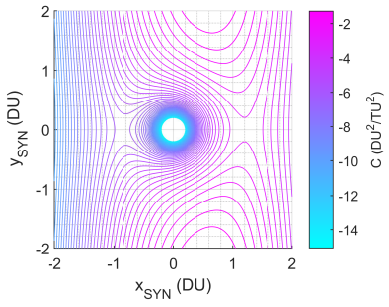

(b) $a_c = 0.01$ *mm/s*^{2}

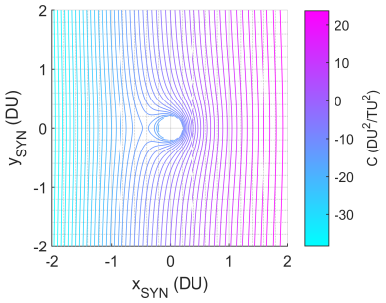

(c) $a_c = 0.1$ *mm/s*^{2}

Figure 3.15: ZVCs for system with sail acceleration included

Sail-Displaced Orbits

The same process, in the calculation of periodic orbits, as shown for the ballistic case can be applied for the AEPs once the solar sail acceleration is included. When the sail performance is increased, and with the sail face on to the Sun, the AEPs are shifted along the x-axis. The E_1 point moves rapidly in the direction of the Sun, and the E_2 point moves towards the asteroid. Figure 3.16 shows the family of planar Lyapunov orbits around E_1 at a sail performance of $a_c = 0.01$ mm/s^2, and E_2 at a sail performance of $a_c = 0.2$ mm/s^2

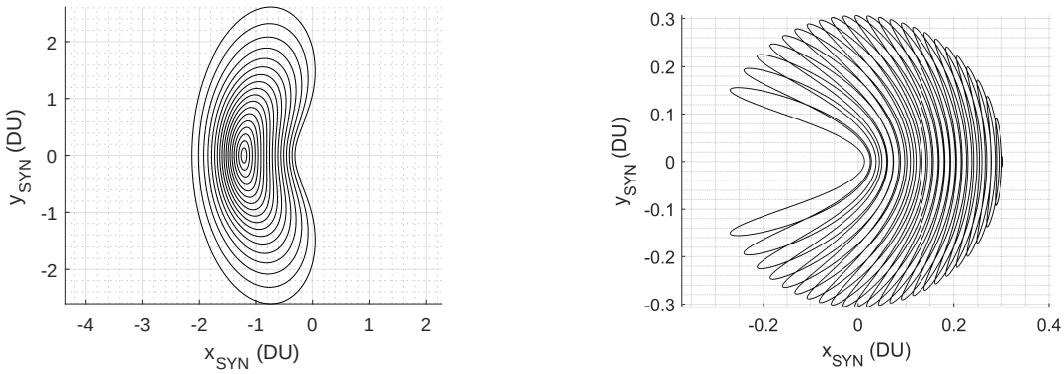

(a) Planar Lyapunov family of orbits for sail with $a_c = 0.01$ mm/s^2.

(b) Planar Lyapunov family of orbits for sail with $a_c = 0.2$ mm/s^2.

Figure 3.16: Planar Lyapunov orbits around AEP_1 and AEP_2

The spatial orbits can also be found using the same principle as for the ballistic case. The vertical stability coefficient is measured for each orbit and where that reaches the critical value of $|a_v| = 1$, there is a bifurcation into the halo orbit family. Figure 3.17 shows the vertical stability coefficient as a function of the orbital energy, C.

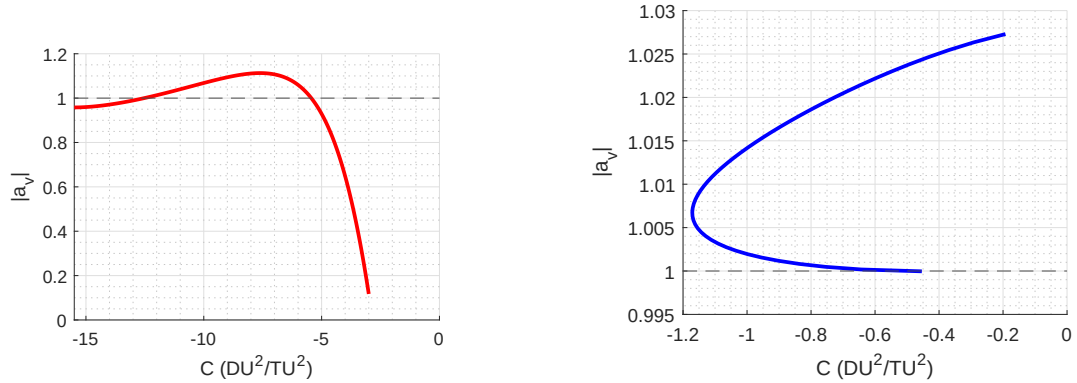

(a) AEP_1 sail displaced orbits of Fig. 3.16a

(b) AEP_2 sail displaced orbits of Fig. 3.16b

Figure 3.17: Vertical stability of the sail displaced orbits from Fig. 3.16

When the instability criteria is met, a small perturbation in the vertical direction allows for the continuation method to bifurcate out of the plane and along the halo family or orbits. The families for the AEP_1 and AEP_2 orbits related to the planar case families in Fig. 3.16, and the vertical stability shown in Fig. 3.17, are shown in Fig. 3.18.

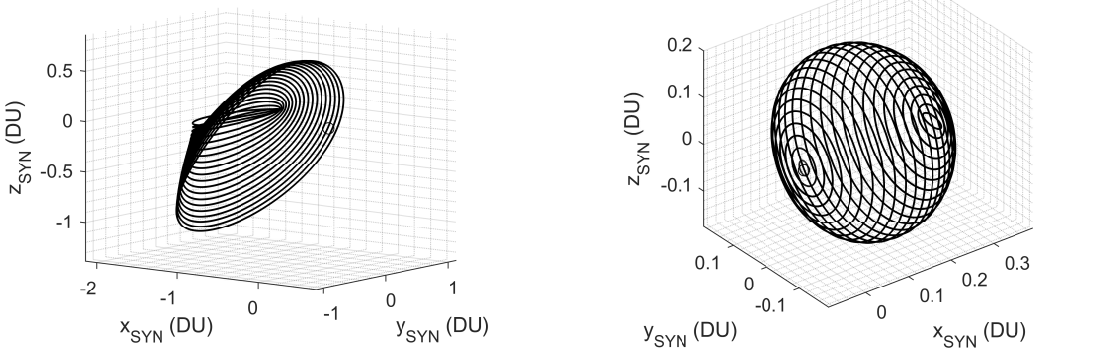

(a) AEP_1 halo family for $a_c = 0.01$ mm/s^2 *(b) AEP_2 halo family for $a_c = 0.20$ mm/s^2*

Figure 3.18: Sail displaced halo orbits around AEP_1 and AEP_2

3.3 Application of the Inner/Outer Regime Throughout this Thesis

With the dynamics of the inner and outer regimes defined and analysed, this section will describe where this work will be used in the subsequent chapters of this thesis.

Firstly, the work carried out here describing the inner regime will be used extensively in the work related to lander deployment in Chapter 5. The potential ridge line, and the associated equilibrium points, are used as the delineation for the regions from which landers are deployed with zero-velocity. The general description of the dynamical regime also becomes instructive for work where the complex shape models are applied.

The work described here for the outer regime is applied wherever the sail is distant from the asteroid. This will find application in the deployment of ChipSat probes in Chapter 5 as well as in the work on gravitational capture using the sail as primary propulsion in Chapter 6. For the latter case, the description on the periodic orbits and invariant manifolds are critical for the calculation of the approach trajectories.

Chapter 4

Control of a Solar Sail Around an Asteroid

This chapter will discuss the work carried out to control the perturbative effects of a non-spherical central body, in this case an ellipsoidal asteroid, on the orbit of a spacecraft equipped with a solar sail. First, section 4.1 provides justification for the choice of an ellipsoidal shape model for the asteroids considered in this chapter. Following this, the objective is to use a solar sail to minimise nodal regression due to the non-spherical shape of the central body. Finally, section 4.3 applies the control transition matrix (CTM), developed during the course of this work, to the problem of maintaining a periodic orbit, established using a genetic algorithm, in the highly perturbed environment.

4.1 Asteroid Shape Model Selection

In this chapter, as the sailcraft is not coming into close contact with the surface of the asteroid, an ellipsoidal shape model is assumed. This allows improved computation time, while still accounting for the major perturbation effects of a non-spherical body. Chapter 2 discusses the many shape models used in the literature and lists the chosen asteroid for this thesis. This section provides some justification for the application of the simplified ellipsoidal model.

The justification is based on analysing the apparent shape of the contours of the gravitational acceleration around several bodies using their high resolution polyhedron shape models. An ellipse is defined at the same radius as a selected contour line and the mean square error (MSE) in position between the contour line and the ellipse is calculated.

Figure 4.1 shows the contours for the magnitude of the gravitational acceleration for four of the asteroids listed in Table 2.3: Castalia, Geographos, Itokawa and Mithra, with the contours plotted in the x_{BF}-y_{BF} plane for each asteroid. The shape of the gravity field can be seen to quickly become more regular with increasing distance away from the surface of the asteroid.

With this increasing regularity, it is reasonable to assume a less computationally expensive model where the calculated trajectory remains at these distances from the surface. In Fig. 4.1, the red dashed line shows an ellipse which is defined close to a particular contour line. The

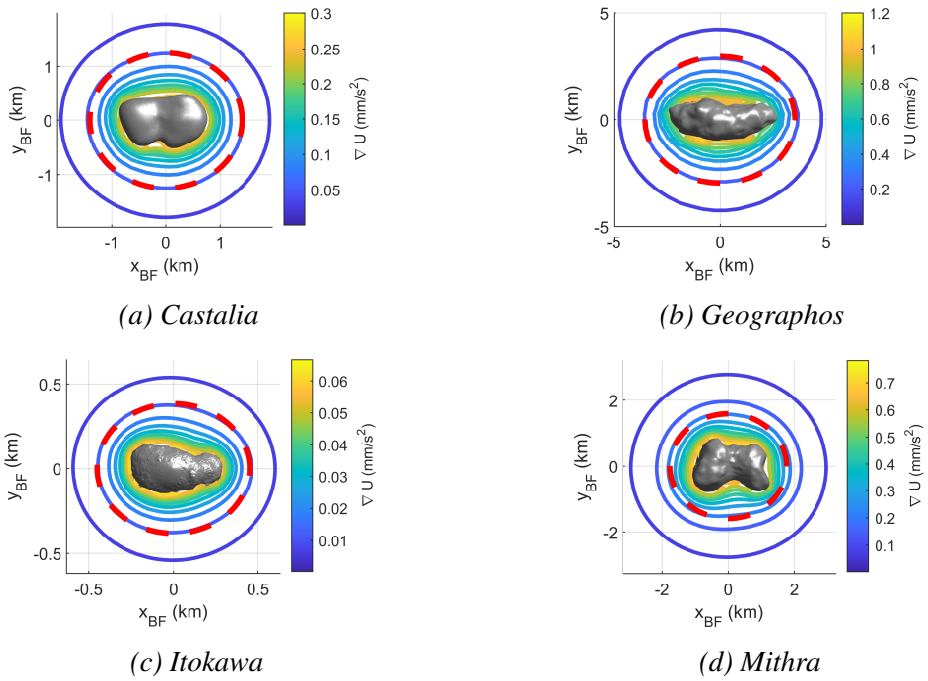

(a) Castalia *(b) Geographos*

(c) Itokawa *(d) Mithra*

Figure 4.1: Contour plots of magnitude of the gravitational acceleration in the x-y plane for asteroids Castalia, Geographos, Itokawa and Mithra. The red line shows the elliptical approximation of the given contour line.

values of the MSE for each asteroid are given in Table 4.1. It is clear from the small values of MSE that an elliptical approximation is indeed accurate for work at these distances from the asteroid.

Table 4.1: Mean squared error of elliptical approximation of gravity field contour lines.

	MSE (km^2)
Castalia	3.03×10^{-4}
Geographos	7.20×10^{-2}
Itokawa	1.03×10^{-4}
Mithra	7.67×10^{-2}

4.2 Reduction of Nodal Regression Using Continuous Solar Sail Acceleration

The objective of this work is to minimise nodal regression using the continuous thrust from a solar sail, while also minimising the effort required by the sail to do so. As discussed in the objectives in Chapter 1, the minimisation of nodal regression is targeted as a demonstration of the capability of the sail to control this effect of the non-spherical shape of a body. It could equally be applied to targeting a specific rate of nodal regression, such as for a Sun-synchronous

orbit, but in order to maintain generality, no specific mission is targeted.

This process of relieving the effects of the perturbations from non-sphericity will be referred to from here on as perturbation relief (PR). To implement this, the Radau collocation method, described in Chapter 2, is applied using the GPOPS-II software package in MATLAB.

In this work, an ellipsoidal shape modelled via spherical harmonics, as described in Chapter 2 is applied with two-body dynamics in the ACI frame. Due to difficulties in obtaining a converged result using the Radau collocation method, only one successful test case as presented here for a single orbit.

4.2.1 Nodal Regression

The secular first-order effects on a spacecraft in orbit around a central body of non-spherical shape come from the even zonal harmonics of the central body's gravity field [5]. To show this, we begin by defining the disturbing potential in the non-spherical gravity field:

$$R = -\frac{\mu}{r}\left[J_2\left(\frac{r_0}{r}\right)^2 P_2\left[\sin(\phi)\right] + \left(\frac{r_0}{r}\right)^2 \left\{P_{2,1}\left[\sin(\phi)\right]\left[C_{2,1}\cos(\psi) + S_{2,1}\sin(\psi)\right] + P_{2,2}\left[\sin(\phi)\right]\left[C_{2,2}\cos(2\psi) + S_{2,2}\sin(2\psi)\right]\right\}\right] \quad (4.1)$$

where J_2 is the second order zonal harmonic of the central body, ϕ is the latitude, ψ is the longitude, $P_{l,m}$ are the Legendre polynomials, $C_{l,m}$ and $S_{l,m}$ are the harmonic coefficients at degree l and order m and:

$$P_2[\sin(\phi)] = \frac{3}{2}\left(\sin^2(\phi) - \frac{1}{3}\right) \quad (4.2)$$

By ignoring the effects of the tesseral and sectoral harmonics, the remainder represents just the J_2 zonal harmonic (remembering that $J_2 = -C_{2,0}$). As such, the disturbing potential function becomes:

$$R = -\frac{\mu J_2}{r}\left(\frac{r_0}{r}\right)^2 \frac{3}{2}\left(\sin^2(\phi) - \frac{1}{3}\right) \quad (4.3)$$

Searching for an expression in terms of orbital elements, relations with inclination, latitude and position can be made [5]:

$$R = -\frac{3\mu J_2}{2r}\left(\frac{r_0}{r}\right)^2 \left(\sin^2(i)\sin^2(\omega_k + \theta) - \frac{1}{3}\right) \quad (4.4)$$

where θ is the true anomaly, i is the orbit inclination and ω_k is the argument of periapsis. Making use of trigonometric identities, ignoring long and short periodic terms in ω_k and θ and replacing

$\mu = n^2 a^3$, where n is the mean motion of the spacecraft orbit, gives:

$$R = -\frac{3}{2} n^2 r_0^2 J_2 \left(\frac{a}{r}\right)^3 \left(\frac{\sin^2(i)}{2} - \frac{1}{3}\right) \tag{4.5}$$

It is shown by Vallado [5] that by averaging the effects over one orbit period we have:

$$\left(\frac{a}{r}\right)^3 = \frac{1}{(1-e^2)^{3/2}} \tag{4.6}$$

where a is the orbit semi-major axis and e is the orbit eccentricity. Replacing this average in the disturbing function acts to average R over the same period:

$$R_{avg} = -\frac{3}{2} n^2 r_0^2 J_2 \frac{1}{(1-e^2)^{3/2}} \left(\frac{\sin^2(i)}{2} - \frac{1}{3}\right) \tag{4.7}$$

The Lagrange variational equations [130] give:

$$\frac{d\Omega_k}{dt} = \frac{1}{na^2\sqrt{1-e^2}\sin(i)} \frac{\partial R}{\partial i} \tag{4.8}$$

where partial derivative is given by:

$$\frac{dR_{avg}}{di} = -\frac{3}{2} n^2 r_0^2 J_2 \frac{\sin(i)\cos(i)}{(1-e^2)^{3/2}} \tag{4.9}$$

Therefore, the time rate of change of the node is given by:

$$\frac{d\Omega_k}{dt} = -\frac{3nr_0^2 J_2}{2a^2(1-e^2)^2} \cos(i) \tag{4.10}$$

It is shown here that the effects of the even zonal harmonics on a spacecraft orbit manifest in the right ascension of ascending node (Ω_k), though it can also be shown that they will also manifest in the time rate of change of the argument of periapsis (ω_k) and mean anomaly. The time rate of change in Ω_k, which is born of the non-spherical gravity field, is referred to as nodal regression. Nodal regression is predominantly affected by i [5], but is also dependant on a and e. Although this work will include higher order terms, it is important to mention that the J_2 coefficient has by far the greatest effect of all of the coefficients on nodal regression.

4.2.2 Optimal Control Problem

The general form of an optimisation problem is given by [133, 155]:

$$J = M\left(\mathbf{s}(t_0), t_0, \mathbf{s}(t_f), t_f\right) + \int_{t_0}^{t_f} L\left(\mathbf{s}(t), \mathbf{u}(t), t\right) dt \tag{4.11}$$

where $\mathbf{s}(t)$ denotes the state, $\mathbf{u}(t)$ denotes the control, t_0 represents the initial time, t_f represents the final time, M is the Mayer cost function and L is the Lagrange cost function. In all simu-

lations, $t_0 = 0$ and is fixed, where t_f is the final time of the guess orbit. The upper and lower bounds are set as $1.1t_f$ and $0.9t_f$ respectively. The initial and final states are constrained to seek a periodic solution within the set tolerance.

The definition of the control is given in cone and clock angles and so $\mathbf{u} = [\alpha, \delta]$. To facilitate convergence in the GPOPS II software, a process of normalisation is conducted. Distance Units (DU) are normalised with DU $= r_0$, time is normalised with one Time Unit (TU) being equal to the reciprocal of the angular velocity of the asteroid rotation.

Given the large moments of inertia for a solar sail, rapid changes in attitude are difficult to achieve without a large attitude control system which brings additional mass to the spacecraft. As such, a control law which requires slower rotational rates is beneficial. Therefore, by minimising the control effort, we can ensure a smooth control law which is feasible for a real-world sail.

However, a minimal effort solution is likely to result in a trajectory which is not periodic. In order to achieve a solution which minimises the effort, but maintains periodicity, a process of numerical continuation is followed. There are two contributions to the objective function: the first minimises the distance in the state-space between two consecutive intersections with a Poincaré Section (described in Chapter 2), the second contribution focuses on minimising the control effort. The weight given to each contribution is defined by the continuation parameter, κ. Applying this parameter to Eq. 4.11 gives the optimal control objective function for this problem which is defined in the ACI frame:

$$J = (1-\kappa)||\mathbf{s}_{\mathrm{ACI}}(t_f) - \mathbf{s}_{\mathrm{ACI}}(t_0)|| + \kappa \int_{t_0}^{t_f} |\ddot{\gamma}| dt \tag{4.12}$$

where $\ddot{\gamma}$ is the angular acceleration of the sail attitude. With $\kappa_0 = 0$, the process iterates until $\kappa = 1$. As such, in the first iteration the objective is to achieve a periodic orbit. Over each iteration, the solution from the previous iterations is used as the first guess of the next and the weighting shifts towards achieving a minimum effort control law.

This effort will be defined by the overall angular velocity changes required by the sail over the orbital period. A minimal value of this therefore constitutes a minimum-effort optimisation and the effort value is given by:

$$\Delta\dot{\gamma} = \int_{t_0}^{t_f} |\ddot{\gamma}| dt \tag{4.13}$$

4.2.3 Application to 3122 Florence$_a$

As one of the largest known NEAs, the target asteroid in this section of the work is an ellipsoidal approximation of 3122 Florence$_a$. The mass, rotational period and mean radius are obtained from the CNEOS database [1] and the ellipsoidal dimensions are given in Table 2.3.

[1] https://cneos.jpl.nasa.gov/, accessed 02/10/2022

The initial orbit eccentricity is fixed at $e = 0.1$, with inclination of 28° and semi-major axis at $a = 2a_e$. Figure 4.2a shows the ballistic orbit propagated for approximately 28 hours (five full orbital periods), giving a clearer example of the effect the non-spherical central body has on the orbit of the spacecraft; a rotation of the line of nodes [5]. The time rate of change of this nodal regression is shown in Fig. 4.2b and is linearly approximated to have a value of $\dot{\Omega}_k \approx 50$ deg/day.

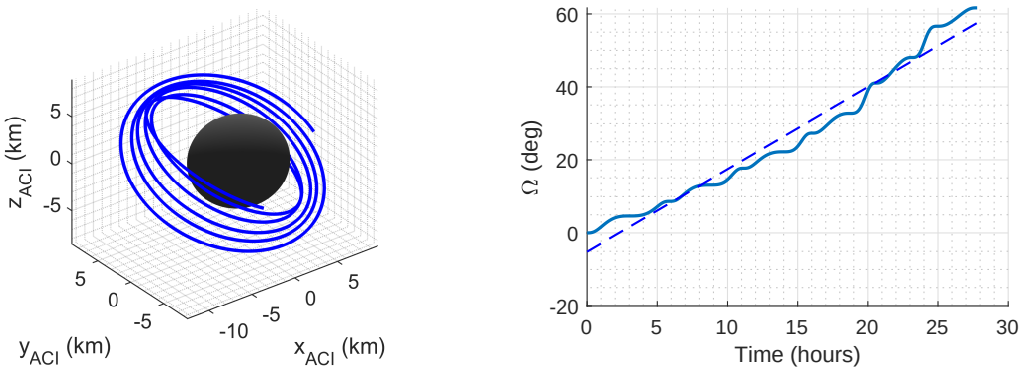

(a) Ballistic trajectory propagated for 5 orbital periods.

(b) Secular trend of Ω_k

Figure 4.2: Nodal regression of a ballistic orbit due to a non-spherical central body with secular trend of $\dot{\Omega}_k \approx 50$ deg/day

With the ballistic orbit established, the solar sail is introduced to the dynamics and the optimisation process begins with $\kappa = 0$, with all weighting given to the Mayer cost function. The control law for the initial guess is constant and given as $\mathbf{u} = [\pi/2, \pi/2]$, where the sail would produce zero thrust. The optimisation successfully converges and the resulting trajectory under PR control is shown in Fig. 4.3a, with the control history shown in Fig. 4.3c and the initial and final points on the Poncaré section shown in Fig 4.3b. The black cross represents the uncontrolled final point and the red cross shows the final point under control of PR.

Now, with successful convergence of the case $\kappa = 0$, these results will be used as a first guess to initiate the iterative continuation process discussed in Section 4.2.2. The process begins with $\kappa = 1 \times 10^{-10}$ and increases by one order of magnitude on each iteration. Between the values of $\kappa = 0.1$ and $\kappa = 1$, it was necessary to increase in steps of 0.1. As the value of κ increases, the value of the integral contribution of the objective (4.12) decreases as expected. This decrease is shown in Fig. 4.4a with the changes in the state error given in Fig. 4.4b.

Once $\kappa = 1$ is achieved, the differences in initial and final state are no longer contained in the objective function. However, in order to constrain the optimisation such that periodicity is maintained within a certain tolerance, a constraint function is applied. Figure 4.5a shows the comparison of the orbit with PR for $\kappa = 1$ compared with the perturbed and unperturbed ballistic orbits, and so this represents the minimum effort optimisation. Figure 4.5b shows the Poincaré section which indicates that, although there is a slight difference, $||\mathbf{s}_{\text{ACI}}(t_f) - \mathbf{s}_{\text{ACI}}(t_0)|| \approx 0$. The

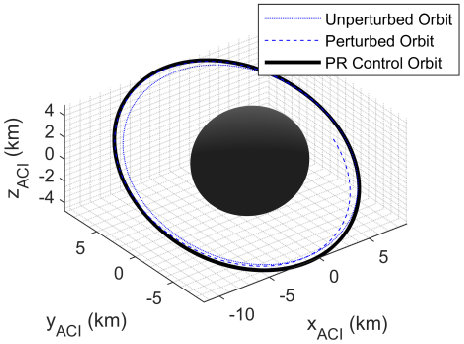

(a) Trajectory

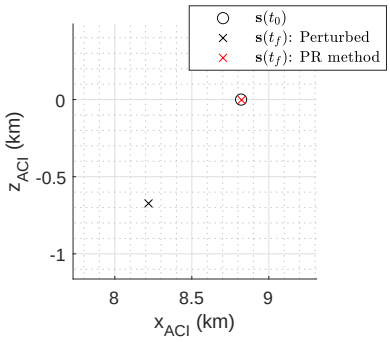

(b) Poincaré section in position space

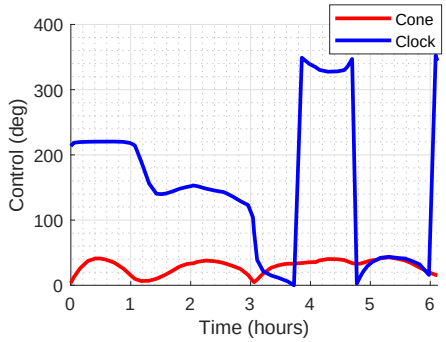

(c) Control history

Figure 4.3: Uncontrolled and PR controlled orbits for $\kappa = 0$

minimum effort control law is shown in Fig. 4.5c.

As the final point does not intersect exactly with the initial point, it can be expected that there is still some residual drift in Ω_k. Fig. 4.6a shows the PR orbit propagated for a total time corresponding to 5 unperturbed orbital periods.

The PR method has reduced the nodal regression from $\dot{\Omega}_k \approx 50$ deg/day for the uncontrolled orbit to $\dot{\Omega}_k \approx 3$ deg/day for the orbit controlled by PR with a minimal control effort required from the sail. The success shown here required an effort of only $\Delta\dot{\gamma} \approx 0.03$ deg/s, a reduction by one order of magnitude from the case where $\kappa = 0$. This low effort control law is well suited to the solar sail, given the high moments of inertia and the slow attitude changes which result.

4.2.4 Challenges encountered in application of Radau collocation

The work presented in this section so far has shown those results where the Radau collocation method successfully converged to an optimal solution. However, there were many situations where this was not the case. The main challenge is in establishing a sufficiently good initial guess to facilitate convergence. As such, the next section will present another method which removes the requirement of defining an initial guess to the optimisation problem.

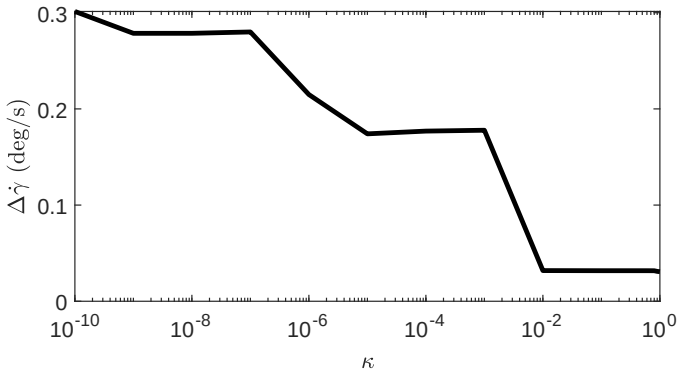

(a) Reduction in value of integral over continuation along κ.

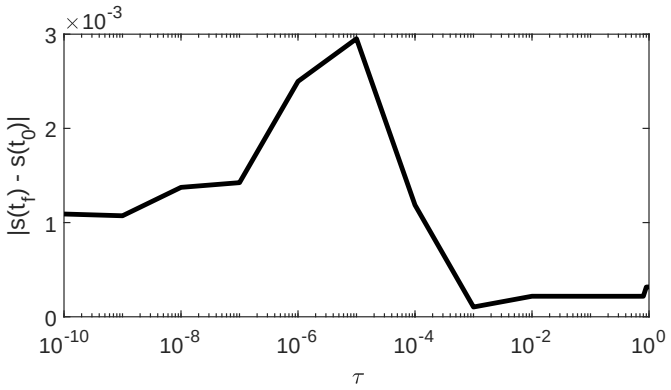

(b) Variation in final state error relative to initial state over continuation along κ.

Figure 4.4: Variation in objectives during change in weighting factor, κ

4.3 Multi-objective Optimisation and the Control Transition Matrix for Designing and Maintaining a Periodic Orbit

This section establishes a periodic orbit for a solar sail around an ellipsoidal asteroid in the ACI frame using a Genetic Algorithm (GA). Once this is established, the problem of maintaining this orbit is addressed using a novel control algorithm; the Control Transition Matrix (CTM).

One of the main difficulties in the work so far has been in establishing a sufficiently good first guess of the optimal solution, such that the optimisation method applied converges successfully. This is largely due to the sensitivity of the system not only to the relatively strong acceleration of the sail, but also to the initial conditions of the orbit. To show this, the following section will study the sensitivity of an orbit to small changes in initial position along each axis. As described in Section 2.4.1, the GA does not require the user to define an initial guess, and so this alleviates some of the issues already experienced in this chapter. After the discussion on the sensitivity of the system, methods by which the efficacy of the CTM in maintaining the periodic orbit can be assessed will be detailed. A statistical approach is taken to this analysis and, to this end, a Monte Carlo method is used. The Monte Carlo method allows us to randomly vary the initial condition of the orbit in order to assess the likelihood of the CTM to successfully achieve its objectives,

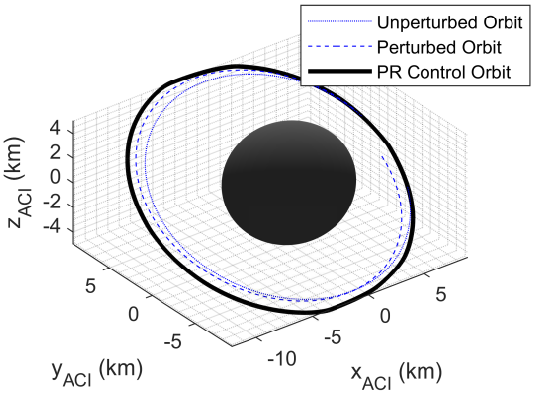

(a) Trajectory comparison showing unperturbed, perturbed and orbit under control of PR method.

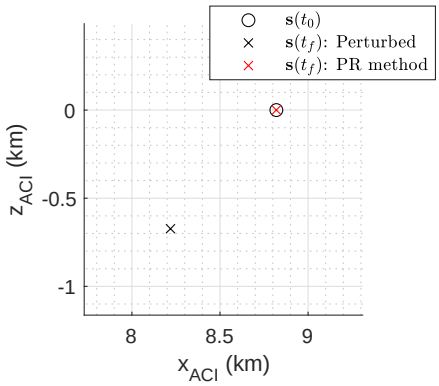

(b) Poincaré section showing $||\mathbf{s}_{ACI}(t_f) - \mathbf{s}_{ACI}(t_0)|| \approx 0$ as before.

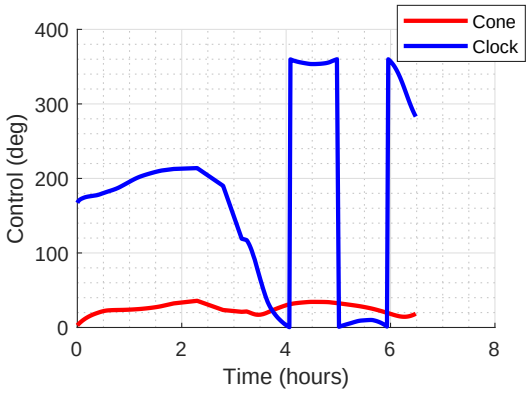

(c) Control law for minimum effort at asteroid 3122 Florence.

Figure 4.5: Application of PR method to asteroid Florence$_a$

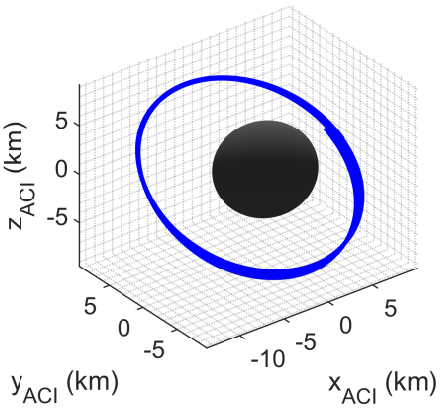

(a) Trajectory

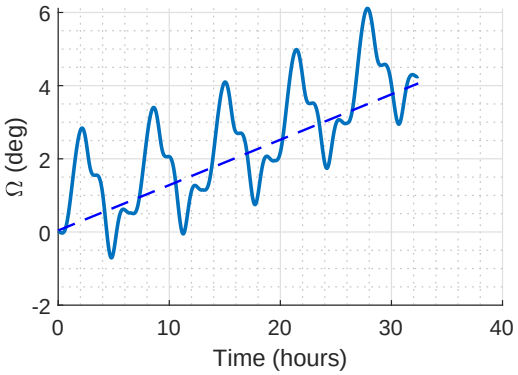

(b) Secular trend in Ω_k

Figure 4.6: PR controlled orbit over a 1.35 day period showing a secular trend of $\dot{\Omega}_k \approx 3$ deg/day.

with the formulation of this method described in Section 4.3.2. These objectives are set out as success criteria and described in Section 4.3.3. With the method established, some success criteria are defined to allow analysis on whether or not the CTM meets certain objectives. These

criteria are defined in Section 4.3.3.

4.3.1 System Sensitivity

In this section, the sensitivity of an orbit to changes in initial condition is analysed. Small changes in initial position are made along each axis and the resulting error in final position is measured.

A range of orbits, with orbital elements shown in Table 4.2, are analysed here and are shown in Fig. 4.7. Small, incremental changes are made in the x_{ACI}, y_{ACI} and z_{ACI} components of the initial position and the error in the final state as measured from the initial reference trajectory are recorded. Figure 4.7 shows the final error in x_{ACI}, y_{ACI} and z_{ACI} as a function of the magnitude of the change in initial position. Therefore, the final point error is the distance between the final point of the reference orbit, and the final point for the perturbed orbit.

Table 4.2: Principal orbital elements for four orbits tested in sensitivity analysis

Test Case	a (km)	e	i (deg)
1	9.80	0.10	0
2	9.80	0.10	15
3	9.80	0.10	30
4	9.80	0.10	60

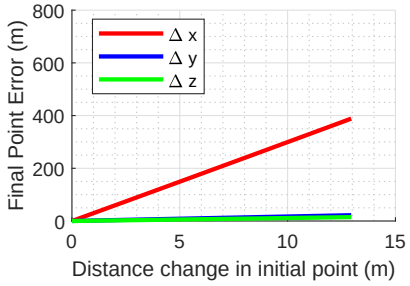

(a) Sensitivity analysis with orbital inclination of 0 degrees

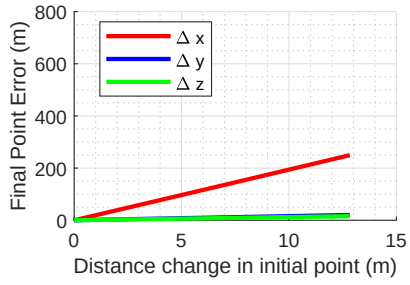

(b) Sensitivity analysis with orbital inclination of 15 degrees

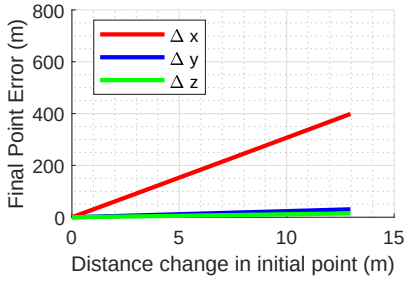

(c) Sensitivity analysis with orbital inclination of 30 degrees

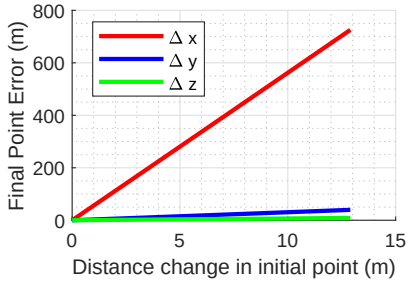

(d) Sensitivity analysis with orbital inclination of 60 degrees

Figure 4.7: Sensitivity analysis for range of orbital inclinations.

The system appears most sensitive to changes along the x_{ACI}-axis for all orbits. As the orbits' initial point is always at periapsis, changes in x_{ACI}-position impact mostly the semi-major axis. Further, it is shown that the system is most sensitive for higher inclination orbits. For the highest inclination orbit shown in Fig. 4.7, a 1 m change of the initial position along the x_{ACI}-axis brings an error of 46 m in the final position compared to the reference orbit.

4.3.2 Monte Carlo Method to Establish Success Rates

Monte Carlo methods are a set of numerical methods based on repetitive random sampling to assess the success of a given system under uncertain initial conditions. This work randomly generates a set of initial states, $\mathbf{s}^{(i)}_{\text{ACI}}(t_0)$, which are used to test the success rates of the CTM method described in Chapter 2. The 500 normally distributed random points are contained within a sphere of radius r_p and are generated by [132]:

$$\mathbf{s}^{(i)}_{\text{ACI}}(t_0) = \mathbf{s}^{nom}_{\text{ACI}}(t_0) + \left(r_p \frac{\text{rndNorm}}{1.96} \right) \mathbf{1}_{(6\times 1)} \tag{4.14}$$

where rndNorm is a randomly generated number with normal distribution, the 1.96 scaling factor guarantees that the randomly generated points are within 3 standard deviations of the mean, giving a 97.5% probability that the points will be contained in the sphere. The $\mathbf{1}_{(6\times 1)}$ matrix is a 6×1 matrix of ones.

4.3.3 Success Criteria

The CTM will be tested for its success in improving upon the final state error of the reference trajectory and control law after delivering the desired updated control laws. This section defines the criteria by which this success will be measured.

Figure 4.8 shows the initial state of the nominal orbit, $\mathbf{s}^{nom}_{\text{ACI}}(t_0)$, on a Poincaré section [130], where the black dot represents the point at which the section is pierced. The success of the method will consider an orbit which begins at the end of the orbit which utilises the nominal control law and is displaced from $\mathbf{s}^{nom}_{\text{ACI}}(t_0)$ by $\delta\mathbf{s}_{\text{ACI}}$. The initial state for this orbit is denoted by $\mathbf{s}_{\text{ACI}}(t_0)$, which will be propagated with both the nominal control law (red line) and the new control law (blue line). Where the propagation uses the nominal control law, the trajectory is denoted with superscript *nom* and where it is propagated with the new control law it will be denoted with the superscript *new*. These will also be referred to as the nominal orbit and the new orbit respectively.

Here, $\mathbf{s}^{new}_{\text{ACI}}(t_f)$ is the final state of the orbit which originates at $\mathbf{s}_{\text{ACI}}(t_0)$ and utilises the new control law, $\mathbf{u}(t)$, and $\mathbf{s}^{nom}_{\text{ACI}}(t_f)$ is the final state of an orbit which originates at $\mathbf{s}_{\text{ACI}}(t_0)$ and is propagated using the nominal control law. $\delta\mathbf{s}_{\text{ACI}}$ is the error between the nominal orbit initial state and the initial state of the orbit originating at $\mathbf{s}_{\text{ACI}}(t_0)$, ε^{new} is the error between the nominal

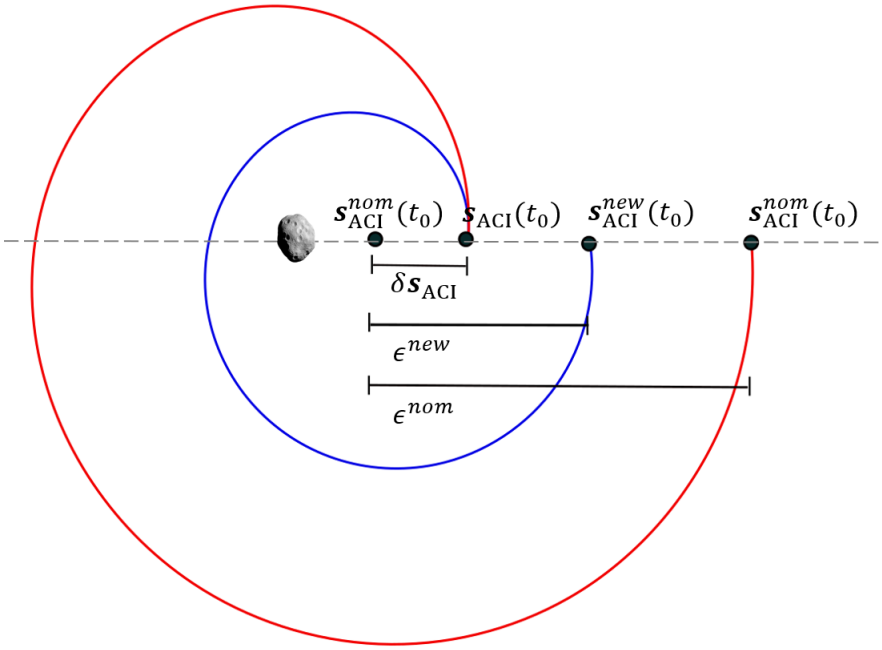

Figure 4.8: Schematic showing the initial and final states of the nominal orbit, new orbit, and the error in the states and their final states if propagated with both the new control and the nominal control. The Poincaré section, which lies in the x_{ACI}-z_{ACI} plane of the asteroid-centred reference frame, is represented by the grey dashed line. Each trajectory orbits once around the asteroid.

initial point and the final point of the orbit originating at $\mathbf{s}_{\text{ACI}}(t_0)$ and propagated using the new control law and ε^{nom} is the error between the nominal initial state and the final state of the orbit originating at $\mathbf{s}_{\text{ACI}}(t_0)$ propagated using the nominal control law.

The success criterion $\varepsilon^{new} < |\delta \mathbf{s}_{\text{ACI}}|$ implies that the control law which has been updated using the CTM has reduced the norm of the error in final state after one orbit when compared to the final state error of the reference orbit. The success criterion $\varepsilon^{new} < \varepsilon^{nom}$ shows that propagation of the orbit using the updated control law has given a reduced final state error when compared with an orbit which employs continued use of the nominal control law.

4.3.4 Results

Design of a Nominal Orbit Using Multi-Objective Optimisation

As previously with the Radau collocation method, there is a coupling between the minimum state error achievable and the effort required by the sail to do so. Previously, these were combined in a single objective function where a continuation parameter applied a weighting until the minimum effort solution was achieved. In this section, the two objectives are split in a multi-objective optimisation using the GA. By doing so, the optimisation delivers a range of solutions which the user can choose from depending on the capabilities of the sail and the acceptable tolerances of a mission objective.

For the continuous time problem to be addressed using the GA, it is necessary to discretise the problem in time. This discretised control law will initially be interpolated using piecewise constant interpolation. Later, the method is changed to cubic spline interpolation to allow a smoother control law to be established. The solution vector again contains the controls, α and δ, at each control node in the discretised system.

The same system of normalisation as that used in the Section 4.2 is applied here where DU $= r_0$ and TU $= \omega^{-1}$, where ω is the angular velocity of the asteroid rotation. A target orbit with the orbital elements listed in Table 4.3 is first sought using the GA in a multi-objective optimisation where the objective functions are given by:

$$J_a = ||\mathbf{s}_{\mathrm{ACI}}(t_f) - \mathbf{s}_{\mathrm{ACI}}(t_0)||$$
$$J_b = \int_{t_0}^{t_f} |\ddot{\gamma}| dt$$

As such, J_a ensures a periodic orbit and J_b brings the minimal control effort. The solution vector for the GA is comprised of the initial state, the control and final time.

Table 4.3: Principal orbital elements for the initial target orbit for the GA multi-objective optimisation.

a (km)	e	i (deg)
9.80	0.10	15.00

The description of the GA in Chapter 2 states the requirement of initialising the GA with multiple seeds in order to establish the true optimal result. As such, this work uses 25 seeds which are used to generate 25 initial populations. The full set of results from these seeds form the full solution set. From this full set, the non-dominated solutions form the Pareto front which is shown in red in Fig. 4.9 with the rest of the full solution set shown in black.

For a minimum amount of control effort, there is a correspondingly high difference in final and initial state. Similarly, for a small error in final and initial state, there is a high control effort requirement. Ref. [156] discusses the methods which are available in the literature for selection of the appropriate solution from the Pareto front. However, it should be noted that data from The Planetary Society's LightSail 2 mission shows that the sail was capable of achieving slew rates of $\dot{\gamma} = 0.4$ deg/s [2]. With this in mind, a solution which offers a value of $J_b < 0.4$ deg/s, while also maintaining a low value of J_a is sought. In fact, the full solution set offers values of $J_b < 0.4$ deg/s and so the solution with min(J_a) is used. The control law and trajectory for the chosen solution are shown in Fig. 4.10. The difference in initial and final states is reduced by allowing variation in initial state from the reference initial state as part of the optimisation. For

[2] https://www.planetary.org/explore/projects/lightsail-solar-sailing/lightsail-mission-control.html, cited March 27th, 2020

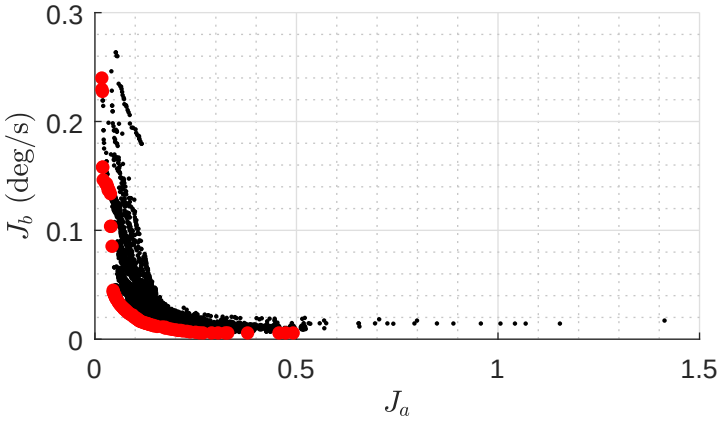

Figure 4.9: Pareto front shown in red with full set of solutions in black.

this orbit the objective values were $J_a = 0.017$ and $J_b = 0.24$ deg/s

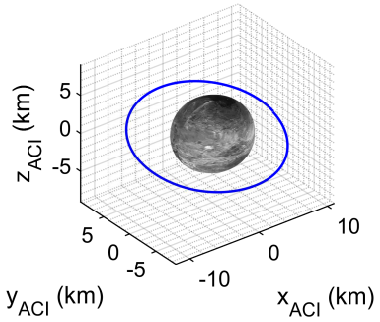

(a) Trajectory plot from GA results.

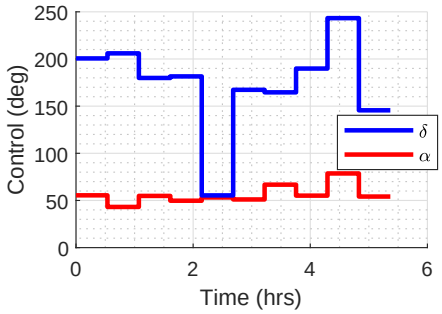

(b) Control history in clock (δ) and cone (α) angles

Figure 4.10: Trajectory and control history for nominal orbit using GA with piece-wise constant interpolation.

Although the value of J_a is very small, in this sensitive system that small error will grow quickly with each subsequent orbit. Figure 4.11 shows how application of the nominal control law over 2 complete orbits causes the sail to diverge from the nominal trajectory. It is for this reason that the CTM will be applied.

Success Rates of CTM in Control Law Correction

In this section, the success rate of the CTM is measured using a Monte Carlo simulation for a sphere of increasing radius, r_p, centred on $\mathbf{s}^{nom}_{\text{ACI}}(t_0)$ and containing the dispersion of the initial states, $\mathbf{s}_{\text{ACI}}(t_0)$. The success criteria described in section 4.3.2 are used and measured for each value of r_p. Fig. 4.12 shows the success rates for $\varepsilon^{new} < |\delta\mathbf{s}_{\text{ACI}}|$ in red, and $\varepsilon^{new} < \varepsilon^{nom}$ in blue up to $r_p = 490$ m. Fig. 4.13 shows the success rates up to $r_p = 9.8$ km.

In the first set of results, the spheres up to $r_p = 490$ m have almost entirely a 100% success

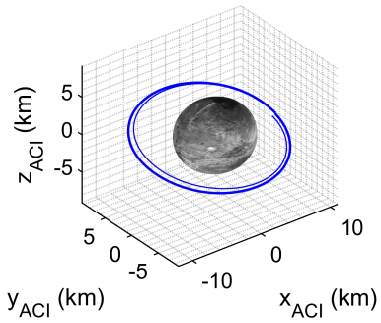

Figure 4.11: Trajectory as in Fig. 4.10a, propagated for two revolutions using same nominal control law shown in Fig. 4.10b

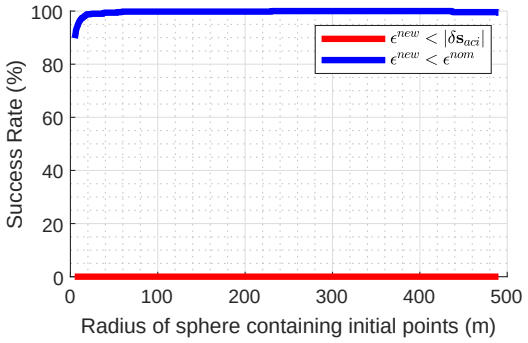

Figure 4.12: Success rates of criteria $\varepsilon^{new} < |\delta \mathbf{s}_{ACI}|$ and $\varepsilon^{new} < \varepsilon^{nom}$ with radius of sphere of dispersion of initial points up to 490 m.

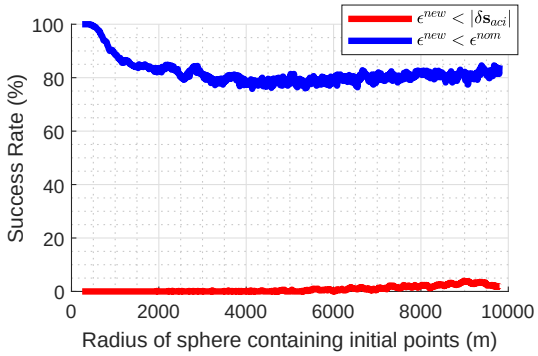

Figure 4.13: Success rates of criteria $\varepsilon^{new} < |\delta \mathbf{s}_{ACI}|$ and $\varepsilon^{new} < \varepsilon^{nom}$ with radius of sphere containing initial points up to 9.8 km.

rate in $\varepsilon^{new} < \varepsilon^{nom}$. Conversely, the success rates for $\varepsilon^{new} < |\delta \mathbf{s}_{\mathrm{ACI}}|$ remain at zero throughout. In the second set of results, for the expanded range of r_p, as the value of r_p increases, the success rate of $\varepsilon^{new} < \varepsilon^{nom}$ drops to around 80%. The second success parameter, $\varepsilon^{new} < |\delta \mathbf{s}_{\mathrm{ACI}}|$, remains at zero until the radius of the sphere approaches 4 km, where there is a very small increase until a peak of approximately 5% success at around 9 km. However, given the linearisation of the system, the drop in success of $\varepsilon^{new} < \varepsilon^{nom}$ may be an indication of the CTM being applied to trajectories which are not sufficiently close to the reference trajectory for the linearisation to be

valid.

Application of the CTM to Multiple Revolutions

The CTM is now applied to update the control law over multiple orbits in order to maintain periodicity. Four test cases are presented which differ by orbital inclination. In each case, the target orbital elements are shown along with those obtained from the GA for the nominal orbit and those achieved by the CTM after many orbit revolutions.

Test Case 1 Test case 1 takes an equatorial orbit, the orbital elements for which are contained in Table 4.4 along with the elements for the GA solution and CTM final orbit. The orbit obtained from the GA is taken as the nominal orbit and will be shown in red in all subsequent plots. The CTM method is then applied on all orbits subsequent to the nominal orbit.

The comparison of trajectories using the nominal control law for several orbits subsequent to the nominal orbit (Fig. 4.14a) and the trajectory where the CTM updates the control law on each orbit (Fig. 4.14b) are shown in Fig. 4.14. As was shown in Section 4.3.4, the CTM will almost always be successful in improving upon the error between the final state and the final state which would have been obtained with continued use of the nominal control law.

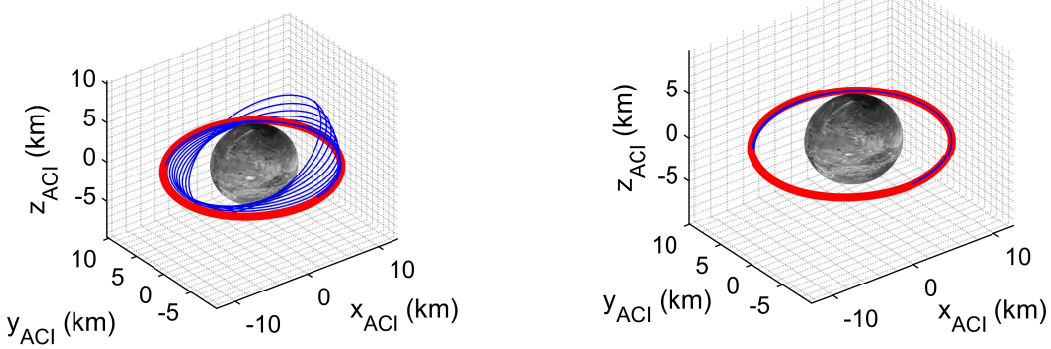

(a) 10 subsequent revolutions with nominal control law

(b) 100 subsequent revolutions with CTM updating control

Figure 4.14: Comparison of trajectories where the nominal control law is applied to subsequent orbital revolutions with the CTM employed to update the control law on each successive revolution. Nominal orbit shown in red, all subsequent orbits shown in blue

A comparison of the piece-wise control laws obtained from the GA and that obtained from the CTM is shown in Fig. 4.15.

The periodicity of the CTM solution is analysed using Poincaré sections in both position (Fig. 4.16a) and velocity (Fig. 4.16b). From this analysis, it is clear that the trajectory converges to a periodic orbit and Table 4.5 shows that the orbital elements obtained by the CTM are close to those of the GA solution for the nominal orbit.

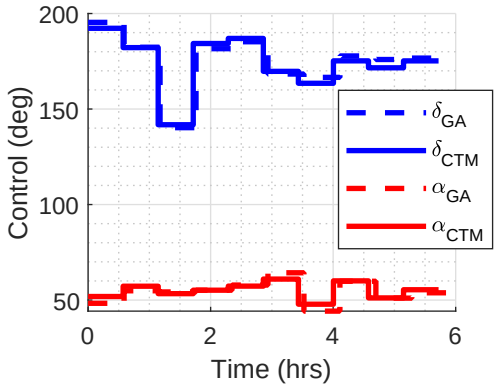

Figure 4.15: Control law for the nominal orbit obtained from the GA (shown in broken lines) along with control law for the periodic orbit (shown in solid lines) for test case 1

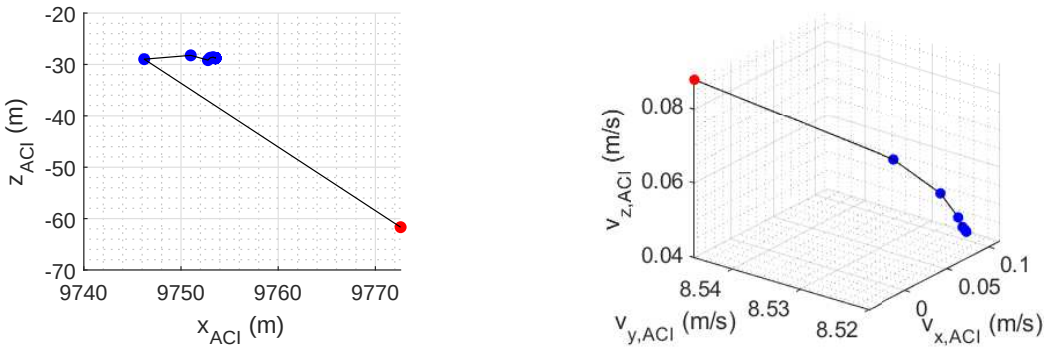

(a) Position *(b) Velocity*

Figure 4.16: Poincaré sections in both position and velocity for 100 orbits where control has been updated using CTM method. Nominal orbit shown in red with all subsequent orbits in blue and the black connecting line showing the progression from the nominal to the final orbit.

Table 4.4: Principal orbital elements for the target orbit in test case 1. The nominal orbit is obtained from the GA and the final periodic orbit is obtained through the CTM control law updating.

	a (km)	e	i (deg)
Target Orbit	9.80	0.10	0
GA Result	9.29	0.06	1.06
CTM Result	9.12	0.07	0.32

Test Case 2 In the second test case the orbit inclination is increased to 15° as stated in Table 4.2. The orbital elements for the target orbit, the GA solution and the CTM result for this test case are given in Table 4.5.

A comparison of the trajectories where the nominal control law is used on orbits subsequent to the nominal orbit and those where the CTM is applied to update the control law on each orbit are shown in Fig. 4.17.

Once again, the periodicity of the CTM orbits are verified using Poincaré sections in position

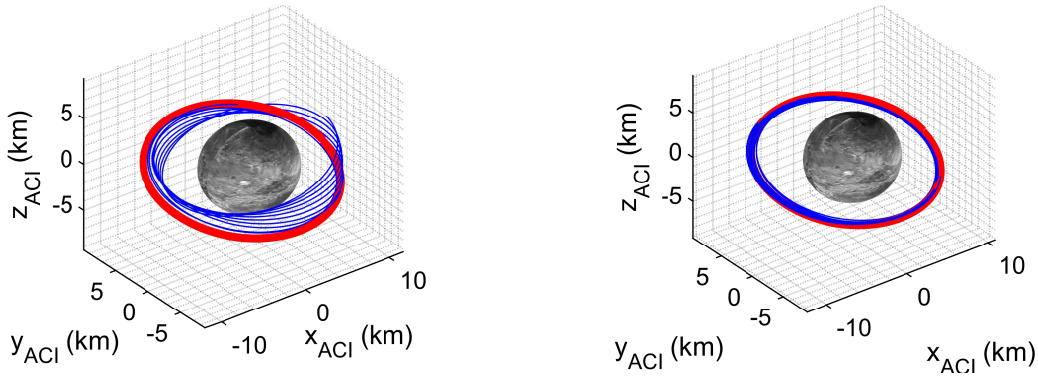

(a) 10 subsequent revolutions with nominal control law

(b) 100 subsequent revolutions with CTM updating control

Figure 4.17: Comparison of trajectories where the nominal control law is applied to subsequent orbits and where the CTM method is employed to update the control law on each successive orbit. Nominal orbit shown in red, all subsequent orbits shown in blue

(Fig. 4.18a) and velocity (Fig. 4.18b). From these sections the trajectory clearly converges to a periodic orbit with the orbital elements shown in Table 4.5 showing the CTM solution being very close to the GA nominal solution.

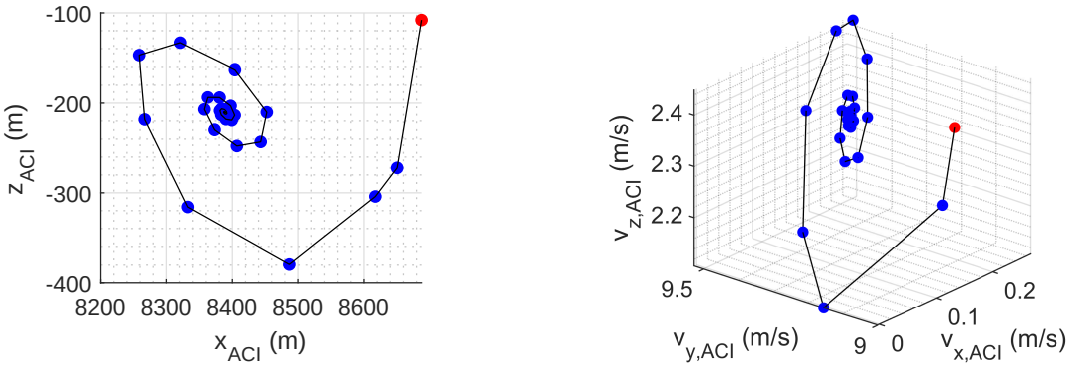

(a) Position

(b) Velocity

Figure 4.18: Poincaré sections in both position and velocity for 100 orbits where control has been updated using CTM method. Nominal orbit shown in red with all subsequent orbits in blue and the black connecting line showing the progression from the nominal to the final orbit.

Table 4.5: Principal orbital elements for the target orbit in test case 2. The nominal orbit is obtained from the GA and the final periodic orbit is obtained by the CTM method of control law updating.

	a (km)	e	i (deg)
Target Orbit	9.80	0.10	15.00
GA Result	8.84	0.01	14.54
CTM Result	8.65	0.03	14.07

Test Case 3 The inclination of the orbit in test case 3 is set at 30°, with the orbital elements shown in Table 4.6 for the target orbit, the GA solution and the CTM result. There is, once again, a considerable improvement in using the CTM to update the control law for each subsequent orbit compared with maintaining the nominal control law, as is shown in Fig. 4.19.

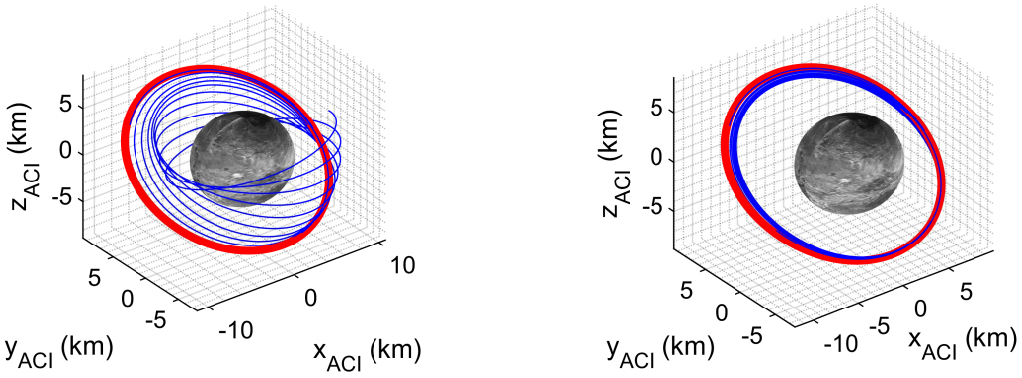

(a) 10 subsequent revolutions with nominal control law

(b) 100 subsequent revolutions with CTM updating control

Figure 4.19: Comparison of trajectories where the nominal control law is applied to subsequent orbits and where the CTM method is employed to update the control law on each successive orbital revolution. Nominal orbit shown in red, all subsequent orbits shown in blue.

The periodicity of the CTM trajectory is once again analysed using Poincaré sections in position (Fig. 4.20a) and velocity (Fig. 4.20b). The orbital elements for the final CTM orbit are shown alongside the GA result in Table 4.6 and show close alignment.

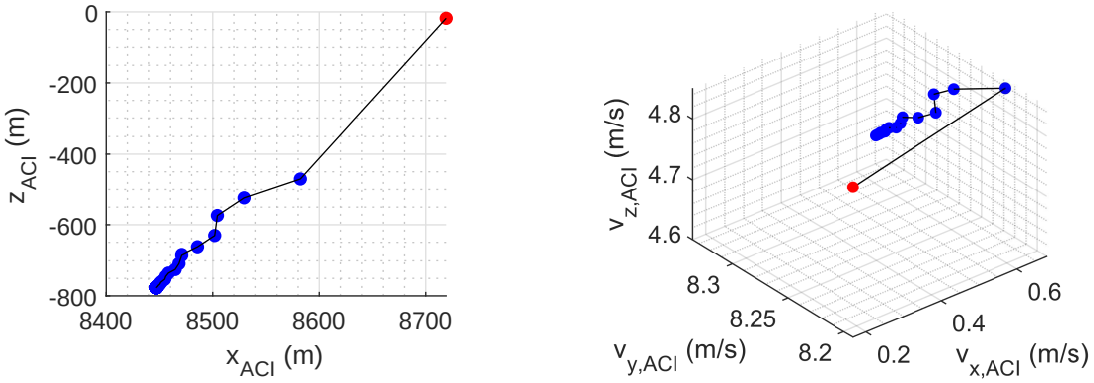

(a) Poincaré section in position.

(b) Poincaré section in velocity.

Figure 4.20: Poincaré sections in both position and velocity for 100 orbits where control has been updated using the CTM. Nominal orbit shown in red with all subsequent orbits in blue and the black line showing progression from nominal to final orbit.

Test Case 4 For the fourth and final test case, the orbit inclination is increased to 60° with the orbital elements for this target orbit, the GA solution and the CTM result shown in table

Table 4.6: Principal orbital elements for the target orbit in test case 3. The nominal orbit is obtained from the GA and the final periodic orbit is obtained by the CTM method of control law updating.

	a (km)	e	i (deg)
Target Orbit	9.80	0.10	30.00
GA Result	9.23	0.08	30.62
CTM Result	8.65	0.03	29.77

4.7. From the result shown in Fig. 4.21, it seems there are no periodic orbits, controllable by the CTM, sufficiently close to the nominal orbit. This presents an interesting question: is there a limit to the inclination of the nominal orbit at which point the CTM is unable to maintain periodicity?

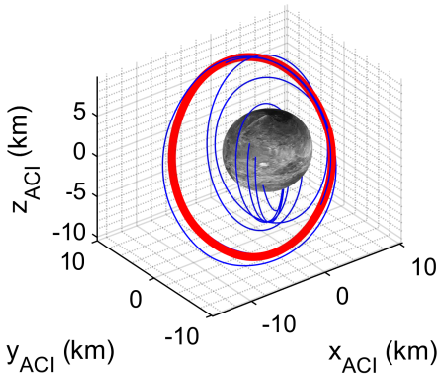

Figure 4.21: CTM method applied over 4 orbital revolutions where GA result stems from initial orbit at $i = 60°$

Table 4.7: Principal orbital elements for the target orbit in test case 4. The nominal orbit is obtained from the GA and the final periodic orbit is obtained through the CTM control law updating.

	a (km)	e	i (deg)
Target Orbit	9.80	0.10	60.00
GA Result	8.84	0.07	63.87
CTM Result	-	-	-

4.3.5 The Limiting Effect of Orbit Inclination

This question of the limitations of the ability of the CTM to converge to a periodic solution as the inclination of the nominal orbit increases will be addressed in this section. As the central body considered here is that of an ellipsoid, it is expected that changes to the initial value of Ω_k would result in a corresponding change to the limit of orbit inclination at which the CTM method can establish a periodic orbit. To analyse where these limits lie, a study is conducted for $i \in [0,90]^\circ$ and $\Omega_k \in [0,90]^\circ$. Only one quarter of the full range of Ω_k is required, given the symmetry of the ellipsoid. It can also be expected that other elements such as semi-major axis or eccentricity would also have an effect. However, this study will look at changes in Ω_k only, with $a = 9.80$ km and $e = 0.10$.

The region in the $[\Omega_k, i]$ space where the CTM converges is labelled the convergent region. The region where the CTM does not converge is labelled the divergent region. Figure 4.22 shows the boundary between the convergent and divergent regions for the CTM method. The convergent region is seen to be quite small and there exist no periodic solutions for either high inclination orbits or those orbits where Ω_k is rotated by a considerable angle.

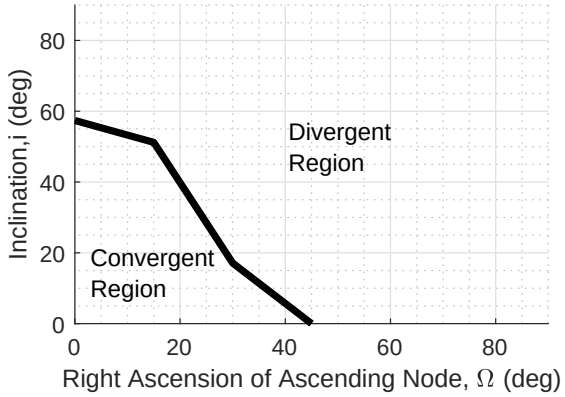

Figure 4.22: Visualisation of the effect of changing Ω_k and i on the convergence of the CTM method. The line represents the boundary at which point the CTM method cannot converge to a nearby periodic solution.

4.3.6 Smoothing the Control Law for Realistic Application

So far in this work, the control laws have been interpolated using a piece-wise constant method. Given the large moments of inertia, a solar sail would not be capable of such instantaneous changes in attitude. To permit application of this work to a real-world sail, it would be preferable to obtain a smooth control law which would be feasible. As such, this section will present control laws interpolated using cubic splines, as described in Ref. [157], where the coefficients are established for the cubic polynomials which make up the interpolating spline.

The resulting nominal orbit obtained from the GA using a smoothed control law is shown in Fig. 4.23.

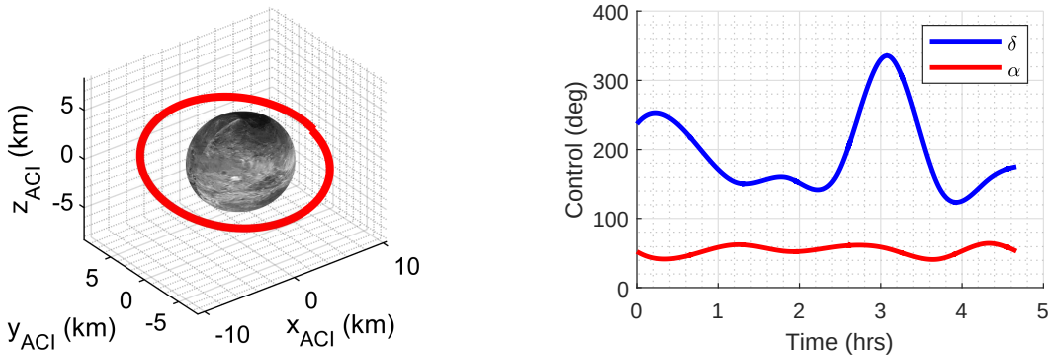

(a) Nominal trajectory from GA using cubic spline interpolated control law

(b) Nominal control law using cubic spline interpolation

Figure 4.23: Nominal trajectory and control law using cubic spline interpolation on control in the GA

Figure 4.24 shows the magnitude of the rigid-body angular velocity, $\dot{\gamma}$, as well as the angular acceleration, $\ddot{\gamma}$, which are required to track the new control law. The angle between any two attitudes is obtained from:

$$\cos(\gamma) = \hat{\mathbf{n}}(t_j) \cdot \hat{\mathbf{n}}(t_{j+1}) \tag{4.15}$$

where $\hat{\mathbf{n}}$ is the unit vector normal to the sail surface, t is the time and j is the indexing variable. Table 4.8 gives the objective function values for the optimal solution obtained from the GA for this nominal orbit.

Table 4.8: Objective function values for the GA nominal orbit and CTM obtained periodic orbit, where cubic splines interpolation method is used.

	$\|\|\mathbf{s}_{\text{ACI}}(t_f) - \mathbf{s}_{\text{ACI}}(t_0)\|\|$	$\Delta\dot{\gamma}$ (deg/s)
GA Nominal Orbit	0.04	0.46
CTM Periodic Orbit	0.01	0.63

After establishing the nominal trajectory and control from the GA, the CTM is again employed to seek a periodic solution over multiple orbits. Once again, the CTM simulation runs for 100 orbits subsequent to the nominal orbit. Figure 4.25 shows the nominal orbit in red and all subsequent orbits controlled by the CTM in blue. The periodicity is verified using the Poincaré sections of Fig. 4.26. In both position and velocity, the CTM can be seen to converge to a periodic solution. The comparison of the control laws obtained from the GA and that of the final CTM orbit are shown in Fig. 4.27.

As for the piece-wise constant control laws, the CTM has again been successful in converging to a periodic orbit for the cubic spline interpolated solution. The smooth attitude transitions

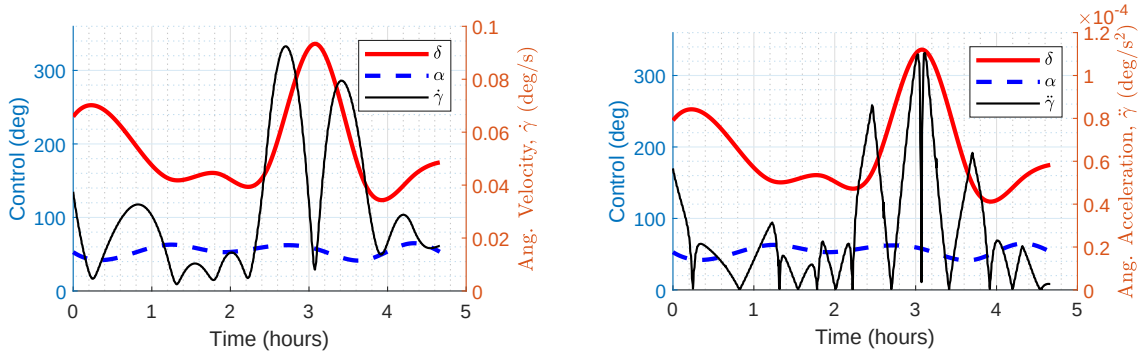

(a) Magnitude of rigid-body angular velocity, $\dot{\gamma}$ *(b) Angular acceleration, $\ddot{\gamma}$*

Figure 4.24: Rigid-body angular velocity, $\dot{\gamma}$, and angular accelerations, $\ddot{\gamma}$, plotted against control history for nominal orbit

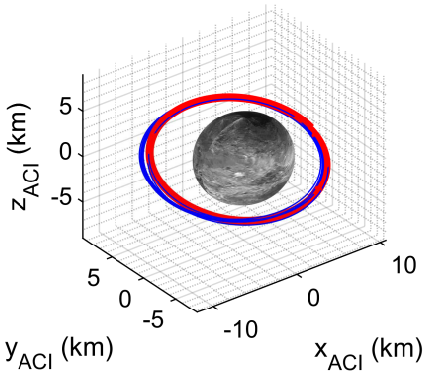

Figure 4.25: Trajectory plot of nominal orbit with spline-interpolated control (red), and subsequent propagation for 100 orbital revolutions with the control law updated at each orbit using the CTM.

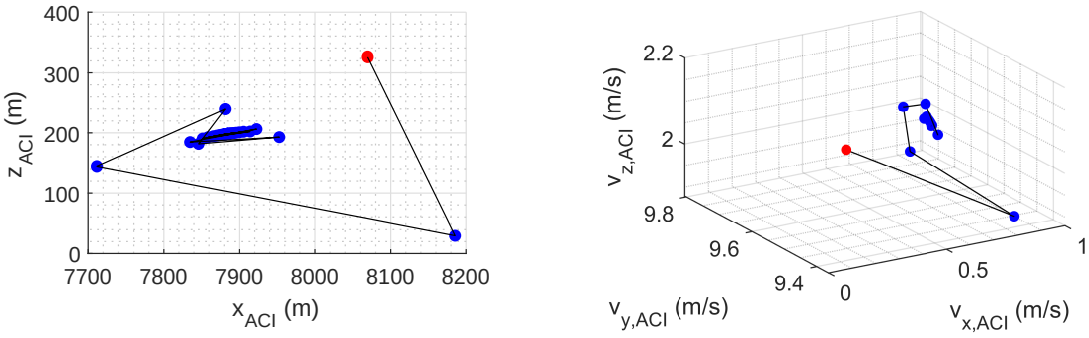

(a) Poincaré section in position *(b) Poincaré section in velocity*

Figure 4.26: Poincaré sections in both position and velocity for 100 orbital revolutions where control has been interpolated using cubic splines and updated using the CTM. Nominal orbit shown in red with all subsequent orbits in blue and the black line showing progression from nominal to final orbit.

obtained by this method of interpolation allow for more realistic slew rates from the sail. Table 4.9 shows the orbital elements of the targeted orbit, the nominal orbit resulting from the GA and

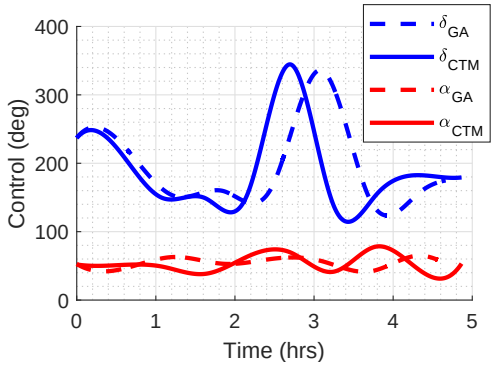

Figure 4.27: Comparison of the control law obtained from the GA and the CTM periodic solution.

the periodic orbit obtained through the CTM.

Table 4.9: Principal orbital elements for target orbit, GA nominal orbit and CTM periodic orbit, using cubic spline interpolation.

	a (km)	e	i (deg)
Target Orbit	9.80	0.10	15.00
GA Result	8.27	0.03	12.89
CTM Result	8.03	0.09	11.73

The time histories for $\dot{\gamma}$ and $\ddot{\gamma}$ are provided in Fig. 4.28 for the CTM periodic orbit with table 4.8 stating the objective function values for the nominal orbit and CTM periodic orbit.

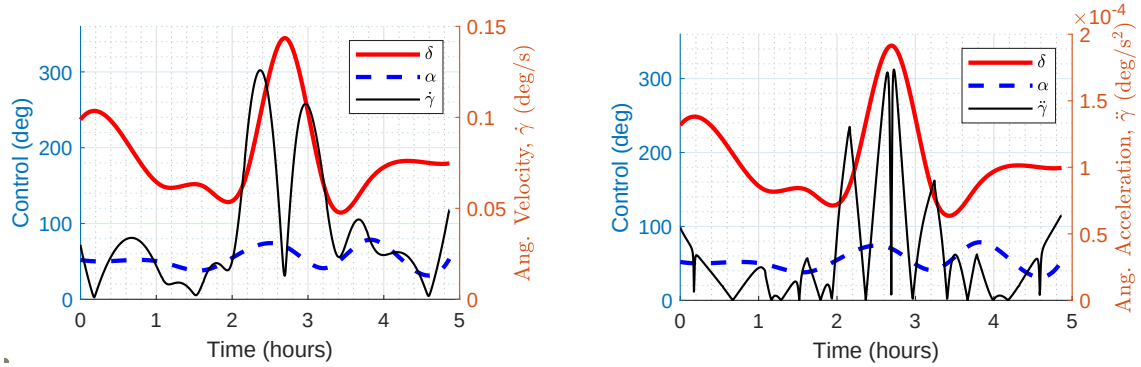

(a) Magnitude of rigid-body angular velocity *(b) Angular Acceleration*

Figure 4.28: Rigid-body angular velocity and angular accelerations plotted against control history for CTM periodic orbit

4.3.7 Torque Analysis

Given the constraints discussed already on the ability of a solar sail to make rapid changes in attitude, it is informative to understand the implications of the proposed control laws on a real-world sail. As such, this section will present the required torques for tracking these control laws.

The sails presented here are considered to be square flat-plates and the spacecraft bus a cube. The principal axes of inertia for a plate with negligible thickness are shown in Fig. 4.29.

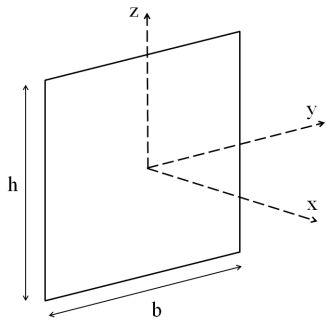

Figure 4.29: Principal axes of inertia for a very thin square plate

So that the most conservative estimate of the torque requirements is taken, the analysis is conducted around one of the principal axes of inertia, where the moments of inertia (MOI) are highest. For a square flat plate ($b = h$), the MOI are highest around the x-axis. However, for the case of a sail these rotations are irrelevant for the sail acceleration. As such, the rotations in this section will be considered around the spacecraft z-axis. As such, and with $b = h$, the moment of inertia for a square flat plate around the principal z-axis are given by:

$$I_{zz} = \frac{1}{12} m_p h_p^2 \tag{4.16}$$

For a cube, with analysis also around the same axis, the MOI is given by:

$$I_{zz} = \frac{1}{6} m_c h_c^2 \tag{4.17}$$

where m_p is the mass of the plate, m_c is the mass of the cube, h_p is the edge length of the plate and h_c is the edge length of the cube. As a simplification of the spacecraft geometry, the centroid of the sail and cube are considered to be coincident such that their principle axes are aligned. Therefore, the total MOI of the spacecraft bus and sail is simply the sum of these components. The torque value is then calculated from $\ddot{\gamma}$

The centroid of the sail and spacecraft bus will be considered coincident and their principal axes aligned, so the total MOI of the spacecraft is the sum of the bus' and the sail's. The torque, ζ, can then be calculated from:

$$\zeta = I\ddot{\gamma} \tag{4.18}$$

Three different classes of spacecraft are presented here, each with different size and mass. The sail characteristic acceleration is maintained in each case at $a_c = 0.2$ mm/s^2. Table 4.10 lists the physical parameters for the sail and bus in each of the three cases. In order to establish the mass of the sail assembly, Ref. [158] states that for a near-term sail, an areal density for

the sail assembly of 10 g/m^2 should be used. For the purposes of scaling the spacecraft bus, a density of 142.4 kg/m^3 is maintained for each of the spacecraft buses. This value was obtained by calculating the bus mass for a sail of 2-m-edge length and with $a_c = 0.2$ mm/s^2, then taking the density required for such a mass in a (10cm)^3 volume.

Table 4.10: Sail and spacecraft bus dimensions, mass and moments of inertia

Sail Edge Length (m)	2	10	20
Sail Area (m^2)	4.00	100.00	400.00
Sail Assembly Mass (kg)	0.10	1.00	4.00
Sail MOI (kg·m^2)	0.01	8.33	133.33
Spacecraft Bus Edge Length (m)	0.1	0.29	0.46
Spacecraft Bus Mass (kg)	0.14	3.56	14.24
Spacecraft Bus MOI (kg·m^2)	2.37×10^{-4}	0.05	0.51

Once again, orbit test case 2, from section 4.3.4, is used as the demonstration orbit here. The nominal orbit torque results are shown in Fig. 4.30 for each of the three sizes of sail. The results for the final CTM controlled orbit for each case are shown in Fig. 4.31.

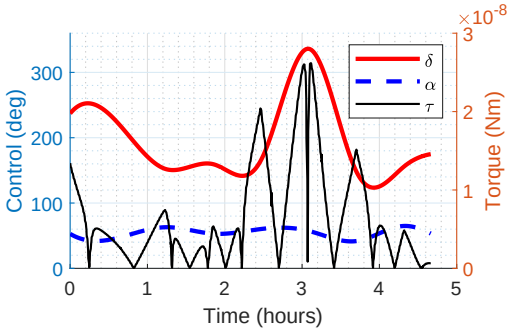

(a) Sail with edge length of 2 m

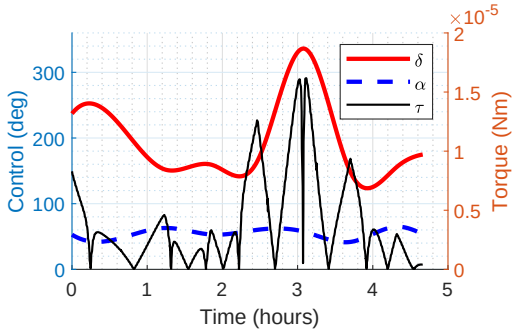

(b) Sail with edge length of 10 m

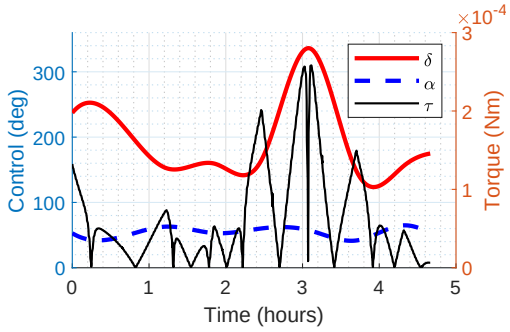

(c) Sail with edge length of 20 m

Figure 4.30: Nominal orbit torque, ζ, shown against control history for square sail

Table 4.11 shows the maximum torques for each case shown in Figs. 4.30 and 4.31. In Ref. [159], the authors discuss the system design of the ADCS for the LightSail-2 mission. The maximum torque established in that work was $\zeta = 0.06$ Nm. Wie *et al* [160] calculated the maximum control torque magnitude to be $\zeta \approx 0.002$ Nm on a sun-pointing ADCS in Earth

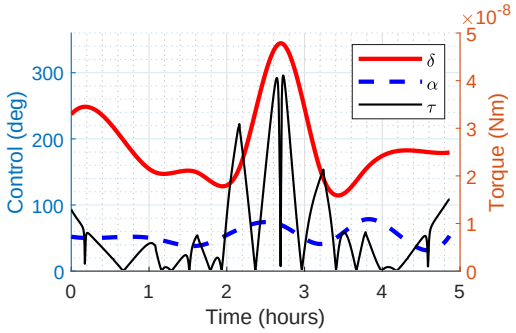

(a) Sail with edge length of 2 m

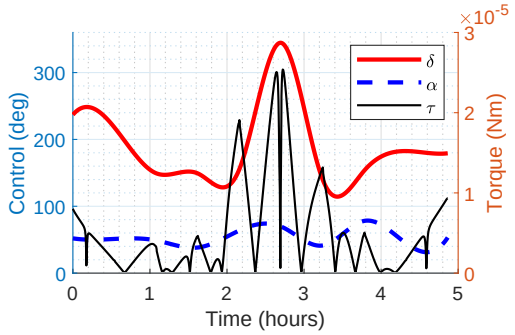

(b) Sail with edge length of 10 m

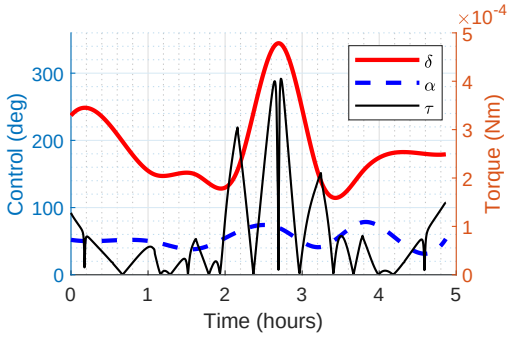

(c) Sail with edge length of 20 m

Figure 4.31: Attitude torque ζ on CTM-controlled orbit, shown against control history for square sails with side lengths of 2 m, 10 m and 20 m.

orbit. As such, the maximum torques presented here would appear feasible for a real-world sail in the context of the works contained in the literature.

Table 4.11: Maximum Torque Values

Sail Edge Length (m)	2	10	20
Nominal Orbit (Nm)	2.62×10^{-8}	1.62×10^{-5}	2.58×10^{-4}
CTM Orbit (Nm)	4.11×10^{-8}	2.54×10^{-5}	4.05×10^{-4}

Chapter 5

Deployment of Small Probes and Large Landers from a Solar Sail

In this chapter, work will be presented on the deployment of small probes and larger landers from a spacecraft where a solar sail is the primary propulsion system. In particular, the small probes will be the "ChipSat" class of probe [161]; small printed circuit boards (PCBs) which contain sufficient peripherals to conduct scientific missions. The larger lander will be based on the MASCOT lander [162] which was employed on the successful Hayabusa2 mission [2].

There are two dynamical models and three shape models used for the motion of the particle (this term generalises where the discussion may involve either the sailcraft or the lander/probe) around the asteroid used in this work, and each is applied depending on the distance at which the particle will operate with respect to the asteroid, and the corresponding dynamical regime (which are defined in Chapter 2 and analysed in detail in Chapter 3) in which it finds itself. Table 2.2 defines the radius at which each regime is applied as well as the corresponding dynamical models, shape models and reference frames.

The first section describes in more detail the choice of probe and lander. The second section describes the target asteroids and their shape models. Following this, the first mission scenario of the deployment of a MASCOT-type lander in the inner regime is investigated in detail where the landing conditions are presented for several scenarios, followed by the control of the sail after deployment. Following this, the landing conditions for the MASCOT-type lander in the second mission scenario are studied, where the lander is deployed from the outer regime. Finally, an alternative mission scenario is presented in which a series of small ChipSat probes are deployed from the outer regime, where again the landing conditions are presented before the control of the sail during this deployment. In this chapter, some of the deployments ae made with zero-velocity. It should be noted that this zero-velocity condition is relative to the reference frame in use, and which is defined in each section.

5.1 Choice of Probe and Lander

The MASCOT ("Mobile Asteroid Surface SCOuT") lander, developed by DLR with close cooperation from CNES and JAXA, is a science platform which was successfully deployed as part of the JAXA Hayabusa2 mission to the surface of asteroid Ryugu [162]. The physical parameters for the MASCOT lander and sailcraft bus are in Table. 5.1.

Table 5.1: Physical parameters of the MASCOT lander [2] and a 12U CubeSat bus [3]

	MASCOT	12U CubeSat
Mass	13 kg	24 kg
Length	28 cm	23 cm
Depth	29 cm	24 cm
Height	21 cm	36 cm

The ChipSat is a small-scale probe which is contained on a printed circuit board (PCB) and which can contain inertial measurement units, attitude determination and control systems and wireless radio frequency communications [161]. Due to its high area-to-mass ratio, the ChipSat is also able to produce thrust from SRP [163, 164]. Due to their small size and mass, these probes are very appealing to solar sail missions, allowing the storage of several on-board without compromising the overall area-to-mass ratio of the sailcraft to a great extent. The physical parameters for the ChipSats and sailcraft bus are contained in Table 5.2

Table 5.2: Physical parameters of the ChipSats and a 12U CubeSat

Parameter	Value
Bus Mass	24 kg
ChipSat Mass	10 g
ChipSat Dimensions	35×35 mm [161]
ChipSat Storage Allocation	3U
Number of ChipSats	20

5.2 Target Asteroids and Their Shape Models

As discussed in Chapter 2, when the spacecraft is outwith a radius approximately five times the mean asteroid radius, the shape of the body is no longer important in terms of the gravitational field. As such, at these distances the asteroid can be modelled as a point mass. However, within these distances the shape must be accounted for. It was also shown in Chapter 2 that the shape of the gravity field very quickly becomes elliptical for elongated bodies. As such, to improve computation times, a simpler ellipsoidal model can be employed. However, as the spacecraft, or probe/lander, approaches the surface, it becomes necessary to account for the true shape of the asteroid. It is here that the high resolution polyhedron models can be employed to great effect.

During the descent of a probe or lander, it is anticipated that it will pass through each of these regions, and so it becomes necessary to define a target asteroid which has the available models. As such, real-world examples must be chosen. In this chapter, the asteroids 4769 Castalia and 4 Vesta are used.

Given the limitations of a relatively powerful sail in the weak gravity field of an asteroid, as discussed in Chapter 2, a larger body allowed the analysis to be conducted where the relative strength of the force from SRP would not cause any issue in the proximity operations. To avoid any potential issues where the asteroid gravitational field may be too weak relative to the sail acceleration to allow bound motion, a larger body was included in this work. The asteroid Vesta met the conditions of size and availability of high resolution model.

For the ellipsoidal models, 4769 Castalia has dimensions of $a_e = 0.80$ km, $b_e = 0.50$ km and $c_e = 0.35$ km [144] and Vesta has ellipsoidal dimensions of $a_e = 286.30$ km, $b_e = 278.60$ km and $c_e = 223.20$ km [165]. The polyhedron model for Castalia was obtained by radar imaging from the Arecibo observatory in August 1989 [166], where the polyhedron model for Vesta was derived from data obtained from in-situ measurements by the Dawn spacecraft [62].

In order that the maximum acceleration available from the sail is maintained and remains constant, the orbit radius of each asteroid is placed at 1 AU in a circular orbit. At this distance, the maximum available acceleration from the sail is the characteristic acceleration, a_c. An eccentric asteroid orbit would simply result in a varying magnitude of sail acceleration. The choice of Castalia and Vesta is made purely for the physical parameters and available high resolution polyhedron shape models of those bodies and not out of interest in a mission specific to either.

5.3 Deployment of a Lander in the Inner Regime

In this section, the deployment of a MASCOT-type lander in the inner regime (as discussed in detail in Chapter 3) is investigated. Given the proximity of the deployment location to the asteroid, it is necessary to account for the true shape of the body. As such, a two-body dynamical model is employed with a polyhedron shape model. The asteroid 4769 Castalia is used first when investigating the landing conditions for the MASCOT lander with a zero-velocity deployment in Section 5.3.2. Following this, it is established that the deployment locations proposed in the vicinity of Castalia would not be feasible for the solar sail. Given the very weak gravity field and the difficulty in maintaining bound motion for a sail with $a_c = 0.2$ mm/s^2, the asteroid used in Section 5.3.3 is 4 Vesta.

5.3.1 Changing Dynamics at the Point of Lander Separation

The proposed sailcraft for this work will carry a lander similar to MASCOT. The lander will be carried by a 12U cubesat with standard parameters [3], which are shown in Table 5.1. The

selection of the 12U model allows for sufficient capacity for storage of the sail as well as the required payloads for relaying the data from the MASCOT lander and surveying the asteroid.

Calculation of the required area of the sail for a given value of a_c is calculated by way of Eq. 2.13. The total sailcraft mass is a combination of the bus mass (m_{bus}) of the 12 U CubeSat, listed in Table 5.1, and the sail mass. The sail mass is dependant on the area of the sail and is given by $m_s = A\rho_A$, where the areal density of the sail structure and materials is taken as $\rho_A = 10$ g/m^2 [149]. With this, Newton's method is used to calculate the required sail area for the stated value of a_c to achieve a minimal value for the objective function, which is given by:

$$J = 2P_{SRP}\eta_r A - a_c(m_s + m_{bus}) \tag{5.1}$$

where $P_{SRP} = 4.56 \times 10^{-6}$ N/m^2 is the magnitude of the SRP at 1 AU [11] and for the ideal sail considered here, $\eta_r = 1$. With this, the physical parameters for the sail and bus are listed in Table 5.3.

Table 5.3: Physical parameters of sail and spacecraft

Spacecraft bus mass	24 kg
MASCOT lander mass	13 kg
Sail mass	10.39 kg
Sail areal density (ρ_A)	10 g/m^2
Sail Area	1039.30 m^2
Square sail side length	32.24 m

Upon release of the lander, the sail performance changes instantaneously, given the new area-to-mass ratio. Table 5.4 shows the pre- and post-separation performance values for the sail. With this changing performance, there is also an instantaneous change in the dynamics of the system. Figure 5.1 shows the changing geometry of the ZVCs in the potential field of Castalia. The two circles represent the only AEP at these levels of a_c. The small blue circle is the AEP for the lower performance, the larger red circle for the higher performance.

Table 5.4: Pre- and post-separation parameters for sail and carrier spacecraft combination

	Pre-separation	Post-separation
Total mass	47.39 kg	34.39 kg
Sail Area	1039.30 m^2	1039.30 m^2
a_c	0.20 mm/s^2	0.28 mm/s^2

The change in dynamics brought about by the changing performance of the sail is considerable. As described in Chapter 2, the ZVCs are boundaries to the motion of a spacecraft at a constant value of C. If a spacecraft wishes to transfer from one region to another, where there is a ZVC restricting just such a transfer, then the spacecraft must perform a propulsive manoeuvre to change the value of C, and accordingly the geometry of the ZVCs in such a way as to facilitate

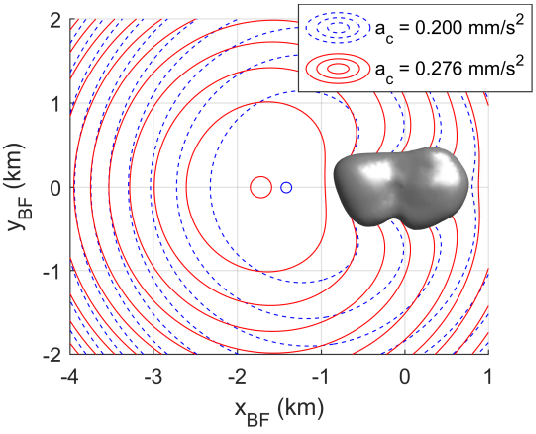

Figure 5.1: Changing geometry of the Zero Velocity Curves for $a_c = 0.20$ mm/s^2 and $a_c = 0.28$ mm/s^2, with $\alpha = \delta = 0°$. The two circles represent the only AEP at these levels of a_c. The smaller blue circle is the AEP for the lower performance, the larger red circle for the higher performance.

this transfer. In Fig. 5.1, there was direct access to the surface from the AEP at $a_c = 0.20$ mm/s^2, this is not the case for $a_c = 0.28$ mm/s^2 as there is now a ZVC blocking the way. An example of the implications of a particle enclosed by ZVCs, and moving ballistically, is shown in Fig. 3.11a.

5.3.2 Analysis of Trajectories of Ballistic Landers with Zero-Velocity at Deployment to 4769 Castalia

The aim of this section is to establish a reliable strategy for the successful deployment of a lander to the surface of the asteroid. In order to do so, a deployment region is sought where the ballistic trajectory will have the best chance of a successful descent. The trajectories presented in this section will be for landers which are released with zero velocity. Once the lander is released from the sail, it no longer experiences the same constant acceleration from SRP and so its dynamics revert to the natural dynamics of the asteroid potential field and this facilitates separation from the sailcraft.

The work here builds on the analysis of the potential field in the inner regime of Chapter 3, where the deployment locations are based around the potential ridge line. Initially, a single zero-velocity deployment is made from each of the four equilibrium points of the inner regime. Following this, there will be three deployment regions which are analysed using a Monte Carlo approach. For this, a uniform random distribution of initial points within the desired deployment region is used. The first deployment region will be deployment from the potential ridge line itself, the second will be the region that lies between the potential ridge line and the asteroid surface and the third region will be the region exterior to the potential ridge line. The results detail the landing velocity, v_L, and the time of flight, TOF. The importance of presenting the

landing velocity is to give some measure of the likelihood of the lander remaining on the surface after touchdown. An excessive landing velocity, and any subsequent bouncing, could lead to the lander escaping the weak gravity field of the asteroid. The escape velocity of 4769 Castalia, calculated here for a point near the surface, is approximately $v_{esc} = 0.52$ m/s [167]. As such, any landing with a velocity above this value could potentially bounce after impact and escape the weak gravitational field. Any trajectory in this section which intersects the surface of the asteroid will be considered a successful landing.

Where the Monte Carlo approach is taken, a large number of uniformly distributed random initial points are selected in each of the three deployment regions. The number of points used was determined by those points interior to the ridge line. Here, 5000 random points were established, but only those external to the asteroid surface were maintained as the only feasible options. The number of points maintained was 1327. As such, this is the number of deployment points considered in this region. For the other regions, other than the deployment from the equilibrium points where only one deployment was made from each point, a total of 1326 uniformly distributed random points were used.

Deployment from Equilibrium Points

As the equilibrium points around asteroid Castalia are unstable, the landers which begin with zero-velocity, will eventually drift from the equilibrium points. Figure 5.2 shows the deployment trajectories from each of the four inner regime equilibrium points at Castalia.

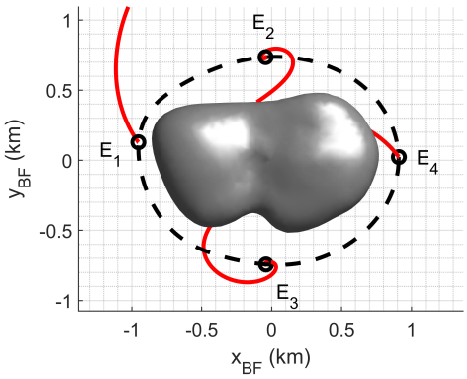

Figure 5.2: Deployment of lander with zero initial velocity from natural equilibrium points

All but one of the deployments eventually intersects the surface of the asteroid. Deployment from E_1 quickly drifts from the equilibrium point into the region exterior to the potential ridge line and eventually escapes the asteroid gravity field. From E_4, the lander drifts into the region interior to the potential ridge line and intersects the asteroid surface. Deployment from points E_2 and E_3 take considerably longer to drift from the equilibrium points. Initially they drift into the region exterior to the potential ridge line, though retrograde to the asteroids rotation, after

which the lander is pulled back across the potential ridge and put on an impact trajectory. Table 5.5 shows v_L and TOF for each trajectory which reaches the asteroid surface.

Table 5.5: Landing velocities and time of flight for trajectories from zero velocity deployment

	E_1	E_2	E_3	E_4
v_L (m/s)	-	0.25	0.22	0.14
TOF (h)	-	8.84	7.01	4.50

Deployment from the Potential Ridge Line

In this section, 1326 simulations of lander trajectories deployed from the potential ridge line are presented. Deployment from any point along the potential ridge line, with zero initial velocity, brings a 53.77% success rate. Figure 5.3 shows the results from analysis for 1326 points uniformly spaced along the ridge line. The results show the trajectory of each lander, the landing velocity compared with the time of flight, the range of v_L and TOF values along the successful deployment region of the potential ridge line and the locations where deployment does not result in a successful landing.

This shows two distinct regions, with some symmetry, where successful deployment to the surface is indeed possible. The time of flight from this region is still mostly short, with the landing velocities still within an acceptable range. The maximum TOF values are concentrated around the equilibrium points, where the zero-velocity initial condition would result in a slower escape from this point, given its nature as an equilibrium point. The region around the equilibrium points also result in the highest values for v_L.

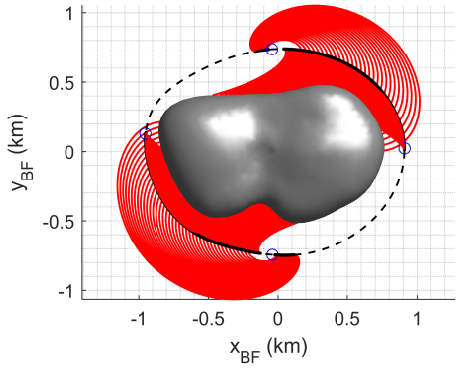

(a) All trajectories which intersect the surface of the asteroid.

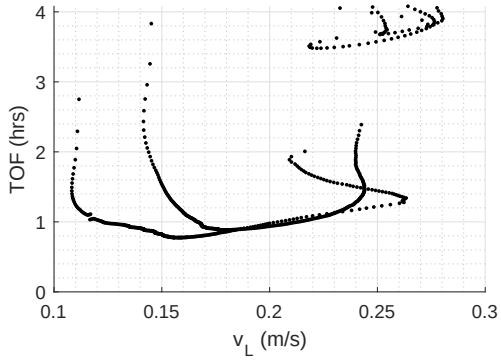

(b) Landing velocity, v_L, and the time of flight, TOF.

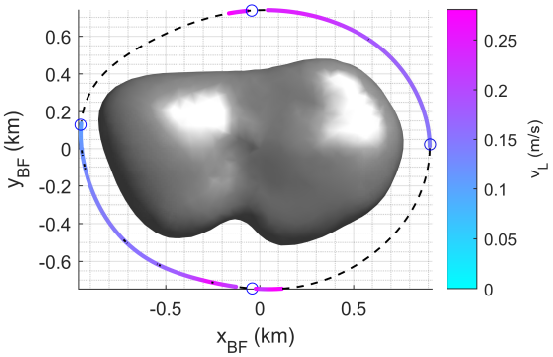

(c) Landing velocity for each deployment location

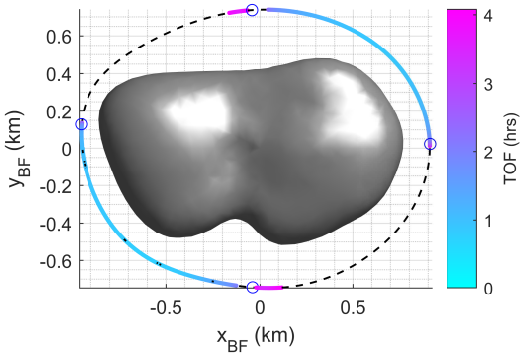

(d) TOF for each deployment location

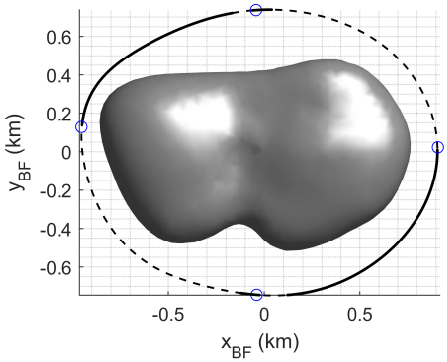

(e) Location of points from which zero velocity release results in escaping trajectory

Figure 5.3: Monte Carlo analysis of success rates for deployment from the potential ridge line.

Deployment Internal to the Ridge Line

It is intuitive to assume that the most successful region for deployment of the lander would be the region interior to the potential ridge line, and this is indeed the case. Figure 5.4 shows the analysis of trajectories from 1327 deployments in this region. The rate of successful deployment to the surface in this region is 92.01%.

The landing velocities remain within the same range as those for trajectories from the ridge

line, though the TOFs are generally, as expected, lower. When the region of unsuccessful trajectories is examined, once again there are two distinct regions, mirrored on the opposite sides of the asteroid, and are in the same area as the unsuccessful ridge line trajectories.

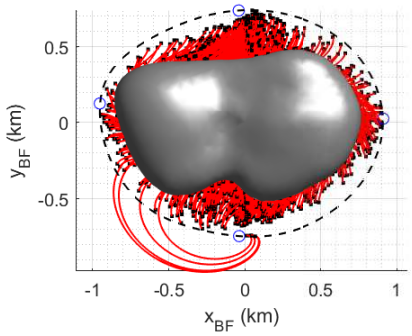

(a) All trajectories which intersect the surface of the asteroid.

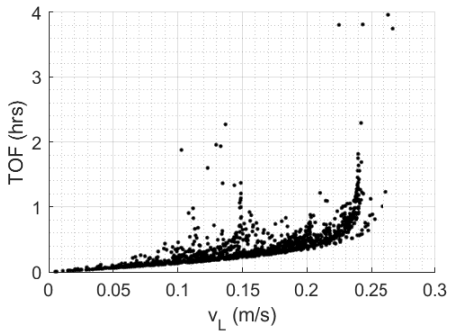

(b) Landing velocity, v_L, and the time of flight, TOF.

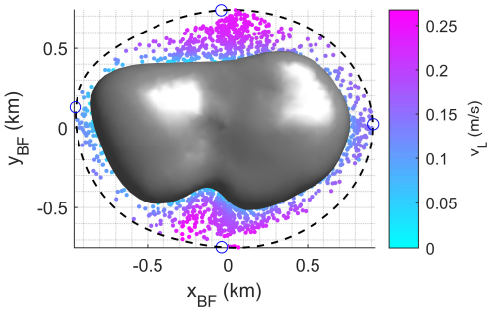

(c) Landing velocity for each deployment location

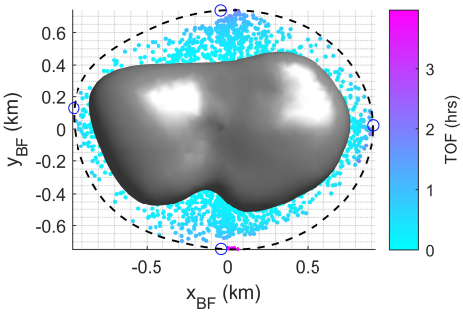

(d) TOF for each deployment location

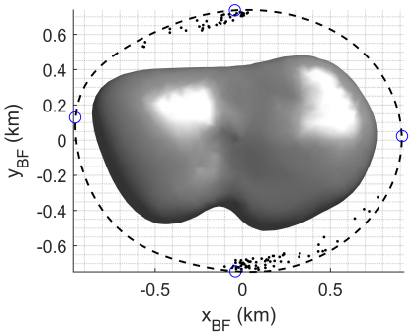

(e) Location of points from which zero velocity release results in escaping trajectory

Figure 5.4: Monte Carlo analysis of success rates for deployment from the interior region to the ridge line.

As with the results for those deployments made from the ridge line, the highest TOF and v_L values are for those deployments made in the region close to the equilibrium point. For v_L, this is intuitive in the sense that the equilibrium points are contained on the boundary of the region. As such, the trajectory has the furthest to travel to reach the surface. This also explains why those deployments around E_2 and E_3 result in higher velocity landings than E_1 and E_4.

Deployment External to the Ridge Line

When the spacecraft is in the region external to the ridge line, the lander has an added challenge in reaching the asteroid surface in that it must get across the potential ridge line, from zero-velocity relative to the asteroid surface, and into the region interior to the ridge line.

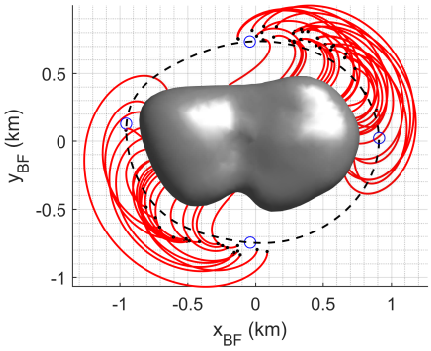

(a) All trajectories which intersect the surface of the asteroid.

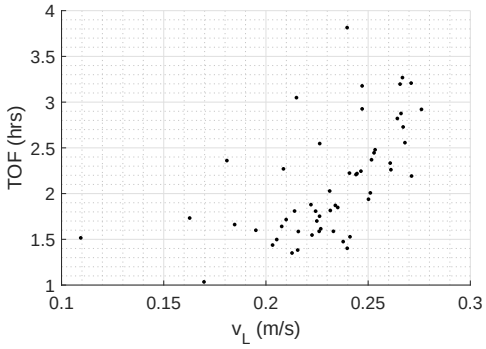

(b) Landing velocity, v_L, and the time of flight, TOF.

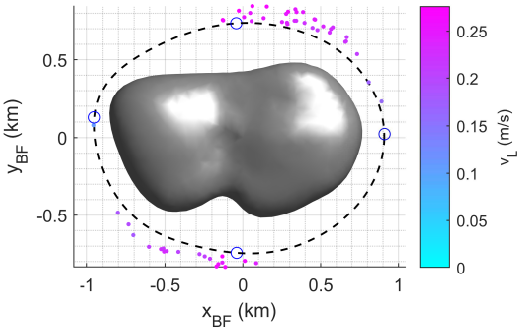

(c) Landing velocity for each deployment location

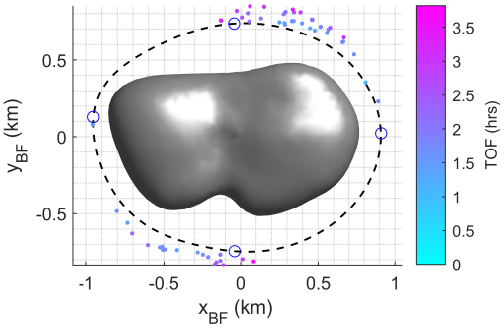

(d) TOF for each deployment location

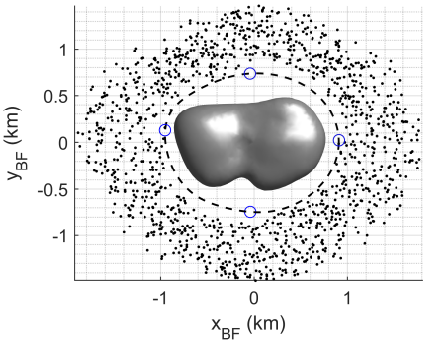

(e) Location of points from which zero-velocity release results in escaping trajectories

Figure 5.5: Monte Carlo analysis of success rates for deployment from the exterior to the potential ridge line.

Figure 5.5 shows the analysis of deployment from this region. This simulation contains 1326 randomly chosen distinct points which lie between the ridge line and another line which follows the ridge line but at twice the distance from the asteroid centre. As is expected, the vast majority

of ballistic deployments in this region do not reach the surface, with only a 4.15% success rate. However, there are two regions close to the ridge line which do offer the potential for descent to the surface. These regions are separated symmetrically as with those of the previous regions, and they are in the same area as the successful ridge line trajectories. It is interesting to note that the trajectories with the highest v_L and TOF are still those nearest points E_2 and E_3.

5.3.3 Deployment from a Low Altitude Orbit at 4 Vesta

Given that the deployment locations in Section 5.3.2 would be impossible for a solar sail to maintain a hover, this section will investigate the deployment from a low altitude orbit. As described previously, the target asteroid here is changed to the larger Vesta such that concerns related to the feasibility of bound motion for a sail of $a_c = 0.2$ mm/s^2 are alleviated.

First, the pre-deployment orbit is established. The strategy for deployment is to release the lander upon completion of the nominal orbit; that is, where the spacecraft reaches the final time-point along the pre-defined nominal orbit, established by the GA. After this, the conditions for the lander upon intersection with the surface of the asteroid are described. Finally, the sail control post-separation is discussed. This is the focus of the work in this section and it is shown that a strategy is required to maintain the sail close to the original orbit due to the instantaneous change in dynamics (discussed in Section 5.3.1) that occurs at the point of lander separation. The method employed here is the Time-Delay Feedback Control (TDFC) described in Chapter 2. As the sail will not approach the asteroid surface, the ellipsoidal shape model is used. When studying the lander trajectory, the polyhedron shape model is employed.

Pre-deployment Orbit Control

First, it is necessary to define the orbit from which the lander will be deployed. Calculation of the nominal, pre-deployment, orbit of the solar sail is achieved using a GA as described in Chapter 2. The objective function for this optimisation is:

$$J = ||\mathbf{s}(t_f) - \mathbf{s}(t_0)|| \tag{5.2}$$

and the solution vector consists of the initial state, final time and the control required to achieve the periodic solution. This control is discretised in equally spaced time and interpolated using cubic splines. Two deployment orbits are established using this method: a lower inclination solution (orbit 1) sought by restricting the search for the initial state to a small region of the phase space near the equatorial region, and a higher inclination solution (orbit 2) is facilitated by relaxing the constraint on this phase space search. Table 5.6 gives the semi-major axis and inclination of the solutions.

Allowing the GA to select the initial conditions in this way allowed for a solution with the smallest possible objective function value, rather than targeting a specific orbit which resulted in

Table 5.6: Semi-major axis and inclination of periodic solutions found by GA

Orbit	a (km)	i (deg)
1	390.81	1.82
2	390.31	14.34

larger objective function values. As the deployment strategy is to release the lander at the final point of this nominal orbit, if these large errors remained then the sail control would not only have to deal with the instantaneous change in sail acceleration due to lander deployment, but also an existing large error in the state at this point. Figures 5.6 and 5.7 show orbits 1 and 2 and their control laws. The trajectories are first presented in the BF frame, in which they were established by the GA. They are then presented in the ACI frame, where the orbital elements calculated and presented in Table 5.6. The control law shown for each orbit describes the required steering for each of the nominal pre-deployment orbits in terms of α and δ.

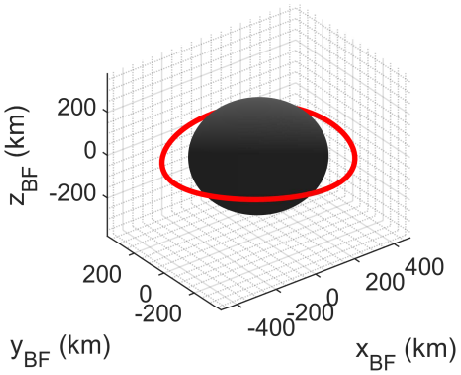

(a) BF frame

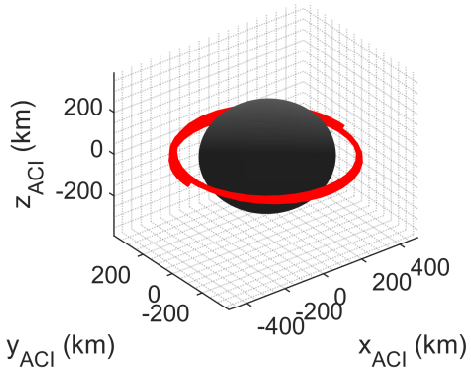

(b) ACI frame

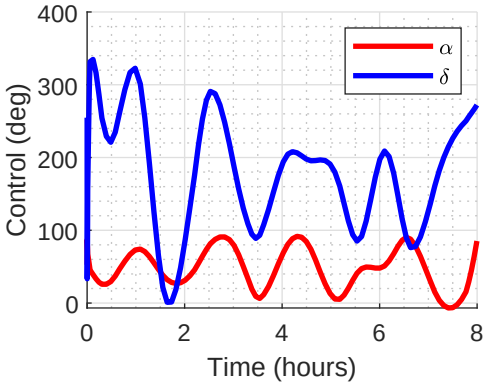

(c) Control

Figure 5.6: Deployment orbit 1

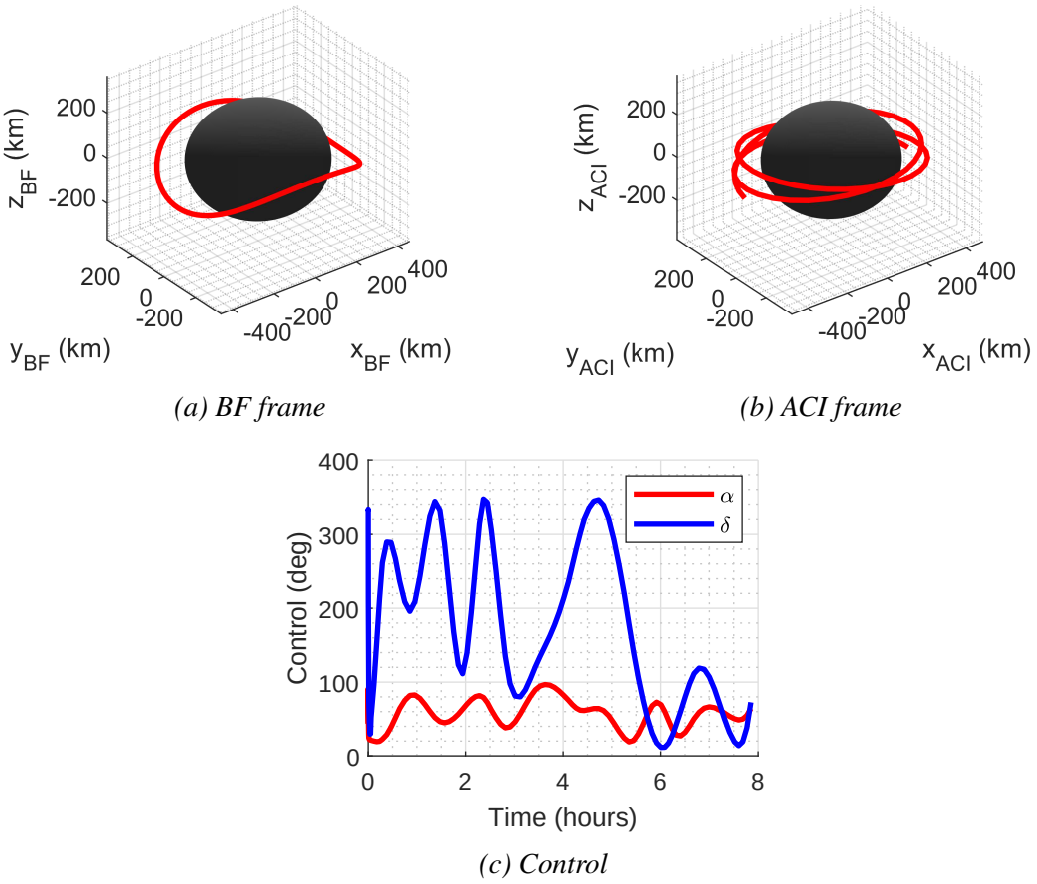

(a) BF frame

(b) ACI frame

(c) Control

Figure 5.7: Deployment orbit 2

Impact Conditions for the MASCOT-Type Lander

Using the deployment orbits obtained in the Section 5.3.3, the landing conditions are now obtained for the MASCOT-type lander. The ballistic descent trajectories are shown in Figs. 5.8 and 5.9 for deployment orbits 1 and 2 respectively. As the landers are now approaching the surface of the asteroid, the polyhedron shape model for Vesta is applied to ensure accurate dynamics very close to, and on, the surface. The numerical values for the landing conditions are given in Table 5.7. It should be emphasised here that the impact conditions were not an objective of this work and are simply presented here for completeness. To facilitate separation from the sailcraft, and to inject the lander on an impact trajectory, it is envisaged that the sailcraft will impart a small impulse (of magnitude 5 m/s) on the lander at deployment. The effect that imparting this impulse on the lander will have on the sailcraft is not considered here. Only the changing sail performance is analysed.

From deployment orbit 1, the lander makes a number of close approaches to the surface before the final impact. In the inertial frame, the trajectory describes an orbit under perturbation from a non-spherical body, with rotation of the apse line, until the approach to periapsis bring the lander into contact with the surface. The lander trajectory from deployment orbit 2 shows the

same behaviour but the time to impact is extended given the higher inclination initial condition.

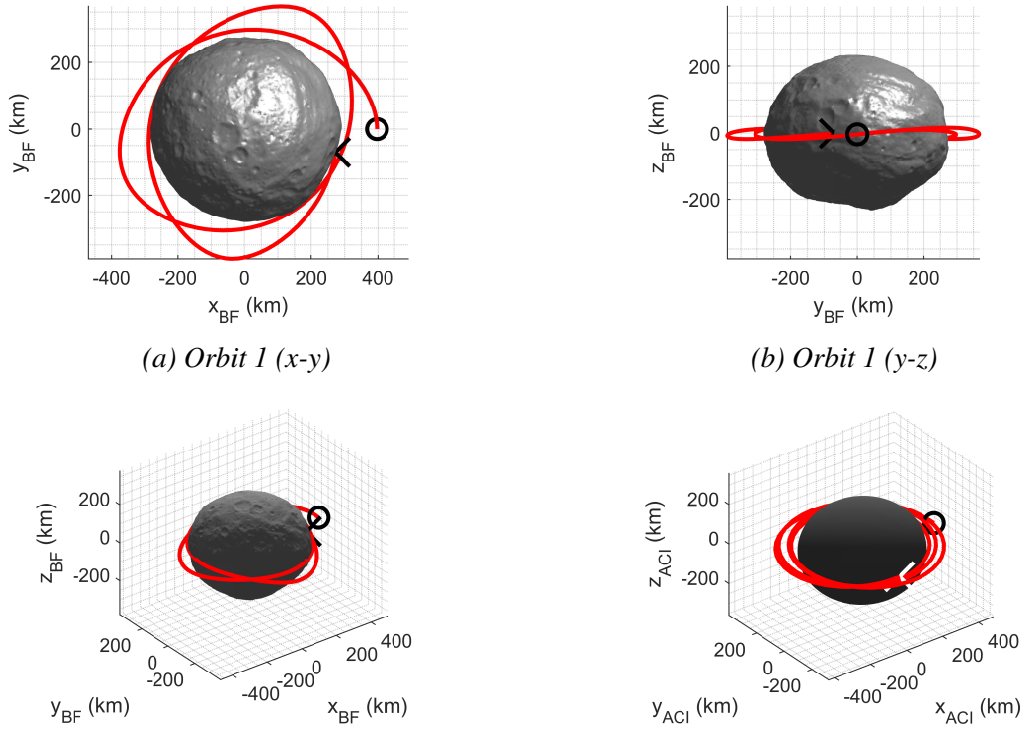

(a) Orbit 1 (x-y)

(b) Orbit 1 (y-z)

(c) Orbit 1 (BF frame)

(d) Orbit 1 (ACI frame)

Figure 5.8: Landing trajectories for deployment from orbit 1

Table 5.7: Impact conditions for MASCOT-type lander

	Orbit 1	Orbit 2
Deployment Δv	[0, -5, 0] m/s	[0, -5, 0] m/s
Impact Velocity	190.03 m/s	190.86 m/s
Impact Latitude	-0.25°	-1.22°
Impact Longitude	-14.37°	179.46°
Time to Impact	9.53 hours	12.63 hours

Post-deployment Orbit Control

When the sailcraft reaches the final point of the nominal orbit, the lander is released, resulting in an instantaneous increase in a_c. Again, the reaction on the sailcraft due to the lander deployment is not considered here. In order to control the sail such that it converges to a periodic orbit, TDFC is applied. This method is chosen as a proven method of stabilising an unstable periodic orbit [86].

For the TDFC, the matrices **Q** and **R** will be weighted such that the solution favours periodicity over control effort. In order to analyse the convergence of the method, a section of the

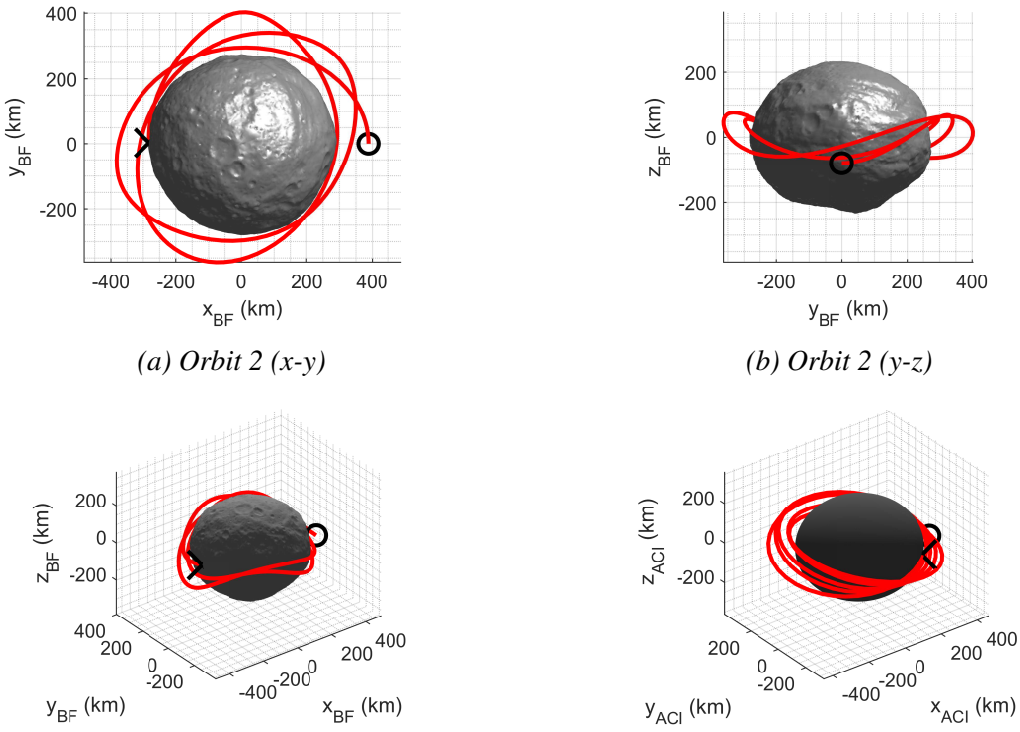

(a) Orbit 2 (x-y)

(b) Orbit 2 (y-z)

(c) Orbit 2 (BF frame)

(d) Orbit 2 (ACI frame)

Figure 5.9: Landing trajectories for deployment from orbit 2

phase space in the *x*-*z* plane will be taken which shows the location where the trajectory intersects that plane on each orbit. For an orbit to be periodic, the final state must converge to the same point in the state space as the initial state [130]. However, for the purposes of illustration, only the positional convergence is shown in the *x*-*z* plane in subsequent figures.

Figure 5.10 shows the results for correction applied to the orbit by the TDFC after deployment from pre-deployment orbit 1. The Poincaré sections in Fig. 5.10 show that the orbit converges in the inertial frame to a near-equatorial orbit.

The trajectories in the BF and ACI frames, along with the sections in the *x*-*z* position space, for orbit 2 are shown in Fig. 5.11. Here, the results similarly appear to converge to a planar orbit. However, as the initial orbit is of a higher inclination, it takes considerably longer to do so. This convergence towards a stable periodic orbit is a feature of the TDFC. As it does not attempt to follow a reference trajectory, the method will tend towards the nearest periodic solution.

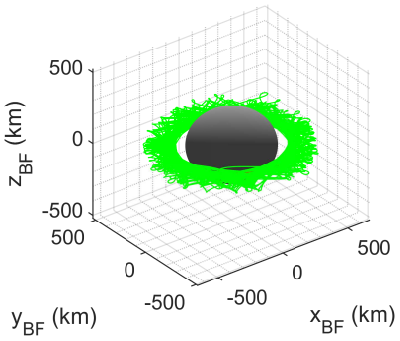

(a) Trajectory (BF frame)

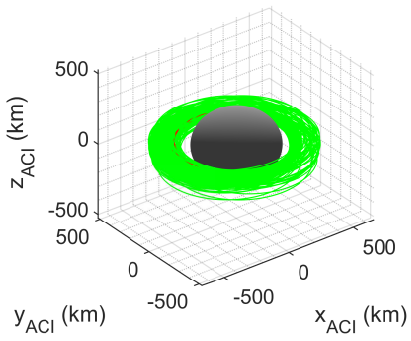

(b) Trajectory (ACI frame)

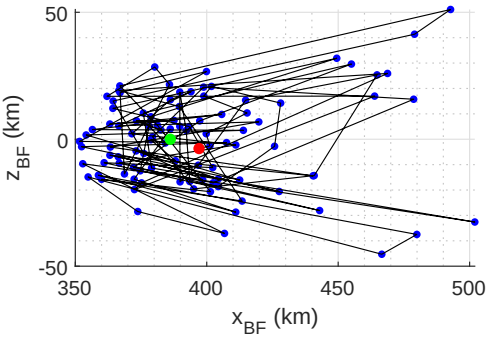

(c) Poincaré Section (BF frame). Red points are the initial intersection with the Poincaré section, where green points are the final intersection.

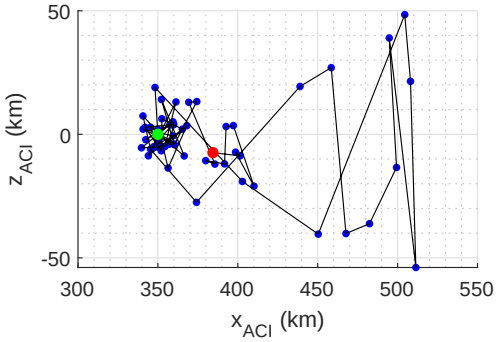

(d) Poincaré Section (ACI frame). Red points are the initial intersection with the Poincaré section, where green points are the final intersection.

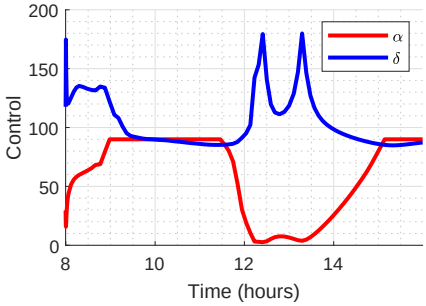

(e) Control during first TDFC orbit

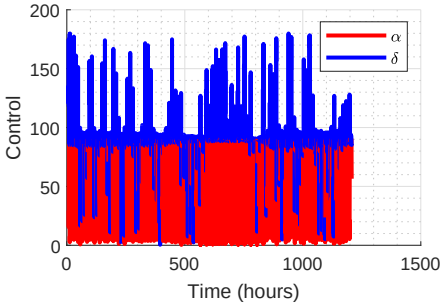

(f) Full Control History

Figure 5.10: Post-deployment trajectory and control of the sail using TDFC method after deployment from orbit 1.

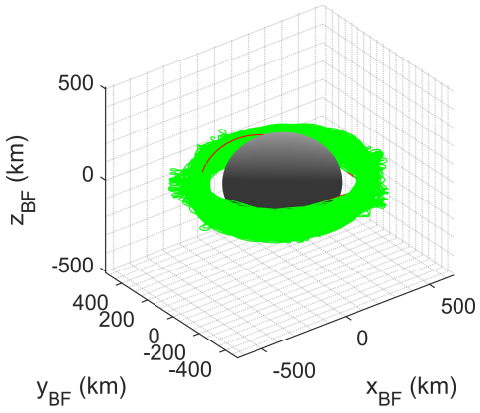

(a) Trajectory (BF frame)

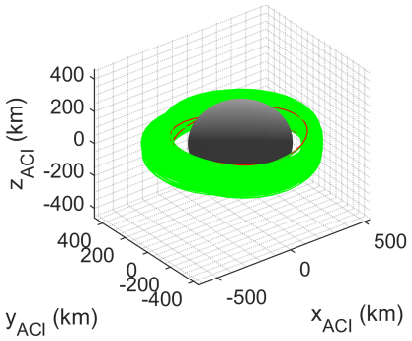

(b) Trajectory (ACI frame)

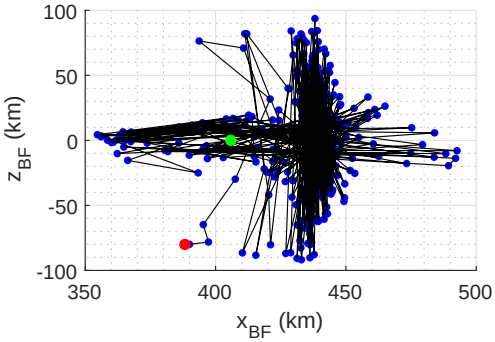

(c) Poincaré Section (BF frame). Red points are the initial intersection with the Poincaré section, where green points are the final intersection.

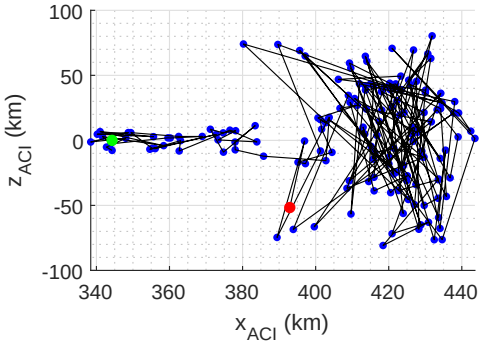

(d) Poincaré Section (ACI frame). Red points are the initial intersection with the Poincaré section, where green points are the final intersection.

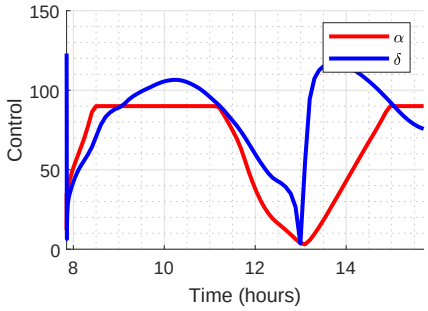

(e) Control during first TDFC orbit

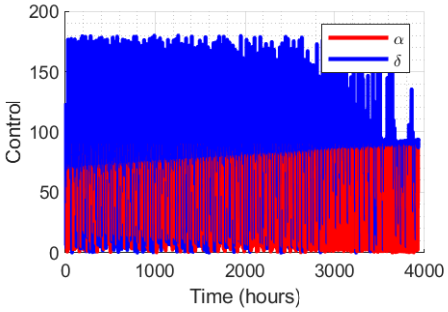

(f) Full Control History

Figure 5.11: Post-deployment trajectory and control of the sail using TDFC method after deployment from orbit 2.

5.4 Deployment of a Lander in the Outer Regime

In this section, the zero-velocity deployment of a MASCOT-type lander from equilibrium points in the outer regime, in the SYN frame, is investigated. It is assumed that the sail begins at one of the AEPs described in Chapter 3 and deploys the lander with zero velocity. Once again, to ensure feasible operations for a sail of $a_c = 0.2$ mm/s^2, the asteroid Vesta is used here. Figure 5.12c shows the surface which contains all AEPs for a sail of $a_c = 0.2$ mm/s^2, where Figs. 5.12a and 5.12b show the effective gravitational and sail accelerations with the residual difference between each.

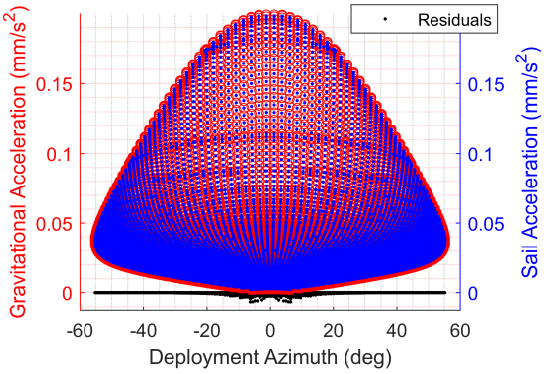

(a) Deployment Azimuth

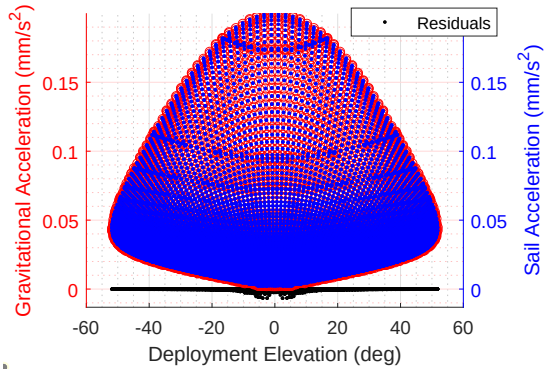

(b) Deployment Elevation

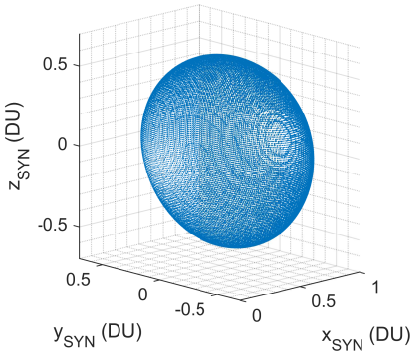

(c) Surface containing all AEPs

Figure 5.12: AEPs for $a_c = 0.2$ mm/s^2 with gravitational and sail accelerations for each point as function of deployment azimuth and elevation.

Figures 5.12a and 5.12b show that there are some data points, concentrated in the centre of the deployment region, where the residual acceleration is not exactly zero, as would be expected for an equilibrium point. The process of calculation of the contours, displayed in Fig. 2.10, is purely analytical. Each point over a grid, in non-dimensional units, of $(x,y,z) \in [-2,2]$ is assigned a value of characteristic acceleration required to produce and AEP at that point. This grid is then interpolated to produce the surface of AEPs shown in Fig. 5.12c. It is possible that, through this process of interpolation, there are some numerical errors.

A ballistic lander is deployed from each of the AEPs of Fig. 5.12c. Not all of these will

intersect the surface. In fact, only 12.72% of trajectories from the full set of AEPs will intersect the surface. Figure 5.13 shows some analysis of landing velocity and impact latitude for the set of trajectories which do intersect the surface. It is immediately clear that the impact velocity will be an issue. Such a high velocity impact is likely to result in destruction of the lander. It is interesting to note, however, that all of the landers impact with a velocity lower than the escape velocity of Vesta.

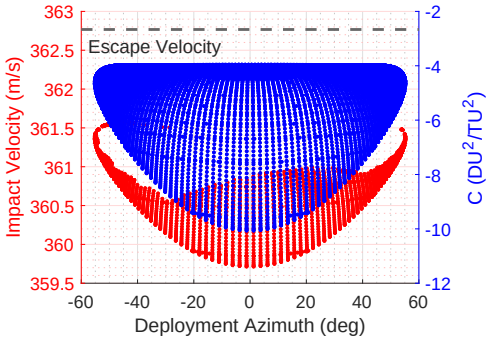

(a) Impact Velocity and Jacobi Constant vs. Deployment Azimuth

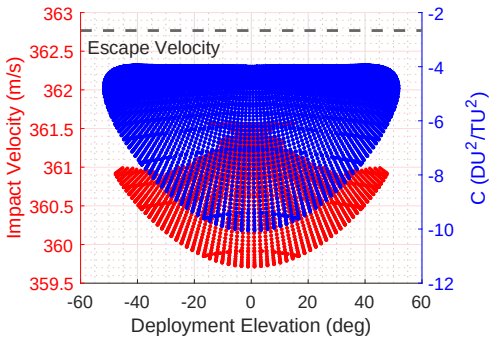

(b) Impact Velocity and Jacobi Constant vs. Deployment Elevation

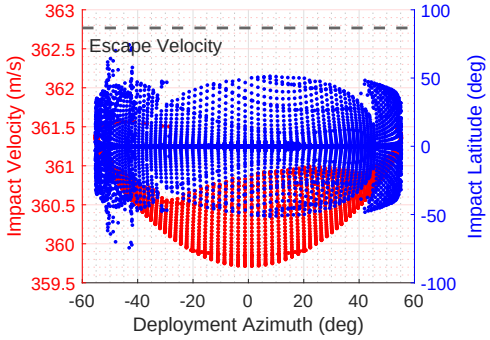

(c) Impact Velocity and Impact Latitude vs. Deployment Azimuth

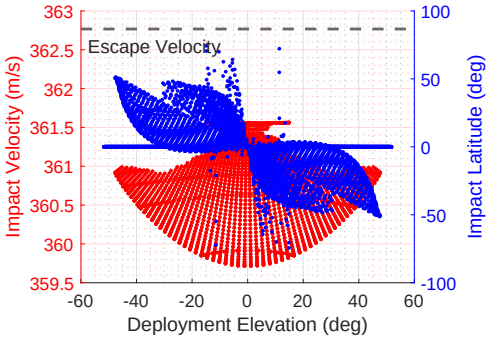

(d) Impact Velocity and Impact Latitude vs. Deployment Elevation

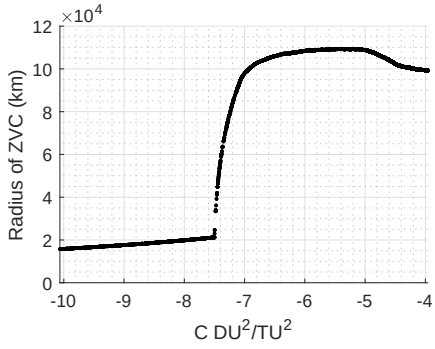

(e) ZVC radius vs. Jacobi Constant

Figure 5.13: Study of trajectories which intersect the surface of Vesta after zero-velocity deployment from full set of AEPs.

5.5 Deployment of ChipSat Probes from the Outer Regime

Given the challenges in impact velocity described in Section 5.4, an alternative mission scenario is presented. The alternative mission scenario is that of deploying a series of small ChipSat probes from five AEPs in the outer regime. As the sailcraft remains in the outer regime, the point mass SSHR3BP model is used for analysis of the sail control strategy, where impact trajectories will be analysed in the inner regime using the high resolution polyhedron shape model for accurate dynamics down to the surface.

5.5.1 Effect of ChipSat Deployment on System Dynamics

Assuming a 12U CubeSat bus, with 3U dedicated to carrying a payload of ChipSats, it is estimated that 20 ChipSats can be accommodated. The bus and sail parameters are detailed in Table 5.8 with those for the bus taken from Ref. [3].

Table 5.8: Sailcraft physical parameters

Parameter	Value
Bus Mass	24.0 kg
ChipSat Mass	10.0 g
No. of ChipSats	20
Bus and Payload Mass	24.2 kg
a_c	0.2 mm/s^2
Sail Area	679.8 m^2
Sail Areal Density	10 g/m^2
Sail Mass	6.8 kg
Total Sailcraft Mass	31.0 kg

As the acceleration of the sail is dependent on the sailcraft area-to-mass ratio, each time a ChipSat is released, there is a corresponding increase in sail acceleration. Figure 5.14 shows the changing characteristic acceleration as the ChipSats are released.

Due to the small mass of each ChipSat released, the change in a_c is also small. In fact, such changes could also be caused by degradation of the sail material over time. As such, it could be possible for the control methods used here to also be used to account for these effects. With this change in sail acceleration, there is a corresponding change to the dynamics and a unique set of AEPs is available for each value of the characteristic acceleration, which is also shown in Fig. 5.14.

5.5.2 ChipSat Descent Trajectory Analysis

This section presents the trajectories and landing conditions of those ChipSats which reach the surface of the asteroid. To do this, five deployment locations are chosen and are listed in Table

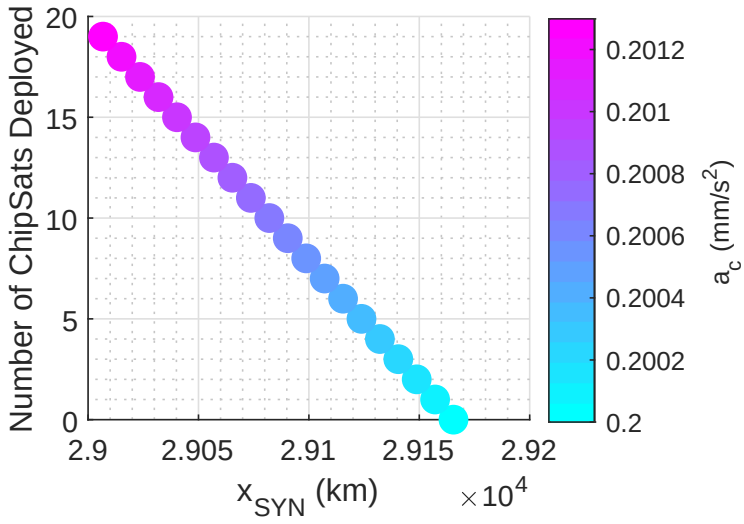

Figure 5.14: Changing sail performance and AEP position with deployment of ChipSats

5.9. The locations are dictated by the attitude of the sail and symmetrical locations in the y and z directions are chosen. These locations can be maintained by rotating the sail by $\alpha = \pm 45°$ with $\delta = 90°$ for locations 2 and 3, and $\delta = [0, 180]°$ with $\alpha = 0°$ for locations 4 and 5. This range of selected deployment locations offer the sailcraft different viewing angles of the surface of the asteroid.

Table 5.9: Hovering locations in the SYN frame and sail attitude for ChipSat deployment

Location	x_{SYN} (km)	y_{SYN} (km)	z_{SYN} (km)	$\hat{n}_{\text{SYN}_x}$	$\hat{n}_{\text{SYN}_y}$	$\hat{n}_{\text{SYN}_z}$
1	15,879	0	0	1	0	0
2	16,387	15,135	0	0.7071	0.7071	0
3	16,387	-15,135	0	0.7071	-0.7071	0
4	16,678	0	14,996	0.7071	0	0.7071
5	16,678	0	-14,996	0.7071	0	-0.7071

In fact, it was found that location 1 exists in the eclipse region. As such, this would not be a feasible deployment location given that the sail would be incapable of providing thrust. However, the data for this deployment point are maintained here. As the trajectories will take the probes to the asteroid surface, the polyhedron shape model is applied when the ChipSats enter the inner regime.

Figure 5.15a shows the descent trajectories of the ChipSats in the outer regime, where the trajectories appear as direct descents towards the surface. At the point which the ChipSat crosses into the inner regime, the trajectories are affected by the rotation and the shape of the asteroid.

It is found that deployment locations 1, 2, 4 and 5 successfully deploy their ChipSats to the surface of the asteroid. However, location 3, as it trails the asteroid direction of rotation, does not successfully deploy its complement of ChipSats to the surface. As such, those trajectories shown in Figs. 5.15b and 5.15c are only those which successfully reach the surface. Figure

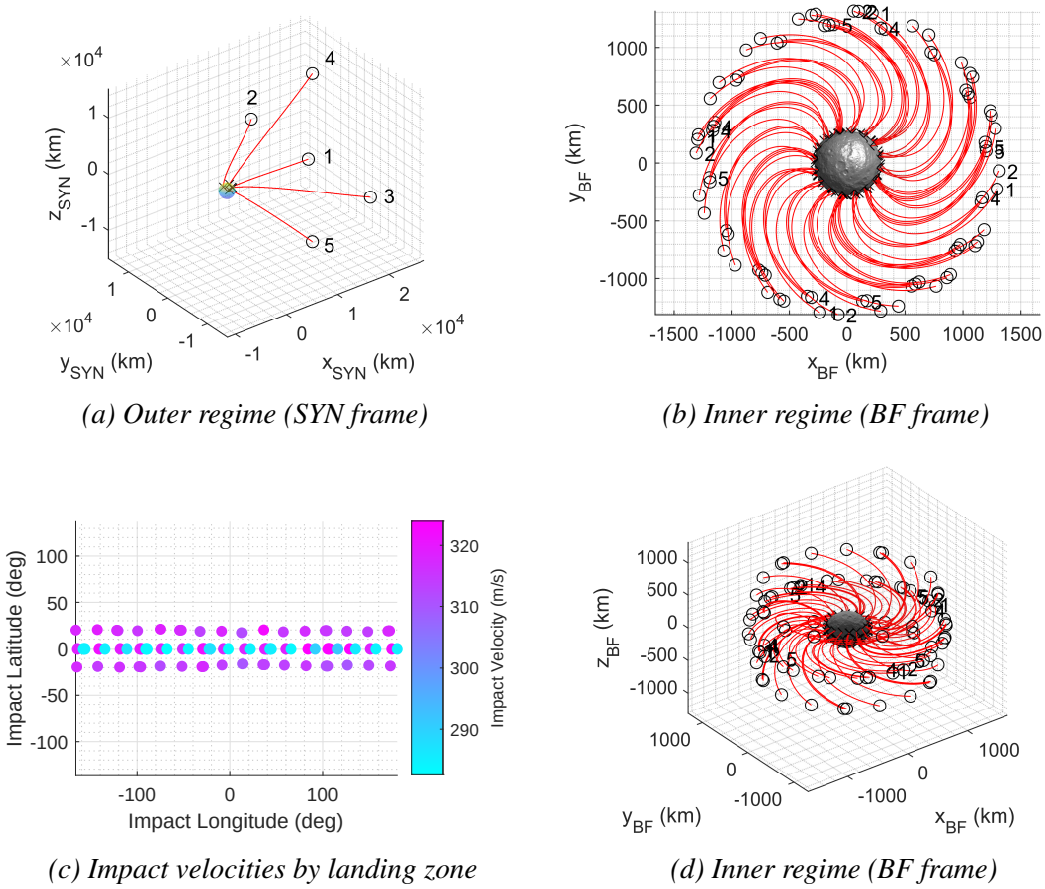

(a) Outer regime (SYN frame)

(b) Inner regime (BF frame)

(c) Impact velocities by landing zone

(d) Inner regime (BF frame)

Figure 5.15: ChipSat trajectories in the outer and inner regions.

5.15b also contains the deployment location number for a selection of the trajectories. Those which do not impact the surface are shown in Fig. 5.16. These trajectories approach close to the surface but then begin a spiralling escape trajectory, demonstrated by the crosses which denote the trajectory final points.

Although not considered in this work, the ChipSats themselves, if of a sufficiently high area-to-mass ratio or operating in a very weak gravity field, could experience significant effects from SRP.

The velocity upon impact is also provided here. Most of the science of the ChipSats is envisaged to be done during their descent, but their probability of survival on the surface will depend on the impact conditions, which is dependent on the size of the asteroid. Figure 5.15c gives the impact locations and velocities, and shows that in-plane deployments provide both some of the highest and lowest velocity impacts. On closer inspection of the results, the deployments from the AEP which lies on the x-axis give the highest velocity impacts. The lowest velocity impacts come from the in-plane deployment at the position which leads the asteroid rotation. These trajectories benefit from a lower velocity relative to the asteroid at the point of entry to the inner regime than those which lie along the x-axis of the outer regime. Given the high velocities, it is not expected that the ChipSats will survive impact. Assuming a ChipSat could survive similar

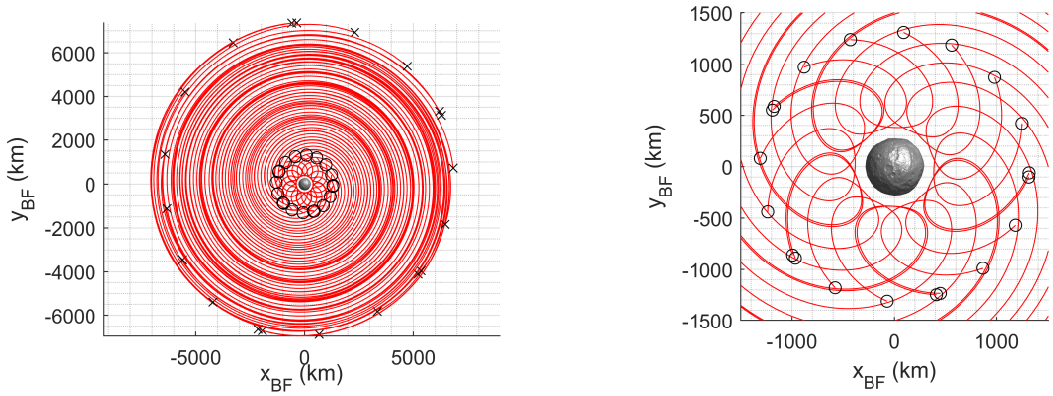

(a) Non-impacting trajectories in the BF frame

(b) Non-impacting trajectories in the BF frame focused around initial trajectories

Figure 5.16: ChipSat trajectories which do not impact the surface of the asteroid.

impact velocities of a cellular telephone on Earth (≤ 4.427 m/s [168]), then an asteroid with a ratio of $\frac{\mu}{r_0} \leq 9.7992$ m^2/s^2 would be the largest body from which deployment could be made from the locations described here and the ChipSats survive impact.

5.5.3 Sail Control During Deployment

The sail control law will now be established for the deployment of 20 ChipSats with a separation of one hour between each, from the five different deployment locations of Table 5.9. Although this separation is chosen arbitrarily here, it may be that mission designers choose to separate the probes for a specific mission objective, or perhaps even to be in resonance with the sail membrane. Given the relatively small mass of each ChipSat to the overall mass of the sailcraft, the reaction of each ChipSat release on the sailcraft is not considered here.

Fixed attitude

In the first instance, the sail attitude remains fixed with respect to the Sun in the SYN frame as set out in Table 5.9. The drift of the sail from the initial hover point is presented in Table 5.10. With the increasing sail acceleration after each ChipSat is released, the fixed attitude sail moves slowly away from the initial deployment point. Although there is some movement of the sail away from the initial point, the distance moved over the full deployment of all ChipSats is still relatively small. As is shown in Fig. 5.14, as each ChipSat is released, there is only a very small change in both the performance of the sail (a_c), and the position of the AEP. Given these small changes, it is logical that the drift from the AEP when using a fixed attitude would not be considerable.

Linear Quadratic Regulator

Following the fixed attitude simulation, the use of LQR control to maintain the initial hover location is analysed. For each deployment point of Table 5.9, there will be three associated simulations (a, b and c), each related to a different weighting on the $\mathbf{Q}$ and $\mathbf{R}$ matrices. In all simulations, $\mathbf{Q} = \mathbf{I}_{6\times6}$ and $\mathbf{R} = \beta\mathbf{I}_{3\times3}$. Here, $\beta_a = 1\times10^{-6}$, $\beta_b = 1$ and $\beta_c = 1\times10^{6}$ for simulations a, b and c respectively. The three simulations give examples where the states are given greater weighting than the control effort in the LQR controller (simulation a), where the states and effort are given equal weighting (simulation b) and where the control effort is given greater weighting (simulation c). The mean position error is calculated by taking the mean of the scalar error between the final position at the end of each 1-hour deployment phase and the reference point. The control effort is a scalar value obtained by performing a trapezoidal integration of the angular accelerations of the control law resulting from each simulation. The integral gives the total changes in slew rate of the sail during deployment, and is measured in radians per second. The results in terms of the mean position error and control effort are given in Fig. 5.17.

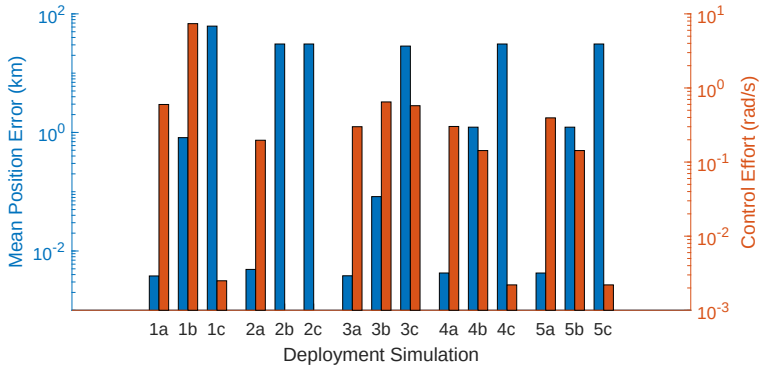

Figure 5.17: Position error vs control effort for each deployment simulation using LQR

It is clear from Fig. 5.17 that the control effort required does not necessarily reduce for simulation b when compared to simulation a. A reduction in control effort requires that the weighting is far more biased towards the $\mathbf{R}$ matrix, such as in simulation c. Where this is the case, it is possible to achieve very low values of control effort, as in simulations 2b and 2c.

Figure 5.17 shows that it is possible to achieve a very small positional error with respect to the initial hover point, at a cost of higher effort required by the sail control system. By reducing the sail control effort, there is an increase in the positional error. For very small values of control effort, there can be considerable positional error values. These errors are far greater than those where the sail remains with a fixed attitude during deployment, as seen in Table 5.10. As an example of the LQR performance, the results from simulation a are used for comparison with the fixed attitude in Table 5.10, which give the most weight to maintaining the hover position for a higher control effort. The control laws from this simulation are given in Fig. 5.18. We note

that viewing angle changes, due to the displacement from the original hover location, are small enough that they would not be a problem for scientific remote observation.

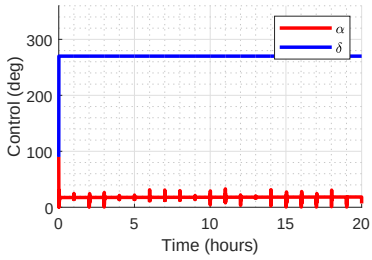

(a) Location 1: Full 20 hours deployment

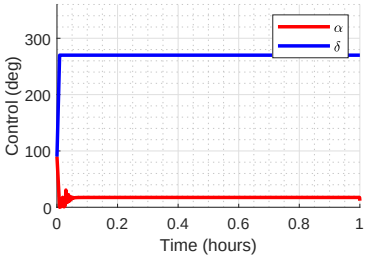

(b) Location 1: First hour of deployment

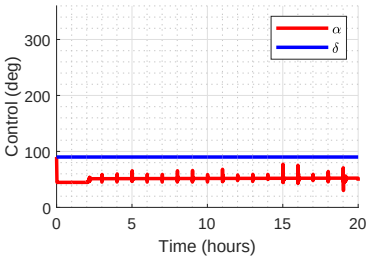

(c) Location 2: Full 20 hours deployment

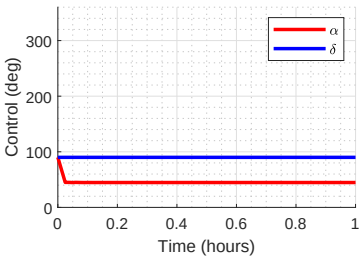

(d) Location 2: First hour of deployment

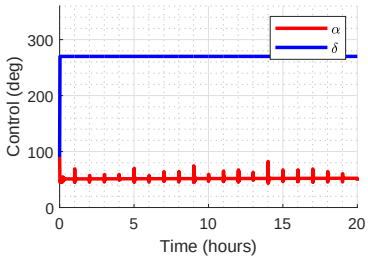

(e) Location 3: Full 20 hours deployment

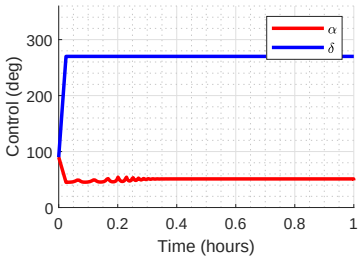

(f) Location 3: First hour of deployment

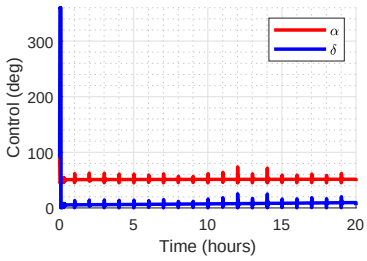

(g) Location 4: Full 20 hours deployment

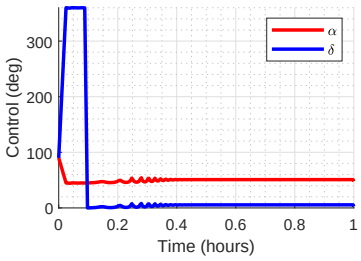

(h) Location 4: First hour of deployment

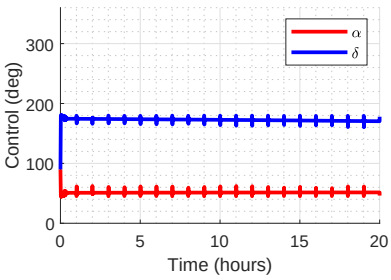

(i) Location 5: Full 20 hours deployment

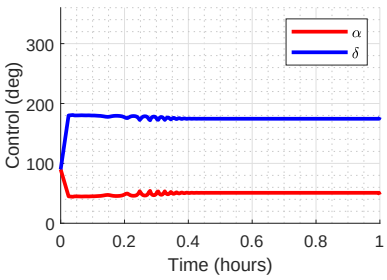

(j) Location 5: First hour of deployment

Figure 5.18: LQR control during hover for ChipSat deployment from all locations of Table 5.9

Comparison of methods

A comparison of the fixed attitude control and LQR control is now made. Consideration is given not only to the ability of the method used to maintain the desired hover, but also the effort required to do so. The results of Table 5.10 show that the LQR control is capable of maintaining the sail close to the original hover location, where maintaining a fixed attitude will result in the sailcraft drifting from the original hover point.

Table 5.10: Comparison of sailcraft drift from initial hover point for fixed attitude and LQR

Location	Fixed Attitude (km)	LQR a (km)
1	0.3416	0.0072
2	0.1728	0.0082
3	0.1728	0.0071
4	0.1728	0.0080
5	0.1728	0.0079

However, the considerable extra effort required by the sail to follow the LQR control does not bring about such an improvement in performance to warrant its inclusion on a real mission. As such, for a real scenario, the recommendation would be to use a fixed sail attitude during ChipSat release. Where the sail acceleration becomes more powerful relative to the asteroid gravitational acceleration, the fixed attitude would result in greater divergence from the desired deployment location. This may also be the case where the ChipSats may have a considerably larger mass than those of 10 g which are considered here. In these situations, it may be worth revisiting a control provided by the LQR.

Chapter 6

Gravitational Capture of a Solar Sail Around an Asteroid

This chapter will investigate the problem of gravitational capture of a solar sail around an asteroid. Initially, an "on/off" approach is discussed. The sail is considered on when the unit vector normal to the sail surface is pointing at the Sun and is considered "off" when the sail is in an edge-on attitude with respect to the Sun. When edge-on, there is no thrust being produced by the sail. Following this, a sub-optimal approach to the capture problem is discussed and is divided into two phases. In the first phase, referred to as the "initial capture" phase, the objective is to reduce the "size" of the orbit by focusing on a reduction of the orbit semi-parameter until the Jacobi constant is of such a value that the orbit is contained within ZVCs of a given radius. The second phase, referred to as the "orbit shaping" phase, aims to circularise the orbit. Finally, optimisation methods are employed to minimise the time to capture and also the orbit semi-parameter. All of the trajectories in this work are planar as the problem of orbit inclination "cranking" has been dealt with in the literature [11].

The intention of this chapter is to progress from a simple "bang-bang" control up to a time-optimal solution, in incremental steps. The reason for this, building on experience gained in the previous chapters, is to obtain solutions which could be useful as initial guess solutions for the optimisations which came later. Time limitations on the PhD meant that this work has not been fully completed, but the results obtained are shown here.

6.1 On/Off Control

The first control technique to be employed is an on/off control law. The sail is considered "on" where $\hat{\mathbf{n}}_{\mathrm{SYN}} = [1,0,0]$ and "off" where $\hat{\mathbf{n}}_{\mathrm{SYN}} = [0,1,0]$. The theory on invariant manifold transfers, described in Section 3.2, is used to establish the initial conditions where the sail enters the asteroid/capture region.

To affect capture, the sail switching law will be based on the ballistic value of Jacobi con-

stant. The sail will be switched off when the ballistic value of Jacobi constant (C) remains inside the dead-band (DB) [169]. The DB is defined as a range of energy values around the targeted value, C_t, which allows the capture to take place within a certain tolerance. When C lies outside on the DB and below C_t, the sail requires a boost in energy. As such, the sail is switched on when it is moving away from the Sun and on the Sun-side of the asteroid. When C lies outside of the energy margin and above C_t, the sail needs to lose energy or risk escape. As such, the sail is switched on when it is moving towards the Sun and is on the Sun-side of the asteroid. This is shown in Fig. 6.1.

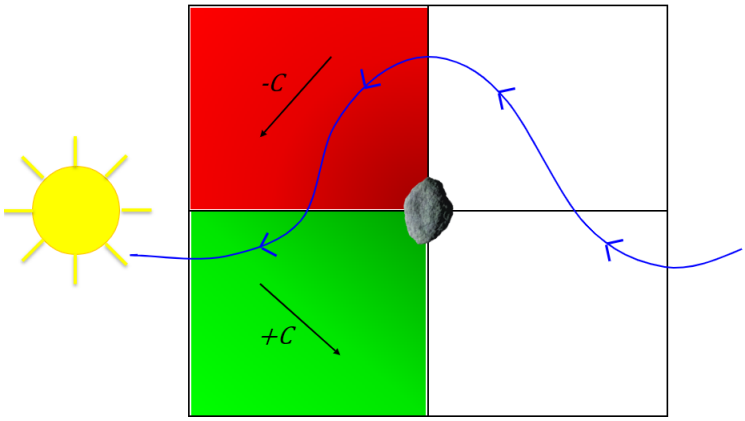

Figure 6.1: Thrusting quadrants in the SYN frame. The green quadrant shows where the sail may thrust in order to boost the sail orbital energy and the red quadrant shows where the sail can thrust in order to reduce its energy. The blue arrowed line shows the transiting trajectory.

The success of the control to bring about capture will be assessed based on whether a trajectory remains captured for a period of five years or if it escapes during this time. As this method of "on/off" control is somewhat rudimentary, there are occasions where the DB targeting overshoots and so there is some oscillation on C in-and-out of the DB. The period of five years was chosen to allow sufficient time for these oscillations to reduce and for the value of C to settle into the DB for those trajectories that would now be considered as captured.

Figure 6.2 shows contours of time to escape, in Earth days, for a range of DB and with targeted values down to $C_t = -9$ DU^2/TU^2, with each sub-plot giving those contours for a different sail a_c. Therefore, any trajectory which is captured for five years is considered to be captured indefinitely. The initial condition for each simulation in this work is obtained from a ballistic trajectory which, if left uncontrolled, would transit from the exterior region, through the asteroid/capture region to the interior region. These transit trajectories are shown in Appendix D.1 for asteroid 4 Vesta.

The lower performance sails, given their relatively weaker acceleration compared to the asteroid gravitational acceleration, give a wider range of captured trajectories. This is due to the reduced sensitivity of the trajectory to sail controls. With this on/off switching, it may be that the higher performance sails give too large an energy boost which leads to escape before

the energy can be reduced again on the subsequent orbit. A larger energy margin is also seen to benefit capture for the lower performance sails.

In order to understand more about the regions containing escaping trajectories in Fig. 6.2, the range of targeted values are limited down to $C_t = -6$ DU^2/TU^2 and with DB $\in [0, 0.2]$ DU^2/TU^2. This is shown in Fig. 6.3. These results make clear that smaller sails are effective at achieving indefinite capture, even with a wider DB, than a larger sail would be. In fact, as the sail performance increases, the number of escaping trajectories with higher DBs increases. As such, for higher performance sails it is necessary to target a smaller DB around the targeted value of C. This result again shows the increasing sensitivity of the weak asteroid gravitational field as the performance of the sail increases.

These contour plots allow for easy selection of the required margins for a successful capture trajectory. As an example, a selection of C_t and DB values are chosen with the capture trajectory simulated for the extended period of 10 years. Figure 6.4 shows a selection of successful capture trajectories, each of which is captured indefinitely.

As the energy margin moves further from the critical value of C, the captured trajectory becomes more and more regular, though the required control effort increases.

The results presented here have shown the utility of the sail, and an "on/off" switching law, in bringing about capture of the sailcraft around an asteroid. However, this rudimentary approach is not suitable for achieving a final orbit with a specific geometry.

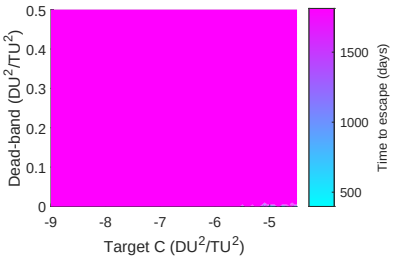

(a) $a_c = 0.01$ *mm/s*^{2}

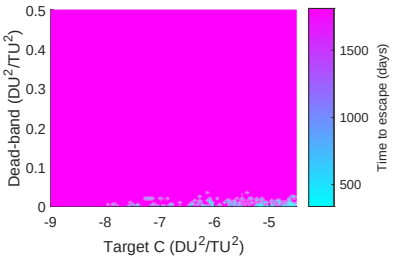

(b) $a_c = 0.04$ *mm/s*^{2}

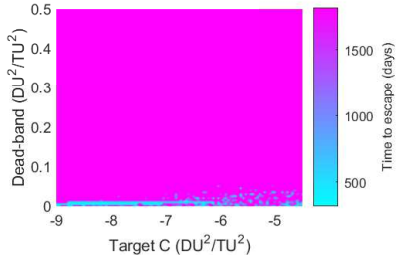

(c) $a_c = 0.07$ *mm/s*^{2}

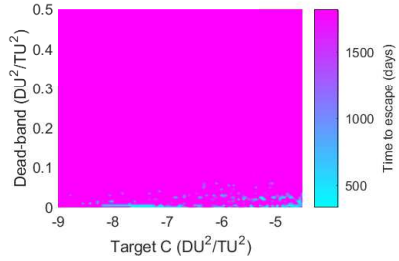

(d) $a_c = 0.11$ *mm/s*^{2}

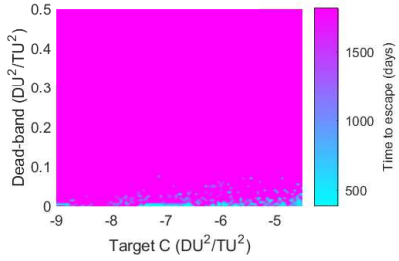

(e) $a_c = 0.14$ *mm/s*^{2}

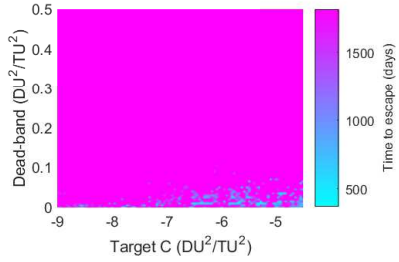

(f) $a_c = 0.17$ *mm/s*^{2}

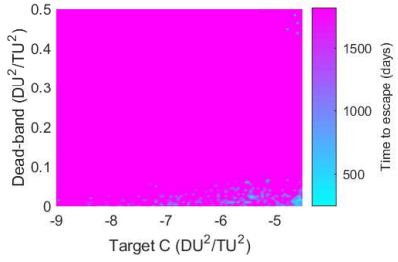

(g) $a_c = 0.20$ *mm/s*^{2}

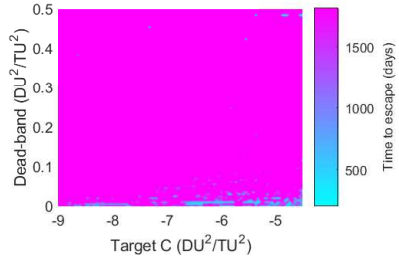

(h) $a_c = 0.24$ *mm/s*^{2}

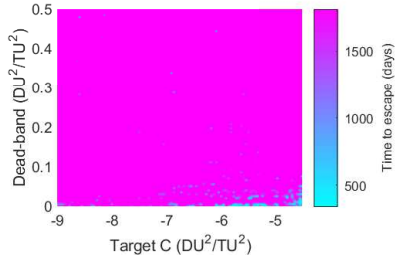

(i) $a_c = 0.27$ *mm/s*^{2}

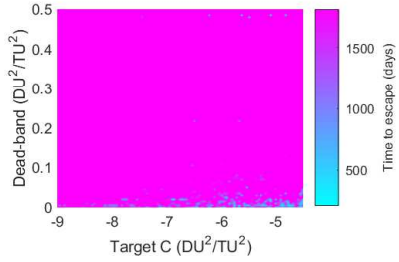

(j) $a_c = 0.30$ *mm/s*^{2}

Figure 6.2: Capture using On/Off control law for $a_c \in (0, 0.30]$ *mm/s*^{2}.

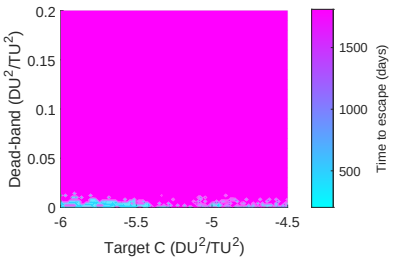

(a) $a_c = 0.01$ *mm/s*^{2}

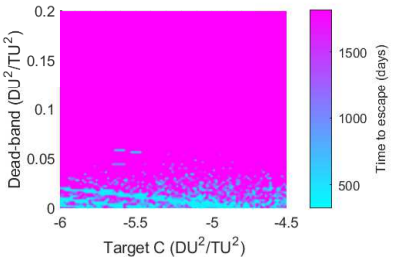

(b) $a_c = 0.04$ *mm/s*^{2}

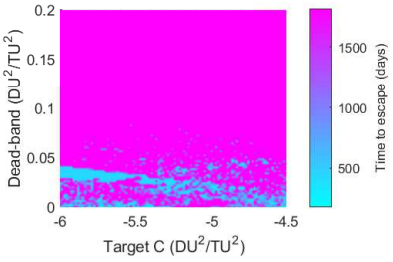

(c) $a_c = 0.07$ *mm/s*^{2}

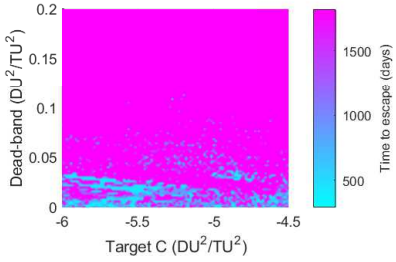

(d) $a_c = 0.11$ *mm/s*^{2}

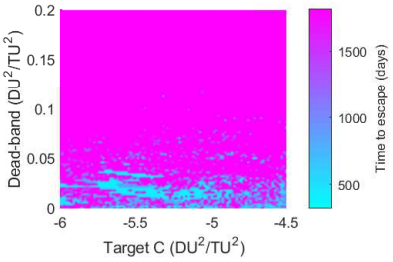

(e) $a_c = 0.14$ *mm/s*^{2}

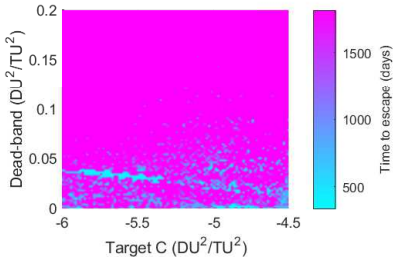

(f) $a_c = 0.17$ *mm/s*^{2}

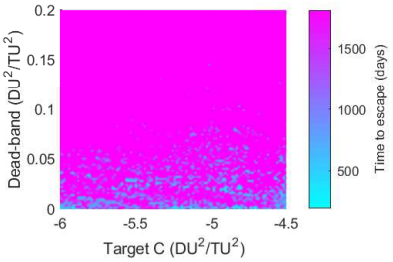

(g) $a_c = 0.20$ *mm/s*^{2}

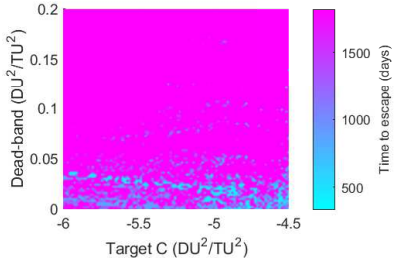

(h) $a_c = 0.24$ *mm/s*^{2}

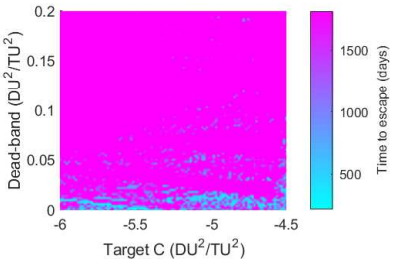

(i) $a_c = 0.27$ *mm/s*^{2}

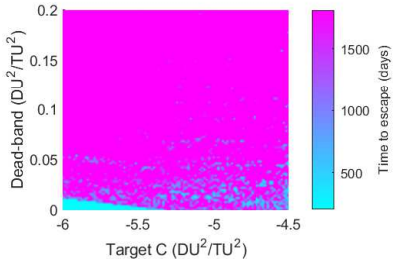

(j) $a_c = 0.30$ *mm/s*^{2}

Figure 6.3: Capture using On/Off control law for $a_c \in (0, 0.30]$ *mm/s*^{2}*. Energy range reduced for clearer interpretation of escaping trajectories.*

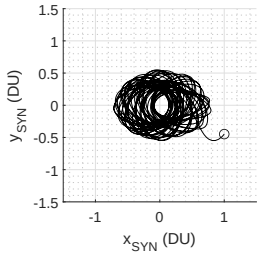

(a) $C_t = -4.66$ DU^2/TU^2, $DB = 0.07$ DU^2/TU^2

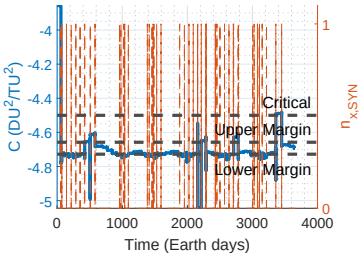

(b) $C_t = -4.66$ DU^2/TU^2, $DB = 0.07$ DU^2/TU^2

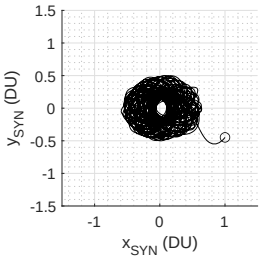

(c) $C_t = -5.21$ DU^2/TU^2, $DB = 0.09$ DU^2/TU^2

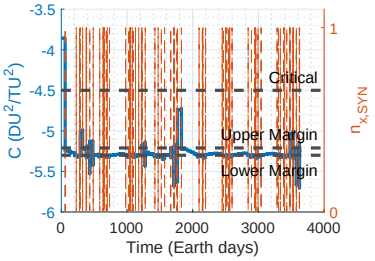

(d) $C_t = -5.21$ DU^2/TU^2, $DB = 0.09$ DU^2/TU^2

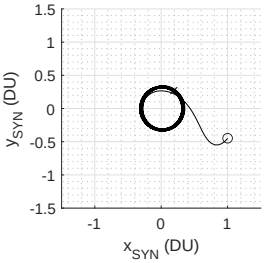

(e) $C_t = -5.60$ DU^2/TU^2, $DB = 0.09$ DU^2/TU^2

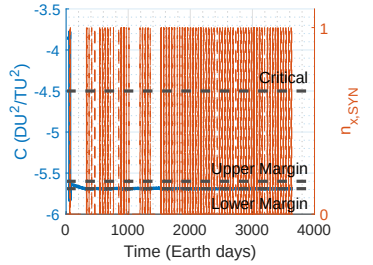

(f) $C_t = -5.60$ DU^2/TU^2, $DB = 0.09$ DU^2/TU^2

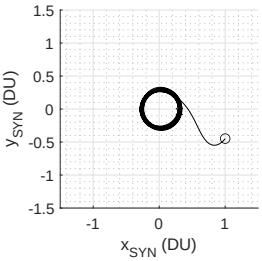

(g) $C_t = -6.00$ DU^2/TU^2, $DB = 0.08$ DU^2/TU^2

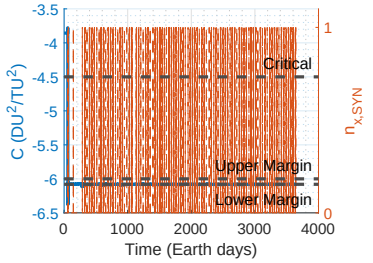

(h) $C_t = -6.00$ DU^2/TU^2, $DB = 0.08$ DU^2/TU^2

Figure 6.4: Set of solutions for on/off control law capture which holds for period of 10 years with $a_c = 0.2$ *mm/s*^{2}.

6.2 Two-Phase Approach

6.2.1 Target asteroids

As has been discussed throughout this thesis, the ability of a sail to operate around a particular asteroid is dependent on the value of a_c. In the weak gravity field, a larger sail may provide too powerful an acceleration to allow bound motion [124]. In order to provide test cases for asteroids of different size, three test cases will be presented while the sail maintains a value of $a_c = 0.20$ mm/s^2. Following this, a study of real NEAs, asteroids 433 Eros and 3122 Florence$_b$, will be conducted where the sail performance is varied starting from a smaller sail and increasing the value of a_c.

For the first three examples with the fixed value of a_c, the reference asteroid will be asteroid Vesta. The data obtained for Vesta is taken from the JPL small-body database. The first body will be an asteroid with the same mass and mean radius as Vesta. These parameters are used to calculate a density value for a spherical Vesta of $\rho = 4.3252$ g/cm^3. The second body is an asteroid of half the mean radius of the first asteroid and the third asteroid is a body with a radius 10% that of the first asteroid. The same value of ρ is applied to each body to establish the mass. As the asteroid Vesta is in fact a main-belt asteroid, it is necessary to study the case of a NEA which tend to be of much smaller size. For this, asteroids 433 Eros and 3122 Florence$_b$ are used as the target bodies and the data are again taken from the JPL small-body database and are listed in Table 2.3. For the asteroids which are used in this chapter and are based on the physical properties of Vesta, the newly established values are listed here in Table 6.1

	Asteroid 1	Asteroid 2	Asteroid 3
r_0 (km)	262.70000	131.35000	26.27000
m ($\times 10^{19}$ kg)	328.45120	4.10560	0.03280
μ (km^3/s^2)	21.92110	2.74010	0.02190

Table 6.1: Physical parameters for target asteroids

6.2.2 Approach Trajectories

In this work, the capture problem is based around a trajectory which is transiting from the exterior region to the interior region via the asteroid/capture region. Such a transit trajectory can be selected using the theory detailed in Section 3.2. In order to establish these trajectories, the energy contained by the spacecraft must be specified. As the critical value is $C = -4.5$ DU^2/TU^2, a value above this must be chosen to allow the transit of the spacecraft. Here, a value of $C = -3.90$ DU^2/TU^2 is chosen as at this value there exist ballistic transit trajectories. At higher energy levels, there exist no ballistic connections between the stable and unstable manifolds.

The trajectories shown in Fig. 6.5 were those calculated for asteroid 433 Eros. Similar trajectories calculated for each of the target asteroids are contained in Appendix D.1. By taking a section along the y-axis at $x = 0$, the intersection of the stable and unstable manifolds (shown in Fig. 6.5a) can be visualised, as shown in Figs. 6.5c and 6.5d. The green trajectories represent stable manifolds and the red represents unstable manifolds. Where these manifolds intersect in the $[y, v_y]$ space, a ballistic transit trajectory exists. This intersection region is shown in the shaded region of Figs. 6.5c and 6.5d. A selection of ballistic transit trajectories for $C = -3.90$ DU^2/TU^2 are shown in Fig. 6.5b, where those which enter via L_1 are shown in blue and those which enter via L_2 are shown in pink.

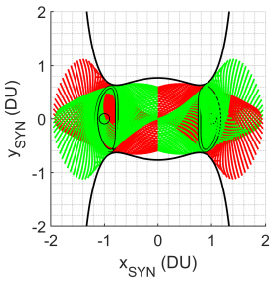

(a) L_1 and L_2 manifolds

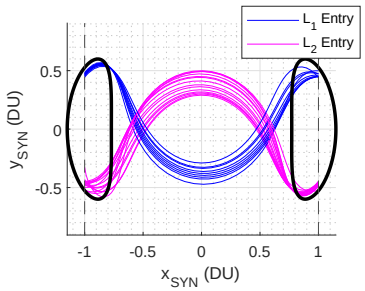

(b) Ballistic transit trajectories via L_1 and L_2

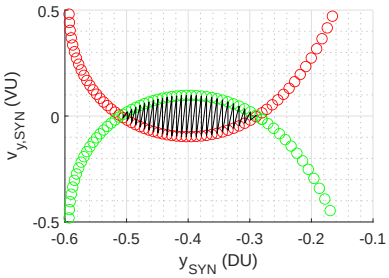

(c) Poincaré section along negative y-axis

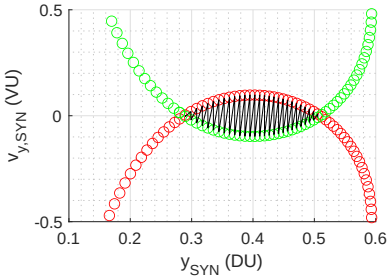

(d) Poincaré section along positive y-axis

Figure 6.5: Ballistic transit trajectories via L_1 and L_2 Lagrange points

From the Poincaré surfaces shown in Figs. 6.5c and 6.5d, the user can select a y and v_y value which are contained in the shaded region. Then, from Eq. 3.15, the value of v_x can be obtained, giving the full set of conditions at the Poincaré surface for that transit trajectory. By integrating both forwards and backwards from that state, the entire trajectory is obtained.

6.2.3 Phase One: Initial Capture

In the initial capture phase the objective is to use the value of Jacobi constant as a guide to bring the radius of the ZVCs enclosing the capture region to such a point that the orbit remains within a region of a certain radius, after which the orbit shaping phase will take over.

The classical orbital elements $(a, e, i, \Omega, \omega, \theta)$ are limited by singularities when $i = 0°$ or when $e = 0$. When these situations occur, the angular elements Ω and ω lack definition. As

such, various modifications have been presented, one such example defined by Walker *et al* in Ref. [170] give the Modified Equinoctial Elements (MEEs) (p, f, g, h, k, L), where:

$$\begin{aligned} p &= a\left(1-e^2\right) \\ f &= e\cos\left(\omega+\Omega\right) \\ g &= e\sin\left(\omega+\Omega\right) \\ h &= \tan\frac{i}{2}\cos\Omega \\ k &= \tan\frac{i}{2}\sin\Omega \\ L &= \Omega+\omega+\theta \end{aligned} \tag{6.1}$$

The Gaussian equations of motion for this set of MEEs are given by [170]:

$$\begin{aligned} \frac{dp}{dt} &= \frac{2p}{w}\sqrt{\frac{p}{\mu}}u_\theta \\ \frac{df}{dt} &= \sqrt{\frac{p}{\mu}}\left[u_r\sin L+\frac{\left[(w+1)\cos L+f\right]u_\theta}{w}-\frac{g\left(h\sin L-k\cos L\right)u_h}{w}\right] \\ \frac{dg}{dt} &= \sqrt{\frac{p}{\mu}}\left[-u_r\cos L+\frac{\left[(w+1)\cos L+g\right]u_\theta}{w}-\frac{f\left(h\sin L-k\cos L\right)u_h}{w}\right] \\ \frac{dh}{dt} &= \sqrt{\frac{p}{\mu}}\frac{s^2u_h}{2w}\cos L \\ \frac{dk}{dt} &= \sqrt{\frac{p}{\mu}}\frac{s^2u_h}{2w}\sin L \\ \frac{dL}{dt} &= \sqrt{\mu p}\left(\frac{w}{p}\right)^2+\sqrt{\frac{p}{\mu}}\frac{\left(h\sin L-k\cos L\right)\right)u_h}{w} \end{aligned} \tag{6.2}$$

where:

$$\begin{aligned} s^2 &= 1+h^2+k^2 \\ w &= 1+f\cos L+g\sin L \end{aligned} \tag{6.3}$$

and $[u_r, u_\theta, u_h]$ are the radial, transversal and normal components of the sail thrust vector. The Gauss equations of motion show that it is the component of the sail acceleration in the transversal direction of the orbit (u_θ) which will reduce the semi-parameter, p, of an orbit.

If the objective is to achieve the fastest reduction in p, such that the orbital radius is confined to the desired region around the asteroid, then the entire sail acceleration vector must be directed against the velocity vector of the spacecraft, with $u_\theta = -1$. As such, in this initial capture phase the sail acceleration is directed against the velocity vector when the sail is moving towards the Sun and is on the Sun-side of the asteroid. In the initial capture phase only, this region will be referred to as the "thrusting quadrant", given that it represents one quarter of the space. At all other points, the sail attitude is set to $\hat{\mathbf{n}}_{\mathrm{SYN}} = [0, 1, 0]$, which results in no thrust.

Although the transversal component of the sail acceleration has an effect on other orbit parameters, this is not considered important in the initial capture phase. The only concern here is to bring the value of C down to a value where the orbit is contained within a defined radius. The radius of this region is what drives the choice of targeted C_t value.

Defining the Radius of the Initial Capture Region

Given the rudimentary nature of this method, it is not possible to target very low altitude orbits at this point. This is again due to the sensitivity of the asteroid gravitational field to the acceleration from the sail. Targeting a low altitude orbit directly with a relatively strong acceleration from the sail, results in an asteroid impacting trajectory. As such, care must be taken in the selection of the targeted initial capture region.

Before conducting the analysis at each of the asteroids, a common radius for the region within which the orbits must be contained has to be defined. This radius will be common to each asteroid in the non-dimensional system. Asteroid 433 Eros is used as the test case. In the first iteration, a radius of 0.3 DU is selected. To avoid any issues regarding relatively powerful sails in weak gravity fields [124], the value of a_c is increased incrementally up to the target value, maintained throughout this thesis, of $a_c = 0.2$ mm/s^2. The full set of results for this study are contained in Appendix D.2. These results show that it was possible for the sail of $a_c = 0.2$ mm/s^2 to affect capture within a region of radius 0.3 DU. As such, the sail of $a_c = 0.2$ mm/s^2 was tested for initial capture to a region of radius 0.25 DU, which was once again successful. It was found in this work that the method results in an asteroid impact when the radius is set to 0.20 DU, where $C_t = -10.6666$ DU^2/TU^2. As such, the minimum radius of 0.21 DU is applied for each targeted asteroid, which by way of Eq. 3.15 gives $C_t = -10.1677$ DU^2/TU^2.

Appendix D.2 contains the full set of initial capture results, as well as the subsequent orbit shaping phase, for the work described here. The impacting trajectory at 0.20 DU is also contained there.

Asteroid 1: 4 Vesta

The first initial capture is around the spherical representation of asteroid 4 Vesta as detailed in Table 6.1. The results of this phase are shown in Fig. 6.6.

The initial capture phase at asteroid 1 took a total of 24.32 days to complete. Given the stronger gravitational field of this larger body, the sail requires almost two full revolutions in the ACI frame to reach the desired value, C_t. The initial capture phase begins at entry to the thrusting quadrant. As such, the largest reduction in C is obtained in the first five days. Figure 6.6c shows the coinciding reduction in semi-major axis, SMA, (defined in mean asteroid radii, r_0) with the reduction in C shown in Fig. 6.6b.

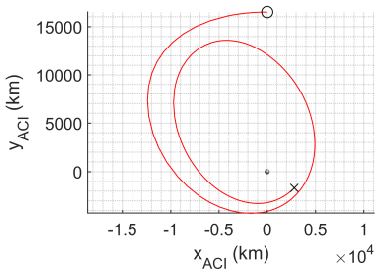

(a) Trajectory (ACI frame)

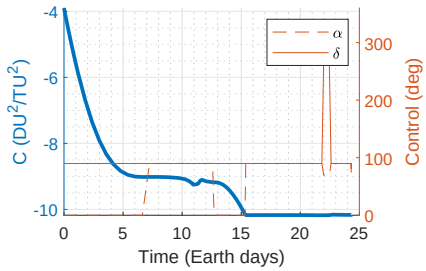

(b) Jacobi constant and control

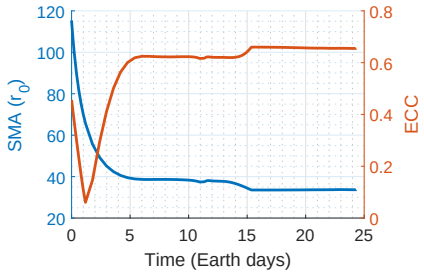

(c) Semi-major axis against eccentricity

Figure 6.6: Initial capture phase: asteroid 1

Asteroid 2: 4 Vesta, 50% Radius

Given the weaker gravity field of asteroid 2, it is expected that this will result in a faster capture time in comparison with asteroid 1, and Fig. 6.7 shows the results.

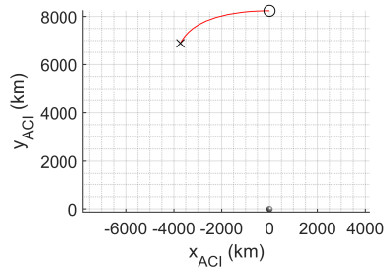

(a) Trajectory (ACI frame)

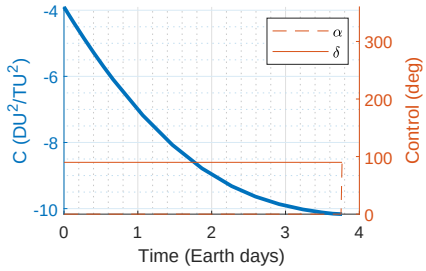

(b) Jacobi constant and control

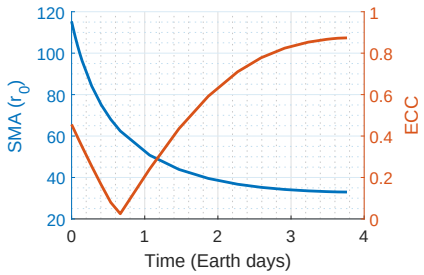

(c) Semi-major axis against eccentricity

Figure 6.7: Initial capture phase: asteroid 2

As is clear, the required reduction in C is achieved far quicker, in only 3.77 days. In fact, the entire phase is completed while the sailcraft is still in the thrusting quadrant of the asteroid/capture region.

Asteroid 3: 4 Vesta, 10% Radius

For asteroid 3, the gravitational field is again weaker than the preceding examples. Figure 6.8 shows the resulting initial capture trajectory and reductions in C and SMA.

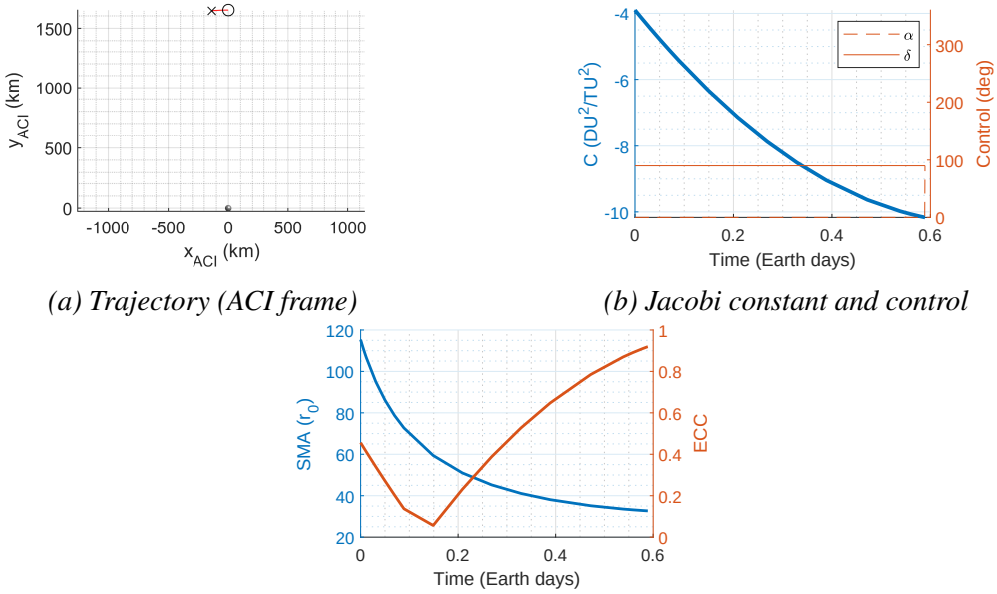

(a) Trajectory (ACI frame)

(b) Jacobi constant and control

(c) Semi-major axis against eccentricity

Figure 6.8: Initial capture phase: asteroid 3

Given the weaker gravitational field, the initial capture is achieved very quickly, in just 0.59 days. However, the cost of the faster initial capture is an increased final value of eccentricity, ECC. The increased value is expected to result in a longer orbit shaping phase than would have been necessary if the eccentricity was smaller for the same asteroid.

433 Eros

After studying the control initial capture phase at three different representations of the main belt asteroid 4 Vesta, and given that an assumption has been made in this work that the radius of the asteroid orbit around the Sun is at 1 AU, it is necessary to apply the methods to NEAs. The first of these is 433 Eros. Table 6.1 shows that the mass of Eros is considerably smaller than those asteroid already studied here. As such, the resulting weaker gravitational field is expected to allow the sail to affect the initial capture even more quickly. This is indeed the case, and is shown in Fig. 6.9.

The initial capture at Eros takes only 0.16 days. Again, this fast initial capture results in a high ECC value, similar to that of asteroid 3. This is once again expected to result in a longer orbit shaping phase.

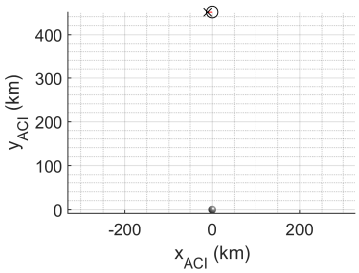

(a) Trajectory (ACI frame)

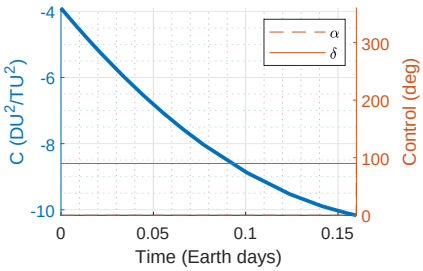

(b) Jacobi constant and control

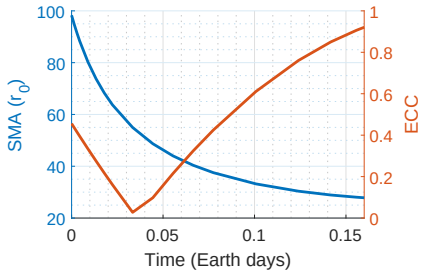

(c) Semi-major axis against eccentricity

Figure 6.9: Initial capture phase: 433 Eros

3122 Florence$_b$

The smallest of all of the asteroids studied here is 3122 Florence$_b$, the object of the part of the work conducted in Chapter 4. The results for the initial capture phase here are shown in Fig. 6.10.

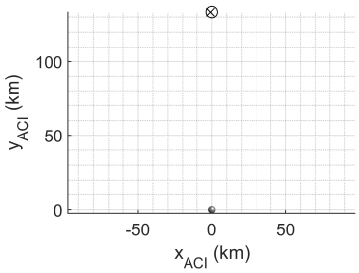

(a) Trajectory (ACI frame)

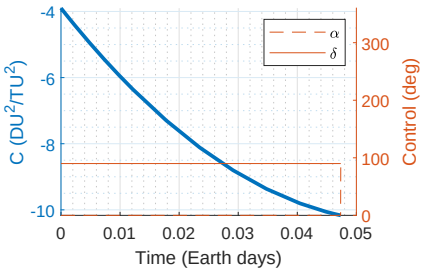

(b) Jacobi constant and control

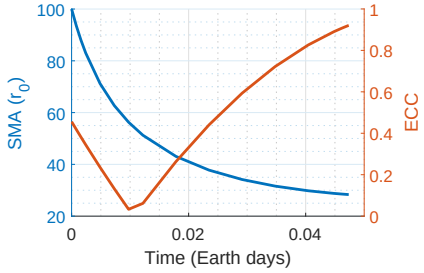

(c) Semi-major axis against eccentricity

Figure 6.10: Initial capture phase: 3122 Florence

Once again, the very weak gravity field results in a rapid initial capture, in this occasion just 0.05 days, and high final ECC.

6.2.4 Phase Two: Orbit Shaping

Once the orbit is contained in the desired region, the strategy changes to circularising that orbit. In order to circularise an orbit, it is necessary to thrust at periapsis against the velocity vector. However, if the radius of the periapsis drops below a desirable value, it is necessary to raise this by thrusting along the velocity vector at apoapsis. As stated in Chapter 2, the shape and spin-state of an asteroid become important factors in the gravitational field within 5 mean asteroid radii ($5r_0$). As such, the radius of the periapsis is not allowed to fall below this value. When it does, the orbit shaping method will raise it by thrusting at apoapsis and in the direction of the velocity vector.

As the thrust provided by a solar sail is not impulsive, it is necessary to define an arc around apoapsis/periapsis along which thrusting is performed. This work will perform thrust along an arc at $\pm 18^\circ$ true anomaly either side of the apoapsis/periapsis (5% of 360°), shown in Fig. 6.11. The strategy is to lower the apoapsis until the orbit eccentricity reaches a value of $e < 0.01$.

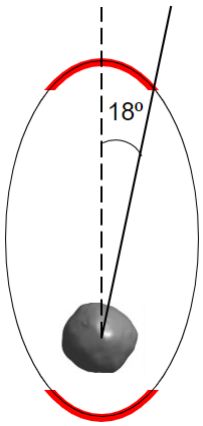

Figure 6.11: Thrusting arcs defined by red lines around periapsis and apoapsis

From Eq. 6.2, we have:

$$\frac{dp}{dt} = \frac{2p}{w}\sqrt{\frac{p}{\mu}}u_\theta \tag{6.4}$$

As such, and similarly to the initial capture phase, the thrust vector will be directed along or against the velocity vector in the SYN frame, as this will achieve the fastest reduction in semi-parameter, p.

In order for the orbit shaping phase to begin, the Sun must be conveniently positioned relative to the orbit such that thrusting manoeuvres are possible. This is assessed in the ACI frame by defining the direction of the eccentricity vector relative to the position of the Sun, $\hat{\mathbf{e}}_{\text{ACI}} \cdot \hat{\mathbf{S}}_{\text{ACI}}$. If $\hat{\mathbf{e}}_{\text{ACI}} \cdot \hat{\mathbf{S}}_{\text{ACI}} = -1$, the eccentricity vector, which points to the orbit periapsis, is in the direction of the Sun. When the sail normal vector points towards the Sun, $\hat{\mathbf{n}}_{\text{SYN}} \cdot \hat{\mathbf{S}}_{\text{SYN}} < 1$, the sail would be unable to thrust. As such, when the Sun and orbit are not adequately aligned, depending on the required operation from the sail, there must be a delay while the alignment changes. An

example of this is shown in Fig. 6.12. By allowing some thrusting to take place outside of the defined arcs, the orbit could be rotated in order to facilitate a faster start to the desired operations. However, this was not investigated in this work.

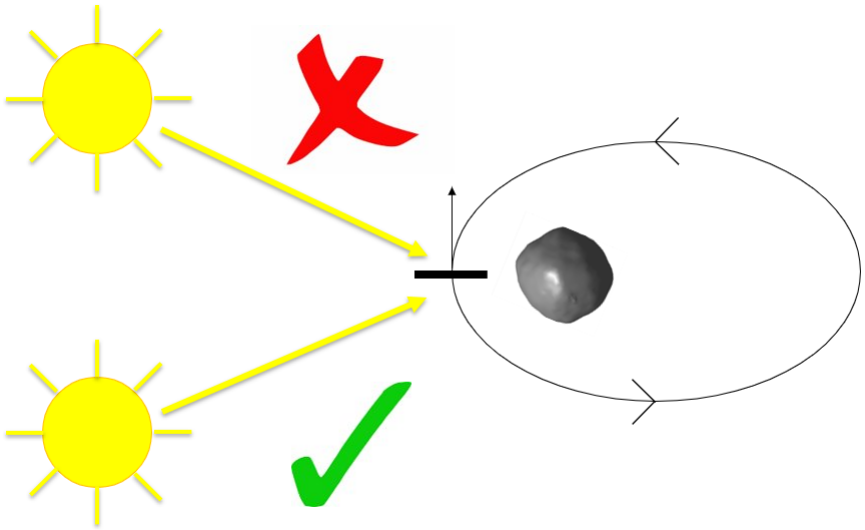

Figure 6.12: Position of Sun relative to the orbit periapsis in ACI frame.

To reduce the apoapsis radius, the sail is only able to thrust where $\hat{\mathbf{v}}_{\text{SYN}} \cdot \hat{\mathbf{S}}_{\text{SYN}} < 0$ at the periapsis thrusting arc. This is shown in the profile of the sail acceleration and sail normal vector. When the Sun is not conveniently positioned, or where the sail is outside of the designated thrusting arc, $\hat{\mathbf{n}}_{\text{SYN}} \cdot \hat{\mathbf{S}}_{\text{SYN}} = 0$, which means the sail does not thrust. To raise the periapsis, the sail can only thrust where $\hat{\mathbf{v}}_{\text{SYN}} \cdot \hat{\mathbf{S}}_{\text{SYN}} > 0$ along the apoapsis thrusting arc.

Asteroid 1: 4 Vesta

For asteroid 1, the initial capture phase takes 24.32 days but maintains a mid-level eccentricity value of approximately $e = 0.65$. After this, and for the orbit shaping phase to commence, it is necessary for the sailcraft to wait for the Sun to be conveniently positioned, which takes approximately 95 days. The results for the orbit shaping phase at asteroid 1 are shown in Fig. 6.13.

After $\hat{\mathbf{e}}_{\text{ACI}} \cdot \hat{\mathbf{S}}_{\text{ACI}} = -1$, the Sun moves to a position which allows the sail to begin shaping the orbit. The first thrusting manoeuvre takes place soon after 120 days from the beginning of the capture process. The sail performs a series of periapsis thrusting manoeuvres which successfully reduce the apoapsis radius to circularise the orbit. The total time from entry into the system to final capture in a circular orbit for the first body has been approximately 558.52 days.

Asteroid 2

In the weaker gravity field of asteroid 2, the sail was able to affect a quicker initial capture at the cost of a higher final eccentricity value. Given this increased eccentricity, Fig. 6.14 shows that

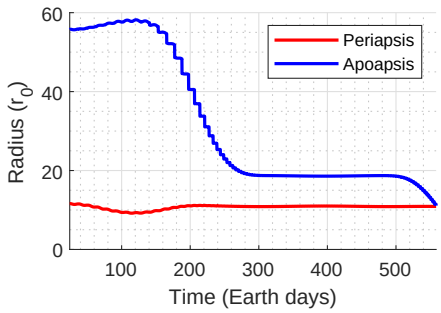

(a) Radius of periapsis and apoapsis

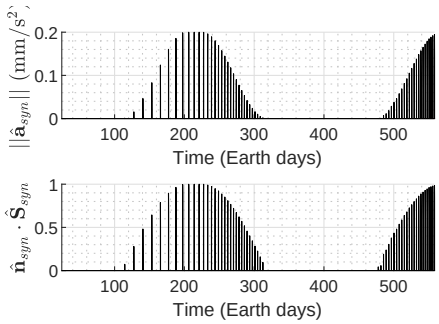

(b) Magnitude of acceleration and direction of sail normal relative to the Sun

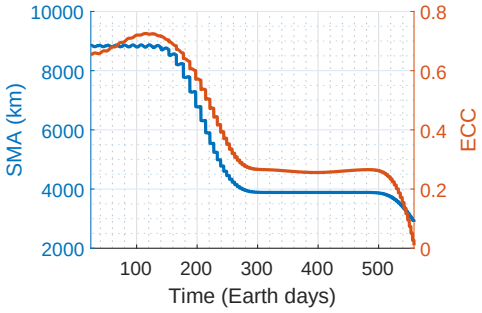

(c) Semi-major axis against eccentricity

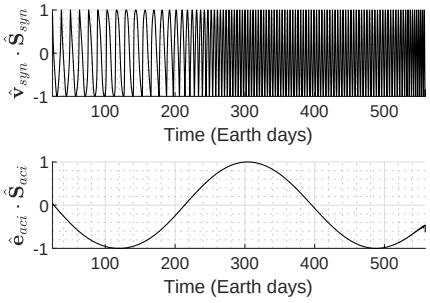

(d) Velocity direction and direction of eccentricity vector relative to the Sun

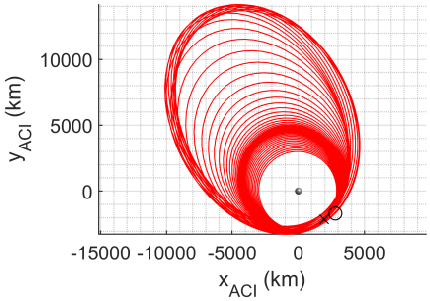

(e) Trajectory (ACI frame)

Figure 6.13: Orbit shaping phase: asteroid 1

the periapsis radius has dropped below the minimum allowed at $5r_0$. As such, this will require thrusting at apoapsis to raise the periapsis as well as the periapsis thrusting to circularise the orbit.

Once again, at the start of the orbit shaping phase the Sun is not conveniently positioned to allow an immediate start to operations. The sail does not begin thrusting until approximately 60 days into the capture process. As the sail must circularise from a high eccentricity value, it takes a considerable time to correct, during which time (between day 320 and 480) the Sun is again not conveniently positioned to allow thrusting. In total, capture is achieved in 572.75 days.

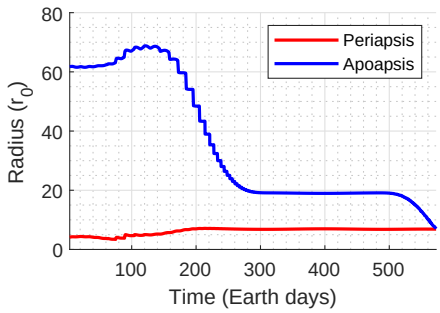

(a) Radius of periapsis and apoapsis

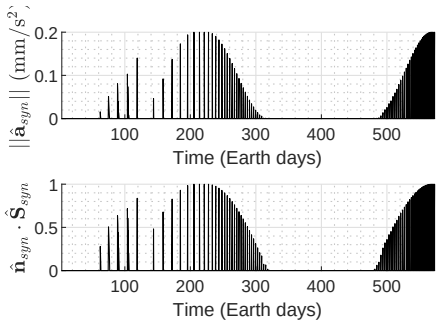

(b) Magnitude of acceleration and direction of sail normal relative to the Sun

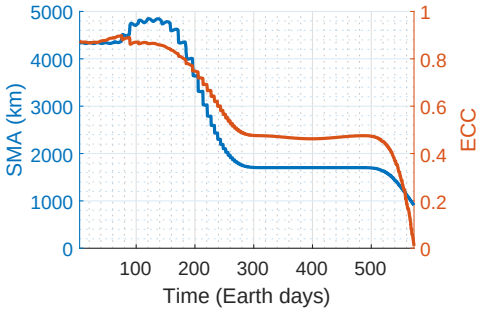

(c) Semi-major axis against eccentricity

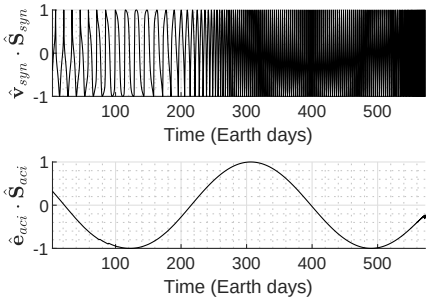

(d) Velocity direction and direction of eccentricity vector relative to the Sun

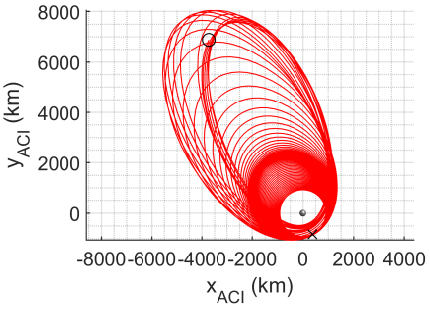

(e) Trajectory (ACI frame)

Figure 6.14: Orbit shaping phase: asteroid 2

Asteroid 3

For asteroid 3, the gravitational field is considerably weaker. This resulted in a further expedited initial capture phase and subsequent high final orbit eccentricity. The results for the orbit shaping phase at this asteroid are shown in Fig. 6.15.

Once again, it is necessary for the sail to wait until the Sun is appropriately positioned before commencing operations. In this case, the radius of the periapsis must first be raised out of the $5r_0$ exlusion zone. After this, the sail proceeds to lower the apoapsis. The total time to affect the capture at asteroid 3 is 193.96 days.

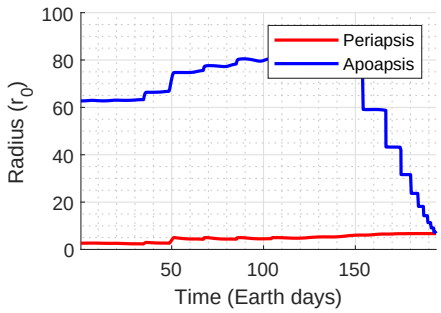

(a) Radius of periapsis and apoapsis

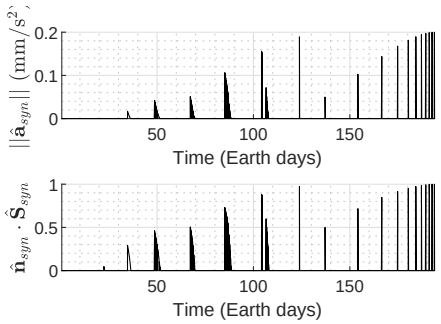

(b) Magnitude of acceleration and direction of sail normal relative to the Sun

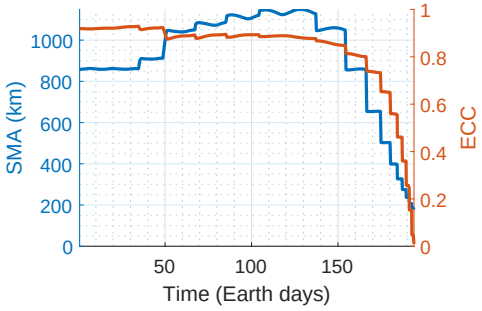

(c) Semi-major axis against eccentricity

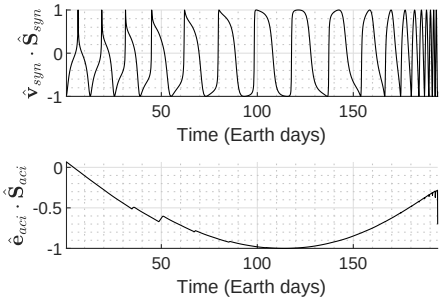

(d) Velocity direction and direction of eccentricity vector relative to the Sun

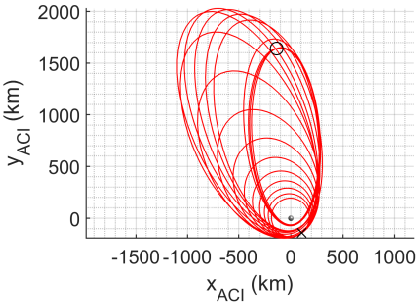

(e) Trajectory (ACI frame)

Figure 6.15: Orbit shaping phase: asteroid 3

433 Eros

As the size of each target asteroid gets smaller, we have shown the initial capture phase time reduce. This is indeed the case again for 433 Eros. Once again, the faster initial capture has resulted in a highly eccentric final orbit which must be corrected by the orbit shaping phase. The results of this phase for 433 Eros are shown in Fig. 6.16.

The initial highly eccentric orbit has its periapsis inside the $5r_0$ exclusion zone. As such, it is necessary for the orbit shaping to raise this as well as to lower the apoapsis. Initially, the sun is not in the correct position to allow immediate operation. After approximately 32 days, the first thrusting maneuvre takes place to raise the periapsis. Once this is achieved, the apoapsis can be lowered. The total time to capture at Eros is 164.36 days.

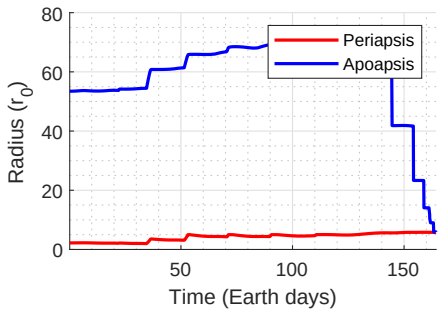

(a) Radius of periapsis and apoapsis

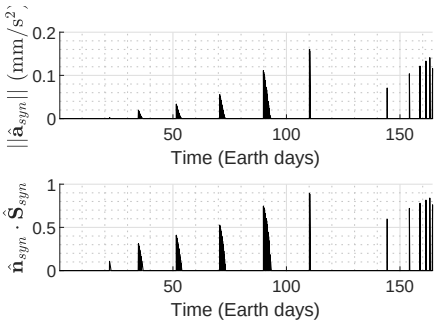

(b) Magnitude of acceleration and direction of sail normal relative to the Sun

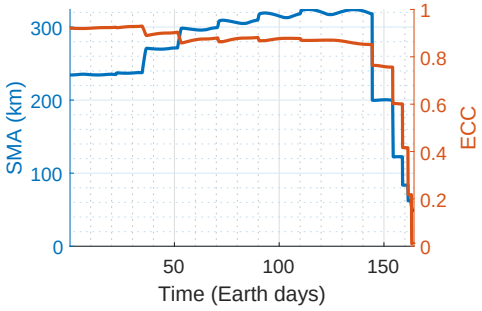

(c) Semi-major axis against eccentricity

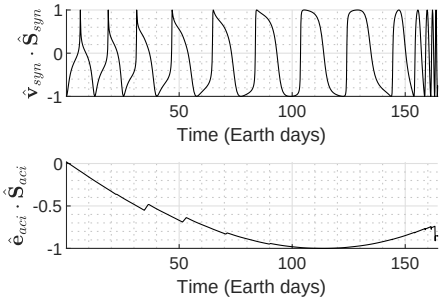

(d) Velocity direction and direction of eccentricity vector relative to the Sun

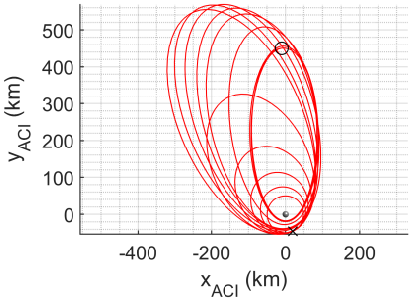

(e) Trajectory (ACI frame)

Figure 6.16: Orbit shaping phase: 433 Eros

3122 Florence$_b$

The final, and smallest, target asteroid is 3122 Florence$_b$. At this asteroid the initial capture took only 0.05 days and again ended with a very highly eccentric orbit. As is shown in Fig. 6.17, the periapsis once again has entered the $5r_0$ exclusion zone which requires it to be raised.

Again, at the initial point of the orbit shaping phase, it has been necessary to wait for the position of the Sun relative to the orbit to change. In this case, the first thrusting manoeuvre takes place after approximately 22 days. For Florence$_b$, the total time to capture is 158.47 days.

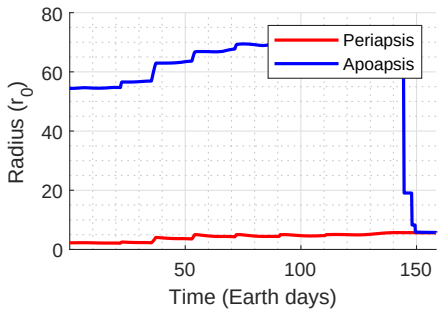

(a) Radius of periapsis and apoapsis

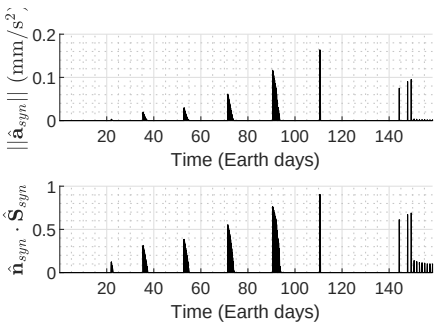

(b) Magnitude of acceleration and direction of sail normal relative to the Sun

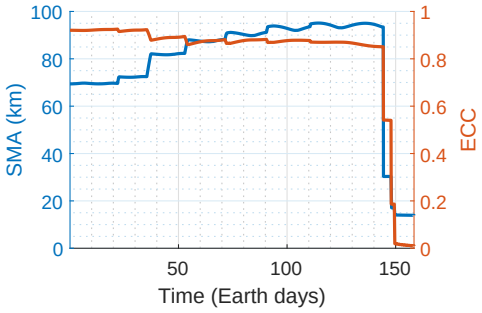

(c) Semi-major axis against eccentricity

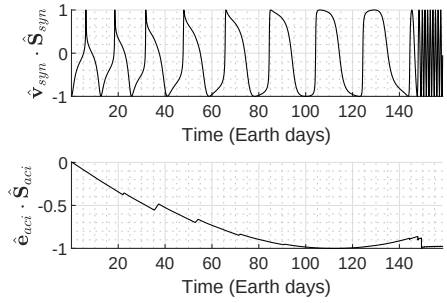

(d) Velocity direction and direction of eccentricity vector relative to the Sun

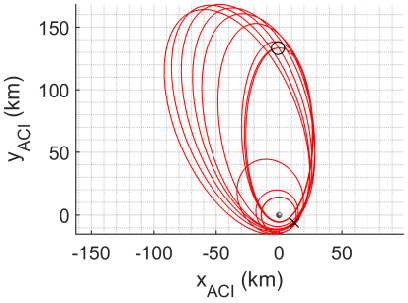

(e) Trajectory (ACI frame)

Figure 6.17: Orbit shaping phase: 3122 Florence$_b$

6.2.5 Summary of Capture at Each Asteroid for the Two-Phase Approach

The two-phase approach has shown the effectiveness of the sail in establishing gravitational capture for a solar sail around 5 target asteroids of varying size. Each asteroid has been placed in the same circular orbit at 1 AU to allow for consistency in the analysis between each. The first three bodies are based around one of the largest asteroids in our solar system, 4 Vesta. Two NEAs were also included in the analysis; 433 Eros and 3122 Florence$_b$. A summary of some key findings are listed in Table 6.2 with the asteroid parameters listed in Table 6.1.

For the two larger bodies, the total time to capture is very long. Given their stronger gravitational fields, the sail acceleration requires more thrusting time. This is then compounded by the relative position of the Sun to the orbit, over these longer time scales. In these cases, there are more periods where the Sun is not conveniently position to allow thrusting manoeuvres to

	Asteroid 1	Asteroid 2	Asteroid 3	Eros	Florence$_b$
Time in initial capture (days)	24.32	3.77	0.59	0.16	0.05
Eccentricity at end of initial capture	0.65	0.87	0.92	0.92	0.92
Periapsis Radius (r_0)	12.00	4.50	2.50	2.20	2.20
Time to first thrust in orbit shaping	118	60	32	31	22
Total Time (days)	558.52	572.75	193.96	164.36	158.47

Table 6.2: Results from two-phase capture approach

take place. As the size of asteroid reduces, and the sail becomes more powerful relative to the gravitational field, the initial capture time reduces accordingly. For these shorter initial capture times, there is a corresponding increase in the eccentricity of the orbit at the end of the initial capture phase. For these higher eccentricity orbits, the radius of periapsis tends to drop below the $5r_0$ exclusion zone where the asteroid shape and spin state become important factors in the gravitational field. In these cases, it was necessary for the sail to raise the periapsis before then lowering the apoapsis and circularising the orbit. The relative position of the Sun to the orbit, $\hat{\mathbf{e}}_{\text{ACI}} \cdot \hat{\mathbf{S}}_{\text{ACI}}$, is an important factor as it defines when the sail is able to thrust for the desired operations. As the sail is not thrusting instantaneously at periapsis and apoapsis, but over an arc of 18° of true anomaly either side, there is a rotation of the orbit with respect to the Sun in each case, in addition to the rotation of the Sun when considered in the ACI frame. This rotation is more pronounced in the weaker gravity fields and there are more pronounced variations in the value of $\hat{\mathbf{e}}_{\text{ACI}} \cdot \hat{\mathbf{S}}_{\text{ACI}}$ over the course of the orbit shaping phase as the asteroids get smaller. It is also clear that the shorter time spent in initial capture results in smaller initial values of $\hat{\mathbf{e}}_{\text{ACI}} \cdot \hat{\mathbf{S}}_{\text{ACI}}$. As such, the time to first thrusting manoeuvre reduces as the size of the asteroid reduces.

This work has shown that simple steering laws for the sail, which exploit the dependency on transversal thrusting to changes in the size of an orbit, are capable of producing effective orbit capture methods from trajectories which are initially distant from the asteroid surface.

6.3 Optimal Control Capture

With a sub-optimal solution now presented, this section will seek optimal capture solutions using the solar sail. In order to facilitate this, a change of the dynamical model to use the MEEs discussed in Section 6.2.3 is required. This work will assume the approach trajectory has targeted an approach much closer to the asteroid than the previous sub-optimal work. As such, being close to the asteroid, a two-body dynamical model is employed where the asteroid is considered ellipsoidal in shape. The larger body, 4 Vesta, is considered here and has a rotational period of 5.34 hours. As the trajectories in this work a relatively short, the position of the Sun is considered fixed with $\hat{\mathbf{S}}_{\text{ACI}} = [1, 0, 0]$. Once again, the asteroid orbit is considered circular at 1 AU.

6.3.1 Definition of the problem

A low-thrust orbital transfer problem is presented in Ref. [9], which takes a low-Earth orbit to a higher orbit of increased inclination using a low-thrust propulsion system. This problem will be used as a starting point for the capture problem as a capture is simply the inverse of this type of outbound transfer trajectory.

This outbound transfer trajectory will be solved using the Radau collocation method, described in Chapter 2, applied using the GPOPS-II software [139]. The objective of this orbital transfer is to minimise the propellant consumption. As such, this can be seen as maximising the final spacecraft mass:

$$J = -w_f \tag{6.5}$$

This optimisation is subject to the path constraint:

$$||\mathbf{u}(t)|| = 1 \tag{6.6}$$

with the control constrained such that $u_r \in [-1,1]$, $u_\theta \in [-1,1]$ and $u_h \in [-1,1]$. A set of boundary conditions is also required and are given by:

$$\begin{aligned}
&p(t_0), && p(t_f),\\
&f(t_0), && \sqrt{f^2(t_f)+g^2(t_f)},\\
&g(t_0), && \sqrt{h^2(t_f)+k^2(t_f)},\\
&h(t_0), && f(t_f)h(t_f)+g(t_f)k(t_f),\\
&k(t_0), && g(t_f)h(t_f)-k(t_f)f(t_f),\\
&L(t_0), && w(t_0),\\
&i(t_0), && i(t_f),
\end{aligned} \tag{6.7}$$

The dynamics for this problem are contained in Eqs. 6.2 and the boundary conditions and results are shown in Appendix D.3

By using this example as a starting point, it is possible to generate an inward spiralling trajectory, such as will be desirable for the capture problem. In the example problem, the first guess is established by propagating a ballistic trajectory and pointing the propulsive thrust along the velocity vector. In order to invert the problem to an inward spiralling problem, the direction of thrust is reversed in the initial guess. So that the problem can be more easily adapted to a solar sail problem, the variable thrust model is changed such that the dynamics contain a constant thrust with the maximum acceleration available from the propulsion system set at the desired characteristic acceleration for this work, $a_c = 0.2$ mm/s^2. The system of units is also converted to SI.

6.3.2 Time-Optimal Capture

Now, the example problem stated in Section 6.3.1 is amended for a time-optimal control problem where the boundary conditions contain the targeted orbit radius in terms of $p(t)$ and the objective function is given by:

$$J = t_f - t_0 \tag{6.8}$$

The first step is to produce a solution for a generic low-thrust propulsion system which can then be used as the initial guess for a solar sail solution. In the first instance, a loose set of boundary conditions are set which allow the solver to accept a final planar orbit with eccentricity, $e \in [0,1]$:

$$\begin{aligned}
&p(t_0) = 10r_0 \text{ km}, && p(t_f) = 5r_0 \text{ km},\\
&f(t_0) = 0, && \sqrt{f^2(t_f)+g^2(t_f)} = 1,\\
&g(t_0) = 0, && \sqrt{h^2(t_f)+k^2(t_f)} = 0,\\
&h(t_0) = 0, && f(t_f)h(t_f)+g(t_f)k(t_f) = 0,\\
&k(t_0) = 0, && g(t_f)h(t_f)-k(t_f)f(t_f) \leq 0,\\
&L(t_0) = \pi \text{ rad}, &&\\
&i(t_0) = 0^\circ, && i(t_f) = 0^\circ,
\end{aligned} \tag{6.9}$$

The results of this simulation are shown in Fig. 6.18. As there is no constraint on the eccentricity value, the optimisation can focus on the fastest possible reduction in the orbit semi-parameter, p. As discussed in Section 6.2.3, this can most efficiently be done my maximising the component of the control vector in the transversal direction, which is the case in this example.

Following this, a tighter set of bounds are placed on the optimal control solver which target a specific set of classical elements for the initial and final orbits which are planar and circular:

$$\begin{aligned}
a(t_0) &= 10r_0 \text{ km}, & a(t_f) &= 5r_0 \text{ km},\\
e(t_0) &= 0, & e(t_f) &= 0,\\
i(t_0) &= 0^\circ, & i(t_f) &= 0^\circ,\\
\Omega(t_0) &= 0^\circ, & \Omega(t_f) &= 0^\circ,\\
\omega(t_0) &= 0^\circ, & \omega(t_f) &= 0^\circ,\\
\theta(t_0) &= 0^\circ, & \theta(t_f) &= 0^\circ,
\end{aligned} \tag{6.10}$$

These elements are converted to MEEs by Eqs. 6.1 and set as the boundary conditions. The results for this simulation are shown in Fig. 6.19.

As the eccentricity must take the value $e = 0$, it is necessary for the control to use both the radial and transversal components. The normal component continues to have zero value given that we

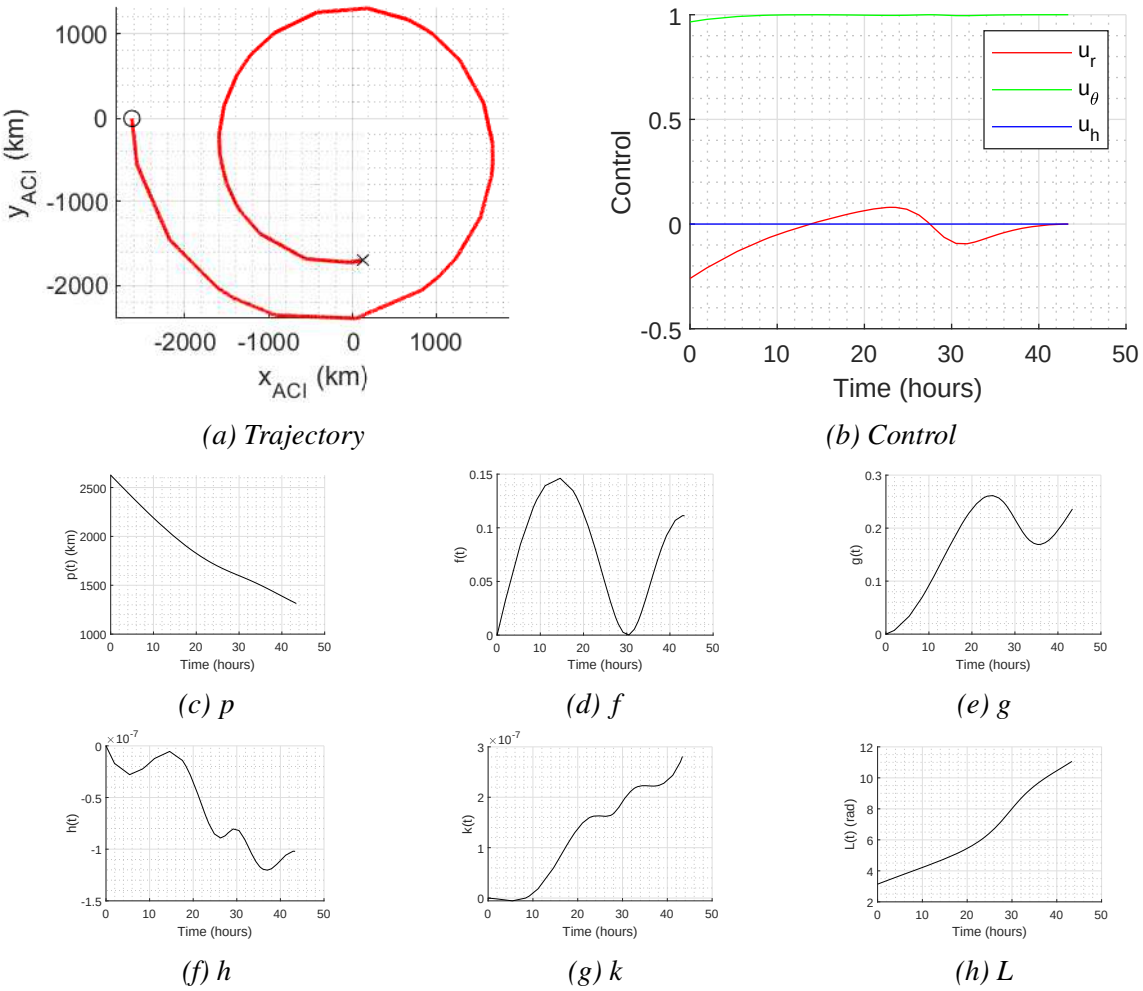

(a) Trajectory *(b) Control*

(c) p *(d) f* *(e) g*

(f) h *(g) k* *(h) L*

Figure 6.18: Adapted problem giving low-thrust inward spiral trajectory at asteroid Vesta.

seek only planar solutions here.

These results have shown the potential for an optimally controlled low-thrust propulsion system of bring about the reduction in orbital radius around an asteroid. However, attempts to use this solution as a first guess for a solar sail solution were not successful as the optimisation did not converge. As such, the optimisation is changed to minimise $p(t)$ during one orbital revolution and to investigate the potential for a successful solar sail control law.

6.3.3 Optimisation of the Reduction of the Orbit Semi-Parameter

The objective is now the minimisation of the semi-parameter, $p(t)$, over a single revolution on the orbit. For this, the boundary conditions are changed to:

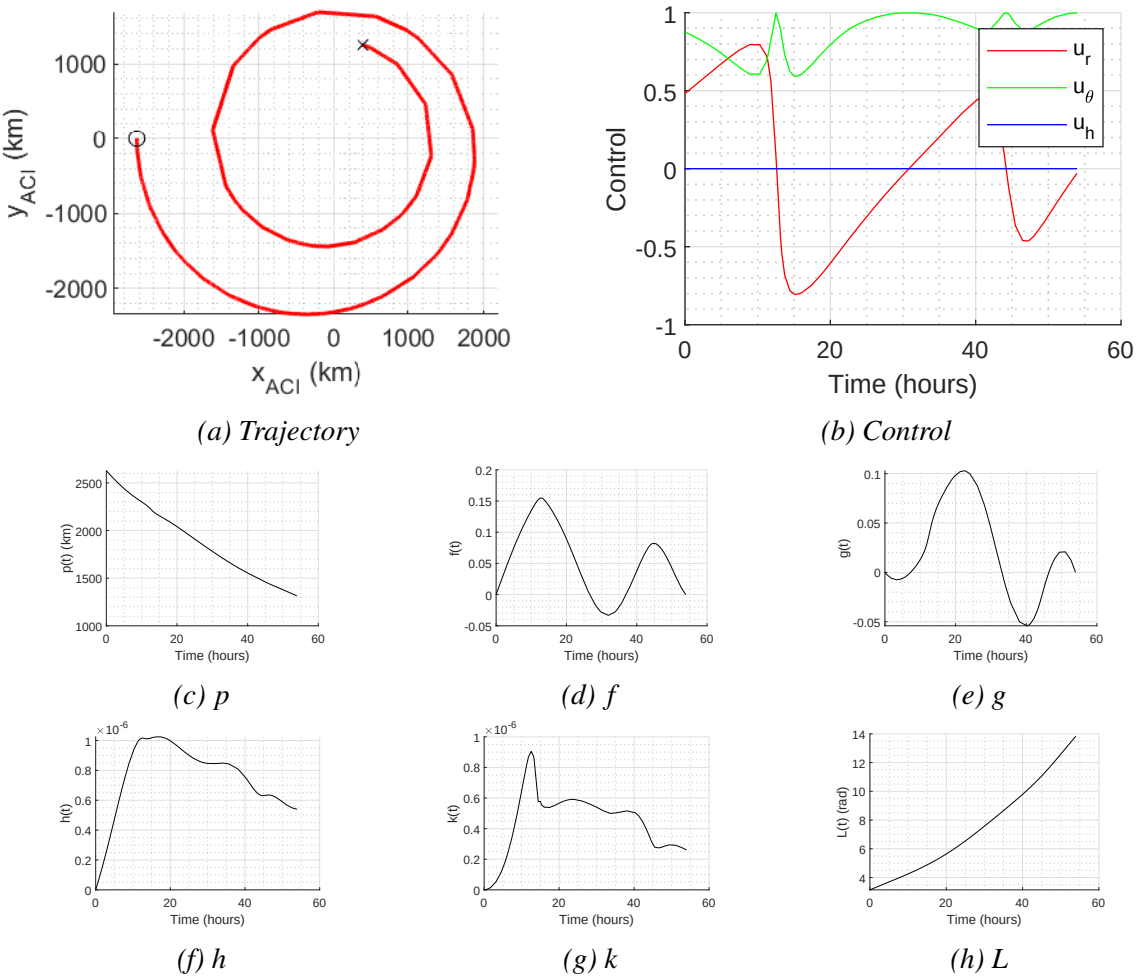

(a) Trajectory *(b) Control*

(c) p *(d) f* *(e) g*

(f) h *(g) k* *(h) L*

Figure 6.19: Adapted problem giving low-thrust inward spiral trajectory at asteroid Vesta with constraint on eccentricity

$$
\begin{aligned}
f(t_0) &= 0, & \sqrt{f^2(t_f)+g^2(t_f)} &= 0,\\
g(t_0) &= 0, & \sqrt{h^2(t_f)+k^2(t_f)} &= 0,\\
h(t_0) &= 0, & f(t_f)h(t_f)+g(t_f)k(t_f) &= 0,\\
k(t_0) &= 0, & g(t_f)h(t_f)-k(t_f)f(t_f) &\leq 0,\\
L(t_0) &= 0 \text{ rad}, & L(t_f) &= 2\pi \text{ rad}
\end{aligned}
\tag{6.11}
$$

with the objective function given by:

$$J = p(t) \tag{6.12}$$

Once again, a solution is first sought using a generic low-thrust propulsion system which will then be used as the initial guess for a solar sail solution. Figure 6.20 shows the results of this simulation for a low-thrust propulsion system.

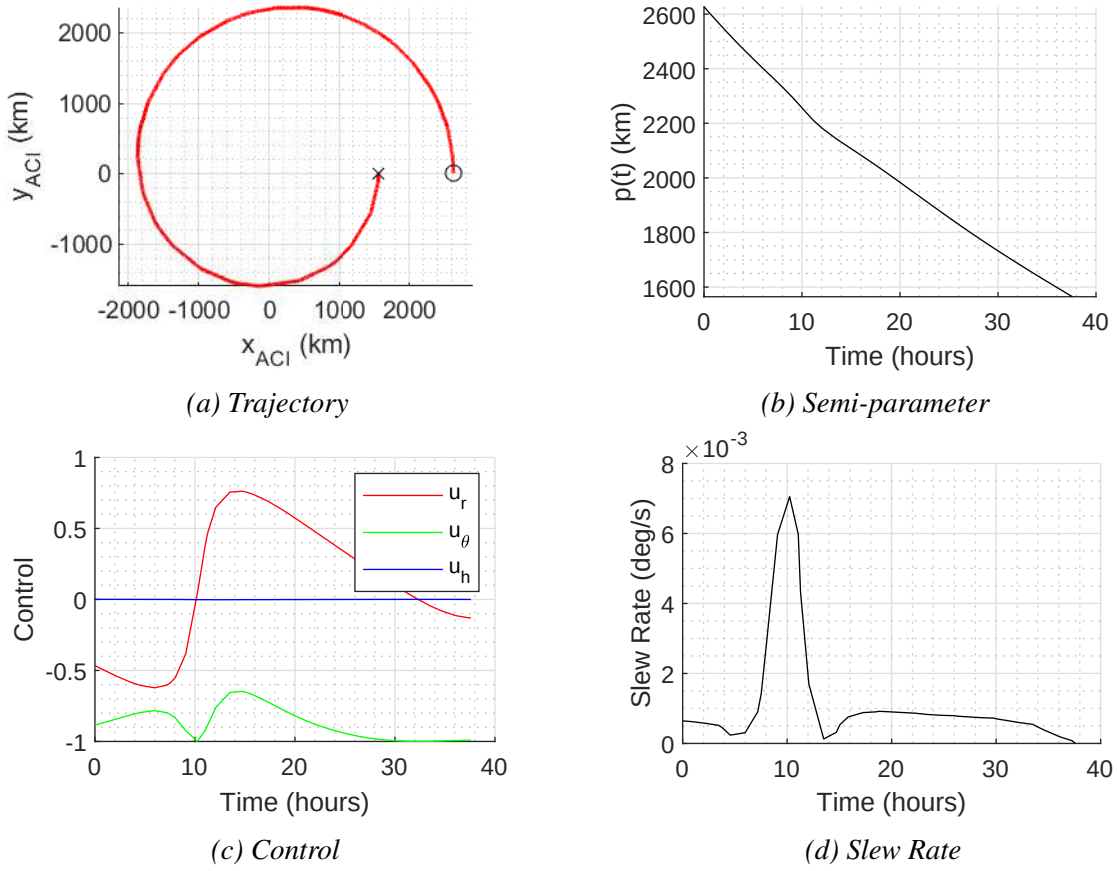

(a) Trajectory *(b) Semi-parameter*

(c) Control *(d) Slew Rate*

Figure 6.20: Low-thrust inward spiral, minimising $p(t)$ during one revolution.

This solution is then applied to a solar sail model as a first guess. In order to ensure feasible control laws, the solar sail is subject to the following path constraints:

$$\begin{aligned} ||\mathbf{u}(t)|| &= 1 \\ \hat{\mathbf{S}}_{\text{ACI}} \cdot \hat{\mathbf{n}}_{\text{ACI}} &\in [0,1] \end{aligned} \tag{6.13}$$

With the constraints applied, the solar sail solution is shown in Figure 6.21. This shows that the sail has successfully reduced the value of $p(t)$ by approximately 300 km over one orbit revolution, which has a period of approximately 40 hours. During this, the slew rates of the sail remain relatively small, which promotes the feasibility of this control for a real-world sail. It is worth noting there are periods where the reduction in $p(t)$ is frozen. This is due to the sail not being able to thrust where $\hat{\mathbf{v}}_{\text{ACI}} \cdot \hat{\mathbf{S}}_{\text{ACI}} < 0$.

6.3.4 Summary of Optimally Controlled Capture

In this section, an optimal control approach has been taken to the capture problem. In the first instance, a particular reduction in orbit radius was sought for a minimal time transfer. This work produced a solution for such a transfer but only for a generic low-thrust propulsion system.

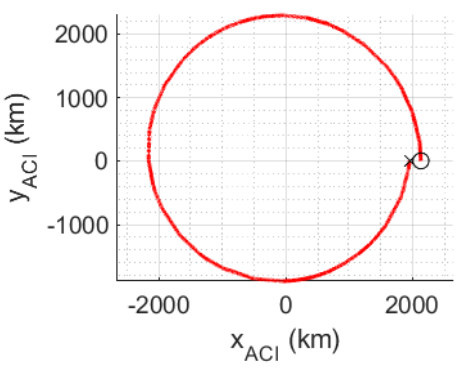

(a) Trajectory

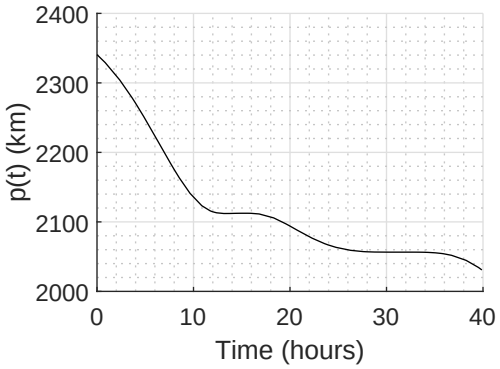

(b) p(t)

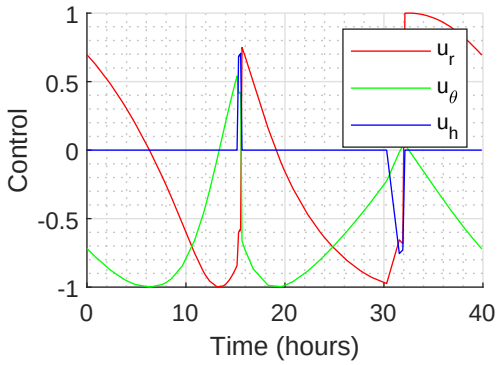

(c) Control

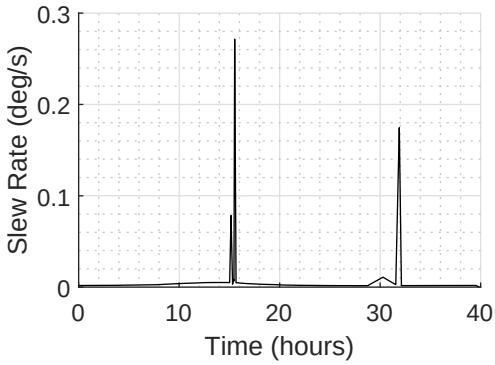

(d) Slew-rate

Figure 6.21: Optimal solution minimising p(t) over one orbital revolution.

This solution was then used as the initial guess of a solar sail solution. However, with the restriction on the control which does not allow thrusting in the direction of the Sun, the solver failed to converge. As such, a second approach was taken: minimisation of $p(t)$ over one orbit revolution. This method showed the successful reduction of $p(t)$ by a value of approximately 300 km during one orbit revolution. In order to reduce to a target orbit altitude, this method could be applied in multiple phases until the orbit reaches a desired altitude above the asteroid. This is not shown here but will be considered for future work which will be detailed in Chapter 7.

Chapter 7

Conclusions

This thesis has aimed to establish techniques in conducting operations for a solar sail in proximity of an asteroid. The three main areas which were addressed were in controlling the effects of a non-spherical gravity field, the control of a sail during and after deployment of a lander and a series of small probes and in the gravitational capture of a spacecraft where the solar sail is the primary propulsion system. This chapter will present a summary of the work performed, the main findings, limitations related to the work contained in this thesis and recommendations for future work.

7.1 Summary of Work

Solar sails provide an attractive option for mission designers of high-energy missions: such as multiple asteroid rendezvous missions. To enable such missions to have scientific merit, the sail must be capable of operating the the relatively weak gravity field of these small bodies. A survey of existing asteroid missions and the potential for a solar sail in this context were presented in Chapter 1. In order to adequately carry out the work required for the proposed research, a number of numerical tools were required. These were outlined in Chapter 2, along with the relevant reference frames and mathematical models.

Before investigating the use of the sail in achieving the mission goals, an extensive study of the so-called "inner" and "outer" dynamical regimes was performed in Chapter 3. In the inner regime, the sail is close enough to the asteroid that the shape and spin-state are important factors in the gravitational field. As such, in this regime, different shape modelling techniques were employed. When the sail is not approaching the asteroid surface, an ellipsoidal shape model is applied. When the sail, or deployable, approaches the surface, the more detailed polyhedron shape models are employed. In the outer regime, the sail is sufficiently distant from the asteroid that the shape and spin-state of the asteroid have a negligible effect on the gravity field, and so the body can be represented by a point mass. In this regime, the 3-body dynamical model is employed given the importance of the gravitational effects of the Sun on the system at these

distances.

After the definition of the the work that has come before, the tools required for the research to be conducted and the dynamical environments in which the work takes place, the thesis moved on to studying three distinct proximity operations for a solar sail at an asteroid: controlling the effects of a non-spherical gravity field, deployment of probes and landers and achieving capture using the sail as the primary propulsion system.

In the first operation, detailed in Chapter 4, the first objective was to reduce the rate of nodal regression using the solar sail. The non-spherical shape of an asteroid can lead to a spacecraft trajectory either impacting the surface or escaping the asteroid system. Given that the science mission goals may require extended and controlled orbits, this work would show the utility of the sail in controlling any perturbative effects. Following this, a method of controlling an orbit was presented which utilised a new tool which aimed to reduce the final state error of one orbit to the next. By doing so, it would be possible for the sail to force the trajectory into a nearby periodic orbit, guaranteeing continued operation of the spacecraft in pursuit of the scientific mission goals.

The second operation is critical to any mission which seeks to interact with the surface of a body: the deployment of a lander and a series of small probes. Chapter 5 describes this operation, beginning with a description of the deployed vehicles and the targeted asteroids. Following this, the zero-velocity deployment of a lander is presented in the inner regime, where the deployment locations are based around the equilibrium points and the potential ridge line, which were discussed in Chapter 3. A Monte Carlo approach was used to analyse the success rate for lander trajectories intersecting the asteroid surface when deployed from each of the defined regions. Following this, a low-altitude orbit deployment is investigated where the nominal orbit for the sail is first defined before the correction required to this orbit to maintain periodicity is investigated upon deployment of the lander. The work then moves to the outer regime, where deployments of the lander from the full range of AEPs are investigated. A different mission scenario is then presented in the deployment of a series of small ChipSat probes towards the asteroid surface. This presents a new problem in that the change in sail performance reduces in small increments, rather than one large instantaneous change.

The final operation presented in this work is in the gravitational capture of a spacecraft where a solar sail is the primary propulsion system. The work centres around three bodies of varying size and mass: 4 Vesta, 433 Eros and 3122 Florence. In the first instance, a simple on/off control law is applied around asteroid 4 Vesta. Following this, six different bodies are targeted using a two-phase approach. The targeted bodies are three representations based on the size of 4 Vesta as well as 433 Eros and 3122 Florence. The two-phase approach consists of an initial capture phase, where the objective is to reduce the orbital radius as well as the orbit shaping phase, which then aims to circularise the orbit. A time-optimal approach is then presented where the sail begins its trajectory closer to the asteroid after a targeted insertion. An established optimal

control problem considering an outbound Earth orbit transfer for a low-thrust spacecraft is then converted to facilitate the capture of a low-thrust spacecraft. Finally, a solar sail solution is presented in the minimisation of the orbit semi-parameter during one orbit revolution.

7.2 Summary of Findings

This section will outline the main findings from the work carried out in this thesis. The section is subdivided based on the three main sections of work, defined as three distinct proximity operations: the control of the sail in the irregular gravity field of an asteroid, the deployment of large landers and small probes and the gravitational capture of a solar sail around an asteroid.

7.2.1 Control of a Solar Sail Around an asteroid

In the first operation, that of controlling the orbit of a sail in an irregular gravity field, the PR method was first applied to reduce the rate of nodal regression around an ellipsoidal representation of asteroid 3122 Florence. By applying a weighting parameter to the optimal control problem, it was possible for the method to first find a periodic orbit solution before continuing towards a minimum effort control law. In doing so, it was possible for the method to reduce the rate of nodal regression from $\dot{\Omega} = 55$ deg/day for the uncontrolled orbit to $\dot{\Omega} = 3$ deg/day for the orbit controlled by the PR method. Given that this is all achievable with the minimum effort required of the sail, the PR method is shown to be a useful tool in orbital station keeping.

Following this, and owing to the difficulties in establishing a sufficiently good initial guess for the direct collocation method used in the preceding work, a new approach was taken. This work used a GA to conduct a multi-objective optimisation to obtain a periodic orbit while also minimising the effort required by the sail. This method proved successful in establishing near-periodic orbits while also presenting solutions with low effort values. It was found that, although the orbits were very nearly periodic, the small discrepancy between final and initial state meant that the control law was not valid for any subsequent orbits, and would lead to divergence from the nominal trajectory on any subsequent orbit. As such, a method of updating the control law for any subsequent orbit was presented. It was in this work that the CTM was presented; a matrix containing information on the effects of variation in control on final state errors, to update the control law, allowing for periodic orbits to be established. This method of updating the control law was found to be limited by the orbital inclination. This inclination limit was also found to vary with the right ascension of the orbit's ascending node. It is known that the magnitude of the tesseral and sectoral harmonics is small relative to that of the zonal harmonics for the ellipsoid studied in this work. As the zonal harmonics dominate, and are invariant in longitude, the asteroid rotation has negligible effect on analysing the effect of parameters which are longitudinal, such as varying Ω. Analysis on this variation was presented with a boundary between the convergent and divergent regions. It is expected that other orbital parameters (such

as semi-major axis and eccentricity) will also affect this convergence study. However, this work presents an initial analysis where these parameters remain fixed.

Finally, to generate a realistic, smooth control law, the piece-wise-continuous interpolation of the control was replaced with cubic splines, which allowed gradual transitions in attitude. The CTM method was once again successful in establishing a periodic orbit from this updated nominal orbit, with a small increase in required effort from the sail. Analysis of the torque which would be required from the ACDS were then shown. These results showed that the maximum required torques lay well within the maximum torques of realistic sail examples from the literature.

The controls established in this work are feasible even for a large structure, such as a solar sail. Indeed, the obtained orbits through this chapter have shown the the sail is capable of almost completely eliminating the effects of a non-spherical body on the orbit of a spacecraft. Consequently, it could be shown that a sail may achieve such control as to permit Sun-synchronous orbits (SSOs), or other classes of orbit which require control of such effects.

7.2.2 Deployment of Small Probes and Large Landers from a Solar Sail

In the deployment of a Lander in the inner regime, the work presented in Chapter 5 provides a probabilistic analysis of successful intersection with the surface of a lander after ballistic deployment with zero initial velocity from four locations in the phase space: natural equilibrium points, along the potential ridge line, interior to the potential ridge line and exterior to the potential ridge line. Unsurprisingly, the interior region provided the highest success rate (92.01%) for the lander to successfully make its way to the surface of the asteroid. This means that any deployment strategy that aims to deliver a ballistic lander to the surface would be best placed to do so by deploying from this region. It is, however, still possible to achieve a successful ballistic deployment from outside the potential ridge line if a small impulse can be given to the lander at release.

Following this, the deployment of a lander from a low-altitude orbit was investigated. In the deployment of the larger MASCOT-type lander, two nominal pre-deployment orbits were first established by a GA. At the end of the nominal orbit period, the lander was deployed and the sail maintained its orbit in the region of the nominal orbit before converging to a near-equatorial orbit using TDFC. This method was successful for both deployment orbits, though deployment from orbit 2 required far longer to converge to the final planar orbit.

With the work related to deployment in the inner regime, the analysis moved to deployment from the outer regime. Here, the work provided analysis of the landing conditions for a ballistic lander from the AEPs of the outer regime. Given the long descent trajectories required for these landers, the landing velocity was found to be significant. As such, the deployment of a ballistic lander from these distances to the surface, would not be recommended.

In an effort to provide options for deployment from the outer regime, a new mission scenario

was envisaged. This involved the deployment of a series of small ChipSat probes towards the asteroid surface. The sail was able to successfully hold a position close to the original deployment point. However, the effort required by the sail to maintain the LQR control did not produce results which were of such an improvement over maintaining a fixed sail attitude to warrant their recommendation for a real-world scenario. It was found that the deployment location which trailed the asteroid rotation was not able to deploy any of its probes to the asteroid surface, but instead they remained in orbit around the asteroid. As such, these probes could support science cases while orbiting, offering further options to mission designers.

7.2.3 Gravitational Capture of a Solar Sail Around an Asteroid

First, an "on/off" switching law was implemented. This study showed that, owing to sensitivities of the weak asteroid gravity field in presence of increasing sail a_c, as the value of a_c increases, so too do the opportunities for this rudimentary control method to result in the sail escaping the asteroid system. These escape trajectories are initiated by a strong thrust being provided by the sail at a point along the orbit which increases the value of C too rapidly for any correction to be made before the sail escapes. In addition to a dependence on the value of a_c, these escaping trajectories were also dependent on the value of DB assigned to the simulation. Larger DB tended to allow for more opportunities for the sail to provide a thrusting manoeuvre which resulted in escape.

Following this initial analysis, a two-phase approach was presented and applied to five bodies of reducing mass, and so of increasing sensitivity to a sail of fixed a_c. This two-phase approach proved successful in achieving the objective of circularising the orbit of a spacecraft within a defined radius from the asteroid using a solar sail. It was found that the orbit shaping phase often had to wait for the orientation of the orbit with respect to the Sun to change such that the Sun was positioned favourably for operations to begin. This often led to considerable times to final capture. It was found that the initial capture time was reduced where the mass of the targeted asteroid was reduced. This is owing to the increased strength of the sail acceleration relative to the asteroid gravitational acceleration. However, faster initial capture times also resulted in higher eccentricity orbits to then be circularised by the orbit shaping phase, and often with the periapsis inside the exclusion zone and so requiring to be raised.

With the two-phase approach defined, the focus moved to providing optimal solutions. Initially, a time-optimal approach was described. This built upon low-Earth orbit transfers for low-thrust propulsions systems as detailed in the literature. By inverting this problem to a spiralling inward trajectory, a low-thrust time-optimal solution was presented. However, issues in convergence for the solar sail control led to a new approach where the orbit semi-parameter was to be minimised over one complete orbit revolution. It was in this scenario that a successful sail control law was established, though once again it was difficult to implement this as a multi-phase process to achieve a specific orbit due to time constraints at the end of the PhD. As such, this has

become a potential area for continued work on asteroid proximity operations using solar sails.

7.3 Limitations of the Current Work

This thesis covers a broad range of topics concerning proximity operations of a spacecraft near a body of interest. In this, there have been simplifications made which will be listed in this section.

7.3.1 Placement of the Asteroid Orbit

The distance of the Sun to the asteroid around which the sail is in orbit is not only important in terms of the gravitational effects where a 3-body system is considered, but also in the magnitude of the SRP which propels the sail. As such, it is necessary to define the Sun-asteroid distance (which in this work, given the proximity of the sail to the asteroid, is considered equal to the Sun-sail distance). Throughout this work, it was decided that all asteroids would be place in a circular orbit at 1 AU. This also applied where bodies such as 4 Vesta, which is actually a main belt asteroid. The justifications for such decisions were as follows:

1. With the Sun at 1 AU, the maximum magnitude of acceleration that can be provided by the sail is the performance metric characteristic acceleration, a_c. Having this maximum be a constant allowed for ease of comparison between different simulations.

2. Although asteroid can be in highly eccentric orbits, the only effect this would have on the problems posed would be in the magnitude of the SRP and the gravitational acceleration from the Sun. In this work, it was decided to maintain these effects constant, rather than have the time-varying situation that an elliptical orbit would bring.

3. Where an asteroid was proposed as the target body, this was not due to any desire to propose a mission to that body specifically, but rather to do with presenting a body with a required set of physical parameters or the availability of detailed shape models. For instance, in the consideration of operations at 4 Vesta, a main belt asteroid, the inclusion of this body related to the need for a large body where any concerns about the feasibility of bound motion due to a relatively powerful sail to be dissuaded in addition to the need for the asteroid to have a well defined high-resolution shape model.

7.3.2 Consideration of the Landing Conditions for Deployed Landers and Probes

The work presented in Chapter 5 established that landers deployed from considerable distances from the asteroid surface would result in high-velocity impacts which the landers would not

survive. In order for the landing velocity to be reduced, the work in Section 5.3.2 shows that very low-altitude deployments are required. This presented considerable difficulties for a solar sail given that close proximity operations may require control laws which for the sail may not be feasible. The limitations on the current work is that further investigation of the required proximity for a safe deployment to the surface was not conducted. In the case where deployment was made from a low-altitude orbit, the attention was focused on the control of the sail after the instantaneous change in sail performance.

7.4 Recommendations for Future Work

As there are numerous tasks a spacecraft may perform while in proximity of a body of interest, there remains not only improvements to the current work, but also new areas of research which would be very interesting. This section will outline some of the areas which the author feels would be of great interest.

7.4.1 Strong Coupling of Attitude and Orbital Dynamics During Payload Pointing

A possible mission objective for a sail in proximity of an asteroid could be in the imaging of the asteroid surface. If the imaging system on-board the spacecraft is fixed to the body, then the sail would be required to point the camera at the target of interest on the surface. This scenario presents a very interesting problem due to the strong coupling of the sail attitude to the orbital dynamics, and would be a very welcome addition to the current body of literature on solar sail missions.

7.4.2 Accounting for Real Asteroid Orbits

As mentioned in Section 7.3, the asteroids considered in this work were all placed on circular orbits at 1 AU from the Sun. The next logical step in the mission design process would be to look at the time-varying effects on SRP and solar gravity that a elliptical orbit model would present. In terms of SRP, this would result in a time-varying magnitude of acceleration, which would impact the control laws presented here. In terms of solar gravity, in those mission scenarios utilising 3-body dynamics, there would be a time-varying change to the geometry of the Sun-asteroid gravity field. Adding to this the effects of changing sail attitude on this geometry would provide a very complex system for the mission designer, and would be of great interest to the solar sailing community.

7.4.3 Control Transition Matrix

The CTM, presented in Chapter 2 and applied in Chapter 4, provided a means by which the control law for the sail could be updated to account for final state errors, allowing the orbit to maintain periodicity. This method was shown to be successful for a range of orbits, though was still lacking in rigour at this point. It is the intention of the author to continue working on this method as it may present a useful tool for future mission designers. The intention is to make more robust the methodology and then to present the results for the application in a range of different scenarios.

7.4.4 Sail Descent to the Surface

In the work presented in Chapter 5, the sail remains in orbit around the asteroid. One scenario which was envisaged was to bring the sail down into contact with the surface of the asteroid. There are considerable challenges in the dynamics of such a problem, which would provide a very interesting contribution to the literature.

7.4.5 Optimal Control for Gravitational Capture

The work presented in Chapter 6 provided an initial investigation into optimal control for gravitational capture. However, this work took place at the end of the PhD and there was insufficient time for the work to be completed. As such, a continuation of this work would be desirable to show that time-optimal capture using a solar sail is possible, given that the scenario presented here was for a low-thrust spacecraft, rather than for a sail. It would also be desirable for the work on the minimisation of the orbit semi-parameter during one orbit revolution to be extended to multiple revolutions, as a multi-phase orbital control problem, such that the semi-parameter can be reduced to a desirable value. Such an optimal approach would also benefit the targeting of final orbits where the orbital plane has been changed.

7.4.6 Investigation of Lander Deployment Orbits for Low-Velocity Landings

As outlined in Section 7.3, the work of Chapter 5 has shown that low-velocity landings are achievable for a ballistic lander only where the deployment is made close to the asteroid surface. However, the challenges of bringing the sail so close to the asteroid meant that the focus of work when deploying from a low-altitude orbit was directed towards the control of the sail at the point of lander separation and thereafter. This was identified as a gap in the current literature, and so the author feels that focus to be justified here. However, it would be interesting for future work to establish deployments which result in survivable landings for the deployed lander.

7.4.7 Application of Machine Learning for Control

Throughout this thesis it has been made clear just how sensitive the weak gravity field of a small body is to the acceleration provided by a relatively powerful sail. As such, any optimal control laws calculated for a real-world spacecraft may, upon arrival at the target asteroid, be rendered obsolete due to the high uncertainties around the true asteroid shape. As such, it would be of great interest to apply machine learning techniques to allow the spacecraft to make a quick assessment of the requirements for variations in that optimal control law to facilitate the required orbit or mission objective. This work may build on the work carried out with the control transition matrix in this work, where the effects of variations in control on the final state error are measured and used to correct the control law to maintain periodicity in an orbit.

Appendix A

Gravitational Field Models

A.1 Ellipsoidal Harmonic Expansion (EHE)

As alluded to in section 1.4.4, a more accurate form of modelling highly irregular bodies comes from use of the Ellipsoidal Harmonic Expansion (EHE). Where the SHE is the solution to Laplace's equation based on spherical coordinates (r, δ, λ), the EHE is the solution to Laplace's equation in ellipsoidal coordinates. These coordinates are found by solving the roots of the following:

$$\frac{x^2}{\lambda^2} + \frac{y^2}{\lambda^2 - h^2} + \frac{z^2}{\lambda^2 - k^2} = 1$$

where λ in this case is the root of the cubic polynomial, not the longitude from the spherical coordinates of section 1.4.4. Also $k > h > 0$ and $\lambda_1 \geq k \geq \lambda_2 \geq h \geq \lambda_3 \geq 0$ [52].

Solving Laplace's equation for the external potential yields the following [52]:

$$V = GM \sum_{n=0}^{\infty} \sum_{m=1}^{2n+1} \bar{c}_{nm} \frac{F_{nm}(\lambda_1)}{F_{nm}(\lambda_1^{(0)})} \bar{E}_{nm}(\lambda_2) \bar{E}_{nm}(\lambda_3)$$

where E_{nm} is the mth normalised Lamé function of degree n and satisfies the following Lamé equation [52]:

$$\begin{aligned} \left(\lambda_j^2 - h^2\right)\left(\lambda_j^2 - k^2\right) \frac{\mathrm{d}^2 E_{nm}(\lambda_j)}{\mathrm{d}\lambda_j^2} + \lambda_j \left(2\lambda_j^2 - h^2 - k^2\right) \frac{\mathrm{d}E_{nm}(\lambda_j)}{\mathrm{d}\lambda_j} + \ldots \\ \ldots + \left[\left(h^2 + k^2\right) p_m - n\left(n+1\right)\lambda_j^2\right] E_{nm}\left(\lambda_j\right) = 0 \end{aligned}$$

with $j = 1, 2, 3$, p_{nm} real constants such that E_{nm} falls into either category K, L, M or N as follows [52]:

$$
\begin{aligned}
K_{nm}(\lambda_j) &= a_{nm}^{(0)}\lambda_j^n + a_{nm}^{(1)}\lambda_j^{n-2} + ... + a_{nm}^{(r)}\lambda_j^{n-2r}, m \in [1, r+1] \\
L_{nm}(\lambda_j) &= \sqrt{|\lambda_j^2 - h^2|}\left(a_{nm}^{(0)}\lambda_j^{n-1} + a_{nm}^{(1)}\lambda_j^{n-3} + ... \right. \\
&\quad \left. ... + a_{nm}^{(n-r-1)}\lambda_j^{(2r-n+1)}\right), m \in [r+2, n+1] \\
M_{nm}(\lambda_j) &= \sqrt{|\lambda_j^2 - k^2|}\left(a_{nm}^{(0)}\lambda_j^{n-1} + a_{nm}^{(1)}\lambda_j^{n-3} + ... \right. \\
&\quad \left. ... + a_{nm}^{(n-r-1)}\lambda_j^{(2r-n+1)}\right), m \in [n+2, 2n-r+1] \\
N_{nm}(\lambda_j) &= \sqrt{|\lambda_j^2 - h^2|}\sqrt{|\lambda_j^2 - k^2|}\left(a_{nm}^{(0)}\lambda_j^{n-2} + a_{nm}^{(1)}\lambda_j^{n-4} + ... \right. \\
&\quad \left. ... + a_{nm}^{(r-1)}\lambda_j^{n-2r}\right), m \in [2n-r+2, 2n+1]
\end{aligned}
$$

where $r = n/2$ and coefficients $a_{nm}^{(i)}, i = 0, 1, ...$ depend on h, k and p_m [52]. F_{nm} is the Lamé function of the second kind [52]:

$$
F_{nm}(\lambda_1) = (2n+1)\, E_{nm}\lambda_1 \int_{\lambda_1}^{\infty} \frac{\mathrm{d}t}{[E_{nm}(t)]^2 \sqrt{t^2 - h^2}\sqrt{t^2 - k^2}}
$$

$\lambda_1^{(0)}$ is chosen as the semi-major axis of the ellipsoid, with focal lengths h and k, and the normalised field coefficients, $\bar{c}_{nm}$, are given by [52]:

$$
\bar{c}_{nm} = \frac{1}{4\pi GM}\int_0^h \int_h^k \frac{V(\lambda_1^{(0)}, \lambda_2, \lambda_3)\bar{E}_{nm}(\lambda_2)\bar{E}_{nm}(\lambda_3)(\lambda_2^2 - \lambda_3^2)\mathrm{d}\lambda_2 \mathrm{d}\lambda_3}{\sqrt{\lambda_2^2 - h^2}\sqrt{k^2 - \lambda_2^2}\sqrt{h^2 - \lambda_3^2}\sqrt{k^2 - \lambda_3^2}}
$$

A.2 Homogeneous Ellipsoid

Another method of modelling an ellipsoid, presented in the literature [56] [57] [58] [4], is that of the tri-axial ellipsoid modelled using elliptical integrals. For an ellipsoid of constant density σ, and using the dimensions set out in figure 2.7, the mass is given by:

$$
M = \frac{4}{3}\pi\sigma\alpha\beta\gamma
$$

and $\mu = GM$ as before. The gravitational potential of the ellipsoid is given by [58]:

$$V(\vec{r}) = -\frac{3\mu}{4}\int_{\lambda(\vec{r})}^{\infty}\phi(\vec{r},u)\frac{du}{\Delta(u)} \tag{A.1}$$

$$\phi(\vec{r},u) = \frac{x^2}{\alpha^2+u}+\frac{y^2}{\beta^2+u}+\frac{z^2}{\gamma^2+u}-1 \tag{A.2}$$

$$\Delta(u) = \sqrt{(\alpha^2+u)(\beta^2+u)(\gamma^2+u)} \tag{A.3}$$

where $\lambda(\vec{r})$ is defined as the maximum real root for the cubic polynomial $\phi(\vec{r},\lambda)=0$. Without derivation, and applying Leibniz's rule, Scheeres [4] defines the partial derivatives of this potential as:

$$V_x = -\frac{3\mu x}{2}\int_{\lambda(\vec{r})}^{\infty}\frac{du}{(\alpha^2+u)\Delta(u)}$$
$$V_y = -\frac{3\mu y}{2}\int_{\lambda(\vec{r})}^{\infty}\frac{du}{(\beta^2+u)\Delta(u)}$$
$$V_z = -\frac{3\mu z}{2}\int_{\lambda(\vec{r})}^{\infty}\frac{du}{(\gamma^2+u)\Delta(u)}$$

At first glance, these expressions look troublesome. However, and somewhat conveniently, they fit with the general form of Carlson's Elliptical Integrals [171] for which the literature provides convenient algorithms for calculation [172] [173].

A.3 Mass Concentration (Mascon) Models

$$\frac{\mathrm{d}^2\vec{r}_i}{\mathrm{d}t^2} = G\sum_{j=1}^{n}\frac{m_j}{r_{ij}^3}(\vec{r}_j-\vec{r}_i) \tag{A.4}$$

where $\vec{r}_i$ is the position vector of the spacecraft, subscript j represents the individual discrete masses and r_{ij} is the distance between the spacecraft and the jth mass. In this summation, the case where $i=j$ is ignored.

A.4 Validation of Spherical Harmonics Model

This section will describe the process of validation conducted to ensure the software developed for modelling irregular gravity fields using the spherical harmonics model, described in Chapter 2, is accurate. This process compared results obtained with those from a mission proven software. The software used here was the open source General Mission Analysis Tool (GMAT)

produced by NASA. GMAT is a powerful mission analysis tool which allows orbit propagation, determination and optimisation. It has also been used on missions such as the Solar and Heliospheric Observatory (SOHO), the Advanced Composition Explorer (ACE) and the Transit Exoplanet Survey Satellite (TESS). The software was also used to optimise the entire 39-day launch period of the OSIRIS-REx mission. This mission ready status gives firm confidence in the accuracy of the models it contains.

In this validation, the Earth JGM-03 gravitational model was used. The harmonic coefficients used in GMAT were copied into the MATLAB scripts to ensure consistency. Table A.1 shows the initial conditions given to both MATLAB and GMAT in Keplerian elements as well as the simulation time.

Table A.1: Initial conditions for validation simulation

a	12756 km
e	0.1
i	28°
Ω	0°
ω	0°
θ	0°
Time	143350 s

The mathematical model presented in Chapter 2 is supplemented by a recursive algorithm [5] for the calculation of the Legenendre polynomials. The results of the subsequent simulation are shown in Fig. A.1.

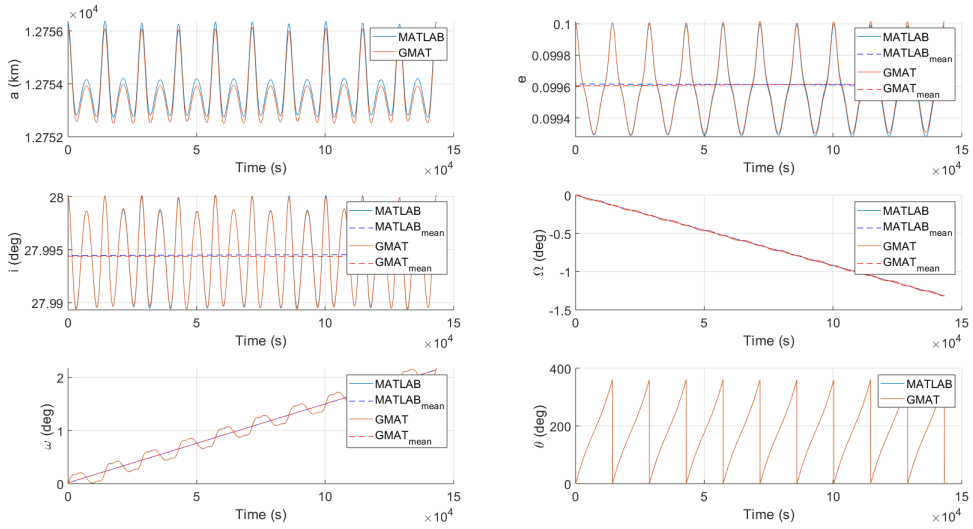

Figure A.1: Keplerian elements over 10 orbits in a 28° Earth orbit showing results in both MATLAB (blue) and GMAT (red).

The results show very good agreement with those of GMAT. However, there is a slight dif-

ference in trend of the inclination and eccentricity changes. To fully appreciate how significant this is, the simulation is propagated over 100 orbits with the results shown in Fig. A.2.

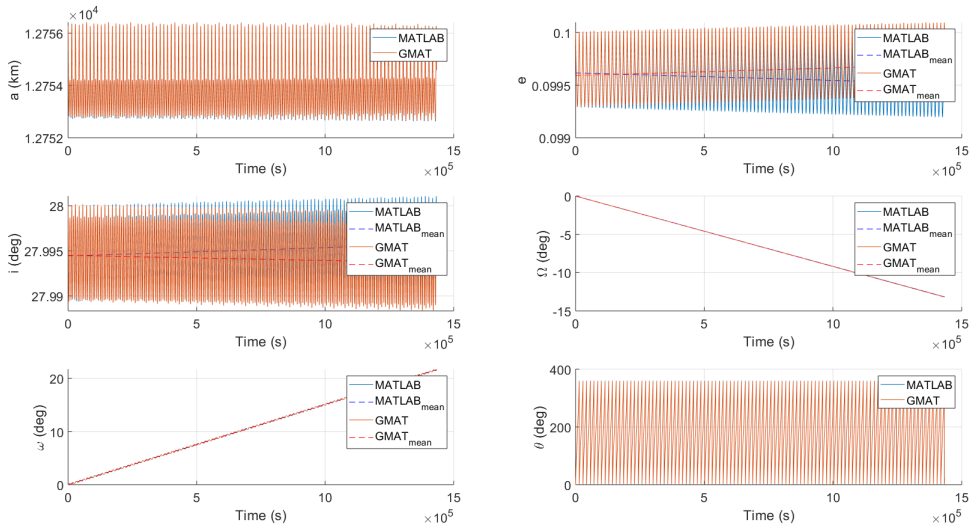

Figure A.2: Keplerian elements over 100 orbits in a 28° Earth orbit showing results in both MATLAB (blue) and GMAT (red).

It is clearly visibly that the trends in inclination and eccentricity are in the opposite direction. The rate of change of both eccentricity and inclination are shown for all four orbit types in Table A.2.

Table A.2: Rates of change of eccentricity (per day) and inclination (degrees per day) for both GMAT and MATLAB. Values shown for four different orbit types.

		GMAT	MATLAB
28° Inclination	$\dot{e}$ (/day)	7.3763×10^{-6}	-5.4401×10^{-6}
	$\dot{i}$ (°/day)	-2.0540×10^{-5}	6.8017×10^{-5}
Molinya	$\dot{e}$ (/day)	9.6635×10^{-7}	2.7634×10^{-6}
	$\dot{i}$ (°/day)	8.1166×10^{-4}	8.2171×10^{-4}
Equatorial	$\dot{e}$ (/day)	2.0900×10^{-6}	-3.4554×10^{-7}
	$\dot{i}$ (°/day)	2.1365×10^{-5}	3.3913×10^{-5}
Polar	$\dot{e}$ (/day)	-4.3741×10^{-6}	4.1989×10^{-6}
	$\dot{i}$ (°/day)	-3.2325×10^{-5}	-5.1534×10^{-5}

It is notable that the orders of magnitudes of any differences are very small. Even where the trends are in opposite directions, the differences even over long time periods would very small indeed. As such, these differences shall be considered negligible and without effect on the accuracy of the model.

Further simulations for the remaining orbit types are shown in Figs. A.3-A.5.

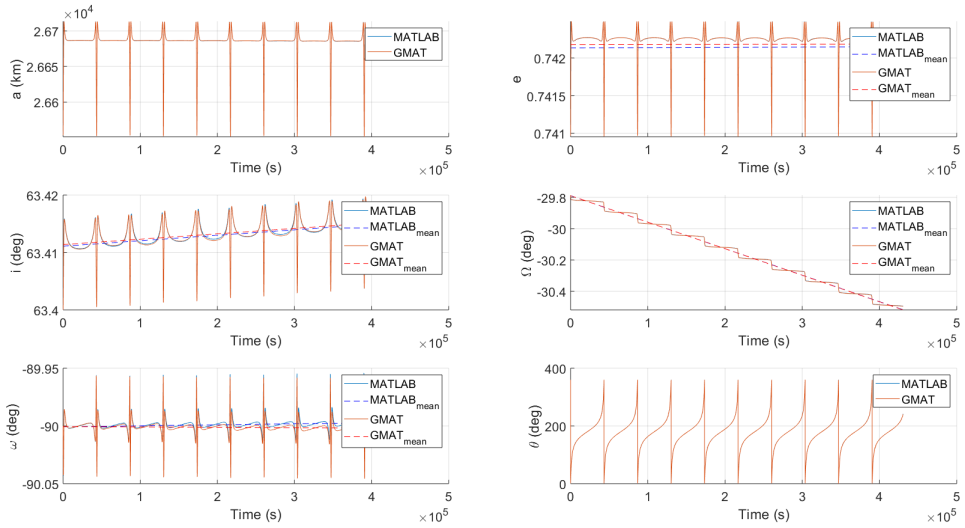

Figure A.3: Keplerian elements over 10 orbits in a Molinya Earth orbit showing results in both MATLAB (blue) and GMAT (red).

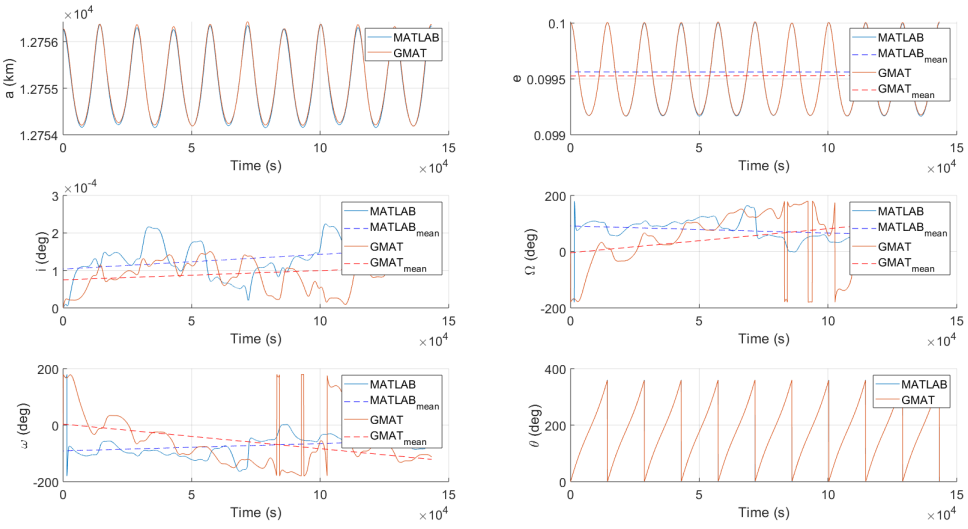

Figure A.4: Keplerian elements over 10 orbits in an equatorial Earth orbit showing results in both MATLAB (blue) and GMAT (red).

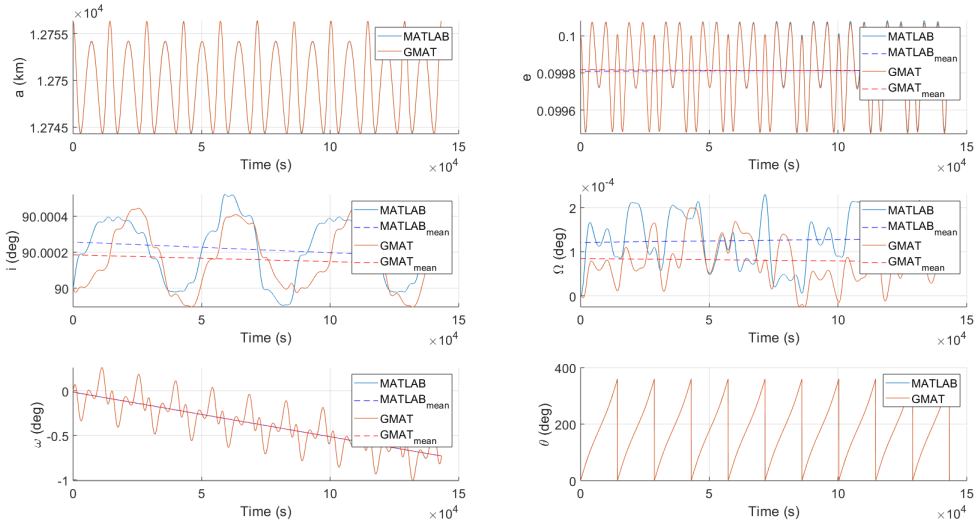

Figure A.5: Keplerian elements over 10 orbits in a polar Earth orbit showing results in both MATLAB (blue) and GMAT (red).

Appendix B

Inner Regime Equilibrium Points and their Stability

B.1 1620 Geographos

Asteroid 1620 Geographos is an Apollo class asteroid with bulk density of 2.0 g/cm^3 and rotational period of 5.222 hours [6]. Figure B.1 shows the equilibrium points and ZVCs for asteroid Geographos. This shape model was obtained via radar imaging, with the data collected from Ref. [174].

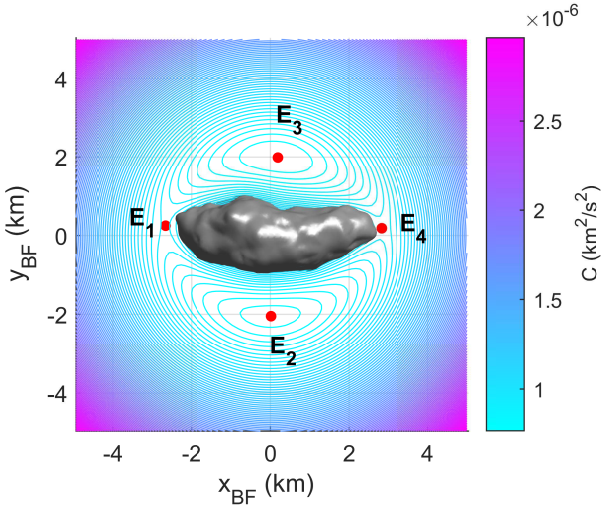

Figure B.1: Zero velocity curves with equilibrium points represented by red dots for asteroid Geographos

Table B.1 shows the Cartesian position of each equilibrium point and Table B.2 shows the respective eigenvalues.

Comparison of the eigenvalues obtained here and those of Ref. [6] are presented in Fig. B.2. The black asterisks represent the eigenvalues from Ref. [6] and the red circles represent the

Table B.1: Position of equilibrium points in the effective potential field of asteroid Geographos

	x_{bf} (km)	y_{bf} (km)	z_{bf} (km)
E_1	-2.6640	0.2490	-0.0070
E_2	0.0170	-2.0470	0.0250
E_3	0.1890	1.9850	0.0060
E_4	2.8220	0.1860	-0.0250

Table B.2: Eigenvalues for equilibrium points in effective potential field of asteroid Geographos

$\times 10^{-4}$ s^{-1}	λ_1	λ_2	λ_3	λ_4	λ_5	λ_6	Case	Stability
E_1	-4.7471	4.7471	4.6894i	-4.6894i	4.7839i	-4.7839i	2	U
E_2	1.5332 + 2.8484i	1.5332 - 2.8484i	-1.5332 + 2.8484i	-1.5332 - 2.8484i	3.2888i	-3.2888i	5	U
E_3	-1.7425 + 2.9828i	-1.7425 - 2.9828i	1.7425 + 2.9828i	1.7425 - 2.9828i	3.2588i	-3.2588i	5	U
E_4	6.3109	-6.3109	5.5045i	-5.5045i	5.6453i	-5.6453i	2	U

eigenvalues of Table B.2. The discrepancies are most likely due to small differences in the shape model used and in possible numerical errors due to differences in tolerances when finding these minima. Although the eigenvalues are similar, and their stability criteria the same, these discrepancies are an indication of the potential uncertainties which surround the available shape models for these asteroids.

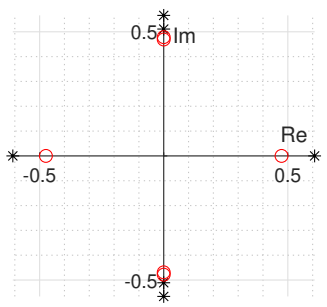

(a) E_1

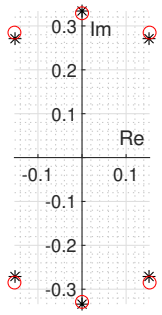

(b) E_2

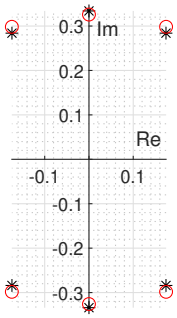

(c) E_3

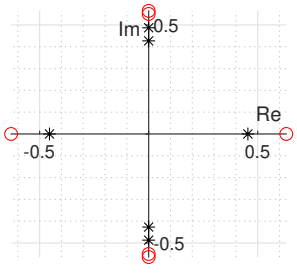

(d) E_4

Figure B.2: Comparison of eigenvalues from [6] for asteroid Geographos (shown by black asterisks) and the eigenvalues of this work (shown by red circles)

B.2 101955 Bennu

Asteroid 101955 Bennu is an Apollo class asteroid with bulk density of 1.26 g/cm^3 and rotational period of 4.288 hours [1]. Figure B.3 shows the equilibrium points and ZVCs for asteroid Bennu. Given the observations made by the OSIRIS-REx spacecraft, very high resolution surface texture maps are also available, such as in Ref. [175].

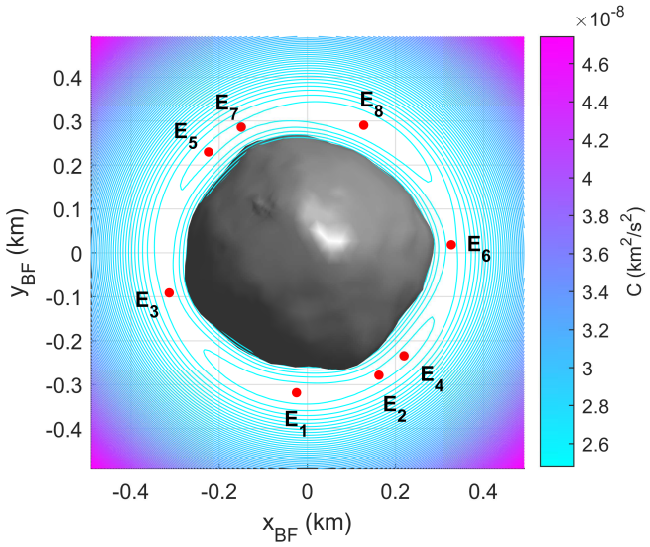

Figure B.3: Zero velocity curves with equilibrium points represented by red dots for asteroid Bennu

Table B.3 shows the Cartesian position of each equilibrium point and Table B.4 shows the respective eigenvalues.

Table B.3: Position of equilibrium points in the effective potential field of asteroid Bennu

	x_{bf} (km)	y_{bf} (km)	z_{bf} (km)
E_1	-0.0246	-0.3183	0.0003
E_2	0.1626	-0.2785	-0.0020
E_3	-0.3135	-0.0912	-0.0023
E_4	0.2195	-0.2343	-0.0028
E_5	-0.2244	0.2297	-0.0073
E_6	0.3270	0.0185	-0.0032
E_7	-0.1499	0.2860	-0.0080
E_8	0.1281	0.2904	-0.0025

Comparison of the eigenvalues obtained here and those of Ref. [7] are presented in Fig. B.4. The black asterisks represent the eigenvalues from [7] and the red circles represent the eigenvalues of Table B.4. In this case there is very good agreement between the values obtained in this work and those of the literature. This provides some validation of the models used here.

Table B.4: Eigenvalues for equilibrium points in effective potential field of asteroid Bennu

$\times 10^{-4}$ s^{-1}	λ_1	λ_2	λ_3	λ_4	λ_5	λ_6	Case	Stability
E_1	-0.3771 + 2.6688i	-0.3771 - 2.6688i	0.3771 + 2.6688i	0.3771 - 2.6688i	4.3620i	-4.3620i	5	U
E_2	-1.5895	1.5895	3.8773i	-3.8773i	4.5256i	-4.5256i	2	U
E_3	2.2060	-2.2060	4.0711i	-4.0711i	4.6131i	-4.6131i	2	U
E_4	1.9853i	-1.9853i	3.0471i	-3.0471i	4.4454i	-4.4454i	1	LS
E_5	0.4908 + 2.6258i	0.4908 - 2.6258i	-0.4908 + 2.6258i	-0.4908 - 2.6258i	4.4362i	-4.4362i	5	U
E_6	2.5899	-2.5899	4.2750i	-4.2750i	4.6282i	-4.6282i	2	U
E_7	-1.8756	1.8756	3.9950i	-3.9950i	4.5327i	-4.5327i	2	U
E_8	-0.448 + 2.7262i	-0.448 - 2.7262i	0.448 + 2.7262i	0.448 - 2.7262i	4.3034i	-4.3034i	5	U

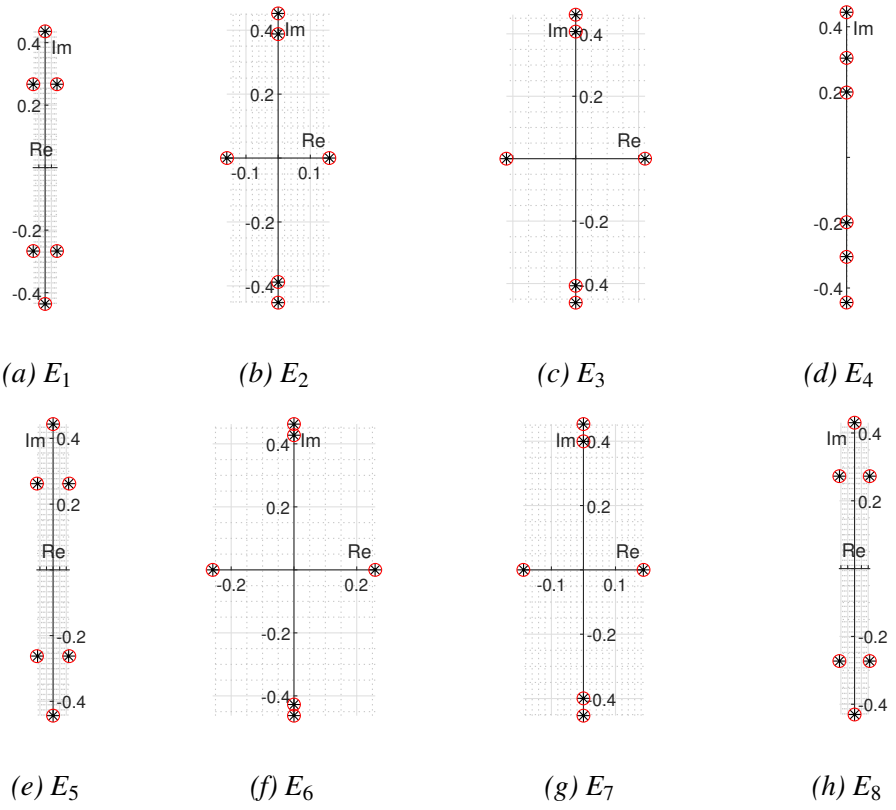

(a) E_1 *(b)* E_2 *(c)* E_3 *(d)* E_4

(e) E_5 *(f)* E_6 *(g)* E_7 *(h)* E_8

Figure B.4: Comparison of eigenvalues from [7] for asteroid Bennu (shown by black asterisks) and the eigenvalues of this work (shown by red circles)

B.3 21 Lutetia

Asteroid 21 Lutetia is a main belt asteroid with bulk density of 3.40 g/cm^3 and rotational period of 8.168 hours [8]. Figure B.5 shows the equilibrium points and ZVCs for asteroid Lutetia, where the shape model was obtained from observation data [176] from the Rosetta spacecraft during a fly-by in July 2010 [177].

Table B.5 shows the Cartesian position of each equilibrium point and Table B.6 shows the respective eigenvalues.

Comparison of the eigenvalues obtained here and those of Ref. [8] are presented in Fig. B.6. The black asterisks represent the eigenvalues from Ref. [8] and the red circles represent the eigenvalues of Table B.6. Once again, there is relatively good agreement between the eigen-

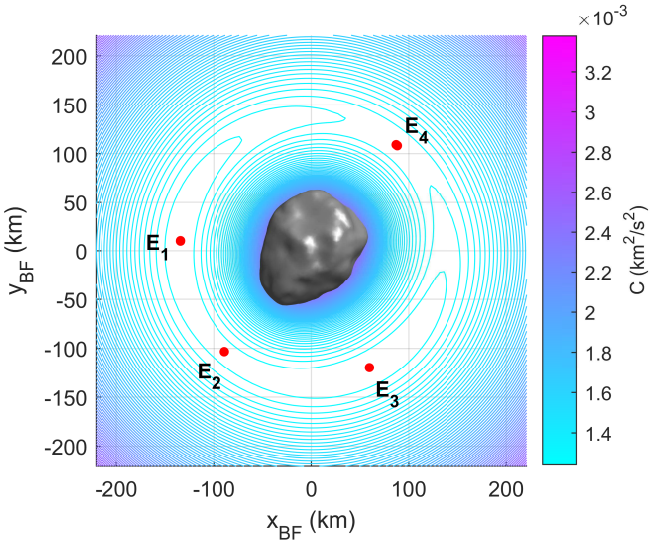

Figure B.5: Zero velocity curves with equilibrium points represented by red dots for asteroid Lutetia

Table B.5: Position of equilibrium points in the effective potential field of asteroid Lutetia

	x_{bf} (km)	y_{bf} (km)	z_{bf} (km)
E_1	-134.3000	10.0700	0.7400
E_2	-89.0600	-103.3200	0.5700
E_3	59.7800	-119.7200	0.7200
E_4	87.0800	109.1600	1.1500

Table B.6: Eigenvalues for equilibrium points in effective potential field of asteroid Lutetia

$\times 10^{-4}$ s^{-1}	λ_1	λ_2	λ_3	λ_4	λ_5	λ_6	Case	Stability
E_1	0.8627i	-0.8627i	1.9112i	-1.9112i	2.1758i	-2.1758i	1	LS
E_2	0.0771	-0.0771	2.1971i	-2.1971i	2.2133i	-2.2133i	2	U
E_3	1.0346i	-1.0346i	1.8460i	-1.8460i	2.1571i	-2.1571i	1	LS
E_4	0.0870	-0.0870	2.2158i	-2.2158i	2.2313i	-2.2313i	2	U

values of Ref. [8] and this work. The discrepancies can again be attributed to the application of shape models which utilised different data. There are several shape models available for asteroid Lutetia, including those taken from photometric data [178], which offer different resolutions.

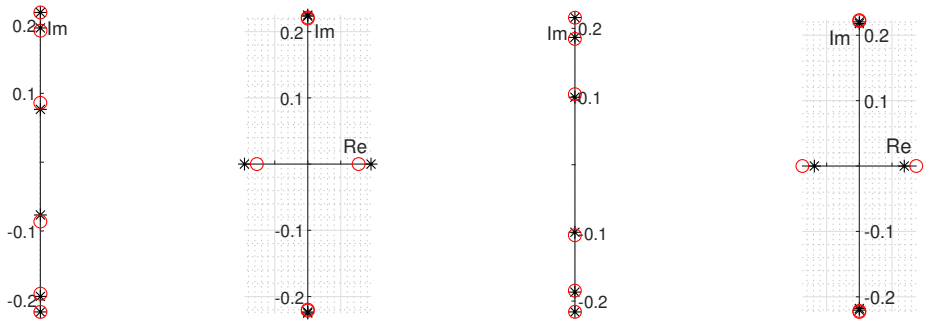

(a) E_1 *(b)* E_2 *(c)* E_3 *(d)* E_4

Figure B.6: Comparison of eigenvalues from [8] for asteroid Lutetia (shown by black asterisks) and the eigenvalues of this work (shown by red circles)

Appendix C

Supplementary Information on the Outer Regime

C.1 Periodic Orbits: Spatial Case

C.1.1 Lissajous Orbits

The Lissajous orbits are quasi-periodic, with the ratio of the in-plane to out-of-plane frequency being an irrational number [102]. In this section the methods by which Lissajous orbits can be calculated is demonstrated. A linear solution to the Lissajous orbit is sought by linearising the dynamics around one of the collinear equilibrium points. First, the reference frame is centred on the desired equilibrium point:

$$\begin{aligned} \xi &= x_{\text{SYN}} + x_E \\ \eta &= y_{\text{SYN}} + y_E \\ \zeta &= z_{\text{SYN}} + z_E \end{aligned} \tag{C.1}$$

where (x_E, y_E, z_E) is the Cartesian position of the equilibrium point in the SYN reference frame and $(x_{\text{SYN}}, y_{\text{SYN}}, z_{\text{SYN}})$ the particle position in the SYN frame. The oscillatory solution is obtained by suppressing the real eigenvalues of the Jacobian matrix [73], thus giving [102, 179]:

$$\begin{aligned} \xi &= \frac{A_y}{\nu} \sin(\lambda_{xy}\tau) \\ \eta &= A_y \cos(\lambda_{xy}\tau) \\ \zeta &= A_z \sin(\lambda_z \tau + \phi) \end{aligned} \tag{C.2}$$

where A_y and A_z are the y and z amplitudes of the orbit, λ_{xy} and λ_z are the in-plane and out-of-plane frequencies respectively, τ is the time on orbit, ϕ is the phasing parameter (set as $\phi = \pi/2$), and ν is given by [179]:

$$\nu = \frac{\lambda_{xy}^2 + U_{xx}}{2\lambda_{xy}} \tag{C.3}$$

The in-plane frequency is given by [102]:

$$\lambda_{xy} = \sqrt{\frac{1}{2}\left((-4\Omega^2 + U_{xx} + U_{yy}) - \sqrt{(4\Omega^2 - U_{xx} - U_{yy})^2 - 4(U_{xx}U_{yy})}\right)} \tag{C.4}$$

and the out-of-plane frequency by:

$$\lambda_z = \sqrt{U_{zz}} \tag{C.5}$$

Initial conditions can be taken from the linear model at $\tau = 0$ and applied as a first guess for the solution in the full non-linear dynamical model. This yields the initial conditions $x_0 = 0$, $y_0 = A_y$, $z_0 = 0$, $\dot{x}_0 = \frac{\lambda_{xy}}{\nu} y_0$, $\dot{y}_0 = -\lambda_{xy}\nu x_0$ and $-\dot{z}_0 = A_y\lambda_z$ [179]. Figures C.1 shows the results for the linear approximation calculated over 50 complete revolutions, and Fig. C.2 shows the result for the linear guess of the initial state, numerically integrated in the full non-linear dynamics.

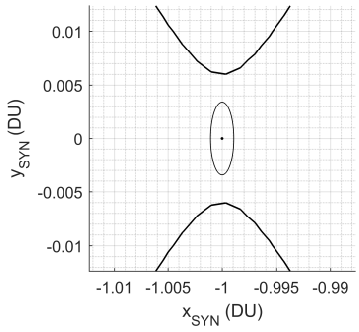

(a) Linear, x-y plane

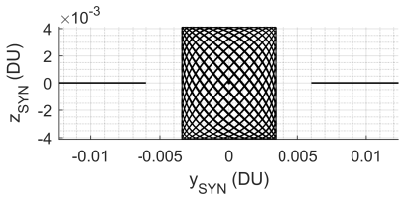

(b) Linear, y-z plane

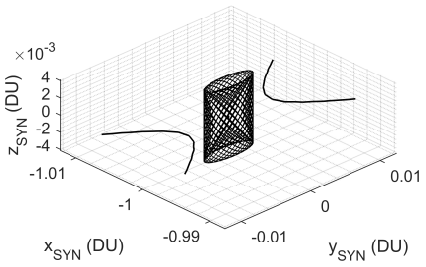

(c) Linear

Figure C.1: Linear approximation of Lissajous orbits

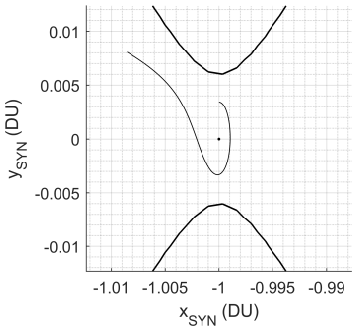

(a) Nonlinear, x-y plane

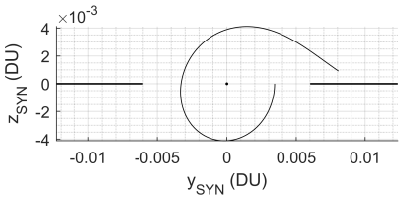

(b) Nonlinear, y-z plane

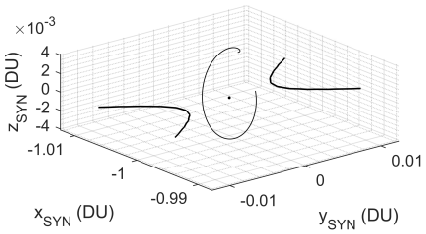

(c) Nonlinear

Figure C.2: Trajectory of Lissajous orbit in the full nonlinear dynamics, using the initial state of the linear approximation

C.1.2 Halo Orbits

The Halo orbit originates after bifurcation from the planar Lyapunov family where there exists a 1:1 resonance between the in-plane and out-of-plane frequencies [98]. It is possible to search for the critical point at which the Halo family bifurcates from the planar family by analysing the coefficients of the vertical stability of the planar orbits [180–183].

If $(x_{\text{SYN}}, y_{\text{SYN}}, z_{\text{SYN}})$ are the Cartesian position coordinates of the particle and $(u_{\text{SYN}}, v_{\text{SYN}}, w_{\text{SYN}})$ are the velocity components, then a vertical perturbation can be given by:

$$\begin{aligned} \frac{d\Delta z_{\text{SYN}}}{dt} &= \Delta w_{\text{SYN}} \\ \frac{d\Delta w_{\text{SYN}}}{dt} &= U_{xx}\Delta z_{\text{SYN}} \end{aligned} \tag{C.6}$$

By numerically integrating the above equations from some initial point on the orbit, a new perturbation is obtained:

$$\begin{pmatrix} \Delta z_{\text{SYN},1} \\ \Delta w_{\text{SYN},1} \end{pmatrix} = \begin{bmatrix} A_v & B_v \\ C_v & D_v \end{bmatrix} \begin{pmatrix} \Delta z_{\text{SYN},0} \\ \Delta w_{\text{SYN},0} \end{pmatrix} \tag{C.7}$$

The condition for stability is $|a_v| < 1$, where:

$$a_v = A_v D_v + B_v C_v \tag{C.8}$$

Vertical instability in the planar orbit signifies the potential for the orbit to bifurcate out of the plane. At the critical point, $|a_v| = 1$, there is a bifurcation from the planar Lyapunov family, to the vertical Halo family of orbits of twice the multiplicity of the planar orbit [149].

By continuing along the value of Jacobi constant for the planar Lyapunov family in the HR3BP, and employing a predictor/corrector method as described in Section 3.2.3, a study of the vertical stability for a family of planar orbits can be conducted. Figure C.3 shows the value of $|a_v|$ as a function of C.

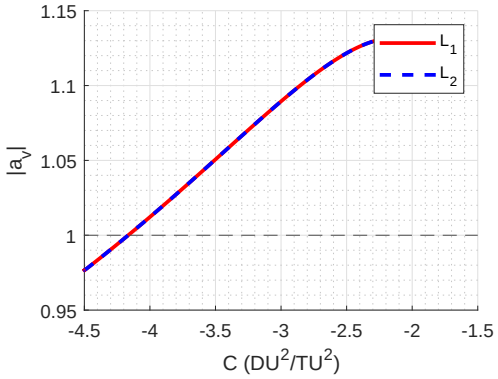

Figure C.3: Vertical stability coefficient for range of orbits, continued along the Jacobi constant, C. Critical value denoted by black dashed line.

The critical value is found to be $C = -4.1657$, for orbits around both E_1 and E_2. The initial state for this critical orbit can then be taken as a first guess, with a small, non-zero, z-amplitude applied, and the predictor/corrector method once again applied as we continue along the bifurcated family of Halo orbits. Figure C.4 shows the Southern family of halo orbits from points E_1 and Fig. C.5 shows the Southern family of halo orbits from E_2 for the ballistic case.

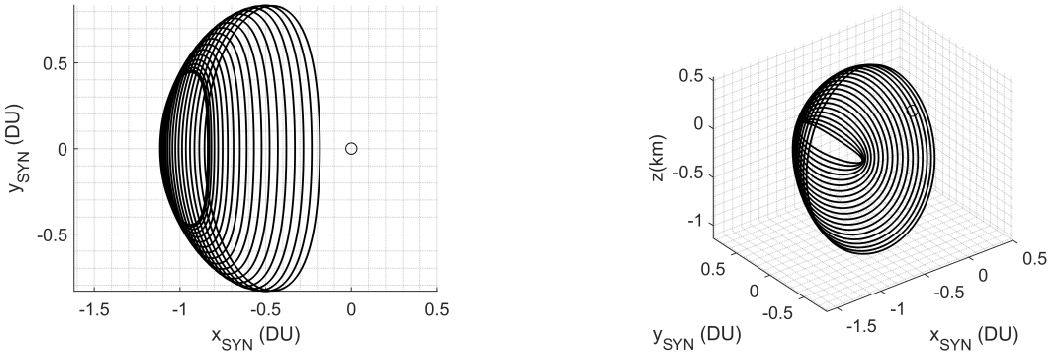

(a) x-y plane *(b) 3-dimensional view*

Figure C.4: Family of Southern halo orbits emanating from E_1.

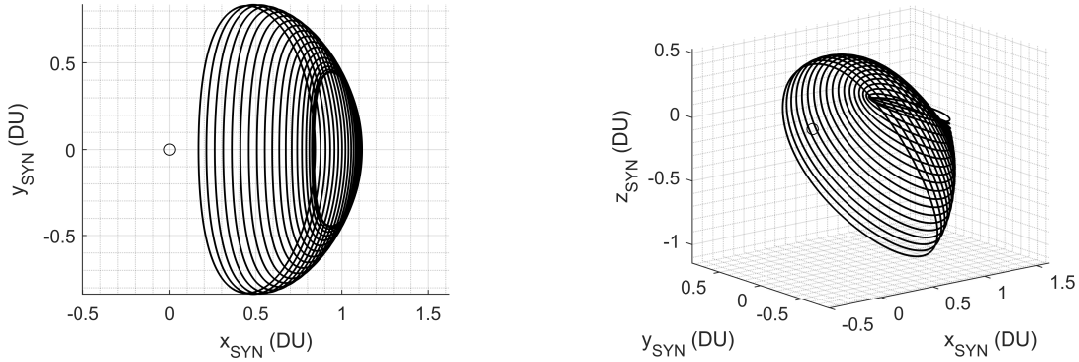

(a) x-y plane *(b) 3-dimensional view*

Figure C.5: Family of Southern halo orbits emanating from E_2.

Appendix D

Supplementary Work Related to Gravitational Capture

D.1 Ballistic Transit Trajectories in the SSHR3BP

This section will present the ballistic transit trajectories, in dimensional units, utilising invariant manifold theory detailed in Chapter 2. The trajectories are provided here as supplementary to the main content of the work in Chapter 6 and so are provided here without further comment.

D.1.1 433 Eros

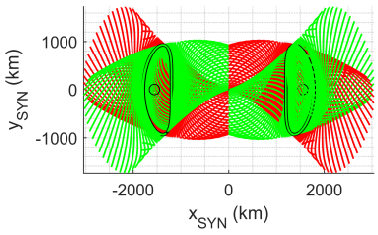

(a) L_1 and L_2 manifolds

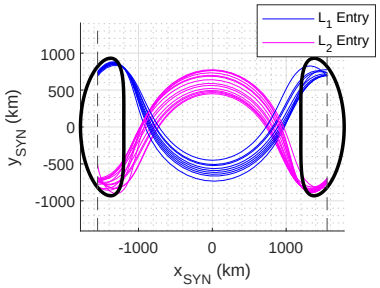

(b) Ballistic transit trajectories via L_1 and L_2

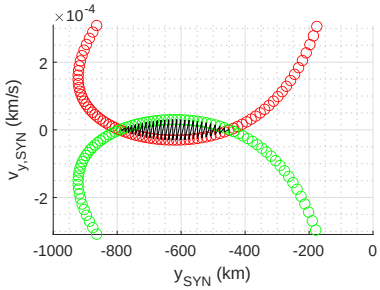

(c) Poincaré section along negative y-axis

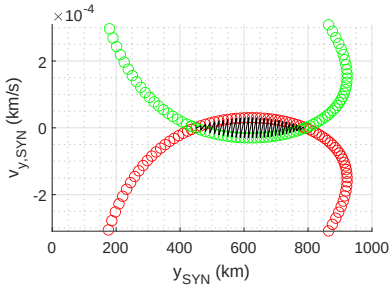

(d) Poincaré section along positive y-axis

Figure D.1: Ballistic transit trajectories via L_1 and L_2 Lagrange points

D.1.2 4 Vesta

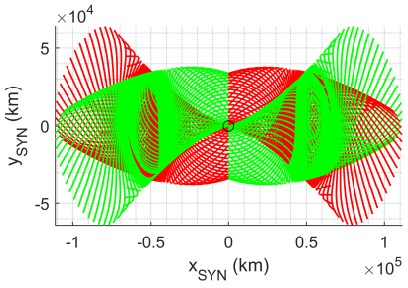

(a) L_1 and L_2 manifolds

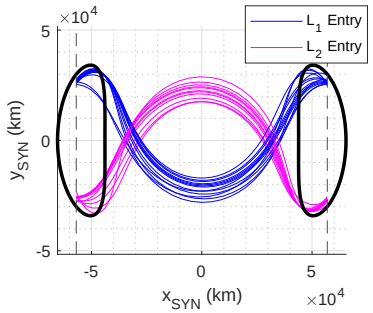

(b) Ballistic transit trajectories via L_1 and L_2

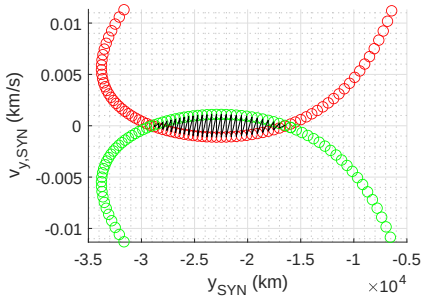

(c) Poincaré section along negative y-axis

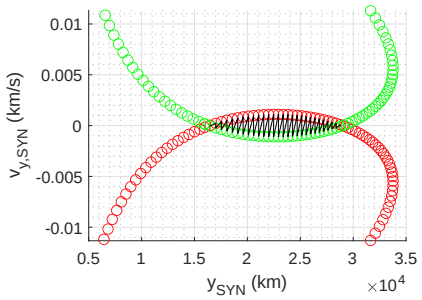

(d) Poincaré section along positive y-axis

Figure D.2: Ballistic transit trajectories via L_1 and L_2 Lagrange points

D.2 Study of Increasing a_c on the Capture of a Trajectory at Asteroid 433 Eros

This section will provide supplementary material to the two-phase capture approach for a solar sail at an asteroid. The work contained here represents the initial investigation of a targeted orbit within 0.30 DU of the asteroid 433 Eros. Given the sensitivity of the weak gravity field of the asteroid to a sail which may have a relatively strong a_c, an continuation approach is taken. In this, the continuation parameter is the value of a_c, where $a_c \in [0.01, 0.2]$ mm/s^2. Following the successful capture with 0.30 DU for a sail of $a_c = 0.2$ mm/s^2, the capture region radius is then reduced; first to 0.25 DU and then to 0.20 DU. Again, as this material is supplemental, any discussion of it is contained in the main text and so no further comment is made here.

D.2.1 Initial Capture

First, the initial capture phase is approached for each value of a_c.

ZVC Radius 0.30 DU

This section presents the results where the targeted capture region has a radius of 0.30 DU.

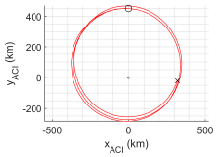

(a) Trajectory (ACI frame)

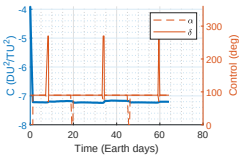

(b) Jacobi constant and control

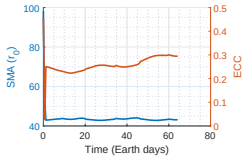

(c) Semi-major axis against eccentricity

Figure D.3: Initial capture phase: 433 Eros, $a_c = 0.01$ mm/s^2

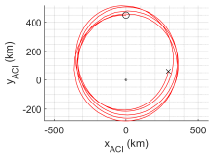

(a) Trajectory (ACI frame)

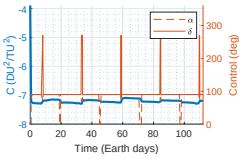

(b) Jacobi constant and control

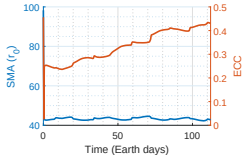

(c) Semi-major axis against eccentricity

Figure D.4: Initial capture phase: 433 Eros, $a_c = 0.02$ mm/s^2

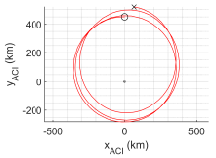

(a) Trajectory (ACI frame)

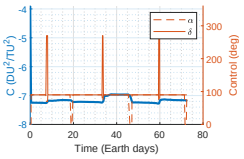

(b) Jacobi constant and control

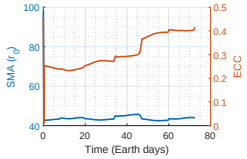

(c) Semi-major axis against eccentricity

Figure D.5: Initial capture phase: 433 Eros, $a_c = 0.03$ mm/s^2

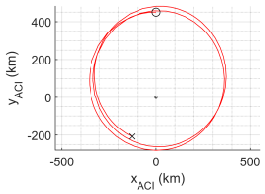

(a) Trajectory (ACI frame)

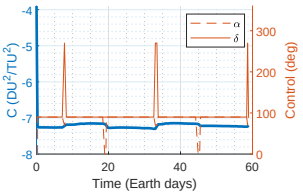

(b) Jacobi constant and control

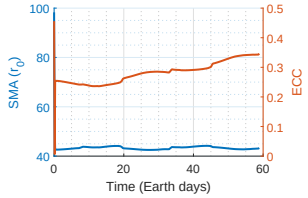

(c) Semi-major axis against eccentricity

Figure D.6: Initial capture phase: 433 Eros, $a_c = 0.04$ mm/s^2

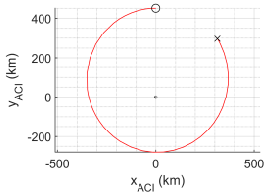

(a) Trajectory (ACI frame)

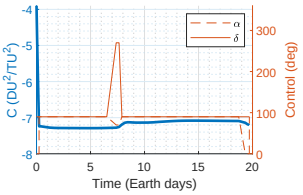

(b) Jacobi constant and control

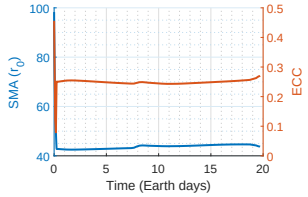

(c) Semi-major axis against eccentricity

Figure D.7: Initial capture phase: 433 Eros, $a_c = 0.05$ mm/s^2

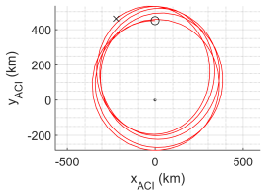

(a) Trajectory (ACI frame)

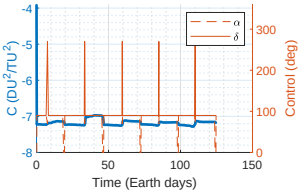

(b) Jacobi constant and control

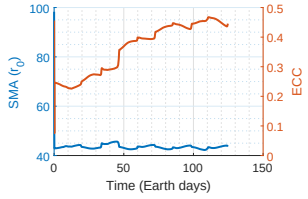

(c) Semi-major axis against eccentricity

Figure D.8: Initial capture phase: 433 Eros, $a_c = 0.06$ mm/s^2

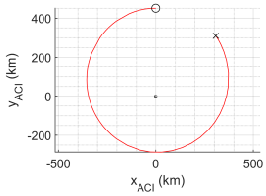

(a) Trajectory (ACI frame)

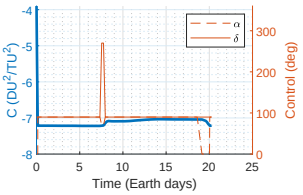

(b) Jacobi constant and control

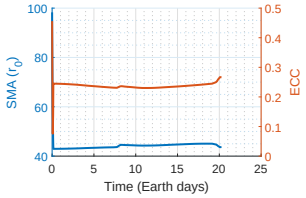

(c) Semi-major axis against eccentricity

Figure D.9: Initial capture phase: 433 Eros, $a_c = 0.08$ mm/s^2

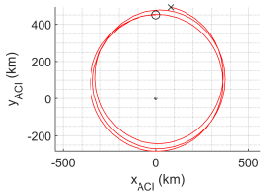

(a) Trajectory (ACI frame)

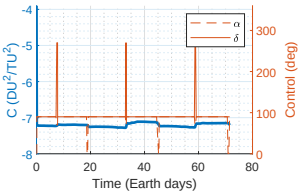

(b) Jacobi constant and control

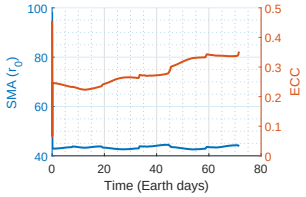

(c) Semi-major axis against eccentricity

Figure D.10: Initial capture phase: 433 Eros, $a_c = 0.10$ mm/s^2

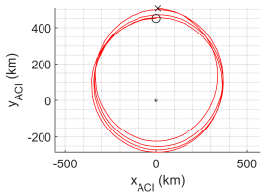

(a) Trajectory (ACI frame)

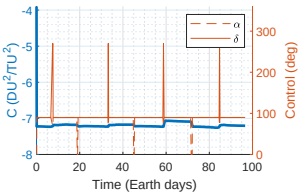

(b) Jacobi constant and control

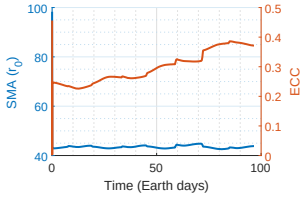

(c) Semi-major axis against eccentricity

Figure D.11: Initial capture phase: 433 Eros, $a_c = 0.12$ mm/s^2

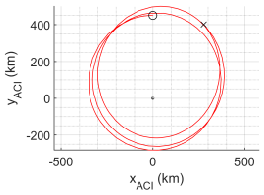

(a) Trajectory (ACI frame)

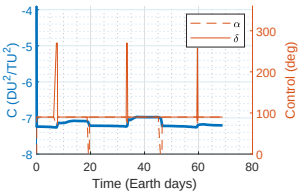

(b) Jacobi constant and control

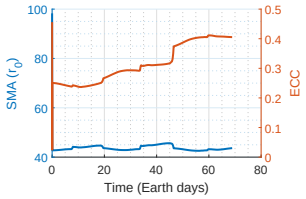

(c) Semi-major axis against eccentricity

Figure D.12: Initial capture phase: 433 Eros, $a_c = 0.14$ mm/s^2

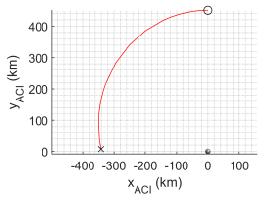

(a) Trajectory (ACI frame)

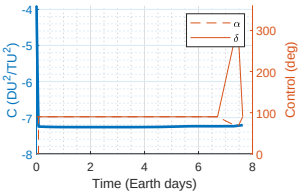

(b) Jacobi constant and control

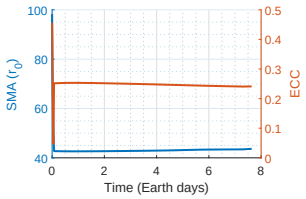

(c) Semi-major axis against eccentricity

Figure D.13: Initial capture phase: 433 Eros, $a_c = 0.16$ mm/s^2

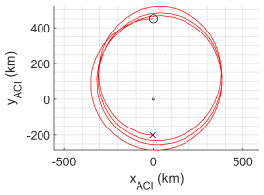

(a) Trajectory (ACI frame)

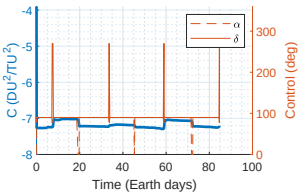

(b) Jacobi constant and control

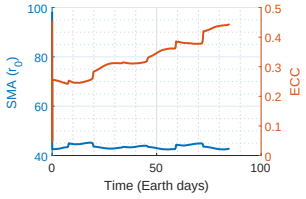

(c) Semi-major axis against eccentricity

Figure D.14: Initial capture phase: 433 Eros, $a_c = 0.18$ mm/s^2

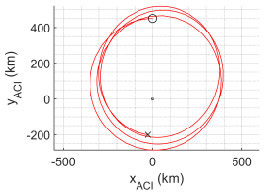

(a) Trajectory (ACI frame)

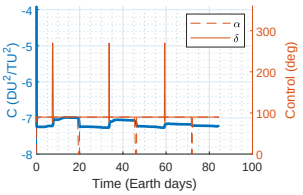

(b) Jacobi constant and control

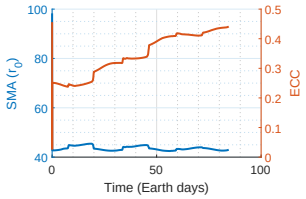

(c) Semi-major axis against eccentricity

Figure D.15: Initial capture phase: 433 Eros, $a_c = 0.20$ mm/s^2

ZVC Radius 0.25 DU

This section presents the results where the targeted capture region has a radius of 0.25 DU.

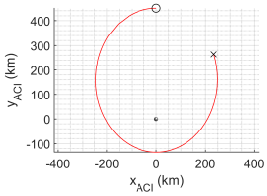

(a) Trajectory (ACI frame)

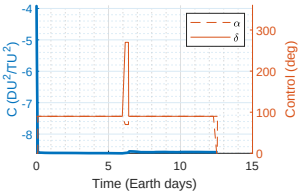

(b) Jacobi constant and control

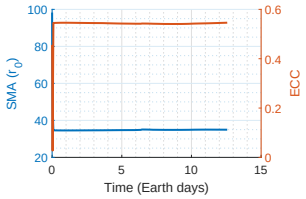

(c) Semi-major axis against eccentricity

Figure D.16: Initial capture phase: 433 Eros, $a_c = 0.20$ mm/s^2

ZVC Radius 0.20 DU

This section presents the results where the targeted capture region has a radius of 0.20 DU.

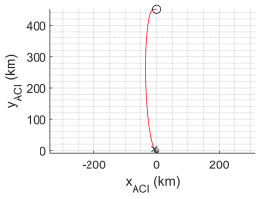

(a) Trajectory (ACI frame)

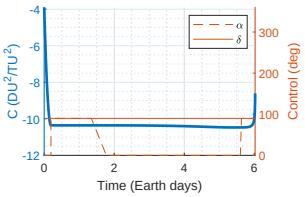

(b) Jacobi constant and control

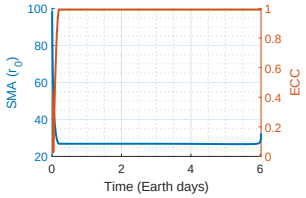

(c) Semi-major axis against eccentricity

Figure D.17: Initial capture phase: 433 Eros, $a_c = 0.20$ mm/s^2

D.2.2 Orbit Shaping

This section will present the orbit shaping results which follow from the initial capture phase of the preceding material.

ZVC Radius 0.30 DU

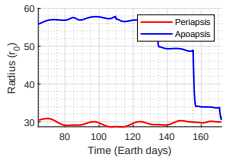

(a) Radius of periapsis and apoapsis

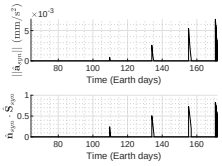

(b) Magnitude of acceleration and direction of sail normal relative to the Sun

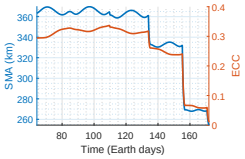

(c) Semi-major axis against eccentricity

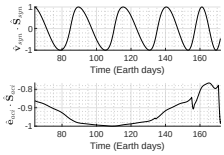

(d) Velocity direction and direction of eccentricity vector relative to the Sun

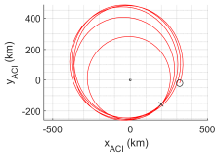

(e) Trajectory (ACI frame)

Figure D.18: Orbit shaping phase: 433 Eros, $a_c = 0.01$ mm/s^2

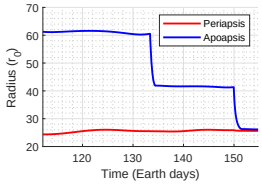

(a) Radius of periapsis and apoapsis

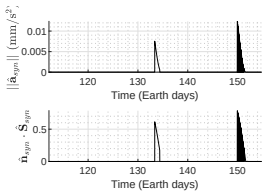

(b) Magnitude of acceleration and direction of sail normal relative to the Sun

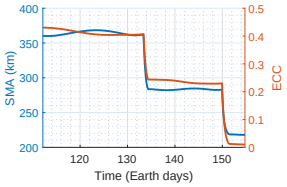

(c) Semi-major axis against eccentricity

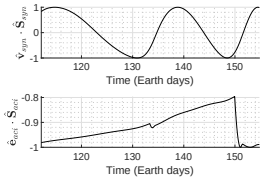

(d) Velocity direction and direction of eccentricity vector relative to the Sun

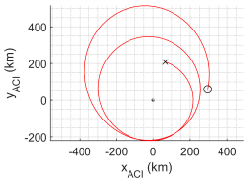

(e) Trajectory (ACI frame)

Figure D.19: Orbit shaping phase: 433 Eros, $a_c = 0.02$ mm/s^2

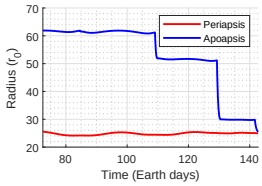

(a) Radius of periapsis and apoapsis

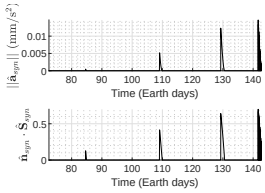

(b) Magnitude of acceleration and direction of sail normal relative to the Sun

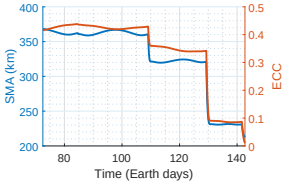

(c) Semi-major axis against eccentricity

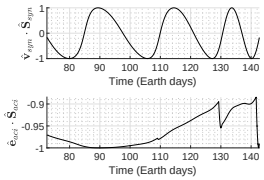

(d) Velocity direction and direction of eccentricity vector relative to the Sun

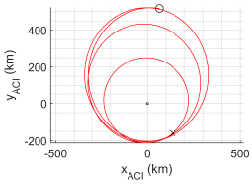

(e) Trajectory (ACI frame)

Figure D.20: Orbit shaping phase: 433 Eros, $a_c = 0.03$ mm/s^2

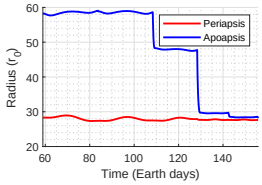

(a) Radius of periapsis and apoapsis

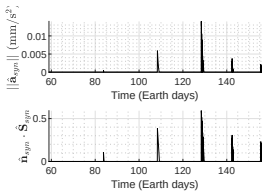

(b) Magnitude of acceleration and direction of sail normal relative to the Sun

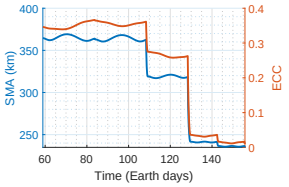

(c) Semi-major axis against eccentricity

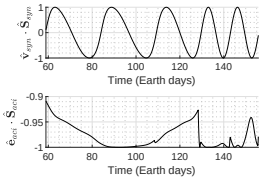

(d) Velocity direction and direction of eccentricity vector relative to the Sun

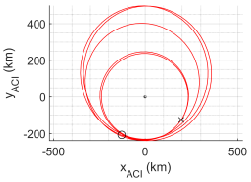

(e) Trajectory (ACI frame)

Figure D.21: Orbit shaping phase: 433 Eros, $a_c = 0.04$ mm/s^2

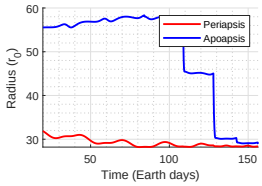

(a) Radius of periapsis and apoapsis

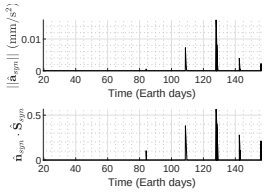

(b) Magnitude of acceleration and direction of sail normal relative to the Sun

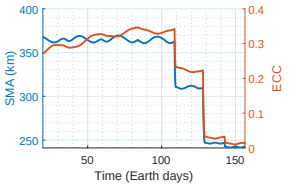

(c) Semi-major axis against eccentricity

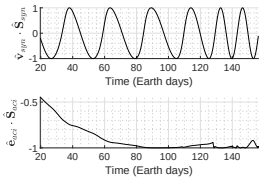

(d) Velocity direction and direction of eccentricity vector relative to the Sun

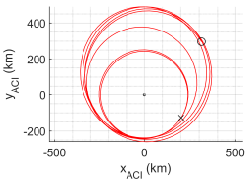

(e) Trajectory (ACI frame)

Figure D.22: Orbit shaping phase: 433 Eros, $a_c = 0.05$ mm/s^2

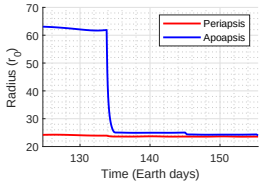

(a) Radius of periapsis and apoapsis

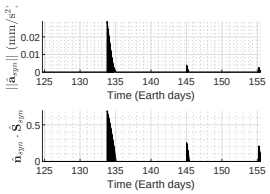

(b) Magnitude of acceleration and direction of sail normal relative to the Sun

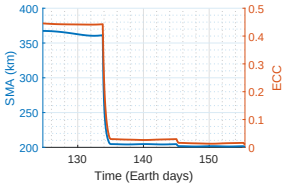

(c) Semi-major axis against eccentricity

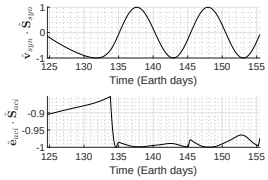

(d) Velocity direction and direction of eccentricity vector relative to the Sun

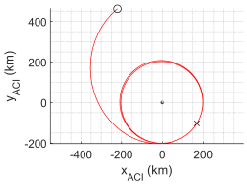

(e) Trajectory (ACI frame)

Figure D.23: Orbit shaping phase: 433 Eros, $a_c = 0.06$ mm/s^2

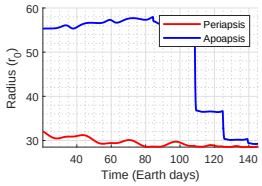

(a) Radius of periapsis and apoapsis

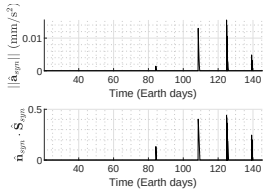

(b) Magnitude of acceleration and direction of sail normal relative to the Sun

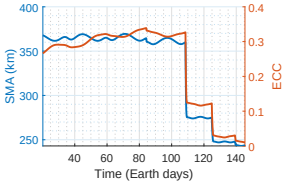

(c) Semi-major axis against eccentricity

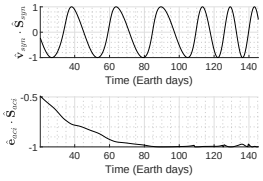

(d) Velocity direction and direction of eccentricity vector relative to the Sun

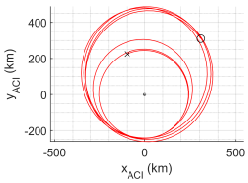

(e) Trajectory (ACI frame)

Figure D.24: Orbit shaping phase: 433 Eros, $a_c = 0.08$ mm/s^2

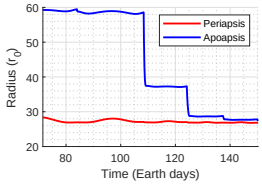

(a) Radius of periapsis and apoapsis

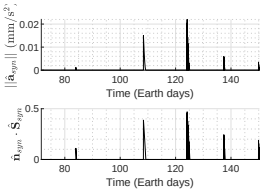

(b) Magnitude of acceleration and direction of sail normal relative to the Sun

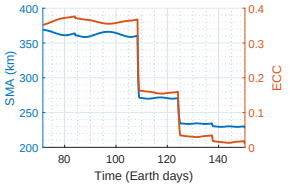

(c) Semi-major axis against eccentricity

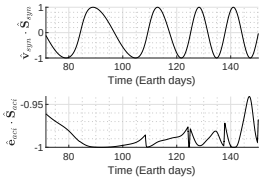

(d) Velocity direction and direction of eccentricity vector relative to the Sun

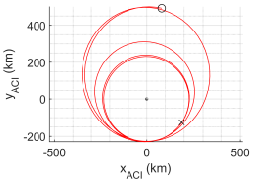

(e) Trajectory (ACI frame)

Figure D.25: Orbit shaping phase: 433 Eros, $a_c = 0.10$ mm/s^2

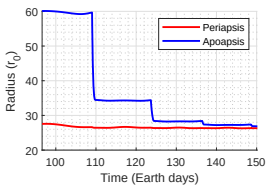

(a) Radius of periapsis and apoapsis

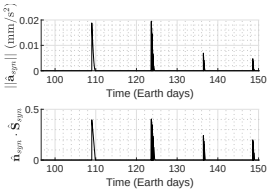

(b) Magnitude of acceleration and direction of sail normal relative to the Sun

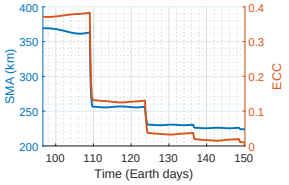

(c) Semi-major axis against eccentricity

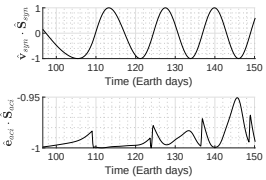

(d) Velocity direction and direction of eccentricity vector relative to the Sun

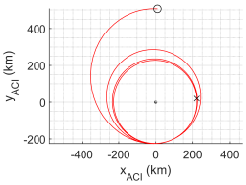

(e) Trajectory (ACI frame)

Figure D.26: Orbit shaping phase: 433 Eros, $a_c = 0.12$ mm/s^2

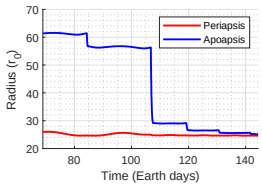

(a) Radius of periapsis and apoapsis

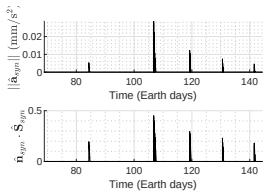

(b) Magnitude of acceleration and direction of sail normal relative to the Sun

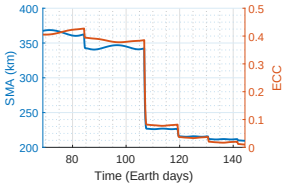

(c) Semi-major axis against eccentricity

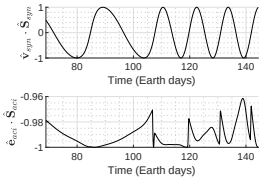

(d) Velocity direction and direction of eccentricity vector relative to the Sun

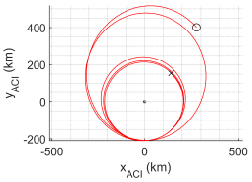

(e) Trajectory (ACI frame)

Figure D.27: Orbit shaping phase: 433 Eros, $a_c = 0.14$ mm/s^2

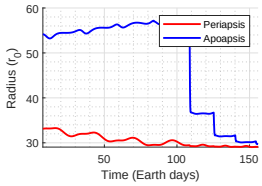

(a) Radius of periapsis and apoapsis

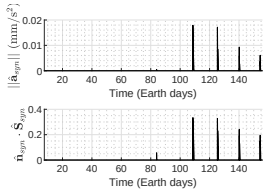

(b) Magnitude of acceleration and direction of sail normal relative to the Sun

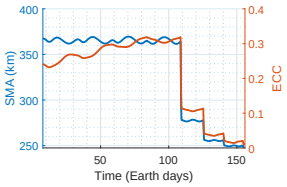

(c) Semi-major axis against eccentricity

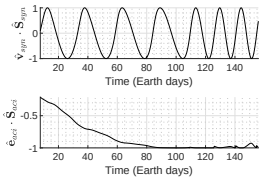

(d) Velocity direction and direction of eccentricity vector relative to the Sun

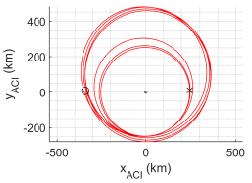

(e) Trajectory (ACI frame)

Figure D.28: Orbit shaping phase: 433 Eros, $a_c = 0.16$ mm/s^2

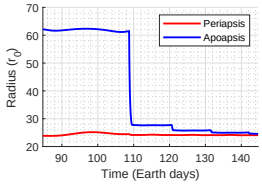

(a) Radius of periapsis and apoapsis

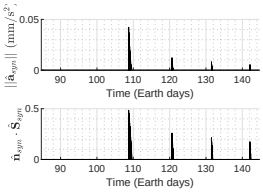

(b) Magnitude of acceleration and direction of sail normal relative to the Sun

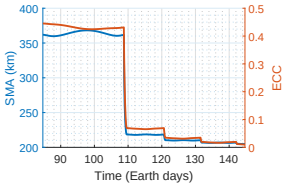

(c) Semi-major axis against eccentricity

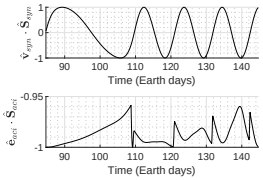

(d) Velocity direction and direction of eccentricity vector relative to the Sun

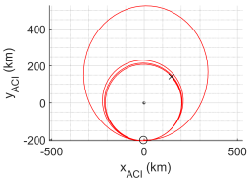

(e) Trajectory (ACI frame)

Figure D.29: Orbit shaping phase: 433 Eros, $a_c = 0.18$ mm/s^2

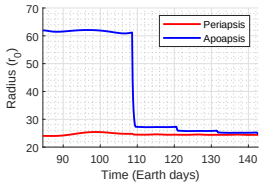

(a) Radius of periapsis and apoapsis

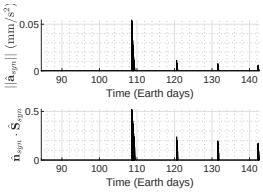

(b) Magnitude of acceleration and direction of sail normal relative to the Sun

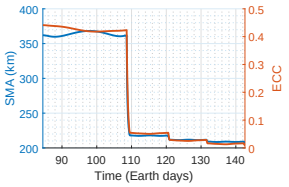

(c) Semi-major axis against eccentricity

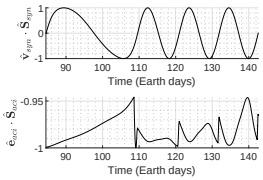

(d) Velocity direction and direction of eccentricity vector relative to the Sun

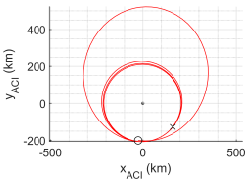

(e) Trajectory (ACI frame)

Figure D.30: Orbit shaping phase: 433 Eros, $a_c = 0.20$ mm/s^2

ZVC Radius 0.25 DU

This section presents the orbital shaping phase where the targeted capture region has a radius of 0.25 DU.

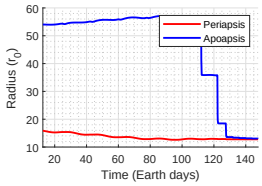

(a) Radius of periapsis and apoapsis

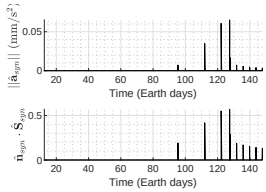

(b) Magnitude of acceleration and direction of sail normal relative to the Sun

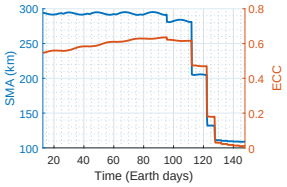

(c) Semi-major axis against eccentricity

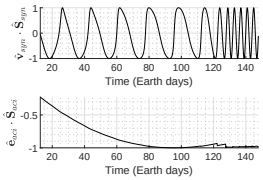

(d) Velocity direction and direction of eccentricity vector relative to the Sun

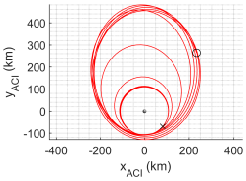

(e) Trajectory (ACI frame)

Figure D.31: Orbit shaping phase: 433 Eros, $a_c = 0.20$ mm/s^2

D.3 Low-Thrust Earth-Orbit Transfer

This section details the problem outlined in Ref. [9] for a low-Earth orbital transfer using a low-thrust propulsion system. First, the boundary conditions are given, in the original imperial units of the problem as stated in the literature, by:

$$
\begin{aligned}
p(t_0) &= 21837080.052835 \text{ ft}, & p(t_f) &= 40007346.015232 \text{ ft},\\
f(t_0) &= 0, & \sqrt{f^2(t_f)+g^2(t_f)} &= 0.73550320568829,\\
g(t_0) &= 0, & \sqrt{h^2(t_f)+k^2(t_f)} &= 0.61761258786099,\\
h(t_0) &= -0.25396764647494, & f(t_f)h(t_f)+g(t_f)k(t_f) &= 0,\\
k(t_0) &= 0, & g(t_f)h(t_f)-k(t_f)f(t_f) &\leq 0,\\
L(t_0) &= \pi \text{ rad}, & w(t_0) &= 1 \text{ lbm},\\
i(t_0) &= 28.5^\circ, & i(t_f) &= 63.4^\circ,
\end{aligned}
\tag{D.1}
$$

With this, the results are shown in Fig. D.32.

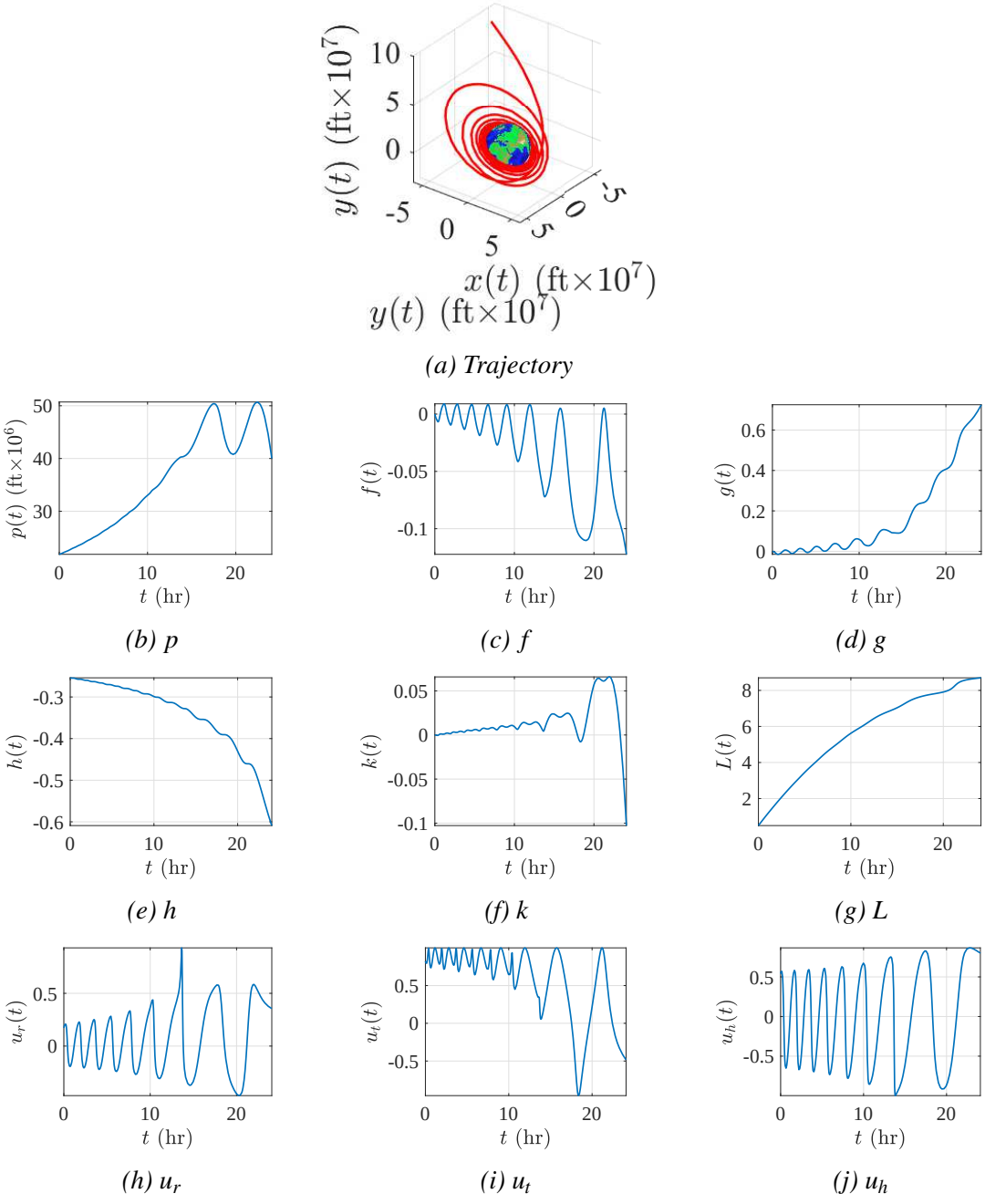

(a) Trajectory

(b) p *(c) f* *(d) g*

(e) h *(f) k* *(g) L*

(h) u_r *(i) u_t* *(j) u_h*

Figure D.32: Low-thrust Earth transfer trajectory as defined in Ref. [9]

Bibliography

[1] X. Wang, J. Li, and S. Gong, "Bifurcation of equilibrium points in the potential field of asteroid 101955 bennu," *Monthly Notices of the Royal Astronomical Society*, vol. 455, pp. 3724–3734, dec 2015.

[2] F. Scholten, F. Preusker, S. Elgner, K.-D. Matz, R. Jaumann, J. Biele, D. Hercik, H.-U. Auster, M. Hamm, M. Grott, C. Grimm, T.-M. Ho, A. Koncz, N. Schmitz, F. Trauthan, S. Kameda, S. Sugita, R. Honda, T. Morota, E. Tatsumi, Y. Cho, K. Yoshioka, H. Sawada, Y. Yokota, N. Sakatani, M. Hayakawa, M. Matsuoka, M. Yamada, T. Kouyama, H. Suzuki, C. Honda, and K. Ogawa, "The descent and bouncing path of the hayabusa2 lander MASCOT at asteroid (162173) ryugu," *Astronomy & Astrophysics*, vol. 632, p. L3, dec 2019.

[3] R. Hevner, W. Holemans, J. Puig-Suari, and R. Twiggs, "An advanced standard for cubesat," in *Proceedings of the 25th Annual AIAA/USU Conference on Small Satellites*, (Logan, UT, USA), 2011.

[4] D. J. Scheeres, *Orbital motion in strongly perturbed environments: applications to asteroid, comet and planetary satellite orbiters*. Springer, 2011.

[5] D. Vallado, *Fundamentals of astrodynamics*. Space Technology Library, fourth ed., 2013.

[6] Y. Jiang, H. Baoyin, J. Li, and H. Li, "Orbits and manifolds near the equilibrium points around a rotating asteroid," *Astrophysics and Space Science*, vol. 349, pp. 83–106, sep 2013.

[7] T. G. G. Chanut, S. Aljbaae, A. F. B. A. Prado, and V. Carruba, "Dynamics in the vicinity of (101955) bennu: solar radiation pressure effects in equatorial orbits," *Monthly Notices of the Royal Astronomical Society*, vol. 470, pp. 2687–2701, may 2017.

[8] M. L. Mota and e Evandro Marconi Rocco, "Equilibrium points stability analysis for the asteroid 21 lutetia," *Journal of Physics: Conference Series*, vol. 1365, p. 012007, oct 2019.

[9] J. T. Betts, *Practical Methods for Optimal Control and Estimation Using Nonlinear Programming*. CAMBRIDGE, Dec. 2009.

[10] R. R. Bate, D. D. Mueller, and J. E. White, *Fundamentals of Astrodynamics*. Dover Publications Inc., 1971.

[11] C. R. McInnes, *Solar Sailing: Technology, Dynamics and Mission Applications*. Chichester: Springer-Praxis, 1999.

[12] Y. Tsuda, O. Mori, R. Funase, H. Sawada, T. Yamamoto, T. Saiki, T. Endo, and J. Kawaguchi, "Flight status of ikaros deep space solar sail demonstrator," *Acta Astronautica*, vol. 69, no. 9-10, pp. 833–840, 2011.

[13] O. Mori, Y. Shirasawa, Y. Mimasu, Y. Tsuda, H. Sawada, T. Saiki, T. Yamamoto, K. Yonekura, H. Hoshino, J. Kawaguchi, and R. Funase, "Overview of IKAROS mission," in *Advances in Solar Sailing*, pp. 25–43, Springer Berlin Heidelberg, 2014.

[14] Y. Tsuda, O. Mori, R. Funase, H. Sawada, T. Yamamoto, T. Saiki, T. Endo, K. Yonekura, H. Hoshino, and J. Kawaguchi, "Achievement of ikaros — japanese deep space solar sail demonstration mission," *Acta Astronautica*, vol. 82, no. 2, pp. 183–188, 2013.

[15] L. Johnson, M. Whorton, A. Heaton, R. Pinson, G. Laue, and C. Adams, "Nanosail-d: A solar sail demonstration mission," *Acta Astronautica*, vol. 68, no. 5-6, pp. 571–575, 2011.

[16] D. Alhorn, J. Casas, E. Agasid, C. Adams, G. Laue, C. Kitts, and S. O'Brien, "NanoSail-D: The Small Satellite That Could!," in *The Small Satellite Conference*, 2011.

[17] J. Vaughn and L. D. Friedman, "Crowdfunding for space science and public engagement: The planetary society shares lessons learned," in *Space Science and Public Engagement*, pp. 245–263, Elsevier, 2021.

[18] J. Mansell, D. A. Spencer, B. Plante, A. Diaz, M. Fernandez, J. Bellardo, B. Betts, and B. Nye, "Orbit and attitude performance of the LightSail 2 solar sail spacecraft," in *AIAA Scitech 2020 Forum*, American Institute of Aeronautics and Astronautics, jan 2020.

[19] M. Leslie, J. Les, K. Pater, C.-R. Julie, and F. Andreas, *Near-Earth Asteroid (NEA) Scout*. SPACE Conferences and Exposition, American Institute of Aeronautics and Astronautics, 2014.

[20] C. Biddy and T. Svitek, "Lightsail-1 solar sail design and qualification," in *Proceedings of the 41st Aerospace Mechanisms Symposium, Jet Propulsion Laboratory, May 16-18, 2012*, 2012.

[21] L. Johnson, "Solar sail propulsion status," in *Interstellar Medium Spacecraft Technology Workshop, 2019*, 2019.

[22] D. S. Lauretta, S. S. Balram-Knutson, E. Beshore, W. V. Boynton, C. D. d'Aubigny, D. N. DellaGiustina, H. L. Enos, D. R. Golish, C. W. Hergenrother, E. S. Howell, C. A. Bennett, E. T. Morton, M. C. Nolan, B. Rizk, H. L. Roper, A. E. Bartels, B. J. Bos, J. P. Dworkin, D. E. Highsmith, D. A. Lorenz, L. F. Lim, R. Mink, M. C. Moreau, J. A. Nuth, D. C. Reuter, A. A. Simon, E. B. Bierhaus, B. H. Bryan, R. Ballouz, O. S. Barnouin, R. P. Binzel, W. F. Bottke, V. E. Hamilton, K. J. Walsh, S. R. Chesley, P. R. Christensen, B. E. Clark, H. C. Connolly, M. K. Crombie, M. G. Daly, J. P. Emery, T. J. McCoy, J. W. McMahon, D. J. Scheeres, S. Messenger, K. Nakamura-Messenger, K. Righter, and S. A. Sandford, "OSIRIS-REx: Sample return from asteroid (101955) bennu," *Space Science Reviews*, vol. 212, pp. 925–984, aug 2017.

[23] T. Gehrels, *Asteroids*. Tucson: University of Arizona Press, 1979.

[24] J. Lewis, *Mining the sky : untold riches from the asteroids, comets, and planets*. Reading, Mass: Addison-Wesley Pub. Co, 1996.

[25] V. Reddy, T. L. Dunn, C. A. Thomas, N. A. Moskovitz, and T. H. Burbine, "Mineralogy and surface composition of asteroids," in *Asteroids IV*, University of Arizona Press, 2015.

[26] A. Mainzer, F. Usui, and D. E. Trilling, "Space-based thermal infrared studies of asteroids," in *Asteroids IV*, University of Arizona Press, 2015.

[27] L. A. M. Benner, M. W. Busch, J. D. Giorgini, P. A. Taylor, and J.-L. Margot, "Radar observations of near-earth and main-belt asteroids," in *Asteroids IV*, University of Arizona Press, 2015.

[28] J. Durech, B. Carry, M. Delbo, M. Kaasalainen, and M. Viikinkoski, "Asteroid models from multiple data sources," in *Asteroids IV*, University of Arizona Press, 2015.

[29] R. P. Binzel, V. Reddy, and T. Dunn, "The near-earth object population: Connections to comets, main-belt asteroids, and meteorites," in *Asteroids IV*, University of Arizona Press, 2015.

[30] D. Vokrouhlický, W. F. Bottke, S. R. Chesley, D. J. Scheeres, and T. S. Statler, "The yarkovsky and YORP effects," in *Asteroids IV*, University of Arizona Press, 2015.

[31] W. Bottke, "Dynamical evolution of main belt meteoroids: Numerical simulations incorporating planetary perturbations and yarkovsky thermal forces," *Icarus*, vol. 145, pp. 301–331, jun 2000.

[32] J. R. Masiero, F. E. DeMeo, T. Kasuga, and A. H. Parker, "Asteroid family physical properties," in *Asteroids IV*, University of Arizona Press, 2015.

[33] J.-L. Margot, P. Pravec, P. Taylor, B. Carry, and S. Jacobson, "Asteroid systems: Binaries, triples, and pairs," in *Asteroids IV*, University of Arizona Press, 2015.

[34] D. S. Scheeres, D. Britt, B. Carry, and K. A. Holsapple, "Asteroid interiors and morphology," in *Asteroids IV*, University of Arizona Press, 2015.

[35] A. F. Cheng, A. S. Rivkin, P. Michel, J. Atchison, O. Barnouin, L. Benner, N. L. Chabot, C. Ernst, E. G. Fahnestock, M. Kueppers, P. Pravec, E. Rainey, D. C. Richardson, A. M. Stickle, and C. Thomas, "AIDA DART asteroid deflection test: Planetary defense and science objectives," *Planetary and Space Science*, vol. 157, pp. 104–115, aug 2018.

[36] E. M. Galimov, "Chelyabinsk meteorite—an ll5 chondrite," *Solar System Research*, vol. 47, no. 4, pp. 255–259, 2013.

[37] L. Gasperini, "Lake cheko and the 1908 tunguska event," *Rendiconti Lincei*, vol. 26, no. 2, pp. 97–108, 2015.

[38] L. Prockter, S. Murchie, A. Cheng, S. Krimigis, R. Farquhar, A. Santo, and J. Trombka, "The near shoemaker mission to asteroid 433 eros," *Acta Astronautica*, vol. 51, no. 1-9, pp. 491–500, 2002.

[39] C. T. Russell, H. Y. McSween, R. Jaumann, and C. A. Raymond, "The dawn mission to vesta and ceres," in *Asteroids IV*, University of Arizona Press, 2015.

[40] M. Yoshikawa, A. Fujiwara, and J. Kawaguchi, "Hayabusa and its adventure around the tiny asteroid itokawa," *Proceedings of the International Astronomical Union*, vol. 2, no. 14, 2007.

[41] M. Yoshikawa, J. Kawaguchi, A. Fujiwara, and A. Tsuchiyama, "Hayabusa sample return mission," in *Asteroids IV*, University of Arizona Press, 2015.

[42] Y. Tsuda, T. Saiki, F. Terui, S. Nakazawa, M. Yoshikawa, and S. Watanabe, "Initial achievements of hayabusa2 in asteroid proximity phase," *Transactions of the Japan Society For Aeronautical and Space Sciences*, vol. 63, no. 4, pp. 115–123, 2020.

[43] T. Ajluni, T. Linn, W. Willcockson, D. Everett, R. Mink, and J. Wood, "OSIRIS-REx. Returning the Asteroid Sample," in *2015 IEEE Aerospace Conference*, 2015.

[44] K.-H. Glassmeier, H. Boehnhardt, D. Koschny, E. Kührt, and I. Richter, "The rosetta mission: Flying towards the origin of the solar system," *Space Science Reviews*, vol. 128, pp. 1–21, jan 2007.

[45] M. A. Barucci, M. Fulchignoni, J. Ji, S. Marchin, and N. Thomas, "The flybys of asteroids 2867 steins, 21 lutetia, and 4179 toutatis," in *Asteroids IV*, University of Arizona Press, 2015.

[46] S. L. Murchie, P. C. Thomas, A. S. Rivkin, and N. L. Chabot, "Phobos and deimos," in *Asteroids IV*, University of Arizona Press, 2015.

[47] B. Cox and A. Cohen, *Forces of Nature*. William Collins, 2017.

[48] B. Bucha and F. Sansò, "Gravitational field modelling near irregularly shaped bodies using spherical harmonics: a case study for the asteroid (101955) bennu," *Journal of Geodesy*, vol. 95, apr 2021.

[49] P. Peñarroya and R. Paoli, "Orbit propagation around small bodies using spherical harmonic coefficients obtained from polyhedron shape models," *Proceedings of the International Astronomical Union*, vol. 15, pp. 203–210, oct 2021.

[50] J. Feng, R. Noomen, P. N. A. M. Visser, and J. Yuan, "Modeling and analysis of periodic orbits around a contact binary asteroid," *Astrophysics and Space Science*, vol. 357, no. 2, 2015.

[51] Y. Takahashi and D. J. Scheeres, "Small body surface gravity fields via spherical harmonic expansions," *Celestial Mechanics and Dynamical Astronomy*, vol. 119, no. 2, pp. 169–206, 2014.

[52] X. Hu and C. Jekeli, "A numerical comparison of spherical, spheroidal and ellipsoidal harmonic gravitational field models for small non-spherical bodies," *Geodesy and Geodynamics*, vol. 89, pp. 159–177, 2015.

[53] J. Sebera, A. Bezdek, and I. P. T. Henych, "Spheroidal models of the exterior gravitational field of asteroids Bennu and Castalia," *Icarus*, vol. 272, pp. 70–79, 2016.

[54] S. Reimond and O. Baur, "Spheroidal and ellipsoidal harmonic expansions of the gravitational potential of small solar system bodies. case study: Comet 67p/churyumov-gerasimenko," *Journal of Geophysical Research: Planets*, vol. 121, no. 3, pp. 497–515, 2016.

[55] D. J. Scheeres, "Orbit mechanics about asteroids and comets," *Journal of Guidance, Control, and Dynamics*, vol. 35, no. 3, pp. 987–997, 2012.

[56] V. Duibout and D. J. Scheeres, "Stability of surface motion on a rotating ellipsoid," *Celestial Mechanics and Dynamical Astronomy*, vol. 87, pp. 263–290, 2003.

[57] D. J. Scheeres, "Satellite dynamics about tri-axial ellipsoids," tech. rep., 1993.

[58] D. J. Scheeres, "Dynamics about uniformly rotating triaxial ellipsoids: Applications to asteroids," *Icarus*, vol. 110, pp. 225–238, 1994.

[59] F. Ferrari, V. Franzese, M. Pugliatti, C. Giordano, and F. Topputo, "Trajectory options for hera's milani CubeSat around (65803) didymos," *The Journal of the Astronautical Sciences*, vol. 68, pp. 973–994, sep 2021.

[60] F. Ferrari, V. Franzese, M. Pugliatti, C. Giordano, and F. Topputo, "Preliminary mission profile of hera's milani CubeSat," *Advances in Space Research*, vol. 67, pp. 2010–2029, mar 2021.

[61] N. Pushparaj, N. Baresi, and Y. Kawakatsu, "Transfers and orbital maintenance of spatial retrograde orbits for phobos exploration," *Acta Astronautica*, vol. 189, pp. 452–464, dec 2021.

[62] F. Preusker, F. Scholten, K.-D. Matz, T. Roatsch, R. Jaumann, C. Raymond, and C. Russell, "Dawn FC2 Derived Vesta DTM SPG V1.0," tech. rep., NASA Planetary Data System, 2016.

[63] B. Carry, M. Kaasalainen, C. Leyrat, W. J. Merline, J. D. Drummond, A. Conrad, H. A. Weaver, P. M. Tamblyn, C. R. Chapman, C. Dumas, F. Colas, J. C. Christou, E. Dotto, D. Perna, S. Fornasier, L. Bernasconi, R. Behrend, F. Vachier, A. Kryszczynska, M. Polinska, M. Fulchignoni, R. Roy, R. Naves, R. Poncy, and P. Wiggins, "Physical properties of esa rosetta target asteroid (21) lutetia: Shape and flyby geometry," May 2010.

[64] Y. Zhang, X. Zeng, C. Circi, and G. Vulpetti, "The motion of surface particles for the asteroid 101955 bennu," *Acta Astronautica*, vol. 163, pp. 3–10, oct 2019.

[65] Z. Li, T. Wenand, and X. Zeng, "Surface locomotion characteristics of the spherical rover in different local terrains of asteroids," in *31st AAS/AIAA Space Flight Mechanics Meeting*, 2021.

[66] Z. Li, X. Zeng, and S. Wang, "Hopping trajectory planning for asteroid surface exploration accounting for terrain roughness," *Transactions of the Japan Society for Aeronautical and Space Sciences*, vol. 64, no. 4, pp. 205–214, 2021.

[67] X. Zeng, T. Wen, Z. Li, and K. T. Alfriend, "Natural landing simulations on generated local rocky terrains for asteroid cubic lander," *IEEE Transactions on Aerospace and Electronic Systems*, pp. 1–1, 2022.

[68] L. Wu, "Modified parker's method for gravitational forward and inverse modeling using general polyhedral models," *Journal of Geophysical Research: Solid Earth*, vol. 126, oct 2021.

[69] F. F. P. Rossi, A; Marzari, "Orbital evolution around irregular bodies," *Earth Planets Space*, vol. 51, pp. 1173–1180, 1999.

[70] S. McArdle and R. P. Russell, "Point mascon global lunar gravity models," *Journal of Guidance, Control, and Dynamics*, vol. 45, pp. 815–829, may 2022.

[71] A. Rathinam and A. G. Dempster, "Octree-based mascon model for small body gravity fields," *Journal of Guidance, Control, and Dynamics*, vol. 42, pp. 2557–2567, nov 2019.

[72] A. J. Gozdziewski, Krzysztof; Maciejewski, "Nonlinear stability of the lagrangian libration points in the chermnykh proble," *Celestial Mechanics and Dynamical Astronomy*, vol. 70, pp. 41–58, 1998.

[73] V. Szebehely, *The Theory of Orbits*. Academic Press, 1967.

[74] Y. Zhang, X. Zeng, and X. Liu, "Study on periodic orbits around the dipole segment model for dumbbell-shaped asteroids," *Science China Technological Sciences*, vol. 61, pp. 819–829, sep 2017.

[75] F. C. F. Venditti and A. F. B. A. Prado, "Mapping orbits regarding perturbations due to the gravitational field of a cube," *Mathematical Problems in Engineering*, vol. 2015, pp. 1–11, 2015.

[76] E. Herrera-Sucarrat, P. L. Palmer, and R. M. Roberts, "Modeling the gravitational potential of a nonspherical asteroid," *Journal of Guidance, Control and Dynamics*, vol. 36, no. 3, pp. 790–798, 2013.

[77] H. Shen, C. M. Roithmayr, and Y. Li, "Dynamics and control of a tethered enhanced gravity tractor performing asteroid deflection," in *AAS Guidance and Control Conference*, 2018.

[78] R. A. Werner, "Spherical harmonic coefficients for the potential of a constant-density polyhedron," *Computers &amp Geosciences*, vol. 23, pp. 1071–1077, dec 1997.

[79] P. T. Wittick and R. P. Russell, "Mixed-model gravity representations for small celestial bodies using mascons and spherical harmonics," *Celestial Mechanics and Dynamical Astronomy*, vol. 131, jun 2019.

[80] B. Dachwald, H. Boehnhardt, U. Broj, U. R. M. E. Geppert, J.-T. Grundmann, W. Seboldt, P. Seefeldt, P. Spietz, L. Johnson, E. Kührt, S. Mottola, M. Macdonald, C. R. McInnes, M. Vasile, and R. Reinhard, *Gossamer Roadmap Technology Reference Study for a Multiple NEO Rendezvous Mission*, pp. 211–226. Berlin, Heidelberg: Springer Berlin Heidelberg, 2014.

[81] A. Peloni, M. Ceriotti, and B. Dachwald, "Solar sail trajectory design for a multiple near-earth asteroid rendezvous mission," *Journal of Guidance, Control, and Dynamics*, vol. 39, no. 12, pp. 2712–2724, 2016.

[82] A. Peloni, B. Dachwald, and M. Ceriotti, "Multiple near-earth asteroid rendezvous mission: solar-sailing options," *Advances in Space Research*, vol. 62, no. 8, pp. 2084–2098, 2018.

[83] G. Viavattene and M. Ceriotti, "Artificial neural networks for multiple NEA rendezvous missions with continuous thrust," *Journal of Spacecraft and Rockets*, vol. 59, pp. 574–586, mar 2022.

[84] D. Scheeres, "The effect of C22 on orbit energy and angular momentum," *Celestial Mechanics and Dynamical Astronomy*, vol. 73, no. 1/4, pp. 339–348, 1999.

[85] M. Macdonald and C. McInnes, "Realistic earth escape strategies for solar sailing," *Journal of Guidance, Control, and Dynamics*, vol. 28, no. 2, pp. 315–323, 2005.

[86] J. D. Biggs and C. R. McInnes, "Time-delayed feedback control in astrodynamics," *Journal of Guidance, Control, and Dynamics*, vol. 32, no. 6, pp. 1804–1820, 2009.

[87] T. C. Oliveira and A. F. B. A. Prado, "Evaluating orbits with potential to use solar sail for station-keeping maneuvers," in *2nd IAA Conference on Dynamics and Control of Space Systems (DYCOSS)*, International Academy of Astronautics, Mar. 2014.

[88] A. Farrés and n. Jorba, "A dynamical system approach for the station keeping of a solar sail," *The Journal of the Astronautical Sciences*, vol. 56, no. 2, pp. 199–230, 2012.

[89] A. Farrés and n. Jorba, *Station Keeping Strategies for a Solar Sail in the Solar System*, pp. 83–115. Cham: Springer International Publishing, 2016.

[90] A. Farrés, À. Jorba, J.-M. Mondelo, and B. Villac, "Periodic motion for an imperfect solar sail near an asteroid," in *Advances in Solar Sailing*, pp. 885–898, Springer Berlin Heidelberg, 2014.

[91] A. Farrés and A. Jorba, "On the station keeping of a solar sail in the elliptic sun–earth system," *Advances in Space Research*, vol. 48, no. 11, pp. 1785–1796, 2011.

[92] A. Farres and M. Ceriotti, "Solar sail station keeping of high-amplitude vertical lyapunov orbits in sun-earth system," in *63rd International Astronautical Congress (IAC 2012), Naples, Italy*, 2012.

[93] D. K. Yeomans, "Radio science results during the NEAR-shoemaker spacecraft rendezvous with eros," *Science*, vol. 289, pp. 2085–2088, sep 2000.

[94] I. Moore and M. Ceriotti, "Solar sails for perturbation relief: Application to asteroids," *Advances in Space Research*, vol. 67, pp. 3027–3044, may 2021.

[95] M. Hénon, "New families of periodic orbits in hill's problem of three bodies," *Celestial Mechanics and Dynamical Astronomy*, vol. 85, no. 3, pp. 223–246, 2003.

[96] M. Giancotti, S. Campagnola, Y. Tsuda, and J. Kawaguchi, "Families of periodic orbits in hill's problem with solar radiation pressure: application to hayabusa 2," *Celestial Mechanics and Dynamical Astronomy*, vol. 120, no. 3, pp. 269–286, 2014.

[97] D. García Yárnoz, D. J. Scheeres, and C. R. McInnes, "On the a and g families of orbits in the hill problem with solar radiation pressure and their application to asteroid orbiters," *Celestial Mechanics and Dynamical Astronomy*, vol. 121, no. 4, pp. 365–384, 2015.

[98] A. Farrés, n. Jorba, and J.-M. Mondelo, "Numerical study of the geometry of the phase space of the augmented hill three-body problem," *Celestial Mechanics and Dynamical Astronomy*, vol. 129, no. 1-2, pp. 25–55, 2017.

[99] J. Heiligers and D. J. Scheeres, "Solar-sail orbital motion about asteroids and binary asteroid systems," *Journal of Guidance, Control, and Dynamics*, vol. 41, pp. 1947–1962, sep 2018.

[100] A. Farrés, S. Soldini, and Y. Tsuda, "Jaxa's trojan asteroids mission: Trajectory design of the solar power sail and its lander," in *International Symposium on Solar Sailing 2017*, (Kyoto, Japan), 2017.

[101] E. Morrow, D. J. Scheeres, and D. Lubin, "Solar sail orbit operations at asteroids," *Journal of Spacecraft and Rockets*, vol. 38, pp. 279–286, mar 2001.

[102] J. Bookless and C. McInnes, "Control of lagrange point orbits using solar sail propulsion," *Acta Astronautica*, vol. 62, pp. 159–176, jan 2008.

[103] Y. Jiang, H. Baoyin, X. Wang, Y. Yu, H. Li, C. Peng, and Z. Zhang, "Order and chaos near equilibrium points in the potential of rotating highly irregular-shaped celestial bodies," *Nonlinear Dynamics*, vol. 83, pp. 231–252, aug 2015.

[104] Y. Jiang, Y. Yu, and H. Baoyin, "Topological classifications and bifurcations of periodic orbits in the potential field of highly irregular-shaped celestial bodies," *Nonlinear Dynamics*, vol. 81, pp. 119–140, feb 2015.

[105] Y. Jiang and H. Baoyin, "Periodic Orbit Families In The Gravitational Field Of Irregular-Shaped Bodies," *The Astronomical Journal*, vol. 152, p. 137, oct 2016.

[106] Y. Jiang, H. Baoyin, X. Wang, and H. Li, "Stability and motion around equilibrium points in the rotating plane-symmetric potential field," *Results in Physics*, vol. 10, pp. 487–497, sep 2018.

[107] Y. Jiang and H. Baoyin, "Periodic orbits related to the equilibrium points in the potential of irregular-shaped minor celestial bodies," *Results in Physics*, vol. 12, pp. 368–374, 2019.

[108] H. Yang, X. Bai, and S. Li, "Artificial equilibrium points near irregular-shaped asteroids with continuous thrust," *Journal of Guidance, Control, and Dynamics*, vol. 41, pp. 1308–1319, jun 2018.

[109] Y. Tsuda, T. Saiki, F. Terui, S. Nakazawa, M. Yoshikawa, and S. ichiro Watanabe, "Hayabusa2 mission status: Landing, roving and cratering on asteroid ryugu," *Acta Astronautica*, vol. 171, pp. 42–54, jun 2020.

[110] F. Thuillet, Y. Zhang, P. Michel, J. Biele, S. Kameda, S. Sugita, E. Tatsumi, S. R. Schwartz, and R.-L. Ballouz, "Numerical modeling of lander interaction with a low-gravity asteroid regolith surface," *Astronomy & Astrophysics*, vol. 648, p. A56, apr 2021.

[111] S. Kikuchi, N. Ogawa, O. Mori, T. Saiki, Y. Takei, F. Terui, G. Ono, Y. Mimasu, K. Yoshikawa, S. V. Wal, H. Takeuchi, H. Ikeda, A. Fujii, Y. Takao, T. Kusumoto, N. Hirata, N. Hirata, K. Shirai, T. Kouyama, S. Kameda, M. Yamada, S. Nakazawa, M. Yoshikawa, S. Tanaka, S. Sugita, S. ichiro Watanabe, and Y. Tsuda, "Ballistic deployment of the hayabusa2 artificial landmarks in the microgravity environment of ryugu," *Icarus*, vol. 358, p. 114220, apr 2021.

[112] G. Ono, F. Terui, N. Ogawa, S. Kikuchi, Y. Mimasu, K. Yoshikawa, H. Ikeda, Y. Takei, S. Yasuda, K. Matsushima, T. Masuda, T. Saiki, and Y. Tsuda, "GNC strategies and flight results of hayabusa2 first touchdown operation," *Acta Astronautica*, vol. 174, pp. 131–147, sep 2020.

[113] G. W. Hughes, M. Macdonald, C. R. McInnes, A. Atzei, and P. Falkner, "Sample return from mercury and other terrestrial planets using solar sail propulsion," *Journal of Spacecraft and Rockets*, vol. 43, pp. 828–835, jul 2006.

[114] M. Macdonald and C. R. McInnes, "Solar sail capture trajectories at mercury," in *AIAA/AAS Astrodynamics Specialist Conference and Exhibit*, 2002.

[115] A. S. Goldhaber and M. M. Nieto, "New geomagnetic limit on the mass of the photon," *Physical Review Letters*, vol. 21, pp. 567–569, aug 1968.

[116] L.-C. Tu, J. Luo, and G. T. Gillies, "The mass of the photon," *Reports on Progress in Physics*, vol. 68, pp. 77–130, nov 2004.

[117] A. Peloni, *Solar-sail mission design for multiple near-Earth asteroid rendezvous*. Thesis, 2018.

[118] M. Ceriotti and C. R. McInnes, "Generation of optimal trajectories for earth hybrid pole sitters," *Journal of Guidance, Control, and Dynamics*, vol. 34, pp. 847–859, may 2011.

[119] L. Johnson, R. Young, N. Barnes, L. Friedman, V. Lappas, and C. McInnes, "Solar sails: Technology and demonstration status," *International Journal of Aeronautical and Space Sciences*, vol. 13, pp. 421–427, dec 2012.

[120] M. E. Leipold and O. Wagner, "Mercury sun-synchronous polar orbits using solar sail propulsion," *Journal of Guidance, Control, and Dynamics*, vol. 19, pp. 1337–1341, nov 1996.

[121] W. K. Wilkie, J. E. Warren, L. G. Horta, K. H. Lyle, J.-N. Juang, J. D. Littell, R. G. Bryant, M. W. Thomson, P. E. Walkemeyer, D. V. Guerrant, D. A. Lawrence, S. C. Gibbs, E. H. Dowell, and A. F. Heaton, "Heliogyro solar sail research at NASA," in *Advances in Solar Sailing*, pp. 631–650, Springer Berlin Heidelberg, 2014.

[122] G. Mengali and A. A. Quarta, "Solar sail near-optimal circular transfers with plane change," *Journal of Guidance, Control, and Dynamics*, vol. 32, pp. 456–463, mar 2009.

[123] M. Macdonald, C. McGrath, T. Appourchaux, B. Dachwald, W. Finsterle, L. Gizon, P. C. Liewer, C. R. McInnes, G. Mengali, W. Seboldt, T. Sekii, S. K. Solanki, M. Velli, R. F. Wimmer-Schweingruber, P. Spietz, and R. Reinhard, "Gossamer roadmap technology reference study for a solar polar mission," in *Advances in Solar Sailing*, pp. 243–257, Springer Berlin Heidelberg, 2014.

[124] E. Morrow, D. Scheeres, and D. Lubin, "Solar sail orbit operations at asteroids," in *Astrodynamics Specialist Conference*, American Institute of Aeronautics and Astronautics, Aug. 2000.

[125] M. Ceriotti, G. Viavattene, I. Moore, A. Peloni, C. R. McInnes, and J. T. Grundmann, "Sailing at the brink – the no-limits of near-/now-term-technology solar sails and SEP spacecraft in (multiple) NEO rendezvous," *Advances in Space Research*, vol. 67, pp. 3012–3026, may 2021.

[126] D. J. Werner, Robert A.; Scheeres, "Exterior gravitation of a polyhedron derived and compared with harmonic and mascon gravitation representations of asteroid 4769 castalia," *Celestial Mechanics and Dynamical Astronomy*, vol. 65, pp. 313–344, 1996.

[127] W. S. Koon, J. E. Marsden, S. D. Ross, M. Lo, and D. J. Scheeres, "Geometric mechanics and the dynamics of asteroid pairs," *Annals of the New York Academy of Sciences*, vol. 1017, pp. 11–38, may 2004.

[128] D. J. Scheeres, *Orbital Motion in Strongly Perturbed Environments*. Springer, 2012.

[129] C. R. McInnes, A. J. C. McDonald, J. F. L. Simmons, and E. W. MacDonald, "Solar sail parking in restricted three-body systems," *Journal of Guidance, Control, and Dynamics*, vol. 17, pp. 399–406, mar 1994.

[130] W. E. Wiesel, *Modern Astrodynamics*. Aphelion, second ed., 2010.

[131] N. Shinozaki, M. Sibuya, and K. Tanabe, "Numerical algorithms for the moore-penrose inverse of a matrix: Direct methods," *Annals of the Institute of Statistical Mathematics*, vol. 24, pp. 193–203, dec 1972.

[132] M. Ceriotti and J. P. Sanchez, "Control of asteroid retrieval trajectories to libration point orbits," *Acta Astronautica*, vol. 126, pp. 342–353, 2016.

[133] R. F. Stengel, *Optimal Control and Estimation*. Dover Publications Inc, 1994.

[134] J. D. Biggs and C. R. McInnes, "An optimal gains matrix for time-delayed feedback control," in *2nd IFAC conference on theControl of Chaos*, 2009.

[135] S. Jain and P. Tsiotras, "Trajectory optimization using multiresolution techniques," *Journal of Guidance, Control, and Dynamics*, vol. 31, pp. 1424–1436, sep 2008.

[136] M. A. Patterson and A. V. Rao, "GPOPS II: A MATLAB Software for Solving Multiple-Phase Optimal Control Problems Using hp–Adaptive Gaussian Quadrature Collocation Methods and Sparse Nonlinear Programming," *ACM Transactions on Mathematical Software*, vol. 39, no. 3, 2013.

[137] S. Kameswaran and L. T. Biegler, "Convergence rates for direct transcription of optimal control problems using collocation at radau points," *Computational Optimization and Applications*, vol. 41, pp. 81–126, nov 2007.

[138] I. Babuška and A. Miller, "The post-processing approach in the finite element method—part 1: Calculation of displacements, stresses and other higher derivatives of the displacements," *International Journal for Numerical Methods in Engineering*, vol. 20, pp. 1085–1109, jun 1984.

[139] M. A. Patterson and A. V. Rao, *GPOPS II: A general-purpose MATLAB software for solving multiple-phase optimal control problems*, Dec. 2016.

[140] D. J. Scheeres, S. J. Ostro, R. S. Hudson, and R. A. Werner, "Orbits close to asteroid 4769 castalia," *Icarus*, vol. 121, no. 1, pp. 67–87, 1996.

[141] S. Tardivel and D. J. Scheeres, "Ballistic deployment of science packages on binary asteroids," *Journal of Guidance, Control, and Dynamics*, vol. 36, pp. 700–709, may 2013.

[142] S. Tardivel, D. J. Scheeres, P. Michel, S. V. wal, and P. Sánchez, "Contact motion on surface of asteroid," *Journal of Spacecraft and Rockets*, vol. 51, pp. 1857–1871, nov 2014.

[143] S. Tardivel, *The Deployment of Scientific Packages to Asteroid Surfaces*. PhD thesis, University of Colorado, 2014.

[144] R. S. Hudson and S. J. Ostro, "Shape of asteroid 4769 castalia (1989 pb) from inversion of radar images," *Science*, vol. 263, pp. 940–943, Feb. 1994.

[145] R. Gaskell, "Gaskell eros shape model v1.0. near-a-msi-5-erosshape-v1.0.," tech. rep., NASA Planetary Data System, 2008.

[146] A. D'Ambrosio, C. Circi, and X. Zeng, "Solar-photon sail hovering orbits about single and binary asteroids," *Advances in Space Research*, vol. 63, pp. 3691–3705, jun 2019.

[147] B. F. Villac and D. J. Scheeres, "Escaping trajectories in the hill three-body problem and applications," *Journal of Guidance, Control, and Dynamics*, vol. 26, no. 2, pp. 224–232, 2003.

[148] J. P. Bookless, *Dynamics, Stability and Control of Displaced Non-Keplerian Orbits*. PhD thesis, University of Glasgow, 2006.

[149] M. Ceriotti and C. R. McInnes, "Natural and sail-displaced doubly-symmetric lagrange point orbits for polar coverage," *Celestial Mechanics and Dynamical Astronomy*, vol. 114, no. 1-2, pp. 151–180, 2012.

[150] W. S. Koon, M. W. Lo, J. E. Marsden, and S. D. Ross, *Dynamical systems, the three-body problem, and space mission design*. Marsden Books, 2011.

[151] L. A. D'Amario, *Minimum Impulse Three-Body Trajectories*. PhD thesis, Massachusetts Institute of Technology, 1973.

[152] R. W. Farquhar, D. P. Muhonen, C. R. Newman, and H. S. . Heubergerg, "Trajectories and orbital maneuvers for the first libration-point satellite," *Journal of Guidance and Control*, vol. 3, pp. 549–554, nov 1980.

[153] G. Gomez, A. Jorba, J. Masdemont, and C. Simo, "A dynamical systems approach for the analysis of the soho mission," in *3rd International Symposium on Spacecraft Flight Dynamics, Darmstadt, Germany*, 1991.

[154] K. C. Howell, D. L. Mains, and B. T. Barden, "Transfer trajectories from earth parking orbits to sun-earth halo orbits," in *AAS/AIAA SpaceFlight Mechanics Meeting, Cocoa Beach, Florida*, 1994.

[155] J. J. Guzmán, J. M. Longuski, and J. E. Prussing, *Optimal Control with Aerospace Applications*. Springer New York, Nov. 2013.

[156] Z. Wang and G. P. Rangaiah, "Application and analysis of methods for selecting an optimal solution from the pareto-optimal front obtained by multiobjective optimization," *Industrial &amp Engineering Chemistry Research*, vol. 56, pp. 560–574, jan 2017.

[157] C. de Boor, *A Practical Guide to Splines*. Springer New York, Nov. 2001.

[158] M. Ceriotti, B. L. Diedrich, and C. R. McInnes, "Novel mission concepts for polar coverage: An overview of recent developments and possible future applications," *Acta Astronautica*, vol. 80, pp. 89–104, nov 2012.

[159] B. A. Plante, D. A. Spencer, B. Betts, S. Chait, J. M. Bellardo, A. Diaz, and I. Pham, "Lightsail 2 adcs: From simulation to mission readiness," in *Fourth International Symposium on Solar Sailing*, 2017.

[160] B. Wie, "Solar sail attitude control and dynamics, part 1," *Journal of Guidance, Control, and Dynamics*, vol. 27, pp. 526–535, jul 2004.

[161] T. Timmons, G. Bailet, J. Beeley, and C. McInnes, "Mars atmospheric characterization with a ChipSat swarm," *Journal of Spacecraft and Rockets*, pp. 1–8, mar 2021.

[162] T.-M. Ho, V. Baturkin, C. Grimm, J. T. Grundmann, C. Hobbie, E. Ksenik, C. Lange, K. Sasaki, M. Schlotterer, M. Talapina, N. Termtanasombat, E. Wejmo, L. Witte, M. Wrasmann, G. Wübbels, J. Rößler, C. Ziach, R. Findlay, J. Biele, C. Krause, S. Ulamec, M. Lange, O. Mierheim, R. Lichtenheldt, M. Maier, J. Reill, H.-J. Sedlmayr, P. Bousquet, A. Bellion, O. Bompis, C. Cenac-Morthe, M. Deleuze, S. Fredon, E. Jurado, E. Canalias, R. Jaumann, J.-P. Bibring, K. H. Glassmeier, D. Hercik, M. Grott, L. Celotti, F. Cordero, J. Hendrikse, and T. Okada, "MASCOT—the mobile asteroid surface scout onboard the hayabusa2 mission," *Space Science Reviews*, vol. 208, pp. 339–374, apr 2016.

[163] L. Niccolai, M. Bassetto, A. A. Quarta, and G. Mengali, "A review of smart dust architecture, dynamics, and mission applications," *Progress in Aerospace Sciences*, vol. 106, pp. 1–14, apr 2019.

[164] A. A. Quarta, G. Mengali, and L. Niccolai, "Smart dust option for geomagnetic tail exploration," *Astrodynamics*, vol. 3, pp. 217–230, aug 2019.

[165] R. Jaumann, D. A. Williams, D. L. Buczkowski, R. A. Yingst, F. Preusker, H. Hiesinger, N. Schmedemann, T. Kneissl, J. B. Vincent, D. T. Blewett, B. J. Buratti, U. Carsenty, B. W. Denevi, M. C. D. Sanctis, W. B. Garry, H. U. Keller, E. Kersten, K. Krohn, J.-Y. Li, S. Marchi, K. D. Matz, T. B. McCord, H. Y. McSween, S. C. Mest, D. W. Mittlefehldt,

S. Mottola, A. Nathues, G. Neukum, D. P. O'Brien, C. M. Pieters, T. H. Prettyman, C. A. Raymond, T. Roatsch, C. T. Russell, P. Schenk, B. E. Schmidt, F. Scholten, K. Stephan, M. V. Sykes, P. Tricarico, R. Wagner, M. T. Zuber, and H. Sierks, "Vesta's shape and morphology," *Science*, vol. 336, pp. 687–690, may 2012.

[166] S. J. Ostro, J. F. Chandler, A. A. Hine, K. D. Rosema, I. I. Shapiro, and D. K. Yeomans, "Radar images of asteroid 1989 PB," *Science*, vol. 248, pp. 1523–1528, jun 1990.

[167] J. Breithaupt, *New Understanding Physics for Advanced Level*. OUP Oxford, fourth ed., 1999.

[168] Z. Liu, M. Fang, L. Shi, Z. Chen, J. Li, H. Long, and W. Zhu, "Numerical and experimental analyses of component failure risk in a mobile phone under drop test," *IEEE Transactions on Components, Packaging and Manufacturing Technology*, vol. 12, pp. 69–79, jan 2022.

[169] J.-H. Choi and S.-I. Moon, "The dead band control of LTC transformer at distribution substation," *IEEE Transactions on Power Systems*, vol. 24, pp. 319–326, feb 2009.

[170] M. J. H. Walker, B. Ireland, and J. Owens, "A set modified equinoctial orbit elements," *Celestial Mechanics*, vol. 36, pp. 409–419, aug 1985.

[171] B. C. Carlson, *Digital library of mathematical functions*, ch. 19. Ames Laboratory, Iowa State University, 2001.

[172] B. C. Carlson, "Numerical computation of real or complex elliptic integrals," *Numerical Algorithms*, vol. 10, no. 1, pp. 13–26, 1995.

[173] W. H. Press, S. A. Teukolsky, W. T. Vetterling, and B. P. Flannery, *Numerical Recipes: The Art of Scientific Computing*. Cambridge University Press, third ed., 2007.

[174] C. Neese, "Radar shape models of small bodies compilation bundle v1.0," 2020.

[175] C. Bennett, D. DellaGiustina, K. Becker, T. Becker, K. Edmundson, D. Golish, R. Bennett, K. Burke, C. Cue, B. Clark, J. Contreras, J. Deshapriya, C. D. dAubigny, G. Fitzgibbon, E. Jawin, T. Nolan, N. Porter, M. Riehl, H. Roper, B. Rizk, Y. Tang, Z. Zeszut, R. Gaskell, E. Palmer, J. Weirich, M. A. Asad, L. Philpott, M. Daly, O. Barnouin, H. Enos, and D. Lauretta, "A high-resolution global basemap of (101955) bennu," *Icarus*, vol. 357, p. 113690, mar 2021.

[176] L. Jorda, R. W. Gaskell, M. K. Kaasalainen, and B. Carry, "Rosetta shape model of asteroid lutetia v1.0," 2013.

[177] R. Schulz, H. Sierks, M. Küppers, and A. Accomazzo, "Rosetta fly-by at asteroid (21) lutetia: An overview," *Planetary and Space Science*, vol. 66, pp. 2–8, jun 2012.

[178] J. Torppa, M. Kaasalainen, T. Michałowski, T. Kwiatkowski, A. Kryszczyńska, P. Denchev, and R. Kowalski, "Shapes and rotational properties of thirty asteroids from photometric data," *Icarus*, vol. 164, pp. 346–383, aug 2003.

[179] D. Cielaszyk and B. Wie, "New approach to halo orbit determination and control," *Journal of Guidance, Control, and Dynamics*, vol. 19, pp. 266–273, mar 1996.

[180] M. Hénon, "Numerical exploration of the restricted problem," *Astronomy and Astrophysics*, vol. 1, pp. 223–238, 1969.

[181] M. Hénon, "Vertical stability of periodic orbits in the restricted problem," *Celestial Mechanics*, vol. 8, no. 2, pp. 269–272, 1973.

[182] M. Henon, "Vertical stability of periodic orbits in the restricted problem," *Astronomy and Astrophysics*, 1973.

[183] M. Hénon, "Vertical stability of periodic orbits in the restricted problem," *Astronomy and Astrophysics Supplement Series*, vol. 30, pp. 317–321, 1974.